A Systematic X-ray Spectroscopic Study of Thermonuclear Supernova Remnants

BY

Cole Nicholas Treyturik

A thesis submitted to the

Faculty of Graduate and Postdoctoral Studies

of The University of Manitoba

in partial fulfilment of the requirements

of the degree of

DOCTOR OF PHILOSOPHY

Department of Physics and Astronomy

University of Manitoba

Winnipeg, Manitoba, Canada

Thesis Advisors
Dr. Samar Safi-Harb
Dr. Gilles Ferrand

Author
Cole Nicholas Treyturik

A Systematic X-ray Spectroscopic Study of Thermonuclear Supernova Remnants

Abstract

Thermonuclear supernovae (SNe) are catastrophic explosions that occur when white dwarfs – the compact remnants of low-mass stars – experience runaway nuclear burning. While it is commonly believed that these explosions emerge from white dwarf stars in binary systems, the exact mechanisms by which these explosions proceed are not fully understood. It is possible, however, to determine a number of the properties of one of these explosions by examining its supernova remnant (SNR). In the interest of connecting these supernova remnants to their supernova progenitors, we perform a systematic spatially-resolved X-ray spectroscopic study of a selection of 15 SNRs that are known to be, believed to be, or which have been suspected of being of a thermonuclear origin. We make use primarily of data from the *XMM-Newton* space telescope, whose sensitivity – combined with its strong spectral and angular resolution – affords us a powerful tool to study the spectra of these objects. For one remnant, we instead make use of data from the *Chandra* space telescope, whose superior angular resolution allows us to examine more closely the thermal-emitting regions for one of our smallest and youngest targets.

To remove possible sources of bias, we make use of an algorithm that generates regions based on surface brightness to determine the extent and distribution of the regions used in

Thesis Advisors
Dr. Samar Safi-Harb
Dr. Gilles Ferrand

Author
Cole Nicholas Treyturik

this study. Using one- or two-component models of thermal plasmas, we determine a variety of physical parameters for each of these regions, including the abundances for a variety of elements between O and Fe. We then compare these abundances to a collection of 335 individual models from 11 sets of simulations of supernova nucleosynthesis yields. We find a wide range of agreement between our observations and the models: while for some objects there is strong agreement between the models and observations, in general, the observed abundances do not match the entirety of the predicted yields for any of the models. Despite this, we present our best estimates for the progenitor details of each SNR based on the models that best reproduce their observed abundances, additionally addressing the progenitor classification for several objects for which this has long been debated. We also discuss a number of limitations present in the current models that may have lead to these disagreements, identifying reaction rates, dimensionality, metallicity, and explosion energy as four possible areas for future simulations to consider. We close by considering the possibility of future work, addressing additional tools, targets, and methods that could lend themselves to such a study.

Acknowledgments

The research communicated within these pages was financially supported by my advisor, Dr. Samar Safi-Harb, through the Natural Sciences and Engineering Research Council of Canada (NSERC) Discovery Grants and Canada Research Chair programs; and by the University of Manitoba Graduate Fellowship (UMGF).

This research has made use of data obtained from the *XMM-Newton* Science Archive and *Chandra* Data Archive maintained by the ESAC Science Data Centre and *Chandra* X-ray Center (CXC), respectively. Further, this research made use of the *XMM-Newton* Science Analysis Software (SAS), developed by the *XMM-Newton* Science Operations Centre; the *Chandra* Interactive Analysis of Observations (CIAO), developed by the CXC; and the XSPEC spectral fitting package developed and maintained by the HEASARC at NASA's Goddard Space Flight Center. We have also made extensive use of NASA's Astrophysics Data System, and the University of Manitoba's high-energy catalogue of supernova remnants, SNRcat.

Words cannot describe the immense appreciation I have for my supervisor, Dr. Samar Safi-

Harb. From the very beginning when I first approached her for an undergraduate summer research position up until now at the end of my degree, she has been nothing but supportive of my efforts, and her infinite patience, guidance, and seemingly boundless knowledge has helped shape this work into what it is today – to say nothing to what it's done for me as a person. Similar thanks must go to my co-supervisor, Dr. Gilles Ferrand, whose insights and suggestions played a pivotal role in both shaping this project and keeping it on track.

My appreciation naturally extends to the members of my committee: both the internal members, Dr. Christopher O'Dea and Dr. Andreas Shalchi, for their time and feedback over the years, which has only served to strengthen this work; and the external member, Dr. Falk Herwig, for his comprehensive and detailed feedback on this manuscript that has led to the revisions found within this final version.

Thanks go out to the support staff in the University of Manitoba's Department of Physics and Astronomy, with a special thanks going to Susan Beshta for taking on so much of the headache that is bureaucracy. I must of course thank the members of the Extreme Astrophysics Group here at the University of Manitoba – both past and present – for all of their support and help over the years, and for being such a wonderful group of people. Thanks in particular to Chelsea Braun, Brydyn Mac Intyre, and Austin MacMaster, whose support and help were invaluable, with whom my conversations were always educational or entertaining, and whose struggles with the software showed me that the issues I frequently encountered were (probably) not my fault.

Outside of academia, I would like to thank my late aunt Teri, without whose generosity my time at the University of Manitoba would have gone much differently. I cannot reasonably thank my parents enough, for the endless and eternal love and support that they have pro-

vided me throughout my life, and for the stability and comfort it has afforded me through these long years. Finally, I have to thank little Mica, who – even though she's since passed – has always been able to make me smile, even in hard times. I miss you, little love.

Per ardua ad astra.

Contents

List of Figures

List of Tables

List of Abbreviations

ACIS Advanced CCD Imaging Spectrometer

ATHENA Advanced Telescope for High Energy Astrophysics

AXIS Advanced X-ray Imaging Satellite

CC Core-Collapse

CCD Charge-Coupled Device

CIAO Chandra Interactive Analysis of Observations

CIE Collisional Ionization Equilibrium

CO Carbon-Oxygen

CSM Circumstellar Medium

DD Double-Degenerate

EM Emission Measure

EPIC European Photon Imaging Camera

ESA European Space Agency

ESAS Extended Source Analysis Software

FITS Flexible Image Transport System

FWHM Full Width at Half Maximum

GTI Good Time Interval

HEASARC High Energy Astrophysics Science Archive Research Center

HRC High Resolution Camera

ISM Interstellar Medium

JAXA Japan Aerospace Exploration Agency

JWST James Webb Space Telescope

LMC Large Magellanic Cloud

MOS Metal-Oxide Semiconductor

NASA National Aeronautics and Space Administration

NEI Non-Equilibrium Ionization

OM Optical Monitor

QE Quantum Efficiency

RGS Reflection Grating Spectrometer

SAS Science Analysis System

SD Single-Degenerate

SN(e) Supernova(e)

SNR(s) Supernova Remnant(s)

SOC Science Operations Center

TN Thermonuclear

WD White Dwarf

XRISM X-Ray Imaging and Spectroscopy Mission

XSPEC X-ray Spectral Fitting Package

1

Introduction

1.1 Motivation

Since time immemorial, humanity has looked up at the night sky with wonder. In our endless pursuit of truth, we have transformed what began as a realm of myth and legend into one of curiosity and discovery, pulling aside the veil of ignorance to grasp at the knowledge

that lies beyond. And yet, no matter how deep we gaze, each answer reveals a new question lurking beneath, another stitch that needs be added to the endlessly growing tapestry that is human understanding. Despite this, one question – and a seemingly simple one at that – had remained unanswered since nigh the beginning: where did we come from? While it was originally answered through the groundbreaking work of Burbidge, Burbidge, Fowler, & Hoyle (1957), it was not until 1973 that Dr. Carl Sagan would give the world an answer as simple as the question itself: we are made of star stuff.

Though evocative, Dr. Sagan's statement was not without merit, for he referred not to the source of *us* so much as to the source of what we *are*. Like all of the matter in the Universe, we are made of the elements. At present, there are 118 elements recognized by the International Union of Pure and Applied Chemistry – from the abundant hydrogen that makes up an estimated 75% of the matter in the Universe to the man-made oganesson whose half-life is a mere 0.7 ms – but that hasn't always been the case. Shortly after the Big Bang, the first particles formed: quarks and electrons. Shortly after that, the quarks aggregated to form protons and neutrons, and soon after that, temperatures cooled enough to allow these new particles to combine to form the simplest of elements in a process known as big bang nucleosynthesis. This cooling continued, however, and eventually, the conditions were no longer right to allow for nucleosynthesis to continue. At this point, the physical Universe was little more than hydrogen and helium.

Clearly, that is no longer the case, which begs the question: where did the other elements come from? Over time, gravity would bring this matter together, forming clouds that would collapse under their own gravity, giving birth to the first stars. Given that nucleosynthesis is a process that requires extreme temperatures and pressures, it was only there, deep in the

hearts of these celestial giants, that the conditions were right to allow for nucleosynthesis to continue, and it is there that we begin to see the creation of new elements. The lifetime of a star is spent mostly on the main sequence, performing nuclear fusion deep in their cores to combine hydrogen into helium. But stellar nucleosynthesis is not limited to this single reaction: the more massive the star, the more extreme the conditions present within its core, and once it exhausts its hydrogen fuel, the heavier and more complex the elements it can create. But this process, too, has a limit, with even the most massive of stars only being able to produce elements up to iron. It takes conditions even more extreme than those found in the hearts of the most massive of stars to reach beyond this point.

Enter: the supernova (SN). Though not the only such source, as the relatively recent discovery of neutron star mergers has shown, these tremendous, cataclysmic explosions caused by the deaths of certain stars are one of the few events in the Universe where the conditions are right to create some of the heaviest elements. These explosions come in two main types, based upon what kind of star they emerge from. The first of these types arises from the death of massive stars – those with a mass greater than $8M_{\odot}$. While on the main sequence, these stars burn through their fuel at a rapid pace, building up layer after layer of heavier and heavier elements. When their core becomes mostly iron, the reactions that create these elements will no longer produce enough energy to support the star against its own gravity, and so they begin to collapse, triggering a violent rebound that will ultimately tear the star apart in what is known as a core-collapse (CC) supernova.

The second type of supernova arises from a much different source: not the death of a massive star, but rather the death of a comparatively less-massive white dwarf star (WD). When a star isn't massive enough to undergo a core-collapse, its death is much less eventful: it will

gradually shed its outer layers until all that is left is its compact, inert core, which becomes known as a white dwarf. While these stars are normally stable, those white dwarfs that end up in binary systems can sometimes find themselves accreting mass from their companion. Should the white dwarf accrete enough mass, the temperatures inside the white dwarf enter a runaway state, temporarily reigniting nuclear fusion before it quickly finds itself torn apart in a thermonuclear (sometimes referred to as a "Type Ia") supernova.

Regardless of from where these events arise, they have in common that, for a short time, they create conditions that are so extreme that some of the heaviest elements in the Universe can be created in what is known as supernova nucleosynthesis. The products of supernova nucleosynthesis are most commonly found in what remains of these stars after their deaths – what are referred to as supernova remnants (SNRs). These remnants are structures created by the death of a star: clouds of gas and dust composed and comprised of the products of supernova nucleosynthesis, which gradually expand over time to spread those products throughout the nearby Universe, facilitating the birth of the next generation of stars – whose compositions differ from those of their forebears – and the planets that accompany them.

By understanding how these elements are made, we are thus able to understand more about where we came from, and so – in the pursuit of truth – it is our duty to do just that. One might expect it to follow that, in order to do so, we would turn to a study of supernova explosions themselves, but this proves problematic for the simple reason that supernova explosions are highly transient in nature: they do not last long, and within our own galaxy, where we would be best able to study them, there have been precious few within the course of written history, and none that we know of within living memory. We are fortunate, then, that we can turn back the clock on these explosions through study of their remnants instead.

Through the use of X-ray spectroscopy, we can learn much about these supernova remnants, which allows us to in turn learn much about their environments, the properties of their progenitor explosion, and the elements synthesised within. By comparing these observed properties to those theorised through simulations of supernova events, it is possible to determine what kind of supernova created these remnants, even without directly observing the explosion itself. However, this method is not without its flaws: the complexities involved in simulating an event as dynamic and energetic as a supernova means that assumptions must be made when creating these models. This in turn may lead to disagreements between observation and theory, even when most of the main assumptions of a model would prove right.

We thus embark upon a journey to perform such an analysis. As there are far more known supernova remnants than one person could conceivably study within the confines of a few years, we choose to limit ourselves to the study of a selection of supernova remnants whose progenitor explosions are known to be, believed to be, or which have been accused of being of a thermonuclear origin. To that end, our objectives are as follows:

(i) To perform a spatially-resolved spectroscopic study on each of the chosen SNRs, in order to determine information about their environment, and specifically to determine the abundances of the ejecta within them;

(ii) To determine the properties of the supernovae that led to the creation of each of these remnants by comparing the abundances and properties noted above to the theoretical yields from the latest models of supernova nucleosynthesis;

(iii) To determine which of the theoretical models noted above produce the most consistent results, and to determine any discrepancies between theory and observation, so as

to provide feedback to the theoretical modelling community; and

(iv) To draw any conclusions that may be found regarding each of the SNRs considered within this study.

1.2 Outline

The chapters within this thesis are arranged as follows:

Chapter 1 This chapter provides an introduction to the subjects of supernovae and their remnants, establishes our objectives, and provides a philosophical motivation for our study.

Chapter 2 This chapter provides a theoretical description of a supernova remnant, detailing their classification and evolution, and explains the mechanisms responsible for the X-ray emission that is the focus of this study.

Chapter 3 This chapter describes the explosion of a thermonuclear supernova, including their origins as white dwarfs, and details the nucleosynthetic models used in this study.

Chapter 4 This chapter describes the detectors, instruments, and methodologies used in this study, including region selection, spectroscopy, and spectral modelling.

Chapter 5 This chapter introduces the criteria used for target selection, and provides details for all of the objects that were selected as targets.

Chapter 6 This chapter details the observations used in this work, and the process of data reduction.

Chapter 7 This chapter covers the spectroscopic analysis performed for this work, presenting results on a per-object basis. It also describes the results of our nucleosynthesis analysis for each object, presenting a comparison between the results of our spectroscopic study and the many models of supernova nucleosynthesis. This chapter contains work which has been submitted for publication, as well as work that is being prepared for additional publications.

Chapter 8 This chapter presents our findings on a broader scale, offering additional insights on some of the more interesting results of our study. As in Chapter 7, this chapter contains work which has been submitted for publication, as well as work that is being prepared for additional publications.

Chapter 9 This chapter summarizes our findings, and provides some possible avenues for future work on this subject.

As stated above, a portion of the work in this thesis has been submitted for publication in the following paper:

(i) Treyturik, Braun, Safi-Harb, Fryer, & Ferrand (in press),"Revisiting the Supernova Engines in the 3C 397 and W49B Supernova Remnants." arXiv:2512.01176

Further, the remaining work is in the process of being prepared for publication across multiple papers. The content of one of these papers has previously been presented in part:

(ii) Treyturik, Safi-Harb, & Ferrand (2024), "The many faces of type Ia SNRs: What can X-Ray observations tell us about their progenitors and explosion mechanism?" Oral presentation at the Supernova Remnants III conference in Greece with papers currently under preparation.

As well as the above, the results presented in within this work is being prepared for publication in the following papers:

(iii) Treyturik, Safi-Harb, & Ferrand, "A Systematic Study of Type Ia Supernova Remnants: Using Nucleosynthesis to Constrain their Supernova Progenitors."

(iv) Treyturik, Safi-Harb, & Ferrand, "A Possible Double-Degenerate Origin for Kepler's SNR."

Finally, in addition to the work mentioned above that has been submitted for publication, the author has made contributions to the following works that have not been included in this thesis, but are relevant to future work and perspectives discussed in Chapter 9:

(v) Safi-Harb et al. (2023), "From Stellar Death to Cosmic Revelations: Zooming in on Compact Objects, Relativistic Outflows and Supernova Remnants with AXIS." arXiv:2311.07673

(vi) The AXIS Collaboration et al. (2025), "The Advanced X-ray Imaging Satellite Community Science Book". arXiv:2511:00253

For the above-mentioned AXIS publications, the author has contributed simulations and text based on work conducted for this thesis.

1.3 A Note on Nomenclature

The Minkowski-Zwicky supernova classification scheme, first proposed in 1941, and from which the term "Type Ia supernova" is derived, is still in use today. However, this scheme is based entirely upon *observable* properties of the supernova – namely, the appearance of

its spectrum, and the behaviour of its light curve. When it was discovered that Type Ia supernovae appeared to originate from the thermonuclear detonation of white dwarf stars, it remained common parlance to refer to these supernovae as "Type Ia" supernovae, rather than as "thermonuclear" supernovae. While it is not entirely inaccurate to use this naming convention – all thermonuclear supernovae observed so far do appear to have resulted in a Type Ia supernova – it can be at times confusing, especially given that the term "core-collapse" can be used to refer to any of the other types of supernovae in the Minkowski-Zwicky classification scheme. In this work, we opt to use the term "Type Ia supernova (SN Ia)" solely when referring to the observable properties of the supernova. When referring to any physical properties, we instead use the term "thermonuclear supernova."

2

Supernova Remnants

A supernova remnant is formed in the immediate aftermath of a supernova, as the material leftover from the explosion is violently ejected from the system. This ejected material forms an outwardly-expanding shock wave that travels at supersonic speeds – typically well in excess of $5 \times 10^3 \ \mathrm{km\,s^{-1}}$ – sweeping up the surrounding interstellar medium (ISM) and heating the swept-up material to temperatures of millions of degrees. This in turn creates a rapidly

expanding shell of hot, ionised gas that emits at various wavelengths, but which is most prominent in the X-ray and radio regimes. Over time, as the shock wave propagates, it compresses and energises the interstellar medium, creating the structure that we identify as a supernova remnant. These supernova remnants undergo several evolutionary stages before ultimately merging with the surrounding ISM, enriching it with heavy elements synthesised during the supernova explosion. Herein, we present a summary of the supernova remnant, detailing their morphological classifications and the several stages of their evolution. We also discuss their X-ray emissions, detailing the many forms in which it comes and the processes responsible for each.

This chapter was written using the following primary sources: the texts *Physics and Evolution of Supernova Remnants* by Vink (2020), and *Exploring the X-ray Universe* by Seward & Charles (2010); and the chapter *Dynamical Evolution and Radiative Processes of Supernova Remnants* by Reynolds (2016), from the living reference work *Handbook of Supernovae*. Other referenced materials are cited where relevant.

2.1 Morphology

No two supernovae are quite the same, owing to differences in the masses and compositions of their progenitor stars, and to the many different explosion mechanisms that exist. The same can be said of the resulting supernova remnants, which take on unique forms that are influenced as much by their progenitor stars as they are by the environment in which they form and evolve. However, while no two supernova remnants look quite the same, their morphologies are not so different as to be unclassifiable. Quite to the contrary, there exist three main types of supernova remnant, based on their morphologies: shell-like, filled-centre,

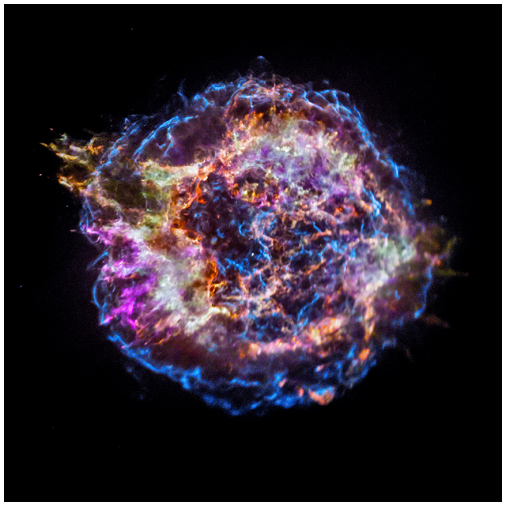

(a) Cassiopeia A, a shell-like SNR

(b) The Crab Nebula, a filled-centre SNR

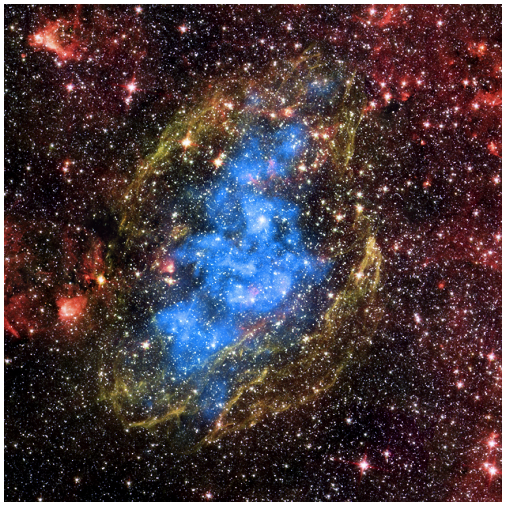

(c) W44, a thermal composite SNR

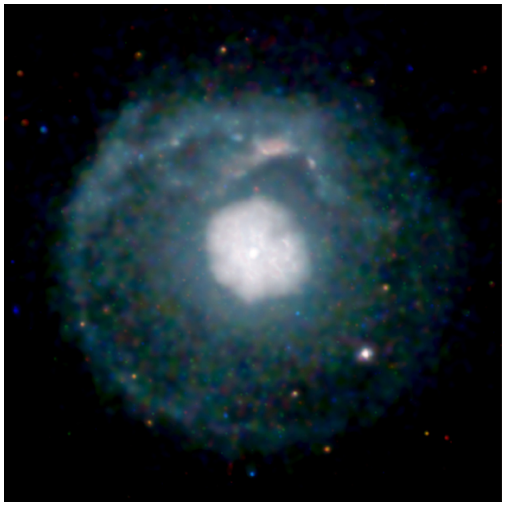

(d) G21.5–0.9, a plerionic composite SNR

Figure 2.1: Examples of the different morphological classifications for SNRs. **(a)** Cassiopeia A in X-rays. Red is Silicon, Yellow is Sulphur, Green is Calcium, Purple is Iron, Blue is Blast Wave/High Energy. Image credit: NASA/CXC/SAO (2017a); **(b)** Multiwavelength image of the Crab Nebula. Purple is X-ray (NASA/CXC/SAO), Blue is Ultraviolet (ESA/XMM-Newton), Green is Optical (NASA/STScI), Yellow-Green is Infrared (NASA/JPL/Caltech), Red is Radio (NSF/NRAO/VLA). Image credit: NASA/CXC/SAO (2017b); **(c)** Multiwavelength image of W44. X-ray is cyan (Chandra: NASA/CXC/Univ. of Georgia/R.Shelton & NASA/CXC/GSFC/R.Petre), Infrared is red, green, and blue (Spitzer: NASA/JPL-Caltech). Image credit: NASA/CXC/SAO (2015). **(d)** G21.5–0.9 in X-rays (NASA/CXC/U.Manitoba/H.Matheson & S.Safi-Harb). Image credit: NASA/CXC/SAO (2005).

and composite. Some of the most well-known examples of each classification can be seen in Figure 2.1.

2.1.1 Shell-like Remnants

Shell-like remnants resemble bubbles, possessing bright outer shells with their interiors often lacking prominent emission. The majority of their emission comes from a ring-like structure with bright limbs that appears where the shock wave collides with the surrounding ISM, sweeping up said material into a thin, outwardly expanding shell of hot gas. The emission from this shell is primarily thermal X-rays from shock-heated plasmas, though nonthermal X-ray emission due to particle acceleration in the shock front is sometimes seen as well. Shell-like remnants are by far the most common type of SNR, with good examples of shell-like remnants including the Cygnus Loop, Cassiopeia A, and Tycho's SNR.

2.1.2 Filled-centre Remnants

Filled-centre remnants are also known as "plerions" or "pulsar wind nebulae," and are possessed of bright centres, with a notable absence of the bright limbs found in a shell-like remnant. They are powered by a rapidly rotating neutron star known as a pulsar, whose strong magnetic fields and relativistic winds generate a nebula of energetic charged particles around it that shines brightly in the optical, X-ray, and radio regimes, with the majority of their radio and X-ray emission being composed of nonthermal synchrotron radiation. Despite being the second non-composite category of SNR, filled-centre remnants make up the least common classification of SNRs, with fewer than a dozen currently confirmed cases. The most prominent example of a filled-centre remnant is the Crab Nebula; other examples include 3C 58,

CTB 87, and G6.1+1.2.

2.1.3 Composite Remnants

Composite remnants appear as hybrids of shell-like and filled-centre remnants, showing emission from both their outer limbs and their inner centres. However, composites can also be further divided into two distinct subcategories: thermal composites, and plerionic composites. Thermal composites – also referred to as "mixed-morphology" remnants – have non-thermal shells when viewed in the radio regime, but a central region filled with thermal X-ray emission. Lastly, plerionic composites have filled centres that are bright in both the radio and X-ray regimes, but also exhibit shell-like structures on their exteriors. The SNR IC 443 is often taken as the best example of a thermal composite remnant, while G21.5–0.9 is a classic plerionic composite.

2.2 Evolution

While supernova remnants are classified based on their morphology, these morphologies are not static: they change and evolve as the remnant ages and grows. This evolution – from the moment of a remnant's creation to its ultimate disappearance as it merges with the ISM – can be described in three phases:

(i) The ejecta-dominated phase, in which the total mass of the system is dominated by that of the ejecta, and in which the explosion's energy is primarily contained in the freely-expanding ejecta.

(ii) The Sedov-Taylor phase, in which the total mass of the system becomes dominated by that of the swept-up material, rather than that of the ejecta, and in which the explo-

sion's energy has mostly been transferred into the internal and kinetic energy of the expanding shell of swept-up material.

(iii) The radiative phase, in which the mass of the ejecta is negligible compared to that of the swept-up material, and in which the system's energy begins to decrease due to radiative losses becoming important.

A fourth phase – known as the merging phase or the dissipation phase – is sometimes considered as well. In this phase, the velocities of the shock approach the local sound speed, and the shock gradually disappears entirely as it continues to lose energy. This ultimately leads to the "death" of the remnant as it fades from view entirely, having merged with the ISM. We elect not to include a separate discussion on this phase, as it is largely similar in behaviour to that of the radiative phase. It's also important to note that an SNR can exist in multiple evolutionary phases at the same time, as the non-uniformity of its progenitor explosion and the surrounding material can cause sections to evolve more or less rapidly than others.

2.2.1 Shock Physics

We begin, however, not with a discussion of the different phases of supernova remnant evolution, but rather with a brief consideration of the physics that underlies this evolution: that of shock waves. The information in this section is largely based upon that contained within the text *The Physics of the Interstellar Medium* by Dyson & Williams (1997).

A shock wave is an energy-carrying disturbance that travels faster than the speed of sound in a given medium, and which is characterised by an abrupt change in pressure, temperature,

and density. We first define the Mach number, $M_{\rm s}$, such that:

$$M_{\rm s} = \frac{V_{\rm s}}{c_{\rm s}} \tag{2.1}$$

where $V_{\rm s}$ is the velocity of the shock, and $c_{\rm s}$ is the local speed of sound. On average, the sound speed in the ISM is $10-100\,{\rm km\,s^{-1}}$, meaning that supernova remnant shocks can have Mach numbers that reach up to 1000 for typical shock velocities of $10^4\,{\rm km\,s^{-1}}$.

A shock forms when a flow moving faster than the local speed of sound encounters another medium, causing an abrupt decrease in the flow's speed. The properties of the resulting shock depend on several variables both in front of and behind the shock front, including the pressure P, the velocity relative to the shock v, and the density ρ. We assume that we are working with a one-dimensional, plane-parallel, adiabatic, steady-state, ideal monatomic gas fluid flow. While magnetic fields do play a part in the evolution of astrophysical shocks, for supernova remnants (where the shock velocities are high), the effect of the magnetic pressure is typically negligible in comparison to that of the ram pressure, and as such, we also elect to neglect the effect of magnetic fields. With these assumptions in mind, we can write a series of conservation relations:

$$\phi = \rho_1 v_1 = \rho_2 v_2 \tag{2.2}$$

$$\zeta = P_1 + \rho_1 v_1^2 = P_2 + \rho_2 v_2^2 \tag{2.3}$$

$$\xi = \frac{1}{2} v_1^2 + \frac{\gamma}{\gamma - 1}\frac{P_1}{\rho_1} = \frac{1}{2} v_2^2 + \frac{\gamma}{\gamma - 1}\frac{P_2}{\rho_2} \tag{2.4}$$

where the subscript 1 indicates the conditions before the shock, the subscript 2 indicates the conditions after the shock, and γ is the adiabatic index, which – for an ideal, monatomic gas

– is taken to be $5/3$. These equations are known as the Rankine-Hugoniot jump conditions and in order, are expressions for the conservation of mass, momentum, and energy.

We now introduce a reference velocity, $\bar{v}$, such that:

$$\bar{v} = \zeta/\phi \tag{2.5}$$

If we assume that the local sound speed c_s is defined by:

$$c_{\mathrm{s}}^2 = \frac{5}{3}\frac{P}{\rho} \tag{2.6}$$

Then, the total energy ξ can be expressed as:

$$\xi = \frac{1}{2}v^2 + \frac{3}{2}c_{\mathrm{s}}^2 = v\left(\frac{5}{2}\bar{v} - 2v\right) \tag{2.7}$$

From this, we can derive several relations that connect quantities on either side of the shock. To begin, we first write (2.7) in the form of a quadratic equation:

$$v^2 - \frac{5}{4}v\bar{v} + \xi/2 = 0 \tag{2.8}$$

For given values of ξ and $\bar{v}$, we have two roots: v_1 and v_2, representing the upstream and downstream velocities, respectively. As a quadratic equation, the sum of these two roots is:

$$v_1 + v_2 = \frac{5}{4}\bar{v} \tag{2.9}$$

We can also use (2.1) to define the upstream and downstream Mach numbers $M_1 = v_1/c_{\mathrm{s}}$

and $M_2 = v_2/c_s$, respectively. Then, from (2.6), we find:

$$M_1 = \sqrt{\frac{3}{5}\frac{v_1}{\bar{v} - v_1}} \tag{2.10}$$

Using all this, and assuming strong shocks for which $M_1 \gg 1$, we can find expressions for the ratios of velocity and density on either side of the shock:

$$\frac{v_2}{v_1} = \frac{1}{4} \tag{2.11}$$

$$\frac{\rho_2}{\rho_1} = 4 \tag{2.12}$$

In other words, the downstream velocity is reduced by a factor of four compared to the upstream velocity, while the downstream density is instead increased by a factor of four compared to the upstream density.

We can calculate the post-shock temperature, as well. By assuming an ideal gas equation of state where $P = (\rho k T)/(\mu m)$, (2.4) becomes:

$$T_2 = \frac{3}{16}\frac{\mu m}{k} v_1^2 \tag{2.13}$$

We now consider the frame in which our point of reference is fixed, i.e. one in which the shock is moving with a velocity V_s. In such a frame, the upstream and downstream velocities u_1 and u_2 can be written as:

$$u_1 = v_1 + V_s \tag{2.14}$$

$$u_2 = v_2 + V_s \tag{2.15}$$

Then, we from (2.11), we find that the speed of the shocked gas relative to the shock velocity can be written as:

$$u_2 = \frac{3}{4} V_s \tag{2.16}$$

In other words, the gas behind the shock moves in the same direction as the shock, but with a speed three-quarters that of the shock itself. We can also derive a relation between the post-shock temperature and the shock speed:

$$T_2 = \frac{3}{16} \frac{\mu m}{k} V_{\mathrm{s}}^2 \tag{2.17}$$

From (2.3), and assuming a strong shock and a negligible upstream pressure P_1, we can find:

$$P_2 = \frac{3}{4} \rho_1 V_{\mathrm{s}}^2 \tag{2.18}$$

Finally, from (2.4) and using what we have recently derived, we can determine the specific internal and kinetic energies of the shocked gas:

$$e_{\mathrm{I},2} = \frac{3}{2} \frac{P_2}{\rho_2} = \frac{9}{32} \rho_1 V_{\mathrm{s}}^2 \tag{2.19}$$

$$e_{\mathrm{k},2} = \frac{1}{2} u_2^2 = \frac{9}{32} \rho_1 V_{\mathrm{s}}^2 \tag{2.20}$$

The Expansion Parameter

Despite the potentially complicated shock physics involved, the evolution of a supernova remnant's shock wave radius can often be simply approximated as:

$$R_{\rm s} \approx R_0 \left(\frac{t}{t_0}\right)^m \tag{2.21}$$

where t is the age of the supernova remnant, R_0 and t_0 are fiducial parameters, and the parameter m is called the "expansion parameter" or the "deceleration parameter." We can solve the above equation for the shock velocity:

$$\begin{aligned} v_{\rm s} &= \frac{dR_{\rm s}}{dt} \\ &= m\frac{R_{\rm s}}{t} \end{aligned} \tag{2.22}$$

This suggests that the expansion parameter can be determined so long as the age, radius, and expansion velocity of the supernova remnant are known. As we will see, this approximation can be applied equally well to all phases of a remnant's expansion.

2.2.2 Ejecta-Dominated Phase

The first phase of a supernova remnant's life is referred to as the the ejecta-dominated phase, sometimes known as the free-expansion phase. The supernova event releases a tremendous amount of energy (the canonical value is 10^{51} ergs) almost instantaneously. This energy propagates outwards in all directions from its source, creating a pressure-driven shock that expands into the surrounding circumstellar medium (CSM) and interstellar medium, sweep-

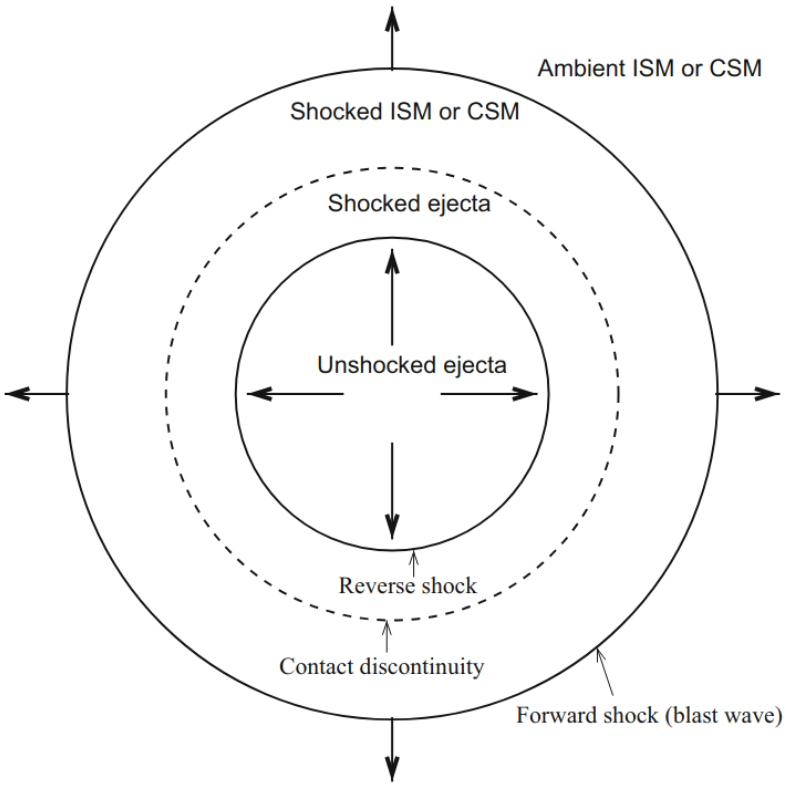

Figure 2.2: A schematic of the basic structure of a supernova remnant. The outward-moving forward shock heats ambient material in the ISM and CSM, while the inward-moving reverse shock re-heats unshocked ejecta. Image from Reynolds (2016).

ing up said media as it travels. Because of the large energies involved, this shock expands essentially unopposed, travelling freely at a relatively constant shock velocity. This velocity varies depending on supernova type and the ambient environment, with average values of $V_\mathrm{s} \sim 5 \times 10^3\,\mathrm{km\,s^{-1}}$ for core-collapse explosions and $V_\mathrm{s} \sim 10^4\,\mathrm{km\,s^{-1}}$ for thermonuclear explosions, though values as high as $V_\mathrm{s} \sim 3 \times 10^4\,\mathrm{km\,s^{-1}}$ have been recorded. As a result, the SNR expands in a mostly linear fashion during the free-expansion phase, with the radius

R_{s} being able to be simply approximated:

$$R_{\mathrm{s}} = V_{\mathrm{s}}\, t \tag{2.23}$$

or equivalently for the shock velocity:

$$V_{\mathrm{s}} = \frac{R_{\mathrm{s}}}{t} \tag{2.24}$$

which would yield an expansion parameter for the free-expansion phase of $m = 1$.

It is important to note that the supernova shock *does* decelerate during this stage; however, given the velocities at which these shocks travel, this deceleration is largely negligible until more material is swept up by the shock. As such, this essentially linear expansion continues until the mass of the material swept up by the shock becomes comparable to that of the mass ejected by the supernova explosion. This typically takes on the order of 100 - 200 years, though this estimate can vary greatly depending on the initial explosion energy and the density of the material into which the shock is expanding.

2.2.3 Sedov-Taylor Phase

Once the mass of the swept-up material (M_{sw}) begins to exceed that of the ejecta (M_{ej}), the supernova remnant enters into the second stage of its evolution: the Sedov-Taylor phase, also known as the adiabatic phase or the energy-conservation phase. In this phase, the total energy of the system is conserved: while the expansion of the shock begins to decelerate as more and more material is swept up, the kinetic energy remains constant, as it is being transferred into the swept-up material. As well, energy is not being lost in significant amounts due to

radiative energy losses as the rate of radiative cooling is negligible as a result of the shock's high temperature and overall low density. Because of all of this, the rate of expansion is determined solely by the initial energy of the explosion, and the density of the ambient medium.

The most well-known model for explaining the evolution of an SNR in this phase is the Sedov-Taylor model, a self-similar solution named for the work of Sedov (1959) and Taylor (1950) who independently came up with the model, and for whom the phase is also named. It is an application of the Buckingham π theorem, which states that physical quantities depending on n parameters can instead be written in terms of $p = n - k$ parameters, where k is the number of physical dimensions involved. For the context of a supernova explosion, the physical parameters involved would be the energy E and the ambient density ρ_0, while the dynamical variables involved are the shock wave radius R_s and the age of the remnant t. We recognise that from these four variables, we have three independent dimensions: length, mass, and time, which we denote as L, M, and T, respectively. Thus, we can construct a dimensionless variable ξ through dimensional analysis:

$$\begin{aligned}
[\xi] &= [R_\mathrm{s}]^a \times [t]^b \times [E]^c \times [\rho_0]^d \\
&= [L]^a \times [T]^b \times \left[ML^2T^{-2}\right]^c \times \left[ML^{-3}\right]^d \\
&= L^{a+2c-3d} \times T^{b-2c} \times M^{c+d}
\end{aligned}$$

ξ will be dimensionless if we choose to set $d = 1$, $c = -d$, $b = 2d$, and $a = 5d$. In doing so, we find:

$$\xi = \frac{R_\mathrm{s}^5 \rho_0}{t^2 E} \tag{2.25}$$

For an ambient medium with adiabatic index of $\gamma = 5/3$, Landau & Lifshitz (1959) found

that the value of the self-similar parameter $\xi = 2.025$. The shock radius can then be written as:

$$R_{\rm s} = 1.15 \left(\frac{E}{\rho_0} \right)^{1/5} t^{2/5} \tag{2.26}$$

and from this, we are able to derive an expression for the velocity of the shock:

$$\begin{aligned} V_{\rm s} &= \frac{dR_{\rm s}}{dt} \\ &= \frac{2}{5} \frac{R_{\rm s}}{t} \end{aligned}$$

suggesting that, in the Sedov-Taylor phase, the expansion parameter will gradually fall to a value of $m = 2/5$.

The Reverse Shock

Due to the supernova shock, the stellar material of the supernova progenitor is rapidly heated at the time of the explosion. However, the fast expansion of this ejecta quickly leads to rapid adiabatic cooling, and the innermost ejecta (i.e. the ejecta not at the shock front) becomes cold within the first few years of the remnant's expansion, resulting in a rapid decline in internal pressure.

During the expansion of the remnant, the shock wave created by the fastest moving, outermost ejecta is responsible for the creation of the shock-heated shell of swept-up material. As this shell expands, it sweeps up more and more material from the surrounding ISM and CSM, resulting in a gradual deceleration. The outermost, unshocked ejecta similarly expands; however, as it is expanding into the region through which the shell has already passed, it does not sweep up nearly as much material as the shell, resulting in it experiencing less deceleration,

until it eventually is moving faster than the shell. When this unshocked ejecta catches up to the shell, the two will collide; should this collision occur at supersonic speeds (i.e. if the shell has decelerated enough to be more than one Mach number slower than the unshocked ejecta), then another, secondary shock wave will form, which is known as the reverse shock.

With respect to the ejecta, the reverse shock always moves inwards, towards the centre of the remnant. To an outside observer, however, the reverse shock will initially appear to propagate outwards, in the same direction as the primary shock (which we now refer to as the forward shock). Once the forward shock has swept up enough material to enter into the Sedov-Taylor phase, the lower internal pressure from the ejecta's rapid cooling will result in the reversal of the reverse shock's motion causing it to – as its name suggests – begin to appear to propagate inwards, away from the shell and towards the centre of the supernova remnant. As the reverse shock propagates, it (re)heats the ejecta, and is a primary reason for the strong X-ray emission often seen in the metal-rich ejecta of young SNRs. After the formation of the reverse shock, the shock-heated shell of the SNR is seen to exist in two distinct parts: an outer shell consisting primarily of ISM and CSM heated by the forward shock, and an inner shell consisting primarily of ejecta heated by the reverse shock, with the boundary between these two regions being known as the contact discontinuity. These features can be seen in Figure 2.2, which shows a schematic diagram of a typical SNR some time after the reverse shock has formed, but before it has managed to reheat all of the ejecta.

2.2.4 Radiative Phase

The final phase of a supernova remnant's life that we will concern ourselves with is the radiative phase, sometimes referred to as the pressure-driven or snow-plough phase. Whereas in

the Sedov-Taylor phase the remnant's evolution was governed by the conservation of energy, in the radiative phase, that is no longer the case: radiative energy losses become much more prominent as the remnant's shell expands, slows down, and cools, and the shell's expansion can no longer be considered adiabatic. With these radiative cooling processes rising to prominence, a thin shell of cool material forms immediately behind the forward shock. As a result, this phase is governed instead by the conservation of momentum:

$$MV_{\rm fs} = \frac{4\pi}{3}\rho_0 R_{\rm fs}^3 \frac{dR_{\rm fs}}{dt} = \text{constant} \tag{2.27}$$

If we take the radius, velocity, and age at which the remnant transitions into the radiative stage to be a constant (denoted by $R_{\rm rad}$, $v_{\rm rad}$, and $t_{\rm rad}$, respectively), then integration of the above equation with respect to time suggests a solution for $R_{\rm fs}$ of the form:

$$R_{\rm fs}^4(t) = C_1(t - t_{\rm rad}) + C_2 \tag{2.28}$$

By initial conditions, we clearly have $C_2 = R_{\rm rad}^4$, and since $dR_{\rm fs}(t_{\rm rad})/dt$ must be equal to $v_{\rm rad}$, we also find that $C_1 = 4R_{\rm rad}^3 v_{\rm rad}$. By using these values and re-arranging (2.28) to solve for t, we find:

$$t = t_{\rm rad} + \frac{R_{\rm rad}}{4v_{\rm rad}}\left[\left(\frac{R_{\rm fs}}{R_{\rm rad}}\right)^4 - 1\right] \tag{2.29}$$

By taking the long-time approximation (for $t \gg t_{\rm rad}$), we find that the expansion parameter m approaches a value of $m = 1/4$.

During the radiative phase, the remnant's emission begins to dim in the X-ray regime while simultaneously becoming bright in optical wavelengths. The hot plasmas responsible for the

bulk of the remnant's X-ray emission have cooled to a point at which their constituent particles are no longer energetic enough to sustain high-energy emission, giving way to recombination processes, such as Hα, [S II], [N II], and [O III]. The remnant will continue expanding and slowing down until, eventually, it will have radiated away the majority of its internal energy. At this point, the shock speed will have approached the local sound speed, and the remnant will eventually fade away entirely as it finally merges with the ISM.

2.3 X-ray Emission and Radiative Processes

As a supernova remnant ages and evolves, the energy released in its progenitor explosion is spread out across a constantly growing area through the expansion of the supernova remnant's shocks. Not only does this process influence and define the remnant's structure and morphology, it also sets the stage for its emission, creating the ideal conditions for a variety of processes which will contribute to its spectrum across many wavelength regimes. Of interest to us is the X-ray emission, which arises from the superheated plasmas created in the wake of the shock. X-ray emission serves as a potent tracer of the high-energy processes that occur within the remnant, allow us to discern information about the temperature, density, and compositions therein. In this section, we introduce the different forms of radiative processes responsible for the generation of X-rays within supernova remnants, and discuss the mechanisms responsible for these emissions.

This section was written using the following additional sources: the texts *Radiative Processes in Astrophysics* by Rybicki & Lightman (1979), and *High Energy Astrophysics* by Longair (2011); and the chapter *X-Ray Emission Properties of Supernova Remnants* by Vink (2016), from the living reference work *Handbook of Supernovae*.

2.3.1 Thermal Emission

In the X-ray regime, we often consider astrophysical emission processes to come in one of two categories. The first of these categories is that of thermal emission, which arises due to the thermal motion of particles in hot, ionised plasmas. These particles possess a thermal velocity distribution (i.e. a Maxwellian distribution), meaning that their velocities are dependent solely on their temperatures. While thermal processes are most commonly found in stellar coronae and the intracluster medium in galaxy clusters, they are also frequently found in supernova remnants, where they play an important role in allowing us to study these objects. In particular, the hot plasmas of young SNRs are optically thin and abundant in the alpha- (O, Ne, Mg, Si, S, Ar, Ca) and iron-group elements (mostly Fe, Ni). These elements have their K-shell transitions in the soft X-ray band, for which thermal processes are the dominant emission mechanisms. In the context of SNRs, the term "thermal emission" is usually used to refer to the combination of continuum emission – of which there are three possible sources when it comes to the emission mechanisms from thermal SNRs – and line emission.

Bremsstrahlung Emission

While there are several possible sources of thermal continuum emission in SNRs, thermal bremsstrahlung – a loanword from German that literally translates to *braking radiation* – is the most common. Also known as free-free emission as it does not involve the capture of any of the involved particles, bremsstrahlung is radiation that occurs when a charged particle is accelerated through interaction with the Coulomb field of another charged particle. In the case of supernova remnants, this is most commonly the acceleration of an electron via interaction with an ion. This holds true for emission from a single electron, for which the

radiation spectrum is:

$$I(\omega) = \frac{Z^2 e^6 N_\mathrm{i}}{12\pi^3 \epsilon_0^3 c^3 m_\mathrm{e}^2} \frac{1}{v} \ln\left(\frac{b_\mathrm{max}}{b_\mathrm{min}}\right) \tag{2.30}$$

where Z is the atomic number, N_i is the number density of nuclei per cubic metre, and b_max and b_min are the maximum and minimum impact parameters, respectively. To find the bremsstrahlung spectrum of a thermal plasma, we must integrate this over a Maxwellian distribution of electron velocities:

$$f(v)\mathrm{d}v = 4\pi \left(\frac{m_\mathrm{e}}{2\pi kT}\right)^{3/2} v^2 \exp\left(-\frac{m_\mathrm{e} v^2}{2kT}\right) \mathrm{d}v \tag{2.31}$$

Although the algebra involved is rather unwieldy, by substituting $\frac{1}{2} m_\mathrm{e} v^2 = \frac{3}{2} kT$ into (2.30), we can eventually arrive at an approximation:

$$I(\omega) \approx \frac{Z^2 e^6 N_\mathrm{i} N_\mathrm{e}}{12\sqrt{3}\pi^3 \epsilon_0^3 c^3 m_\mathrm{e}^2} \left(\frac{m_\mathrm{e}}{kT}\right)^{1/2} g(\omega, T) \tag{2.32}$$

where N_e is the number density of electrons per cubic metre, and $g(\omega, T)$ is a Gaunt factor which is added to account for quantum mechanical effects on a classically-derived emission equation. By integrating this over all frequencies, we can find the emissivity:

$$\epsilon_\mathrm{ff} = 6.8 \times 10^{-51}\, Z^2 N_\mathrm{e} N_i T^{-1/2} \exp\left(-\frac{h\nu}{kT}\right)\, \bar{g}_\mathrm{ff}\ \left(W\, m^{-3}\, Hz^{-1}\right) \tag{2.33}$$

or, more familiarly in terms of CGS units:

$$\epsilon_\mathrm{ff} = 6.8 \times 10^{-38}\, Z^2 n_\mathrm{e} n_\mathrm{i} T^{-1/2} \exp\left(-\frac{h\nu}{kT}\right)\, \bar{g}_\mathrm{ff}\ \left(ergs\, s^{-1}\, cm^{-3}\, Hz^{-1}\right) \tag{2.34}$$

where $\bar{g}_{\rm ff}$ is the velocity-averaged Gaunt factor. This factor is usually considered to be constant, but can take on a range of values between 1.1 and 1.5. The emissivity is largely dependent upon the $Z^2 n_{\rm e} n_{\rm i}$ term; for the conditions and environments present within an SNR – specifically, within the shocked ISM – this is dominated by interactions between electrons and hydrogen, so it is often chosen to set $Z = 1$ and $n_{\rm i} = n_{\rm H}$, where $n_{\rm H}$ is the hydrogen density. One important implementation of this is the emission measure (EM), which is often used in spectral fitting codes to produce the observed flux. The emission measure is a measure of the amount of plasma along the line of sight that is available to emit the observed flux, and is defined as:

$$EM = \int n_{\rm e} n_{\rm H} dV \tag{2.35}$$

This in turn is usually parametrised via a normalisation factor, K, given by:

$$K = \frac{10^{14}}{4\pi D^2} \int n_{\rm e} n_{\rm h} dV \tag{2.36}$$

where D is the distance to the source. In turn, the flux of a source can be derived from the normalisation factor, by multiplying it by the emissivity.

Other Continuum Emission Processes

The other types of continuum emission that are sometimes considered include radiative recombination and two-photon emission. The first of these, radiative recombination – also known as free-bound emission – occurs when an ion is struck by an electron. The two "recombine" and, in the process of doing so, emit a photon whose energy is equal to the kinetic energy of the incoming electron combined with the binding energy of the electron after re-

combination. This form of emission is very similar to that of thermal bremsstrahlung: the main difference lies in the temperature dependence of the respective Gaunt factors. For the hot, optically thin plasmas common to thermal SNRs, the emission from radiative recombination is negligible, because the electron temperatures are too large and thus the electrons are moving too fast to become bound. For plasmas with lower electron temperatures, however, radiative recombination becomes more important, and can even dominate the emission spectrum over that of thermal bremsstrahlung. Because the electron's kinetic energy can take on a wide range of values, this emission is classified as continuum emission, despite the binding energy being well-defined.

Finally, two-photon emission is quantum mechanical process that occurs when electrons occupy quantum states for which any downward transition violates transition rules, and thus is forbidden. To get around this, it is possible that the electron instead decays exponentially, emitting two photons rather than one. Two-photon emission is most frequently encountered in low-density ionised gases, as it requires that spontaneous emission occur before collisional de-excitation has a change to occur. The most common source of two-photon emission is the Lyα recombination line of the Hydrogen atom, between the energy levels of $n = 2$ and $n = 1$. While the $2p \rightarrow 1s$ transition is allowed, the $2s \rightarrow 1s$ transition is instead forbidden, and thus requires the emission of two photons to occur. Due to the quantised energy involved in quantum state transitions, one might expect this process to result in line emission; however, this is not the case with two-photon emission, owing to the fact that the only requirement on the energies of the emitted photons are that they sum up to the energy difference associated with the transition: while the most common configuration is the one in which the two photons have identical energies, any combination that satisfies the requirement is possible,

resulting in a "continuum" emission that resembles a very broad emission line.

Line Emission

While continuum emission makes up the bulk of the radiation detected from thermal SNRs, it is line emission that is perhaps the most important form of thermal emission, as it provides us with numerous diagnostic tools that can inform us as to the nature, structure, and composition of the remnant. The vast majority of line emission in these objects arises as a result of collisional excitation, which itself occurs when two charged particles pass nearby to each other; as with thermal bremsstrahlung, the most common occurrence of this in SNRs is when a free electron passes by an ion. When this happens, it is possible that one of the electrons in the ion changes (i.e. is excited) to a higher energy level through a Coulomb interaction with the free electron. The target electron will remain at this higher energy level briefly before being de-excited back down to its ground state through the emission of a photon; as with all energy level transitions, this emitted photon will have a specific energy, entirely dependent upon which ion and energy states are involved, thus resulting in line emission at said energy. Collisional de-excitation, another form of line emission, is not typically considered in the study of SNRs, owing to the generally low densities of the involved plasmas.

The conditions present in the plasmas of young SNRs are the ideal laboratory for the study of many emission lines: for temperatures above $\sim 10^6$ K (temperatures commonly found in such objects), most of the alpha-group elements are in the helium-like or hydrogen-like ionisation state, and the line emissions corresponding to these states range from 0.5 to 10 keV. Similarly, the iron-group elements exhibit strong emission lines in this range, with the Fe-L shell being prominent between 0.7-1.5 keV, and the Fe-K shell being prominent between

Table 2.1: Energies (in keV) of line transitions commonly found in SNR spectra.

Element	Kα	Heα (w)	Heα (x+y)	Heα (z)	Heβ (w)	Lyα	Lyβ
C	0.277	0.308	0.304	0.299	0.355	0.368	0.436
N	0.392	0.431	0.426	0.420	0.552	0.500	0.593
O	0.525	0.574	0.567	0.561	0.666	0.654	0.775
Ne	0.849	0.922	0.915	0.905	1.074	1.022	1.211
Mg	1.253	1.352	1.343	1.331	1.579	1.472	1.745
Si	1.740	1.865	1.854	1.840	2.182	2.005	2.376
S	2.307	2.461	2.448	2.431	2.884	2.622	3.106
Ar	2.958	3.140	3.125	3.104	3.684	3.321	3.935
Ca	3.962	3.902	3.885	3.861	4.583	4.105	4.863
Fe	6.403	6.700	6.675	6.636	7.881	6.966	8.251

6-8 keV. Table 2.1 shows the energies at which several different transitions occur for many of these elements.

Time-Dependent Ionisation

When studying thermal plasmas, line emission plays an extremely important role. However, to calculate the line emission from a plasma, it's necessary to know the concentration of each species of ion. To that end, we consider two states of ionisation equilibrium: collisional ionisation equilibrium (CIE), and non-equilibrium ionisation (NEI).

Many hot, optically-thin thermal plasmas – such as stellar coronae and the intracluster medium that permeates galaxy clusters – are commonly assumed to be in a state of CIE. In such a state, the electron velocity distribution of a plasma is Maxwellian in nature, and the ionisation levels of the plasma is determined solely by the balance between ionisation and recombination processes. In other words, the plasma's ion population is no longer time-dependent: for every ionisation event that results in the generation of a free electron, there is a corresponding recombination event that results in the opposite. This state can only be reached after the

plasma has remained at a stable temperature and density for a long enough time such that these processes have been able to equilibrate. The time this takes can be parametrised with the ionisation timescale as a function of the electron density, $\tau = n_{\mathrm{e}}t$; when this value is on the order of $10^{13}\ \mathrm{cm}^{-3}\ \mathrm{s}$, a plasma is typically considered to be in CIE. Additionally, for the low-density limit of optically-thin plasmas, radiative decay occurs on a much shorter timescale than do collisions; as a result, collisional de-excitation is generally ignored.

Supernova remnants, on the other hand, are more frequently found to be in a state of NEI. Conventionally speaking, a plasma being in NEI is defined as it not being in CIE; however, for the ionising plasmas common to young SNRs, being in a state of NEI also requires that the plasma be undergoing more ionisations than it is recombinations. The reason that SNR plasmas are so commonly in NEI is because of the low densities involved: the shocks in SNR shells are largely collisionless, meaning that the transition between pre- and post-shock states occurs on a length scale that is smaller than that of a particle's collisional mean free path. Because of this, only a few ionising collisions have occurred per atom, and the ionisation state of the plasma thus lags behind the electron temperature. A plasma enters into a state of NEI when it experiences a sudden change in temperature, such as from the passage of a shock. When this occurs, the kinetic energy of the ions which carry the bulk of the mass becomes thermalised, and the ions acquire a motion that corresponds to a higher temperature than their current state would suggest. The plasma thus needs time to respond to this, as the ionisations needed to correct for this difference are reliant upon collisions.

2.3.2 Nonthermal Emission

The second emission category is that of nonthermal emission. Where thermal emission occurs in hot plasmas near to thermal equilibrium, and its intensity is dependent upon temperature, nonthermal emission instead occurs most frequently in environments characterised by strong particle acceleration, such as shock fronts, areas of strong magnetic fields, or turbulent regions. The intensity of this nonthermal radiation is largely temperature-independent, and usually results in power-law (or other, non-Maxwellian) energy distributions.

Synchrotron Radiation

The main form of nonthermal emission encountered in supernova remnants is that of synchrotron radiation. The relativistic form of cyclotron radiation, synchrotron radiation arises from charged particles gyrating in a magnetic field: where in cyclotron radiation the frequency of emission is simply the frequency of the gyration, for the relativistic particles of synchrotron radiation, this emission can extend to several times that of the gyration frequency. In this way, synchrotron radiation can be found across the electromagnetic spectrum; in the context of supernova remnants, synchrotron emission is most commonly found in the radio regime, but several remnants have been found to exhibit X-ray synchrotron radiation, as well. As our study focuses on the X-ray regime, we only consider synchrotron emission in this context.

Traditionally, X-ray synchrotron emission in SNRs has been associated with the presence of a pulsar wind nebula, but advancements in recent decades have established the shells of young SNRs as a source as well. In general, this X-ray synchrotron emission occurs primarily nearby to the shock fronts, where the magnetic fields are expected to range in strength from

a few μG up to around 0.5 mG. For such field strengths, the presence of X-ray synchrotron emission implies the presence of electrons with energies exceeding 10^{13} eV – much higher than the 10^{9} eV of radio synchrotron emitting electrons. These highly-energetic electrons are produced through a mechanism known as diffusive shock acceleration, which is capable of energizing particles up to TeV energies.

However, the rate at which an electron loses energy to synchrotron radiation is proportional to E^2. As a result these electrons lose their energy much more rapidly than their lower-energy counterparts. The detection of X-ray synchrotron radiation thus requires that the regions in which it is produced be regions in which active, rapid acceleration of particles is taking place. Observationally, this is supported by the fact that the majority of X-ray synchrotron radiation is detected in thin filaments at or near to the edges of supernova remnants.

3

Thermonuclear Supernovae

Broadly speaking, supernova explosions can be classified into one of two types, based upon the nature of their progenitor: core-collapse supernovae, which occur when massive stars reach the end of their lives; and thermonuclear supernovae, which involve instead the destruction of white dwarf stars. However, even when we opt to narrow our focus to only one of these forms of supernova, we still find ourselves presented with a wide range of progeni-

tors, mechanisms, and scenarios through which they may occur. Herein, we present a review of thermonuclear supernovae, including where they come from, how they occur, and what they produce. We also present a summary of the methods employed by modellers to produce models of nucleosynthetic yields for these events, and we explore and compare seven of the most current sets of these models.

This chapter was written using the following primary sources: the textbooks *Supernovae and Nucleosynthesis*, by Arnett (1996), and *Supernova Explosions*, by Branch & Wheeler (2017); the living reference work *Handbook of Supernovae* – specifically, the chapters *Type Ia Supernova* by Maguire (2016), *Nucleosynthesis in Thermonuclear Supernovae*, by Seitenzahl & Townsley (2017), and *Explosion Physics of Thermonuclear Supernovae and Their Signatures*, by Hoeflich (2017); and the review papers *Type Ia Supernova Explosions in Binary Systems: A Review*, by Liu et al. (2023), and *Towards an understanding of Type Ia supernovae from a synthesis of theory and observations*, by Hillebrandt et al. (2013). Other referenced materials are cited where relevant.

3.1 White Dwarfs and the Progenitor Channels

It is widely accepted that thermonuclear supernovae are the result of the thermonuclear explosion of a white dwarf in a binary system. More specifically, they arise from the explosion of carbon-oxygen (CO) white dwarfs; while other types of white dwarfs – such as oxygen-neon-magnesium (ONeMg or ONe) white dwarfs and helium white dwarfs – exist, only CO white dwarfs exist in sufficient number and possess the needed properties to be able to reproduce the observed rate of Type Ia supernovae. Herein, we introduce the basic properties of white dwarfs, including the process through which they are formed, and discuss the two primary

channels by which they can be expected to reach the point of supernova.

This section was written using the following additional sources: the review paper *On the Progenitors of Type Ia Supernovae*, by Livio & Mazzali (2018); the chapters *Evolution of Solar and Intermediate-Mass Stars* by Herwig (2013), and *White Dwarf Stars* by Koester (2013), in the reference work *Planets, Stars and Stellar Systems, Volume 4: Stellar Structure and Evolution*; and the *White Dwarf* section by Isern (2023) in the reference work *Encyclopedia of Astrobiology*. Additionally, Subsection 3.1.2 made use of the chapters *Dynamical Mergers* by García-Berro & Lorén-Aguilar (2016) and *Violent Mergers* by Pakmor (2016), from the living reference work *Handbook of Supernovae*.

3.1.1 Stellar Evolution and White Dwarf Formation

White dwarf stars are the endpoint of evolution for the vast majority of stars: those with an initial mass below 8 $M_\odot$, which accounts for roughly 95% of all stars. During their times on the main sequence, these stars will use stellar nucleosynthesis to burn hydrogen into helium, starting in their cores. This process proceeds according to either the proton-proton chain or the CNO cycle, depending on the star's initial mass. As they run out of hydrogen fuel, the conditions within the core become insufficient to burn the helium products, and so the burning zone will begin to move outwards, transitioning from core burning into shell burning. At the same time, the lack of nuclear burning in the core disrupts the fragile equilibrium between outwards radiation pressure and inwards gravitational pressure, causing the core to contract. This contraction alters the conditions in the core, increasing the density and temperatures to a point at which helium core burning is possible. This transition – from hydrogen core burning to helium core burning – marks the beginning of the He-burning

phase, and of the star's transition off of the main sequence.

During the He-burning phase, the helium core is slowly converted into roughly equal amounts of ^{12}C and ^{16}O through the triple-alpha process, while H-burning continues in the hydrogen shell surrounding the core, resulting in a carbon-oxygen core surrounded by a helium shell. Once the core has been completely depleted of He, it once again contracts, and He-burning will switch from He-core burning to He-shell burning. However, unlike in the previous contraction, burning does not resume in the core: the densities and temperatures, while higher than before, are insufficient to commence carbon-burning. With He-core burning complete, the star enters onto the asymptotic giant branch (AGB) of the Hertzsprung-Russel diagram, where it will remain until it finally becomes a white dwarf.

Throughout the star's time on the AGB, it will undergo a number of thermal pulses: as H-burning continues in the outer H-shell, eventually, the accumulation of the products of this burning onto the inner He-shell will result in the temporary re-ignition of He-burning in the He-shell. These pulses are short-lived, highly-energetic, and cause two main things: dredge-ups, which result in the mixing of material within the star, and which can bring the products of the thermal pulse closer to the surface; and mass loss, due to the stellar winds caused by energy release in the pulse. By the time of the star's last thermal pulse, its composition is essentially in its final configuration.

Once the star has finally shed the last of its outer layers, all that is left is its inert core: the newly-born white dwarf. The white dwarf consists of a core composed carbon and oxygen, surrounded by a thin envelope of helium and potentially an even thinner envelope of hydrogen (see Figure 3.1). Though it possesses a mass comparable to that of the sun, its radius is comparable to that of the earth, meaning that the white dwarf has an average density in ex-

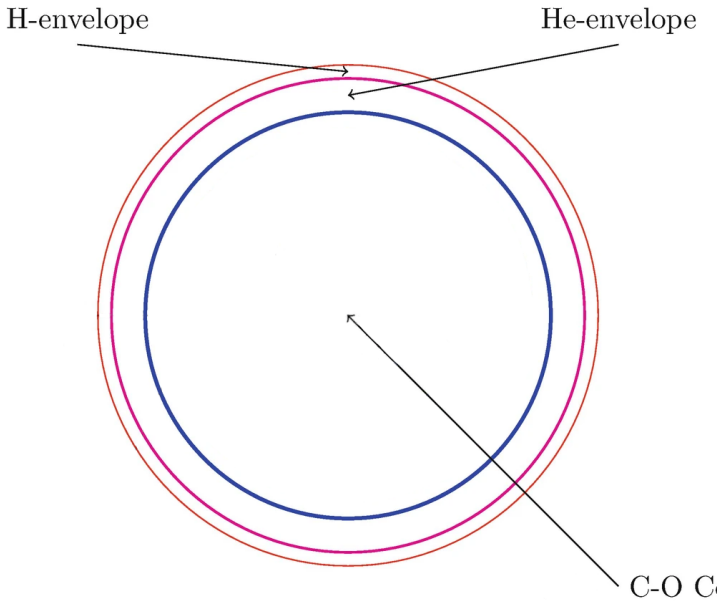

Figure 3.1: Internal structure and composition of a CO white dwarf (not to scale). Image adapted from Figure 2 of Isern (2023).

cess of 10^6 g cm^{-3}. It is this density that allows the core to resist the compressional forces of gravity: since the core is inert, it must rely on the pressure from degenerate electrons – a consequence of the Pauli exclusion principle – to support it. As a further consequence of this fact, white dwarfs have a maximum possible mass of approximately 1.4 $M_\odot$. This mass – known as the Chandrasekhar-mass, or the Chandrasekhar limit – is the mass above which the pressure from degenerate electrons is incapable of supporting the star against gravity. Should a white dwarf exceed this limit, it will likely collapse until the degeneracy pressure from neutrons prevents it from collapsing further, at which point it will become a neutron star.

3.1.2 Progenitor Channels

That being said, the formation of a white dwarf will not, in itself, result in a supernova. As stated previously, thermonuclear supernovae are largely believed to arise from white dwarfs

in binary systems. Since the companion star appears important, we consider two progenitor channels through which a white dwarf can reach the conditions necessary to undergo a thermonuclear supernova explosion, with the primary difference lying in the nature of the companion: the single-degenerate (SD) scenario, and the double-degenerate (DD) scenario.

Single-Degenerate Scenario

In the SD scenario, a white dwarf accretes mass in the form of hydrogen-rich or helium-rich material from a stellar companion until it approaches the Chandrasekhar mass, at which point it undergoes a thermonuclear explosion. This companion can be of many types: main-sequence stars, sub-giants, red giants, asymptotic giant branch stars, and helium stars are all valid options. Similarly, there are multiple possible methods through which the mass can be transferred, with Roche-lobe overflow (in which the white dwarf accretes matter that is not gravitationally bound to the companion) and transfer through stellar winds (in the case of giant stars) being the two most viable possibilities.

Regardless of the source of the matter or the method through which it is transferred, the actual rate of mass transfer is quite important. Should the accretion rate be too low ($\dot{M} \lesssim 10^{-8} M_\odot$ yr^{-1}), then the white dwarf is likely to lose more mass via periodic nova outbursts than it gains through accretion. Similarly, when the accretion rate is too high ($\dot{M} \gtrsim 10^{-6} M_\odot$ yr^{-1}), then the white dwarf is likely to expand into a red giant, causing the binary system to experience a common envelope and preventing further mass accretion onto the white dwarf. Consequently, the rate of accretion for a viable thermonuclear supernova must be between these values: the general consensus is that the rate of accretion must be within the range at which stable burning can occur – that is, when the rate at which hydrogen is transformed

into helium is equal to the rate of accretion.

The most promising aspect of the SD scenario is that it provides a simple, natural, and clear way through which a white dwarf can reach the Chandrasekhar mass, and thus explode. It also explains the apparent homogeneity in the observed SNe Ia. However, some observed properties of SNe Ia – such as the ranges of brightness and decline rates – are difficult to explain using this scenario, and it also fails to reproduce the observed rate of SNe Ia. Additionally, in such a scenario, one must ask: what of the companion? It is expected that the companion star will generally survive the supernova event, but to date, no firm observational evidence for such survival has been found. Attempts to locate possible companions from pre-explosion observations have also been lacking, though potential candidates have been found for a certain subset of SNe Ia.

Double-Degenerate Scenario

The DD scenario sees two white dwarfs interacting, but like the SD scenario, there are multiple avenues through which it can play out. The originally-proposed DD model (sometimes referred to as the "tidal accretion" model) saw two CO WDs of different masses (with a combined mass that exceeds the Chandrasekhar mass) brought together through the emission of gravitational radiation. The lighter WD, after filling its Roche lobe, initiates a mass-transfer process which is dynamically unstable. This would lead to the complete tidal disruption of the smaller WD, and to the creation of a disk, primarily composed of carbon- and oxygen-rich material, around the primary WD.

Another possible method through which the DD scenario can proceed is the so-called "violent merger" model, in which two white dwarfs are in a close binary (the exact mass of these

white dwarfs is less important than in the tidal accretion model; rather, the ratio of the masses is important, and should be upwards of 0.80). Rather than the secondary white dwarf being torn apart by tidal forces, resulting in an explosion after the merger, in this scenario, the explosion occurs either before or during the merger, as a result of compressional heating: as material from the companion hits the surface of the primary, it is compressed and heats up. If the temperature reaches a critical point ($T > 2.5 \times 10^9$ K), a detonation may be formed. For more massive companions, the detonation will be deeper inside the primary white dwarf due to the increased density of the accretion stream allowing it to reach deeper into the white dwarf. Should the detonation be within the core, carbon core detonation will be accomplished, resulting in a thermonuclear runaway process that swiftly yields a thermonuclear supernova.

The DD scenario is promising in a number of ways that the SD scenario is not: the non-detection of both pre- and post-explosion companions favour the DD scenario, as does its ability to reproduce both the brightness distribution and the observed rate of SNe Ia. However, it also falls short in a few areas: the tidal accretion model, despite being the most straightforward version of the scenario, may result in carbon-burning on the outer layers of the white dwarf, which could transform the white dwarf from a CO white dwarf into an ONeMg white dwarf. Further accretion onto this white dwarf would lead to the accretion-induced collapse of the white dwarf into a neutron star, rather than to a supernova. Additionally, the much wider range of possible explosion masses makes it difficult to explain the homogeneity in observed SNe Ia.

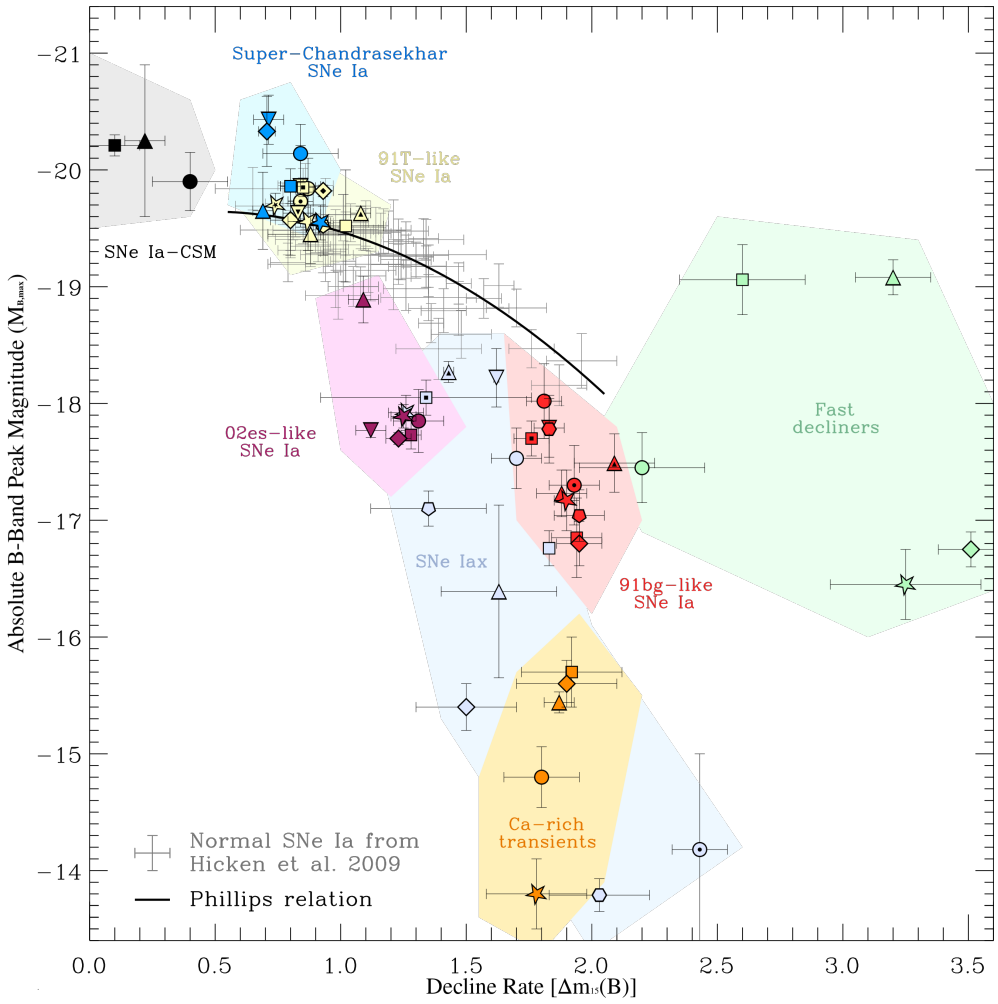

Figure 3.2: Distribution of different types of SNe Ia, based on peak luminosity vs. decline rate. Different subclasses of SNe Ia are highlighted in different colours. Image adapted from Figure 1 of Taubenberger (2016).

3.2 Thermonuclear Supernova Explosions

Thermonuclear supernovae were, for quite some time, believed to be a largely homogeneous class of supernova. However, the last few decades of observations have revealed a pronounced diversity among these supernovae: in addition to the "normal" SNe Ia, which exhibit a clear relation between peak luminosity and light curve width (known as the "Philips relation," or

the width-luminosity relation), several subclasses clearly exist which do not follow this relation, and whose differences are too pronounced to be able to be reasonably explained by a single progenitor scenario or explosion model – see Figure 3.2. In this section, we present the different explosion models that have arisen to explain the diversity in observations, and identify their differences and the situations in which they may arise. We also discuss the physics behind these models, including how the explosions form, and how they propagate through the white dwarf after their formation.

This section was written using the following additional source: the chapter *Thermonuclear Explosions of Chandrasekhar Mass White Dwarfs* by Nomoto & Leung (2017), in the living reference manual *Handbook of Supernovae*.

The apparent homogeneity in SNe Ia was largely explained by the belief that all such explosions arose as a result of a white dwarf accreting matter from a companion until it reached the Chandrasekhar-mass – the SD scenario described in Subsection 3.1.2. The combined discoveries of the DD progenitor scenario and of the deviation from homogeneity in SNe Ia light curves suggested that this is not, in fact, the case. As a result, in addition to the two progenitor scenarios detailed in Subsection 3.1.2, multiple explosion models have been proposed in attempt to explain the different scenarios through which a white dwarf might explode in a thermonuclear supernova. These models can largely be categorised in one of two models: the Chandrasekhar-mass (Ch-Mass) model, and the sub-Chandrasekhar-mass (subCh-Mass) model.

3.2.1 Chandrasekhar-Mass Explosions

The main discriminator of these two models lies in the mass of the exploding white dwarf at the moment of supernova explosion. The Ch-mass model pertains to those white dwarfs that explode at or near to the Chandrasekhar mass. Like the SD progenitor model with which it is typically associated, the Ch-Mass model is considered the "traditional" model of thermonuclear explosions, as it is reasonably able to explain the previously-perceived homogeneity among SNe Ia.

Initially, it was suggested that a supersonic prompt detonation, originating somewhere nearby to the core of the white dwarf, could be responsible for the Ch-mass explosions. However, this model predicts nearly the entire white dwarf to be converted into iron-group elements: since the detonation is supersonic, the unburned material is unable to expand prior to burning and the entire star burns at the high initial densities ($\rho \sim 10^9\ \mathrm{g\ cm^{-3}}$) of a white dwarf in hydrostatic equilibrium. This is something which is at odds with our observations, as the production of a significant amount of intermediate-mass elements (IME) is expected. To correct for this discrepancy, the star must expand prior to detonation, in order to bring the average densities down to a level within which the synthesis of IMEs is possible; as such, the explosion cannot start off as a detonation, and must instead begin as a deflagration.

If the burning must indeed start as a deflagration, it is only logical to ask whether it may remain as such. These models – known as "pure deflagration" models – were, for some time, the predominant models for thermonuclear supernovae (the W7 model of Nomoto et al. (1984) being the most well-known example). In such models, the accretion of mass onto the white dwarf leads to the increase in temperature in its central layers, through conduction. This increase in temperature results in the ignition of carbon, restarting the fusion process.

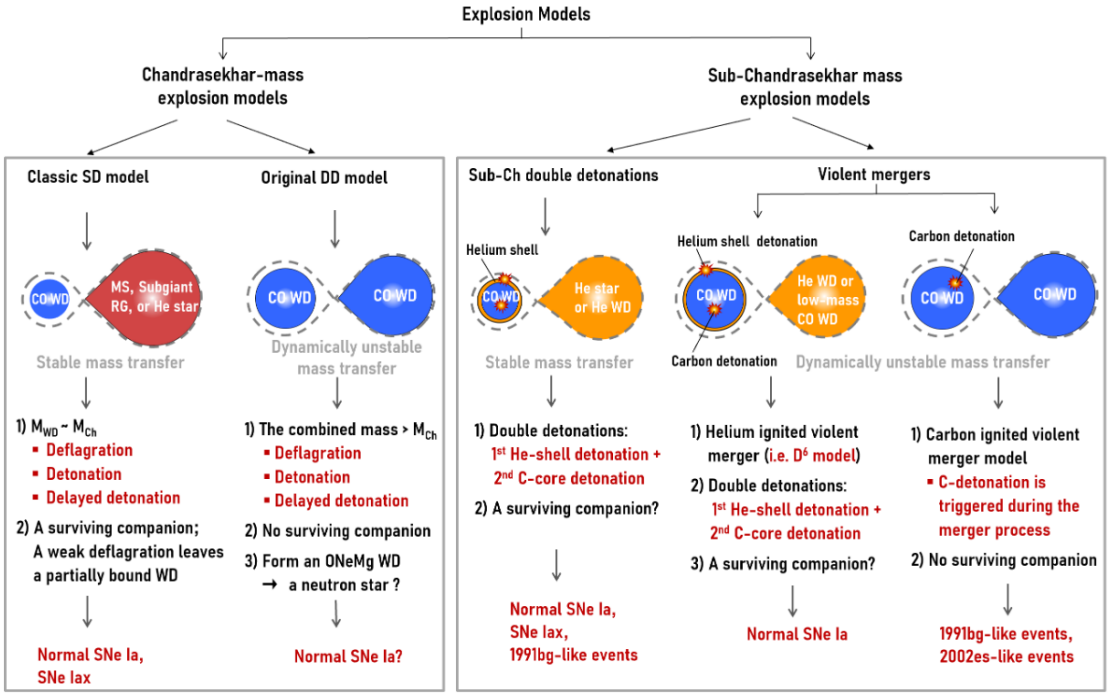

Figure 3.3: Several different explosion models for thermonuclear supernovae, categorised in the context of Chandrasekhar-mass explosions versus sub-Chandrasekhar-mass explosions. Note that this image is not a comprehensive list of all model types. Image adapted from Figure 3 of Liu et al. (2023).

However, the strong electron degeneracy within the white dwarf means that this process is unstable, giving rise to what is known as a "carbon flash." This flash releases a large amount of energy in a very short amount of time, leading to further heating in the core, and resulting in a thermal runaway effect. This, in turn, causes a carbon burning front to begin to propagate outwards at subsonic velocities – a deflagration wave. This wave incinerates the inner layers, causing the material there to enter into nuclear statistical equilibrium (NSE) and producing IGEs – namely, ^{56}Ni. The energy released by this burning is redistributed over the entire white dwarf, allowing it to expand as a whole, even while the deflagration wave compresses the material in front of it as it travels. The reduction in density that results from this expansion eventually makes it so that as the deflagration expands, it can no longer convert

the burned material into NSE, and instead begins to produce IMEs. Eventually, the nuclear-binding energy released through the burning process exceeds the overall binding energy of the white dwarf, unbinding it and resulting in a thermonuclear supernova. The greatest argument against pure deflagration models is that they produce relatively low amounts of ^{56}Ni, which means that they are unable to account for the observed brightness of the majority of SNe Ia, as the predicted peak luminosities from these models are simply too low. However, the model has found some success in explaining some low-luminosity events (known as "Type Iax" supernovae – see Figure 3.2), for which the low production of ^{56}Ni produces comparable luminosities.

Burning in the majority of Ch-mass explosions must therefore transition away from deflagration, and models in which this occurs are known as "delayed detonation" models. In these scenarios, nuclear burning is first ignited in a deflagration, as described above. This produces mainly IGEs, owing to the high initial densities of the white dwarf. The star expands, owing to the energy released via this burning, which causes the unburned nuclear fuel to move into a state of lower density. Some time after the deflagration front forms, a detonation – a burning front that propagates supersonically, as opposed to subsonically like the deflagration – also forms. This detonation front quickly travels through the white dwarf, including the unburned fuel, producing primarily IMEs, resulting in abundances being present in ratios quite close to those found in observations. Various forms of the delayed detonation models exist, such as the deflagration-to-detonation transition (DDT) model, the pulsating delayed detonation (PDD) model, the gravitationally confined detonation (GCD) model, and the pulsational reverse detonation (PRD) model. The main difference between these models lies in how they explain (or attempt to explain) the transition from deflagration to detonation.

While these models are very capable of explaining our observations – both the ratios of IGEs and IMEs, as well as the light curves and spectra – this discrepancy in explanations for the transition to detonation is the greatest drawback for this class of models: this transition has proven incredibly difficult to model, and to date, no simulation has been able to conclusively demonstrate that this transition really occurs.

3.2.2 Sub-Chandrasekhar-Mass Explosions

The subCh-mass model pertains to white dwarfs that explode at a mass below the Chandrasekhar mass. These models are most commonly associated with the DD scenario, though they aren't exclusively so. Simulations have shown that detonations in white dwarfs below the Chandrasekhar limit are expected to produce observable parameters comparable to those of actual observations, which suggests that this case is a promising one. The question that must be answered, then, is how such a detonation can be triggered.

One form of subCh-mass model is the "double detonation" model. In this model, a detonation is first triggered in a He shell on the surface of the white dwarf (or the primary white dwarf, in the case of the DD scenario). This detonation is triggered by the accumulation of He by the white dwarf from its binary companion. In the event that this mass transfer is stable, the He is able to accumulate atop the white dwarf until it reaches a critical mass (original models placed this critical mass at around 0.2 $M_{\odot}$, but more recent simulations have shown that such a detonation may be possible for He shell masses 10-100 times smaller. The exact value is uncertain, but certainly varies based upon the composition and mass of the white dwarf in question). When this critical mass is reached, compressional heating causes nuclear fusion to be reignited in the material of the He shell, and a detonation is triggered. This

causes a shockwave to travel through the white dwarf, compressing and heating material as it does. When the shock reaches the CO core, the core is likewise compressed, leading to a thermonuclear runaway as carbon fusion is ignited. Unlike the Ch-mass scenario, no deflagration is needed, as the lower initial mass (and therefore, densities) of the white dwarf allow for the synthesis of IME. Several binary systems that match the required criteria have been found, which lends support to this scenario. However, it has been predicted that a detonation in a thick He shell will lead to the production of an outer ejecta layer enriched with additional IGEs (including extra ^{56}Ni) which would result in inconsistency between the predictions and observations. Thinner He shells, possibly polluted with C from the core, have been proposed to resolve this issue, and such a model seems able to reproduce the spectra from normal SNe Ia, but how exactly such a thin shell would ignite is not well understood.

Another type of subCh-mass model is the violent merger, the basics of which were described in Subsection 3.1.2. These models are inherent to the DD scenario, as they rely on the dynamically unstable transfer of mass from one white dwarf to another. The scenario described in Subsection 3.1.2 was the most simple version of this process, wherein the mass transfer is between two CO white dwarfs of comparably large mass. In this scenario – known as a "carbon-ignited violent merger" – the mass transfer causes compressional heating in the primary white dwarf, which – if the rate of mass transfer is sufficient – will lead to the ignition of a detonation in the CO core of the primary, resulting in a thermonuclear supernova. This scenario is able to reliably reproduce most of the observational properties of some subluminous SNe Ia, and is also able to do so for many properties of the normal case. However, the actual mechanism responsible for the triggering of the detonation is poorly understood.

A third possibility for the subCh-mass scenario exists, and is most often known as the

"helium-ignited violent merger" model. This model – sometimes referred to as the "dynamically driven double-degenerate double detonation" or "D^6" model – is essentially a hybrid of the two subCh-mass models described above. In this scenario, a He detonation is triggered on the surface of the primary white dwarf, due to the unstable transfer of He from its companion. Notably, however, the He detonation is not ignited in a massive, stable He layer like in the normal double detonation scenario, and instead occurs during a dynamic stage in the white dwarf's evolution – in other words, during the violent merger of two white dwarfs. This detonation then proceeds as normal for the double detonation scenario, with a resulting shockwave causing compression of the CO core, resulting in the second detonation and ultimately giving rise to the thermonuclear supernova. The benefit of this model is that because the He layer involved is necessarily smaller, the products of He burning during the He detonation are reduced when compared to the regular double detonation model, producing explosions that can quite closely reproduce the observed properties of most normal SNe Ia. An added interesting feature of this model is that the secondary white dwarf is not necessarily predicted to be destroyed in the explosion, and may in fact survive, ejected from the system at a velocity $\gtrsim 10^3\ \mathrm{km\,s^{-1}}$, which would provide for a novel way to detect and diagnose these explosions. Indeed, several of these so-called "hypervelocity" white dwarfs have been detected by Shen et al. (2018), including one that could be associated with an SNR.

3.3 Thermonuclear Nucleosynthesis

Though it is not inaccurate to state that the primary difference between the two categories of supernovae – that of core-collapse and thermonuclear – lies in the nature of their progenitor star, it is perhaps more accurate to say that the difference lies in how their expansion

against gravity is powered. For core-collapse supernovae, this expansion is largely powered by the release of gravitational binding energy during the collapse of the stellar core. In the case of thermonuclear supernovae, this energy instead comes from the synthesis of light nuclei (known as "fuel") into heavier nuclei (known as "ash"): an exothermic reaction not unlike that which powers a main-sequence star. Herein, we discuss some of the processes responsible for the production of new nuclei during a thermonuclear supernova.

This section makes use of the following supplementary sources: the paper *Explosive nucleosynthesis in carbon deflagration models of Type I supernovae*, by Thielemann et al. (1986); and the textbook *Essentials of Nucleosynthesis and Theoretical Nuclear Astrophysics*, by Rauscher (2020);

3.3.1 Carbon, Oxygen, and Silicon Burning

The burning of carbon plays a role of vital importance in a thermonuclear supernova, but it actually begins well before the explosion itself. At sufficient central densities, carbon-burning will ignite deep within the white dwarf's core, where it will will remain modest for some time. This phase – known as the "smoldering" or "simmering" phase – will continue up until the rate of carbon-burning exceeds the rate of neutrino losses, which (for the SD scenario) will take between 100-1000 years. During this simmering phase, ^{12}C is gradually converted into heavier elements, predominantly ^{20}Ne, ^{24}Mg, and ^{28}Si through $^{12}\mathrm{C}(^{12}\mathrm{C},\alpha)^{20}\mathrm{Ne}$[1] and subsequent alpha captures. Other important channels are the $^{12}\mathrm{C}(^{12}\mathrm{C},p)^{23}\mathrm{Na}(p,\alpha)^{20}\mathrm{Ne}$ and $^{12}\mathrm{C}(^{12}\mathrm{C},n)^{23}\mathrm{Na}$ reactions, as these reactions produce light particles – alpha particles, protons, and neutrons – that are important for further reactions.

[1] This notation – known sometimes as Bethe's notation – is common in nuclear physics. In this form, a reaction A(b, c)D is the equivalent to saying that A + b will produce D + c.

Once the rate of burning exceeds neutrino losses, the thermonuclear runaway begins and the burning mode switches from convective to explosive as a burning front forms and begins to propagate through the white dwarf (in the form of either a deflagration or a detonation; see Section 3.2). At this point, explosive oxygen burning begins, which yields mostly ^{28}Si, as a result of $^{16}\mathrm{O}(^{16}\mathrm{O},\alpha)^{28}\mathrm{Si}$. Also important in this process is ^{24}Mg: while Mg is not depleted, the vast majority of the reactions during oxygen burning result in Si. This is due to the fact that, because of the previously stated reaction, as well as $^{24}\mathrm{Mg}(\alpha,\gamma)^{28}\mathrm{Si}$, two ^{16}O and one ^{24}Mg combine to exactly make two ^{28}Si. Once Mg has been depleted, excess alpha particles are produced for each ^{28}Si produced, and so we have further alpha captures, producing species such as ^{32}S, ^{36}Ar, and ^{40}Ca.

Explosive silicon burning can occur in the core of the white dwarf, but how it proceeds is highly dependent upon temperature. At high temperatures, silicon burning enters the realm of nuclear statistical equilibrium (NSE), leading to the resulting abundances to follow their equilibrium values (see Subsection 3.3.2). For lower temperatures, an incomplete burning of silicone is instead achieved. The primary products of incomplete silicon burning are ^{32}S, ^{56}Fe, ^{40}Ca, and ^{36}Ar. The ^{56}Fe is produced in the form of ^{56}Ni, which then decays. Silicon burning is also the primary source of the other IGEs, such as Ti, Cr, and Mn.

3.3.2 Nuclear Statistical Equilibrium

When considering the differences between nucleosynthesis in Ch-mass and subCh-mass explosions, one finds that many of these differences arise as a result of the involved central densities. The Ch-mass white dwarf has a central density exceeding $10^9\ \mathrm{g\ cm^{-3}}$, which allows for the rather rapid formation of nuclei. Similarly, the temperatures in such an environment are

consequently high, which allows for the photo-dissociation of nuclei into nucleons. In such an environment, explosive nuclear burning is able to reach a state known as nuclear statistical equilibrium.

When the nuclear reactions in a system are in equilibrium, then that system is said to be in nuclear statistical equilibrium. In such a state, all fusion reactions are directly balanced by their inverses, including photo-dissociations, meaning that, although nuclear reactions occur, the composition of the system is largely unchanging. A notable exception to this are weak interactions, such as β-decay, which are not in equilibrium. In such a state, we can approximate all reactions as occurring quickly, due to the temperatures and densities involved. In addition, the abundances of a nuclei are determined solely by the density, temperature, and electron fraction Y_{e}, and as such, only the relative binding energies of each species of nuclei is relevant to the composition of the system: the individual reaction rates of each species can largely be ignored.

In the conditions present within a Ch-mass white dwarf at the moment of thermonuclear supernova, NSE is dominated by the IGEs, though specifically which isotopes are most prominent depends largely on the electron fraction in the white dwarf (see Figure 3.4). The mass fraction X_{i} of any isotope in NSE is given by:

$$X_{\mathrm{i}}(A_{\mathrm{i}}, Z_{\mathrm{i}}, T, \rho) = \frac{A_{\mathrm{i}}}{\rho N_{\mathrm{A}}} \omega(T) \left(\frac{2\pi k T M(A_{\mathrm{i}}, Z_{\mathrm{i}})}{h^2} \right)^{3/2} \exp\left[\frac{\mu(A_{\mathrm{i}}, Z_{\mathrm{i}}) + B(A_{\mathrm{i}}, Z_{\mathrm{i}})}{kT} \right] \tag{3.1}$$

where A_{i} is the atomic number; Z_{i} is the charge; T is the temperature; ρ is the mass density; N_{A} is Avogadro's number; $\omega(T)$ is the temperature-dependent partition function; and $M(A_{\mathrm{i}}, Z_{\mathrm{i}})$, $B(A_{\mathrm{i}}, Z_{\mathrm{i}})$, and $\mu(A_{\mathrm{i}}, Z_{\mathrm{i}})$ are the mass, binding energy, and chemical potential

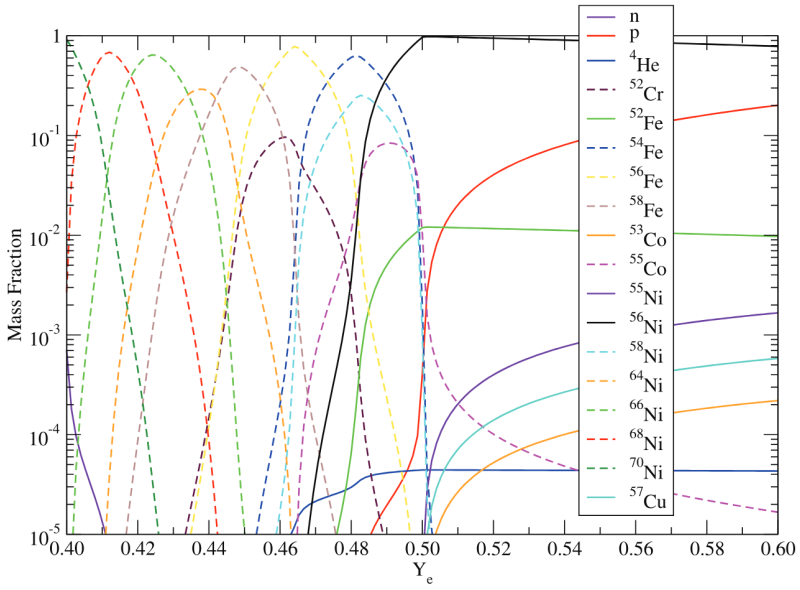

Figure 3.4: Mass fractions as a function of electron fraction Y_{e} for a number of nuclei in NSE, given a constant density $\rho = 10^7\,\mathrm{g\,cm^{-3}}$, and temperature $T = 3.5 \times 10^9\,\mathrm{K}$. Only nuclei with mass fractions above 10^{-5} are shown. Image from Figure 3 of Seitenzahl et al. (2008).

of the isotope, respectively.

3.4 Models of Thermonuclear Supernova Nucleosynthesis

To this point, our discussion has been largely theoretical in nature. We turn our attention now to the application of this knowledge – more specifically, to its implementation, through the creation of models. Creating models of supernovae, and of supernova nucleosynthesis, are two ways by which the modelling community attempts to simulate these scenarios. For thermonuclear supernova, the multiple possible progenitors, as well as the wide variety of methods by which they might explode, means that no single model is presently capable of explaining the zoo of available observations.

This section was written using the following additional sources: the paper *Nucleosynthe-*

sis in multi-dimensional SN Ia explosions, by Travaglio et al. (2004); the paper *Models for Type Ia Supernovae and Related Astrophysical Transients*, by Röpke & Sim (2018); the paper *Thermonuclear Supernovae: Simulations of the Deflagration Stage and Their Implications*, by Gamezo et al. (2003); and the chapter *Nucleosynthesis and Tracer Methods in Type Ia Supernovae*, by Seitenzahl & Pakmor (2023), from the reference work *Handbook of Nuclear Physics*.

3.4.1 Methods for Modelling

Modelling and simulating a scenario as large, complex, and violent as a supernova is not an easy task. These models themselves are large and complex, and as such, are computationally demanding, often requiring the use of powerful supercomputers for them to be completed in any reasonable amount of time. Even then, simplifications must be made: the physics involved may take too long to solve alongside the simulation, or the resolution necessary to create a simulation with absolute accuracy is simply unfeasible, even given modern equipment. In this section, we present the methods most commonly used to perform these simulations.

Hydrodynamical Simulations

The simulation of a thermonuclear supernova explosion can best be described as a boundary problem, where the boundary in question is the flame front as it propagates through the white dwarf. The most common solutions to this kind of problem are based on fluid dynamics: specifically, the Euler equations for an ideal fluid. The basic set of equations, then, are those that define the conservation of mass, momentum, and energy. Relativistic effects and viscosity are oftentimes ignored in the study of thermonuclear explosions, and so the set of

equations is given by:

$$\frac{\partial \rho}{\partial t} + \nabla \cdot (\rho \mathbf{v}) = 0 \tag{3.2}$$

$$\rho \left[\frac{\partial \mathbf{v}}{\partial t} + (\mathbf{v} \cdot \nabla) \mathbf{v} \right] = -\nabla P - \rho \nabla \Phi \tag{3.3}$$

$$\frac{\partial E}{\partial t} = -\nabla \cdot [(E + P)\mathbf{v}] + \rho \mathbf{v} \cdot \nabla \Phi + \rho \dot{q} \tag{3.4}$$

where $\mathbf{v}$ is the flow velocity; E is the total energy density (specifically, the sum of the inner energy U and the nuclear energy q); and Φ is the solution of the Poisson equation for arbitrary density distributions:

$$\nabla^2 \Phi = 4\pi G \rho \tag{3.5}$$

where G is the gravitational constant. Additional equations are needed to account for the reactions from nuclear burning, such as the balance of species, and heat conduction.

Problems begin to arise, however, when one considers the range of scales involved: physically, white dwarfs are on the order of 10^8–10^9 cm, while the thickness of a thermonuclear flame is between 10^{-6}–10^{-3} cm. Temporally, the white dwarf can explode with time scales on the order of seconds to minutes, while the burning time scale of a thermonuclear flame can range from 10^{-12}–10^{0} seconds. Even the conditions involved range greatly, with densities between 10^0–10^{10} $\mathrm{g\,cm^{-3}}$, and temperatures between 10^3–10^{10} K.

The temporal differences present a problem in that, while the evolution of the progenitor may last centuries, the numerical time steps used in simulations must be much less than a second in order to properly simulate the propagation of the flames. Because of this, explosion

simulations will usually begin at the point of ignition, allowing the progenitor's evolution to be treated as an initial condition, rather than something to be simulated. Similarly, simulations tend to end once the ejecta from the explosion reaches a state of near-homologous expansion. Further evolution, such as those required to reproduce the observables commonly found in SNe Ia, only begin to emerge days, weeks, or even months after this point, and as such, it is necessary to separate this phase from the hydrodynamics simulations. Post-processing techniques, such as radiative transfer simulations and the tracer particle method, are typically used for this stage of evolution.

The differences in spatial scale, however, require a different approach. For full-star simulations, two options are available: either the physical structure of the fronts can be artificially broadened, such that it can be represented in the computational grid used for the simulations; or it can be ignored, and treated simply as a sharp discontinuity that serves to separate the fuel from the ashes. This second approach is the most commonly used one, and the most commonly used technique to represent the propagation of these fronts is known as the level-set approach, which was introduced for the simulation of deflagration fronts by Reinecke et al. (1999). In it, a time-dependent set of points representing the front's geometry is associated with an isoline of a level-set function such that, at all points on the isoline, the level-set function is zero.

Reaction Networks

Nuclear reactions play an important role in many astrophysical scenarios, and nucleosynthesis in thermonuclear supernovae is no exception. As described in Section 3.3, a wide variety of processes are involved in these reactions, processing and producing an even wider variety

of particles. Keeping track of all of these reactions is a difficult task, and for this purpose, a reaction network is used.

In essence, a reaction network keeps track of the composition of a large system composed of several different species of nuclei, alongside electrons, protons, neutrons, and (for some reaction networks) neutrinos. They are coupled, linearised systems of differential equations, which allow one to evolve different nuclei in a system, assuming one knows the relevant reactions and the rates at which they occur. In a generalised form, a reaction network can be written as:

$$\dot{Y}_{\mathrm{i}} = \frac{1}{\rho N_{\mathrm{A}}} \left(\sum_{\mathrm{j}} {}^{1}_{\mathrm{i}}K_{\mathrm{j}}\, {}^{1}_{\mathrm{i}}r_{\mathrm{j}} + \sum_{\mathrm{j}} {}^{2}_{\mathrm{i}}K_{\mathrm{j}}\, {}^{2}_{\mathrm{i}}r_{\mathrm{j}} + \sum_{\mathrm{j}} {}^{3}_{\mathrm{i}}K_{\mathrm{j}}\, {}^{3}_{\mathrm{i}}r_{\mathrm{j}} + \cdots \right) \tag{3.6}$$

where $\dot{Y}_{\mathrm{i}}$ is the change over time in abundance Y for some nuclide i, with $1 \leq i \leq n_{\mathrm{net}}$; ${}^{1}_{\mathrm{i}}r_{\mathrm{j}}$, ${}^{2}_{\mathrm{i}}r_{\mathrm{j}}$, and ${}^{3}_{\mathrm{i}}r_{\mathrm{j}}$ are the jth rates for reactions involving species i for one-body, two-body, and three-body interactions, respectively; and ${}^{1}_{\mathrm{i}}K_{\mathrm{j}}$, ${}^{2}_{\mathrm{i}}K_{\mathrm{j}}$, and ${}^{3}_{\mathrm{i}}K_{\mathrm{j}}$ are integers that specify the amount of nuclei i produced or destroyed in the one-, two-, or three-body reactions, respectively. Reactions involving additional bodies, while possible, are generally unlikely to occur in any relevant scenario, and are usually neglected as a result. Here, one-body interactions are generally photodisintegration, lepton capture, or spontaneous decay, while two- and three-body interactions involve nuclei and depend upon the cross-sections of the involved species. The determination of the reaction rates can either be done through direct measurement of cross-sections via experimental observations, or through theoretical estimation, depending on the accessibility and stability of the nuclide in question.

Tracer Particle Method

With modern computational capabilities, it is possible to solve large reaction networks directly while computing the hydrodynamics of a simulation, but only in one dimension. The reason for this is that most one-dimensional codes are Lagrangian in nature, which allows one to record the temperature and density evolution for different elements, since the grid moves with the fluid. For two- or three-dimensional simulations, however, most hydrodynamic schemes are Eulerian in nature, for which the grid is fixed in space. For these simulations, it is not feasible to solve large reaction networks alongside the hydrodynamics. Instead, one can make use of the tracer particle method.

In the tracer particle method, the hydrodynamic simulation is performed as normal, but it is not coupled to a large reaction network – a small network, consisting of only a handful of isotopes, is often used in this stage, as this allows for the reasonably precise modelling of the energy release from nuclear burning during the simulations. Instead, a set of tracer particles is added to the simulation at its start. Typically, these particles are distributed evenly across mass coordinates, such that each particle represents the same amount of mass, though it is possible to assign further particles to regions of interest. These particles are then propagated, one timestep at a time, according to the velocity field at its current location. Each particle records the temperature and density at each step in the hydrodynamic simulation, creating a record of the evolution for these properties. Then, in post-processing, one is able to couple a large reaction network to these recordings, rather than to the simulation itself. By applying an appropriate weighting to each tracer particle (generally, the mass associated with each tracer), it is possible to calculate detailed information about the yields of the explosion's nuclear reactions.

Table 3.1: Summary and comparison of the basic properties of the seven sets of models described in Subsection 3.4.2.

Paper	No. Dim.	Progenitor Type	Explosion Mechanism	No. Sims.	Init. RN	Final RN	Tracers
M10	2	Ch-mass	DDT, Def.	3	5	384	6400
S13	3	Ch-mass	DDT	17	5	384	1000000
F14	3	Ch-mass	Def.	14	5	384	1000000
LN18	2	Ch-mass	DDT	21	7	495	25600
T18	3	subCh-mass	D^6	1	13	-	-
B19	1	Ch-mass subCh-mass	DDT Det.	100	722	-	-
LN20	2	Ch-mass subCh-mass	Def. Dbl. Det.	57	7	495	25600

3.4.2 Published Models

We now turn to a discussion of specific simulations. There are many different models that have been proposed and put forth in an effort to explain the many differing aspects of thermonuclear supernovae, both theoretical and observational, with different models addressing different progenitor properties, explosion methods, initial conditions, and in some cases, different physics. In this section, we present seven of the most prominent models put forth in recent years, and discuss the basic modelling methods and assumptions used by each. A summary of each model can be found in Table 3.1.

Maeda et al. 2010 (M10)

In Maeda et al. (2010), the authors explore the nucleosynthetic characteristics of multiple explosion mechanisms through the use of three two-dimensional explosion models: a pure turbulent deflagration (C-DEF), a delayed detonation following a spherical initial deflagration (C-DDT), and a delayed detonation following a highly asymmetric initial deflagration

(O-DDT). All models made use of a white dwarf with an initial central density of 2.9×10^9 $\mathrm{g\,cm^{-3}}$, and burning was treated in a simplified way, making use of only five species – C, O, alpha particles, an IGE representative, and an IME representative. For the DDT models, a fuel density of $\rho_{\mathrm{DDT}} \leq 1.0 \times 10^7\ \mathrm{g\,cm^{-3}}$ was used to determine when the deflagration-to-detonation transition took place.

The propagation of the explosion fronts in the hydrodynamics simulations were calculated using the level-set approach, which treats the fronts as discontinuities. The tracer particle method was utilised for the calculation of nucleosynthesis products, making use of 6400 (80^2) tracer particles distributed uniformly in mass coordinates across the white dwarf, and a reaction network of 384 isotopes up to ^{98}Mo.

Seitenzahl et al. 2013 (S13)

Seitenzahl et al. (2013) presents a collection of 17 three-dimensional, high-resolution simulations of DDT models. The main difference between these models is the strength of the initial deflagration phase, which was determined by using a different number of initial ignition kernels: N1, N3, N5, N10, N20, N40, N100, N150, N200, N300, and N1600, with the number corresponding to the number of kernels. The majority of simulations were performed on a white dwarf with initial central density of $2.9 \times 10^9\ \mathrm{g\,cm^{-3}}$, but two additional simulations – one with a higher central density of $5.5 \times 10^9\ \mathrm{g\,cm^{-3}}$, and one with a lower central density of $1.0 \times 10^9\ \mathrm{g\,cm^{-3}}$ – were performed for the N100 kernel configuration, and the N1600 kernel configuration was performed twice: once with a normal configuration, and once with a configuration that was significantly more compact. Three more simulations were performed on the standard N100 configuration with varying degrees of metallicity.

The deflagration and detonation fronts in the simulations were treated as separate discontinuities between the fuel and the ash, and as such their propagation was calculated using the level-set approach. A small reaction network consisting of 5 species was used for the hydrodynamics simulations. Following that, nucleosynthesis calculations were performed using the tracer particle method, with 10^6 (100^3) particles of equal mass distributed so as to reproduce the underlying density profile of the white dwarf, and a reaction network of 384 isotopes was used for this post-processing.

Fink et al. 2014 (F14)

Fink et al. (2014) is very similar to S13: it also presents 14 three-dimensional, high-resolution simulations, with initial deflagration phase strength being determined by using a different number of initial ignition kernels: N1, N3, N5, N10, N20, N40, N100, N150, N200, N300, and N1600, again with the number corresponding to the number of kernels. The difference, however, is that F14 looks to address the pure deflagration scenario, rather than that of the DDT scenario. Like S13, most simulations were performed on a white dwarf with initial central density of $2.9 \times 10^9\ \mathrm{g\,cm^{-3}}$, with the N100 kernel configuration being performed twice more for high- and low-density situations, and the N1600 kernel configuration being performed with both a normal and compact kernel configuration.

As in S13, the deflagration front is treated as a discontinuity, and the change in its position is described through a level-set approach. The same 5-species reaction network from S13 was used for the hydrodynamics simulations. For post-processing, the tracer particle method was again employed, with with 10^6 (100^3) particles of equal mass. A 384-isotope reaction network was coupled to this, to obtain the final results of the explosive yield.

Leung & Nomoto 2018 (LN18)

A collection of 41 simulations (for which 21 have reported nucleosynthesis yields) of DDT models are presented in Leung & Nomoto (2018). Though they are two-dimensional simulations, LN18 performs a parameter survey, exploring the effects that a wide variety of initial parameters have on the resulting explosion. These parameters include metallicity, C/O mass ratio, flame shape, DDT criteria, and turbulent flame formula. The initial density of the white dwarf was also varied, using several values ranging from 5.0×10^8 g cm^{-3} to 5.0×10^9 g cm^{-3}, meaning that several of the scenarios addressed in this study could be considered subCh-mass scenarios.

For the hydrodynamics simulations, an initial reaction network comprised of 7 species was used. The nucleosynthesis calculations were performed in post-processing using the tracer particle method, with 25600 (160^2) particles. For this, a 495-isotope reaction network was used.

Tanikawa et al. 2018 (T18)

The work of Tanikawa et al. (2018) concerns itself with a very specific type of thermonuclear supernova: that of the D^6 model. In addition to this particular model, the authors took a different approach than most others, in that they used a smoothed particle hydrodynamics (SPH) code to perform simulations, rather than the common hydrodynamics code used by most others. This allowed them to begin their simulations not from the merger process, but during the orbital period. Two white dwarfs – a primary, with a total mass of 1.0 $M_\odot$ (composed of a 0.95 $M_\odot$ CO core and a 0.05 $M_\odot$ He shell); and a secondary, with a total mass of 0.6 $M_\odot$ (composed entirely of CO) – were established, with a total of $\sim 6.7 \times 10^7$ particles

between them, distributed equally by mass. A "hot spot" was created in the He shell of the primary white dwarf, in order to easily initiate the He detonation.

The SPH simulation was itself coupled to a reaction network consisting of 13 isotopes following the alpha process. The authors were able to successfully demonstrate a CO core detonation following the He shell detonation, and showed that the companion white dwarf survived the explosion, being ejected from the system at a velocity of $\sim 1700\,\mathrm{km\,s^{-1}}$.

Bravo et al. 2019 (B19)

Bravo et al. (2019) looks to explore a wider variety of scenarios than most simulations: both the Ch-mass DDT scenario and the subCh-mass pure central detonation scenario are addressed, using a one-dimensional hydrodynamics simulation. The Ch-mass models addressed a variety of deflagration-to-detonation transition densities, ranging from $1.2 \times 10^7\,\mathrm{g\,cm^{-3}}$ to $4.0 \times 10^7\,\mathrm{g\,cm^{-3}}$, while the subCh-mass models addressed masses from 0.88 $M_\odot$ to 1.15 $M_\odot$. All of the exploding white dwarfs were also characterised by their temperatures and chemical compositions. 50 scenarios were explored, with 25 being of the Ch-mass case, and 25 being of the subCh-mass case. However, these scenarios were all explored twice: once with the standard C/O reaction rate, and once more with a C/O reaction rate that is attenuated by 90% of the classical value (indicated via $\xi_{\mathrm{CO}} = 0.9$). This was done to explore the possibility of the classical C/O reaction rate being overestimated by up to a factor of 10, as suggested by Martínez-Rodríguez et al. (2017).

Unlike most simulations, B19 did not make use of post-processing to determine nucleosynthetic yields. Instead, the use of a one-dimensional model allowed the authors to make use of a large nuclear reaction network of 722 isotopes directly in the computation of the

hydrodynamic evolution, which allowed for full coherence between the explosion and the resultant nucleosynthesis.

Leung & Nomoto 2020 (LN20)

For LN20, Leung & Nomoto (2020b,a) performed two-dimensional hydrodynamical simulations of both near Ch-mass white dwarfs (Leung & Nomoto 2020a), as well as for subCh-mass white dwarfs (Leung & Nomoto 2020b). For the near Ch-mass simulations, a focus was placed on the SNe Iax model, simulating pure deflagration models, with the central density, CO mass, and flame geometries being variable parameters. Also variable was the composition of the white dwarf, with both traditional CO white dwarfs, as well as a "hybrid" composed of a C, O, and Ne mixture being used. For the subCh-mass simulations, the double-detonation mechanism was examined, with the metallicity, white dwarf mass, and He envelope mass being the variable parameters. For the Ch-mass scenario, 28 models were examined, while 57 models were examined for the subCh-mass scenario.

For both scenarios, the level-set method was used to track the propagating fronts: the deflagration front in the case of the Ch-mass model, and the two detonation fronts in the case of the subCh-mass model. The simulations in both cases were coupled to a simplified seven-isotope reaction network. Post-processing was done using the tracer particle method, with 25600 (160^2) particles for each simulation, and a large nuclear reaction network consisting of 495 isotopes was used for the calculations of nucleosynthesis.

4

Instrumentation and Methodology

This study makes use of archival data obtained by the *XMM-Newton* and *Chandra* telescopes. Herein, we present a discussion of these telescopes, including a brief look at the unique design necessary for X-ray telescopes, and an examination of the device responsible for much of modern astronomy, the charge-coupled device (CCD). We also discuss the process of data analysis, including the reprocessing steps followed for each telescope's data; the pro-

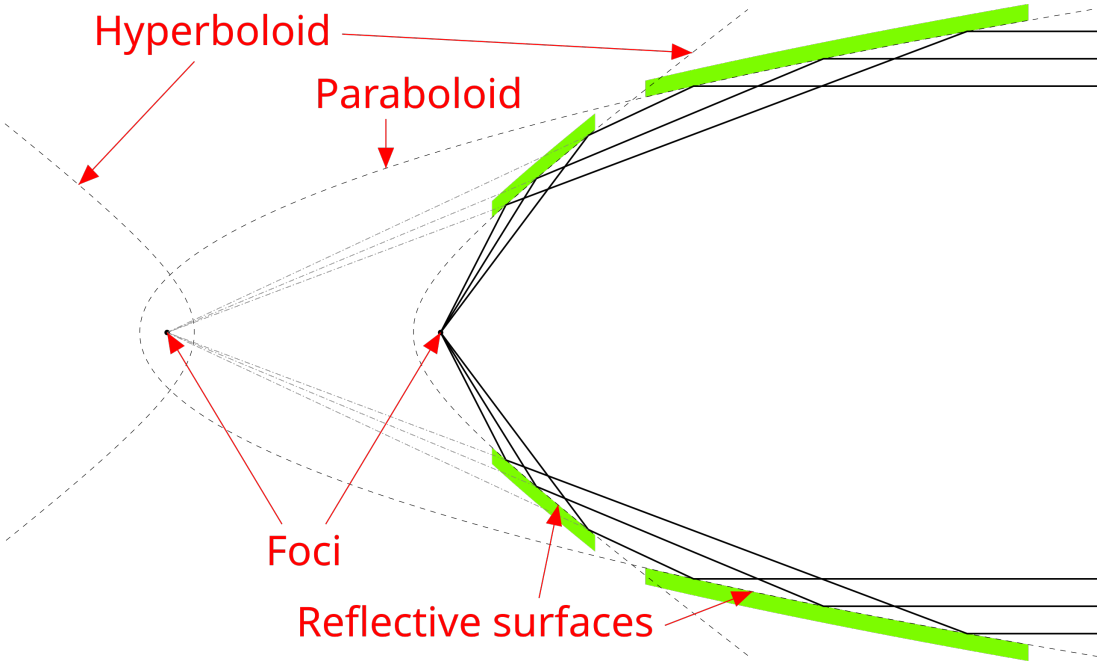

Figure 4.1: The mirror arrangement for the Wolter Type I telescope design. Image from Wikipedia[1].

cess of region selection; and the process of spectral analysis, including a look at the software responsible for spectral fitting, and the models used therein.

4.1 Grazing Incidence Optics

When it comes to the physical realities of X-ray astronomy, there are two major issues that need be addressed. The first is the atmosphere itself, which strongly attenuates X-rays and thus ensures that essentially none will reach the ground. The solution to this is to place the telescope outside the majority of the atmosphere. For early X-ray missions, this was done through the use of balloon-borne tests and sounding rockets, while more modern telescopes are placed instead into orbit.

[1] Image by Andreas 9384 - Own work, CC BY-SA 4.0, https://commons.wikimedia.org/w/index.php?curid=54729753

The second issue is that of optics. As high-energy photons, there is a difference in how X-rays interact with matter in comparison to their optical counterparts. When an X-ray photon encounters a traditional mirror surface at angles that would – for optical observations – be sufficient to reflect it, it will instead undergo a transmission (i.e. pass through) or absorption, rather than a reflection. Because of their high energies, X-rays will only reflect when the surface in question is both highly polished and at low angles of incidence.

The solution to this second problem, then, is to construct an optics system in which the incident X-rays strike the mirror surface not head-on, as is typical in the optical-regime analogues, but rather at a very shallow angle: a technique known as grazing incidence optics. The critical angle at which this technique becomes viable is dependent upon both the energy of the incident photon and the material of which the mirror surface is made, but for typical X-ray energies of a few keV, it is on the order of 1 degree of less (Willingale 2000).

The most commonly-used form of grazing incidence optics is the Wolter design (Wolter 1952a,b), which itself comes in three subclasses known as Type I, Type II, and Type III. These designs make use of multiple mirrors of different shapes – paraboloids, hyperboloids, or ellipsoids – to gradually focus the incident photons onto a detector. The Wolter Type I design – which can be seen in Figure 4.1 and features a paraboloidal mirror that first focuses the incident photons onto a hyperboloidal mirror, that then brings them to the detector – is the most common of these designs, and is featured aboard the majority of X-ray missions since the launch of EXOSAT in 1983, as this design allows for the optical system to have the shortest dimensions.

This approach, while effective, comes with trade-offs. The shallow reflection angles mean that mirrors must be quite long in the direction of the incident X-rays to collect a reasonable

number of photons, and the geometric constraints limit the field of view compared to optical telescopes. This latter issue can be somewhat rectified through the use of nested mirrors: as these mirrors must be placed nearly parallel to the path of the incident photon, it is often the case that multiple of these mirror setups are nested within each other in order to increase the effective field of view of a telescope.

4.2 Charge-Coupled Devices

The invention of the CCD by Boyle & Smith (1970) was a monumental one for the field of astronomy. Prior to this, astronomers largely relied on the use of photographic plates for the capture of astronomical images, which was a cumbersome and slow process. The CCD heralded the beginning of the digital age of astronomy, and very few of the many significant discoveries made since would have been possible without it. Nearly all modern X-ray telescopes make use of CCDs, and neither *XMM-Newton* nor *Chandra* – whose designs and functionalities are discussed in Subsections 4.3 and 4.4, respectively – are an exception.

At its simplest, a CCD is a thin wafer of silicon placed atop a grid of pixels, which are typically a form of metal-oxide semiconductors. When light strikes the silicon, electrons are dislodged through the photoelectric effect, creating electron-hole pairs. The electrons are then drawn towards the pixels, due to the potential wells generated through an applied positive voltage, and are then collected within the pixels below, with the amount of electrons generated in such a way being directly proportional to the energy of the incident photon. By applying a further voltage, the electrons can be drawn from pixel to pixel, bringing them towards the readout amplifier. Due to the highly sensitive nature of the equipment required for astronomical observations, the CCDs used for such purposes tend to feature a "storage"

section – essentially, a secondary set of pixels which are shielded from inbound photons – to which the electrons are moved first, to shield the image during readout by preventing the pixels from receiving photon counts during the transfer phase. The reason for this is that the readout process is significantly slower than the transfer of electrons between pixels, though it also has the benefit of allowing for very little downtime between frame time. The readout can be done row-by-row, if using a single amplifier, or simultaneously, which allows for faster readout times but requires multiple amplifiers and thus greater electronic complexity and calibration is needed.

CCDs can be designed with different performance characteristics in mind, such as spectral, spatial, and temporal resolutions; detection efficiency; and instrumental background. Perhaps the most important characteristic, however, is the quantum efficiency (QE) of the CCD: in essence, the percentage of incident photons that the device can convert into electrons, and thus into a detection event. An ideal QE of 100% represents the conversion of every incident photon into a detection event; modern CCDs can have QEs upwards of 90% for the energy bands to which they are most sensitive, though this value is not constant, and will vary across energy bands. Several design choices can influence the QE of a CCD, but the most prominent impact comes from whether the chip is front-illuminated or back-illuminated. In front-illuminated chips, incoming light must pass through the electronics of the CCD (the electrodes and circuitry) before they reach the photosensitive silicon substrate, while back-illuminated chips are flipped, and have the field-free region etched away; essentially, the electronics of front-illuminated CCDs block a portion of the incoming light, whereas back-illuminated CCDs expose the silicon substrate directly to the light, preventing this absorption. While back-illuminated chips offer a higher potential QE, that improvement

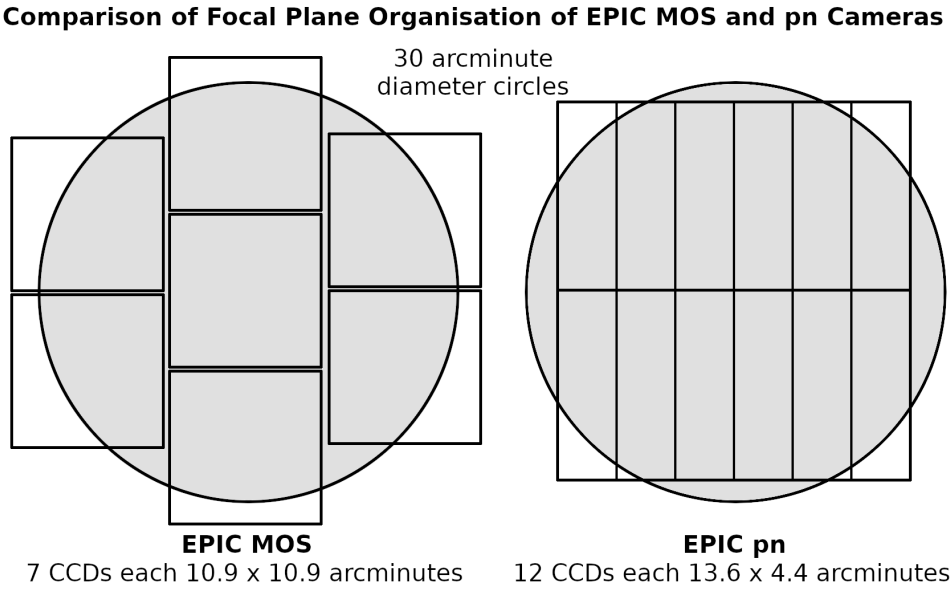

Figure 4.2: A rough sketch of the field of view and arrangement of the two types of EPIC cameras: MOS (left) and pn (right). The shaded circles represent areas with a diameter of 30' – the canonical field of view of *XMM-Newton*. Image reproduced from the XMM-Newton User's Handbook.

comes at the cost of a need for slightly more complicated mechanical support, and a greater need for protection against environmental degradation.

4.3 The XMM-Newton X-ray Telescope

The X-ray Multi-Mirror Mission – more commonly known as *XMM-Newton* – is the premier X-ray telescope of the European Space Agency (ESA). Launched in 1999, *XMM-Newton* uses a Wolter Type I design and features three CCD cameras which together comprise the European Photon Imaging Camera (EPIC): two metal-oxide semiconductor (MOS) CCD arrays, known as the MOS1 and MOS2 cameras; and a pn CCD array known as the pn camera. *XMM-Newton* also features two Reflection Grating Spectrometers (RGS), each of which are mounted to the telescopes equipped with the EPIC-MOS cameras. Approximately 56%

of the incoming X-ray photons are diverted away from the MOS cameras towards the RGS cameras. These CCDs possess a notably higher spectral resolution than the primary MOS cameras, allowing for the more precise measurement of a target's X-ray spectral properties; however, this increase in precision comes at a cost of a significantly reduced energy range and field of view, with the RGS cameras possessing roughly 20% of the energy range of the EPIC cameras. Additionally, the telescope also features an Optical Monitor (OM) designed to provide optical / ultraviolet observations simultaneously with the primary EPIC instruments.

The MOS cameras are each comprised of seven square, front-illuminated CCDs, each of which possesses a field of view of approximately 10.9 arcminutes. The only difference between the MOS1 and MOS2 cameras is the orientation of the cameras with respect to one another: the MOS2 CCDs are rotated 90 degrees from those of MOS1, so that the gaps between the CCDs are not similarly aligned. The pn camera, meanwhile, is composed of 12 rectangular, back-illuminated CCDs, each being roughly 13.6 arcminutes by 4.4 arcminutes; the arrangement of the CCDs for both instruments are shown in Figure 4.2. All three of the primary EPIC CCDs possess a canonical field of view of approximately 30 arcminutes; a spatial resolution of better than ~ 6" at FWHM; an effective energy range of 0.15 – 15 keV; and a spectral resolution of 70-80 eV, depending on whether one is using a MOS CCD or a pn CCD.

The EPIC cameras can be operated in several different science modes which allow for the better acquisition of certain types of data. For EPIC MOS, the outer ring of CCDs are always operating in standard imaging mode, while the central CCD can be operated in Full Frame, Large Window, Small Window, or Timing mode. For EPIC pn, the available modes are Full Frame, Extended Full Frame, Large Window, Small Window, Timing, and Burst; in

Small Window, Timing, and Burst modes, only a single EPIC pn CCD is active. The different modes allow the observer to sacrifice field of view for an increase in time resolution and maximum count rate.

Additionally, there have been two incidents in which some of the EPIC detectors have been damaged over the years since *XMM-Newton* launched. On 09 March 2005, the MOS1 camera was struck by a micrometeoroid, and as a result, CCD6 no longer functions. Similarly, on 11 December 2012, a second micrometeoroid struck the MOS1 camera, causing significant damage to CCD3, resulting in it no longer functioning. Further, noisy features have appeared on MOS1 CCD4 following the event in which CCD3 was lost.

4.3.1 Science Analysis System

The *XMM-Newton* mission is run by ESA's Science Operation Center (SOC), which provides and maintains the Science Analysis System (SAS) software necessary for interacting with *XMM* data. The SAS is a collection of tasks, scripts, and libraries created for the purpose of reducing and analysing data from the *XMM-Newton* instruments. It operates on the raw instrumental data and converts them into a familiar FITS format; these reformatted data files are known as Operation Data Files (ODFs), which contain uncalibrated science data for each CCD from the EPIC instruments, alongside housekeeping files, radiation monitor files, and spacecraft files necessary for the reduction of this data into usable products. The SAS contains the tools necessary to rerun the *XMM-Newton* data analysis pipeline, apply appropriate calibrations, and filter observational data, all of which are needed to perform data analysis. The SAS also contains guides and tools for use in the filtering and analysis of data beyond initial steps.

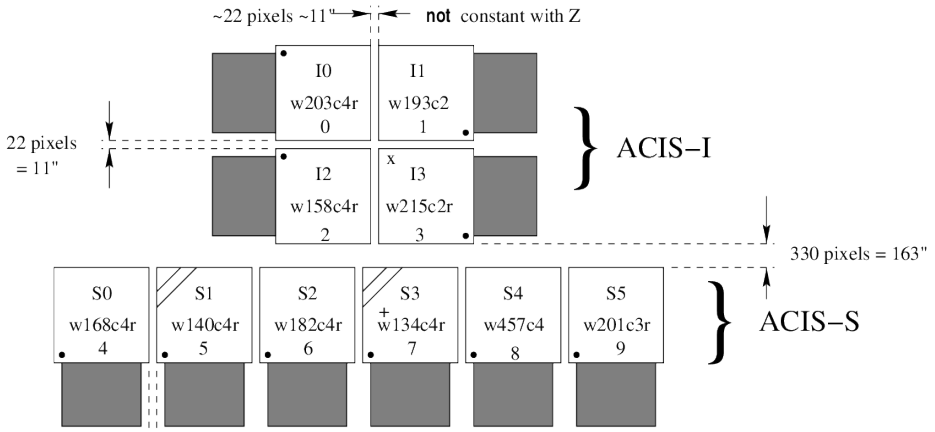

Figure 4.3: A schematic drawing of Chandra's ACIS focal plane. The ACIS-I CCDs are on top, while the ACIS-S CCDs are below. The 'x' and '+' indicate the aimpoints of ACIS-I and ACIS-S, respectively. A band in the upper left indicates a back-illuminated CCD. Image adapted from the Chandra Proposers' Observatory Guide.

4.4 The Chandra X-ray Observatory

One of the Great Observatories, the *Chandra* X-ray Observatory – more commonly known simply as "*Chandra*" – has for some time been NASA's primary X-ray mission. Launched in 1999, *Chandra* was designed with a focus on high-resolution imaging and spectroscopy. To that end, it uses a Wolter Type I design and is equipped with two primary instruments: the Advanced CCD Imaging Spectrometer (ACIS), and the High Resolution Camera (HRC). It also features two transmission gratings – the High Energy Transmission Grating and the Low Energy Transmission Grating – which can be placed in the path of incoming X-rays to produce improved spectral resolution for certain targets.

Of these instruments, ACIS constitutes the primary instrument aboard *Chandra*. Com-

posed of two arrays of CCDs, it is responsible for *Chandra*'s impressive < 0.5 arcsecond angular resolution. ACIS-I, the first of these arrays, is primarily designed for imaging, and is comprised of four identical front-illuminated CCDs arranged in a 2x2 grid. The second of these arrays, ACIS-S, is comprised of six CCDs arranged in a 1x6 grid, and is optimised for use as a readout with the High Energy Transmission Grating. Two of the CCDs that make up ACIS-S are back-illuminated, affording them a a wider energy range at the expense of a decreased spectral resolution, while the remaining four are front-illuminated. All of the CCDs feature a field of view of roughly 8.3 arcminutes by 8.3 arcminutes; *Chandra*'s canonical field of view is approximately 16 arcminutes, though this can only be accomplished through the use of ACIS-I. In addition to the previously mentioned angular resolution, *Chandra*'s CCDs afford it an effective energy range of roughly 0.08 – 10 keV, alongside a spectral resolution of 95-150 eV for the front-illuminated CCDs, and 130-280 eV for the back-illuminated CCDs.

Like *XMM-Newton*, *Chandra*'s CCDs can be operated in a variety of modes, known as operating modes. Three such modes exist: timed exposure mode, alternating exposure mode, and continuous clocking mode. These modes differ in the duration of their frame time – the length of time for which observations are made before the charge contained in the CCDs is passed to the read-out – which allows them to study objects of varying brightness, or with different timing requirements. *Chandra* also features three different telemetry formats, which define the type of information that is returned from the observation. All observing modes can make use of the Graded and Faint telemetry formats, while only the timed exposure mode can make use of the Very Faint format. In addition to these specific operating modes and telemetry formats, the ACIS CCDs can be operated in a variety of different configurations by choosing to enable or disable particular CCDs. Nominally, any combination of CCDs up

to six can be operated at a given time, though the most common configurations include the Wide Field Imaging mode (all ACIS-I CCDs, alongside CCD 2 & 3 of ACIS-S); the High Resolution Imaging mode, which uses only CCD 3 of ACIS-S; the Bright Source Fast Timing mode, which uses only CCD 3 of ACIS-S in continuous clocking mode; and the Bright Source High Resolution Spectroscopy mode, which uses all six ACIS-S CCDs alongside the High Energy Transmission Grating.

While *Chandra* has not suffered from damage in the same way as *XMM-Newton* has, it has experienced a non-insignificant amount of degradation from multiple sources. The front-illuminated CCDs (all of ACIS-I and four of the six CCDs of ACIS-S) have experienced radiation damage, reducing their effective energy resolution. Further, due to the sensitivity of the ACIS detectors to optical light, it was necessary to install optical blocking filters. These filters have proven prone to molecular buildup of hydrocarbons from the spacecraft's lubricant, resulting in a contamination that significantly reduces the low energy (< 2 keV) response of the ACIS CCDs. Both of these issues are able to be partially corrected for via software, with the radiation damage being corrected via an algorithm in the analysis software, and the contamination being accounted for via a contamination model that is updated each year to account for changes in the build-up.

4.4.1 Chandra Interactive Analysis of Observations

As with all of NASA's high-energy missions, *Chandra* is run under the umbrella of the High Energy Astrophysics Science Archive Research Center (HEASARC). Support specifically for *Chandra* is handled by the Chandra X-ray Center (CXC), which runs the *Chandra* Data Archive, and provides active development of the *Chandra* Interactive Analysis of Observa-

tions (CIAO) software (Fruscione et al. 2006). CIAO is a software package comprised of several scripts, tools, and guides that allow for the analysis of *Chandra* data. Through the use of the standard data processing system, the CXC performs pipeline processing that takes data from raw spacecraft telemetry, converts it into a FITS format, and applies various levels of processing. These processing levels range from L1 (instrument-dependent corrections have been applied), to L2 (time filters, cosmic ray rejections, and position transformations), up to L3 (source detection and characterisation, and cross-correlation with other catalogues). Following this, the data is verified and validated by a team of CXC scientists to ensure its quality. CIAO allows one to perform these steps themselves, though the data acquired from the *Chandra* Data Archive is typically in L2 or L3 format. Despite its name, and while it does contain several tools that are specific to *Chandra* – mainly, instrumental tools – CIAO is mission independent, and can be used for the analysis of data from a wide range of X-ray telescopes.

4.5 Region Selection

Following the processing and filtering of the data using the analysis software for the relevant telescope, we must determine the regions upon which our analysis will be performed. In a normal spectroscopic study, the SNR as a whole is considered as a single region; while this method is a viable one, and it does offer some advantages over the alternative method (most notably, it is faster, both in setup and computationally), it does not make much use of the resolving power of modern detectors. Because this study is a spatially resolved one, we instead must divide the SNR up into a collection of regions, based upon the morphology of the SNR in question.

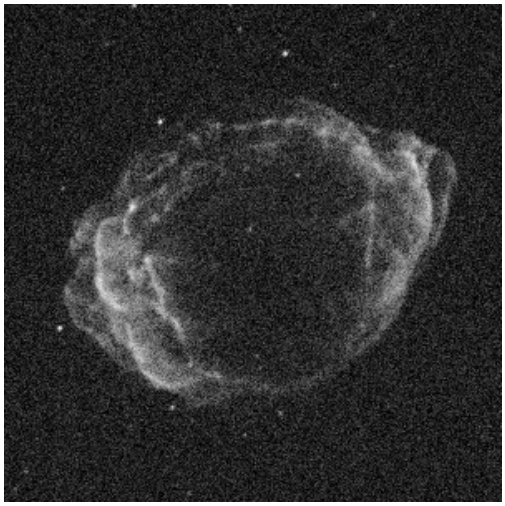

(a) Combined *Chandra* observation of the SNR G1.9+0.3.

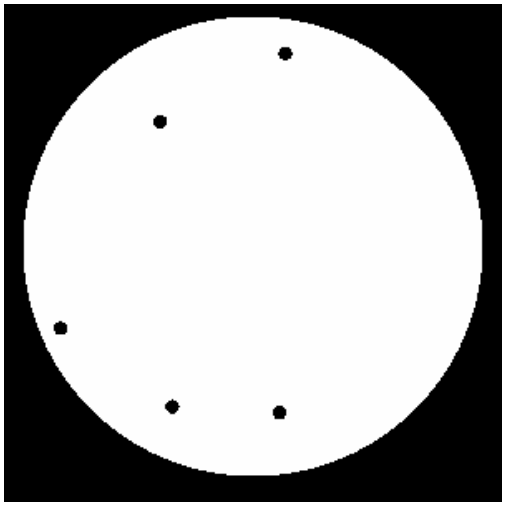

(b) Mask used to constrain the target and block out unwanted sources.

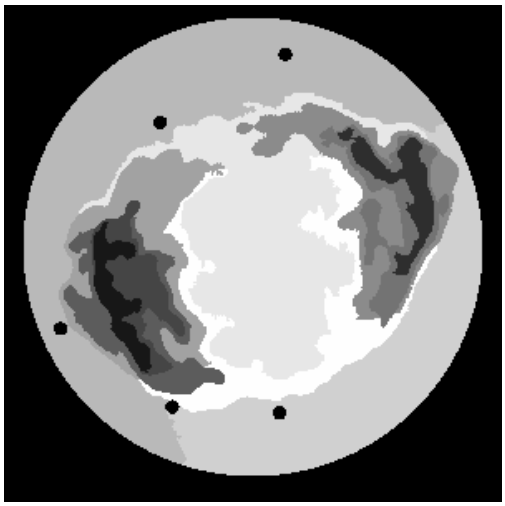

(c) Resulting region map output of *contbin*.

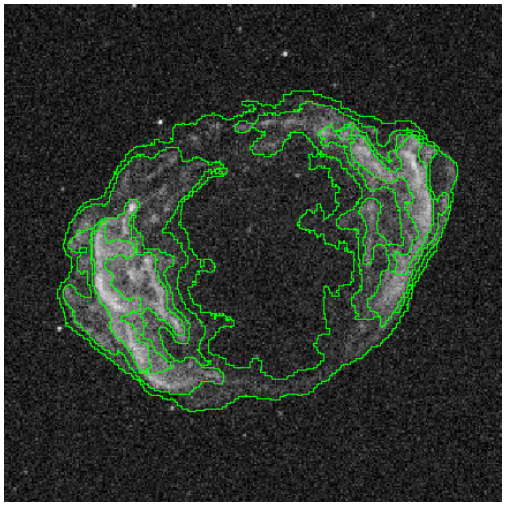

(d) Final regions overlayed atop the observation.

Figure 4.4: Various steps of the *contbin* region generation process for the SNR G1.9+0.3.

Traditionally, region selection for spatially resolved studies has been done by eye. As the approach to this study is a systematic one, we wanted to avoid any potential sources of bias, and produce our regions in a way that was consistent across all SNRs. To this end, we made

use of a contour binning and adaptive smoothing algorithm known as *contbin*[2]. This method allows us to avoid any potential human bias in the region generation step, while further allowing us to cover the entire SNR for analysis, ensuring no gaps between regions. Further, *contbin* allows our regions to be generated with a consistent amount of counts, increasing the overall quality of our spectra and ensuring that no region has a spectrum too poor to analyse.

Developed by Sanders (2006), the *contbin* algorithm operates based upon the principle that many of the physical parameters of an SNR (e.g. abundances, density, and temperature) have a correlation with the X-ray surface brightness. The algorithm must be provided an input image, and can be used on images that are smoothed, exposure corrected, or otherwise; in our case, all input images were produced by merging observations. For objects that were able to fit entirely into *XMM-Newton's* central MOS CCD, the EPIC-MOS1 and EPIC-MOS2 images were merged, in order to increase the quality of the input image and avoid potential detector bias. For the objects that were too large to fit into the single central CCD, all instruments and observations were merged for similar reasons as previously mentioned, but also to remove any chip gaps from the final image. The *contbin* algorithm adaptively smooths the input image, and regions are generated based upon a variety of input parameters: the smoothing parameter, which determines how smooth the region edges are, though at the expense of possibly missing finer structural details; a signal-to-noise value, to determine the minimum S/N of each bin; and a geometrical constraint, to determine how far from a circular shape the generated regions are allowed to deviate.

The *contbin* algorithm functions as follows: first, the user provides the algorithm with the required inputs: an image, and optionally, a mask. If the mask is provided, then it is used to

[2] https://github.com/jeremysanders/contbin/

remove regions for which there is no interest, such as background emissions, point sources, or other external sources of contamination. The input image (sans masked areas, if applicable) is then smoothed according to the algorithm's inbuilt "accumulative smoothing" function. Then, the brightest pixel lying within the image is selected, and added to the current bin. All neighbouring pixels (optionally including diagonals) are then considered; if the brightest amongst them meets the desired threshold, it is also being added to the current bin. All pixels neighbouring those in the current bin are then considered in the same way. This process is repeated until either all neighbouring pixels fail to meet the required threshold, no neighbouring pixels exist that are not already part of a bin, or the region's size exceeds the constraints specified by the user. At this point, the region is considered complete, and the process begins again with the algorithm selecting the brightest remaining pixel. Once the entire image has been binned, a "clean-up" process is begun, whereby bins that failed to meet the required thresholds are combined with the neighbouring bin to which it is closest in brightness. This repeats until all bins meet the user-specified constraints, at which point the region generation is complete and we are left with a selection of regions all possessing similar surface brightness, total counts, and statistics for spectral analysis.

4.6 Spectral Analysis

Following region selection and the extraction of data using the relevant telescope's software, spectral analysis can be performed using the XSPEC software. XSPEC, spectral fitting, and the various models used in the spectral fitting process are detailed herein, with all relevant information being provided by the XSPEC manual[3].

[3] https://heasarc.gsfc.nasa.gov/xanadu/xspec/

4.6.1 XSPEC

XSPEC – the X-ray Spectral Fitting Package (Arnaud 1996) – is an interactive, command-driven X-ray spectral-fitting program that was designed to be detector-independent to allow its use with a wide range of X-ray missions past, present, and future. It provides the user with a variety of tools useful for analysing X-ray spectra, including those of SNRs, and allows for the plotting of data and results in addition to its main use in spectral fitting. For spectral fitting, XSPEC contains a large collection of parameterised models (see Subsection 4.6.3 for a list of relevant examples) representing a wide variety of physical scenarios, and can be used to determine a variety of properties such as elemental abundances, ionisation timescale, and temperature.

4.6.2 Spectral Fitting

The process of fitting spectral models to a given set of data begins by choosing the model itself. At present, XSPEC contains nearly 200 models used to describe different forms, sources, and aspects of X-ray emission. The majority of these models are classified as either "additive" or "multiplicative" models, and can be combined in a wide variety of ways in order to create a final model that best describes the physics of the chosen object.

Once a model (or combination thereof) has been chosen, the fitting process can begin in earnest. By default, the XSPEC software utilises a modified Levenberg-Marquardt algorithm which performs a search of the parameter space for each parameter of the chosen model (though individual parameters can be frozen to specific values if known ahead of time, or if deemed irrelevant to the fit). The algorithm works by varying each parameter slightly from its user-provided initial value, searching for changes that provide the largest improvement to

the fit so that it more closely recreates the observed data. The algorithm used by XSPEC is a local optimiser, which can result in the fitting process getting stuck in so-called "local minima," where the algorithm's small adjustments in either direction do not improve the fit, but neither is the fit the best possible fit to the data. This can be avoided by careful consideration of the initial conditions, thus helping the algorithm find the true global minimum.

The quality of a fit is typically determined by its fit statistic. The default fit statistic used by XSPEC is that of the χ^2 (chi-squared), though it also supports other forms of statistics, such as C statistic. Chi-squared statistics are more commonly reported in terms of the χ^2_ν (reduced chi-squared) value, which is based upon the number of degrees of freedom, ν. Typically speaking, a reduced chi-squared value of 1 indicates a fit that accurately reproduces the data, with larger values becoming increasingly less accurate reproductions (underfitting), and smaller values suggesting an overestimation of the variation of the error (overfitting). An ideal fit, then, is represented by a reduced chi-squared value close to one; in this work, an acceptable fit was any $\chi^2_\nu < 2$. Any model that resulted in a larger value was discarded, while the model with the lowest value was selected for use as our result.

The last aspect of the spectral fitting process is that of error analysis. During the fitting process, XSPEC reports uncertainties as a single value alongside the determined parameters. However, these uncertainties are only reported to a confidence interval of 68% (1σ), where the accepted standard for astrophysical data is 90%. Fortunately, XSPEC has multiple built-in tools for error analysis, which allow the determination of errors to arbitrary confidence intervals. This work made use of XSPEC's Markov Chain Monte Carlo method for error analysis, in which the model's parameter space is explored by a user-defined number of "walkers" for a chain whose length (i.e. number of steps) is also defined by the user. By plotting the

variation in statistics over each step in the chain, one can determine whether or not the chain has converged to a steady state, in which case the best fit has been found. In order to increase the likelihood of convergence, it is typical to set a burn-in phase, in which the chain's length is effectively extended by some value N, with the first N steps in the chain being discarded before the final values are recorded.

4.6.3 Spectral Models

We now give a brief description of each of the spectral models used in this work. For lists of all parameters for a given model, see Appendix A.

TBABS & TBVARABS

TBABS is the Tuebingen-Boulder ISM absorption model. This model calculates the total cross section of X-ray absorption due to the ISM, and includes the contributions from gas-phase ISM, grain-phase ISM, and the molecules in the ISM. This model is used for the determination of the amount of matter observed along the long-of-sight to the target, also known as the hydrogen column density, N_H, and is reported in terms of 10^{22} atoms cm^{-2}. This parameter is extremely important when considering low-energy X-rays (< 1.0 keV), as absorption effects can significantly reduce the observed impact of line emission from elements in this range.

TBVARABS is a variation of TBABS which allows the user to vary elemental abundances, redshift, and various grain parameters, in addition to the hydrogen column density. In this work, TBVARABS was used for the study of the objects in the Large Magellanic Cloud, to account for the difference in local elemental abundances between our galaxy and the LMC.

The grain density, sizes, and depletion fractions were left at default values in all cases.

VNEI

VNEI (Borkowski et al. 2001) is a collisional model representing a plasma that is outside of ionisation equilibrium; specifically, one that is said to be in "non-equilibrium ionisation" (NEI). It is characterised by a constant electron plasma temperature, kT, given in keV, and a single parameter representing the ionisation timescale, $\tau = n_{\mathrm{e}}t$ given in terms of s cm^{-3}, where n_{e} is the post-shock electron density and t is the time that elapsed since the passage of the shock. VNEI allows for the variation of the abundances for the elements of He, C, N, O, Ne, Mg, Si, S, Ar, Ca, Fe, and Ni. Other variants of this model – known as NEI and VVNEI – exist, and allow for the variation of fewer and greater elements, respectively.

VPSHOCK

VPSHOCK (Borkowski et al. 2001) is a model representing a plane-parallel shock characterised by a constant electron plasma temperature, kT, given in keV. Like VNEI, it is an NEI model; however, it differs in that rather than considering a single ionisation timescale, τ, VPSHOCK allows for the consideration of two ionisation timescales: one representing the lower limit, τ_l, and one representing the upper limit, τ_{u}. Both timescales are given in terms of s cm^{-3}. In addition, the VPSHOCK model allows for the variation of the elements He, C, N, O, Ne, Mg, Si, S, Ar, Ca, Fe, and Ni; other variations of this model – PSHOCK and VVPSHOCK – allow for the variation of fewer and greater amounts of elements, respectively.

VRNEI

VRNEI (HEASARC XSPEC Development Team 2014) is another NEI model for a collisional plasma. Specifically, the VRNEI model represents a plasma that is currently in the process of recombining – that is to say, it represents a plasma that is assumed to have cooled or heated rapidly from some initial state. While it is characterised by a single ionisation timescale parameter, τ, it is additionally characterised by two plasma temperatures: kT, representing the current plasma temperature, as in the other models; and kT_{init}, representing the initial plasma temperature. When kT_{init} is lower than the current kT, then the model represents an object in the process of ionisation; conversely, when kT_{init} is higher than the current kT, then the model represents an object currently undergoing the process of recombination. Both plasma temperatures are reported in terms of keV. The abundances for the elements of He, C, N, O, Ne, Mg, Si, S, Ar, Ca, Fe, and Ni may be varied for the VRNEI model. Fewer or greater elements can be varied using the RNEI or VVRNEI model variants, respectively.

VAPEC

VAPEC (Smith et al. 2001) is the Astrophysical Plasma Emission Code, representing the emission spectrum of a hot, optically-thin plasma that is in CIE. Unlike the NEI models, VAPEC is characterised only by a constant electron plasma temperature, kT (in keV); it does not feature a parameter for ionisation timescale. This model calculates line emission using the AtomDB atomic database (Foster et al. 2023). The VAPEC model allows for the abundances of the elements He, C, N, O, Ne, Mg, Al, Si, S, Ar, Ca, Fe, and Ni to be varied; for the consideration of fewer or greater elements, the APEC and VVAPEC models can be used, respectively.

5

Target Compilation

By its nature as a systematic study, this work involved the analysis of several target objects. As of this writing, there are 383 known SNRs in our galaxy (Ferrand & Safi-Harb 2012); however, not all of these objects are viable candidates for this study. Herein, we introduce the SNRs which were selected as the targets of our systematic study, presenting the results of previous studies performed in other wavelengths, as well as a more detailed look at the results

of any previous X-ray studies. The criteria for our target selection is as follows: we required our targets to be SNRs that:

(i) Are known to be, or suspected of being, of a thermonuclear origin;

(ii) Could be considered young, in that their age is less than $\sim$ 10 kyr;

(iii) Have been observed by at least one – and ideally, by both – of either ESA's *XMM-Newton* and NASA's *Chandra* X-ray Observatory.

To that end, 15 targets were selected for this study, including 9 SNRs located in the galaxy (see Section 5.1), as well as six SNRs located in the Large Magellanic Cloud (see Section 5.2). It should be noted, however, that this is not an exhaustive list. A summary of the most relevant information on each target is presented in Tables 5.1 and 5.2. Unless otherwise specified, the data on each object was sourced from SNRcat[1], the high-energy SNR catalogue created and maintained by the University of Manitoba (Ferrand & Safi-Harb 2012).

Table 5.1: Basic information for the 9 Galactic SNRs

Galactic Coordinates	Unique Name	Distance (kpc)	Size (arcmin.)	Age (yrs)
G1.9+0.3		8.5	1.7	~120
G4.5+6.8	Kepler	5	3.6	421
G41.1−0.3	3C 397	8.5	4.5 x 2.5	1350 - 5000
G43.3−0.2	W49B	8.0 - 11.3	4	1000 - 6000
G120.1+1.4	Tycho	3.6	8	453
G272.2−3.2		2.0 - 10	15	3600 - 6000
G337.2−0.7		2.0 - 9.3	4.5 x 5.5	750 - 5000
G344.7−0.1		6.1 - 14	6	3000 - 6000
G352.7−0.1		7.5 - 11	8 x 6	2200 - 7600

[1] http://snrcat.physics.umanitoba.ca/

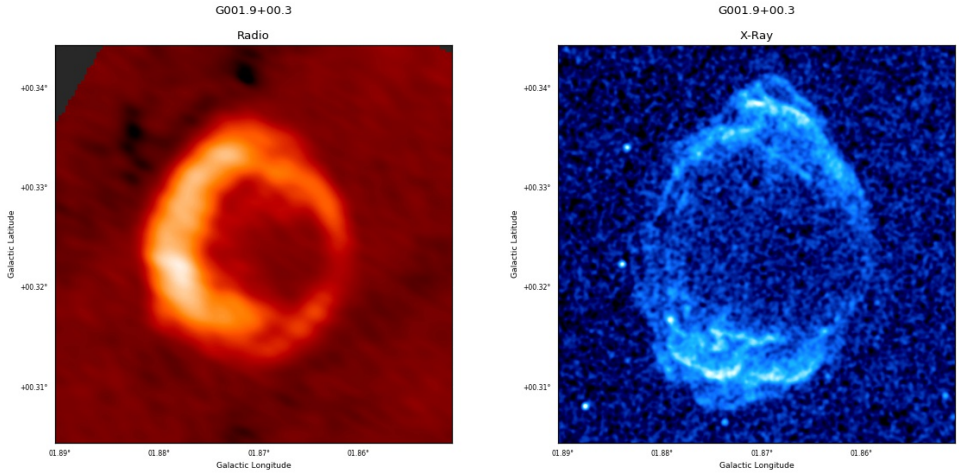

Figure 5.1: Radio and X-ray images of G1.9+0.3. Images from SNRcat[2].

5.1 Galactic SNRs

5.1.1 G1.9+0.3

Discovered in 1984 through the radio observations of Green & Gull (1984), G1.9+0.3 is the youngest known SNR in our galaxy, at roughly 120 years old (Reynolds et al. 2008; Borkowski et al. 2013). Despite its youth, no supernova event was recorded, likely owing to the proximity of G1.9+0.3 to the Galactic centre and the many magnitudes of extinction that accompanies such closeness. G1.9+0.3 possesses a somewhat asymmetric shell a mere 1.7 arcminutes in diameter; with an estimated distance of 8.5 kpc (placing it near to the Galactic core, and determined due to heavy interstellar X-ray absorption), this corresponds to a physical diameter of 5 pc. Given the remnant's age, a high average expansion velocity of almost $2 \times 10^4\ \mathrm{km\,s^{-1}}$ would be needed to explain this size, which is not terribly far from the currently-detected $1.4 \times 10^4\ \mathrm{km\,s^{-1}}$.

[2] http://snrcat.physics.umanitoba.ca/SNRrecord.php?id=G001.9p00.3

The angular size of G1.9+0.3 limits the ability for many X-ray telescopes to observe it. As a result, there have been 12 previous studies of G1.9+0.3 in the X-ray regime: two with *Suzaku*, and two with *NuSTAR*, while the remaining eight studies were performed using data acquired by *Chandra*, the high angular resolution of which makes it the only X-ray telescope capable of making spatially resolved spectroscopy possible. As a result of this, G1.9+0.3 is the only object in our study for which the spatially-resolved spectroscopy was performed using data from *Chandra*, rather than from *XMM-Newton*.

The majority of the X-ray emission from G1.9+0.3 is in the form of nonthermal synchrotron emission (Reynolds et al. 2009), which makes determining the chemical composition and possible abundances present within the remnant somewhat difficult. However, Borkowski et al. (2010) detected the presence of thermal emission from the northern rim of the SNR, and in Borkowski et al. (2013), they were able to reveal the presence of enhanced emission from Si, S, and Fe in this region. Using a PSHOCK model, they determined electron temperatures of 3.2 keV, a low ionisation timescales of $2.4 \times 10^{9}\ \mathrm{cm}^{-3}\ \mathrm{s}$, a hydrogen column density of $7.0 \times 10^{22}\ \mathrm{cm}^{-2}$, and super-solar abundances for all three measured elements.

5.1.2 G4.5+6.8

G4.5+6.8 is an SNR of historical importance: it is the last Galactic SNR for which the progenitor explosion was visible with the naked eye, having occurred in 1604 CE. Although not the first to observe or record their findings on the object, G4.5+6.8 is more often referred to as "Kepler's SNR", after German astronomer Johannes Kepler, who published a detailed account of observations made by him and other European colleagues. The supernova remnant itself was first discovered by Baade (1943), and appears as a roughly circular shell with two

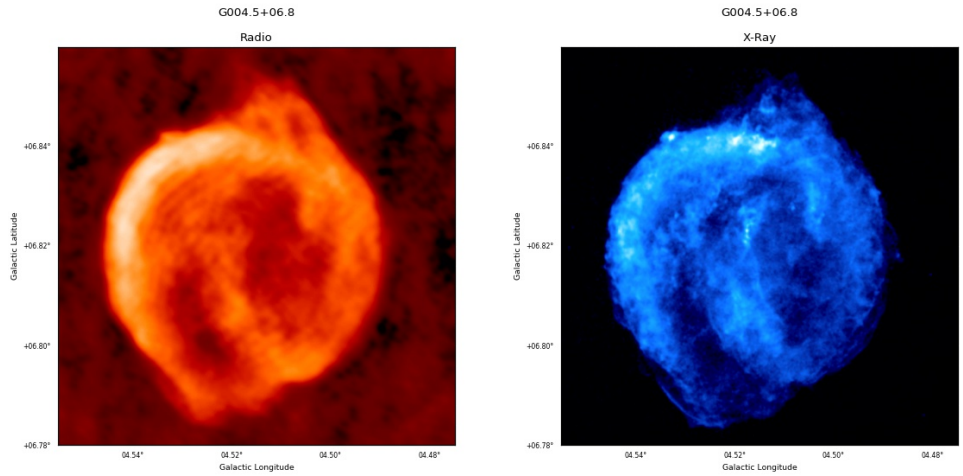

Figure 5.2: Radio and X-ray images of G4.5+6.8. Images from SNRcat[3].

"ears" on its northwestern and southeastern edges, and has an angular size of approximately 3.6 arcminutes across.

As it is associated with a historical supernova event, the age of G4.5+6.8 is well known at 421 years. The distance to the remnant, however, is more poorly constrained: initial estimates – based on historical records of the maximum visual magnitude for the supernova event – ranged from 3.2 kpc (Danziger & Goss 1980) to 12 kpc (van den Bergh et al. 1973). More recent estimates range from 3.9 ± 1.4 kpc, based on proper motion and Doppler broadening of Hα emission (Sankrit et al. 2005), to $6-7$ kpc based on measurements of the remnant's energetics and size (Aharonian et al. 2008; Chiotellis et al. 2012; Patnaude et al. 2012). Radio measurements of absorption towards the remnant are largely consistent with these estimations at $4.8-6.4$ kpc (Reynoso & Goss 1999), and the commonly adopted distance is 5 kpc as a result.

G4.5+6.8 is one of the most well-studied SNRs, owing to its relatively close distance and

[3] http://snrcat.physics.umanitoba.ca/SNRrecord.php?id=G004.5p06.8

young age. For some time, there was a debate as to the type of the remnant's supernova origin, with its position well above the Galactic plane being used as an argument for a thermonuclear origin, whereas evidence of emission from high-density material with enhanced abundances of N were interpreted as signs of CSM, which supported a CC origin (Minkowski 1943; Dennefeld 1982; Leibowitz & Danziger 1983; Blair et al. 1991). *ASCA* observations by Kinugasa & Tsunemi (1999) showed evidence of a large amount of Fe, which strongly supported a thermonuclear origin, and the argument was largely put to rest with the *Chandra* observations of Reynolds et al. (2007), who showed strong Fe emission (from both Fe L and Fe K), strong Si emission, and little-to-no emission from O or Mg. However, while the remnant's origin as a thermonuclear supernova is now well-established, it is still undetermined as to whether it resulted from the SD or the DD scenario.

In terms of X-ray spectroscopy, G4.5+6.8 is well-fit by NEI models, but the number of components needed to describe the emission varies greatly depending on whether one is focusing on a global study, or on a spatially-resolved one. For global studies, upwards of four NEI or PSHOCK components are required (Katsuda et al. 2015; Holland-Ashford et al. 2023), as the SNR's spectrum is quite complex, partially owing to its overall brightness and therefore high S/N. Spatially-resolved studies tend towards using two NEI or PSHOCK components, instead (Cassam-Chenaï et al. 2004; Sato & Hughes 2017; Sun & Chen 2019; Kasuga et al. 2021). All studies tend to show evidence of strong emission from Si, S, and Fe and sub-solar abundances of O and Mg, as well as evidence for emission from Ar and Ca. In some cases, there has been evidence of nonthermal emission from the SNR – particularly from its outer rims (Tsuji et al. 2021) – likely due to particle acceleration at the shock fronts.

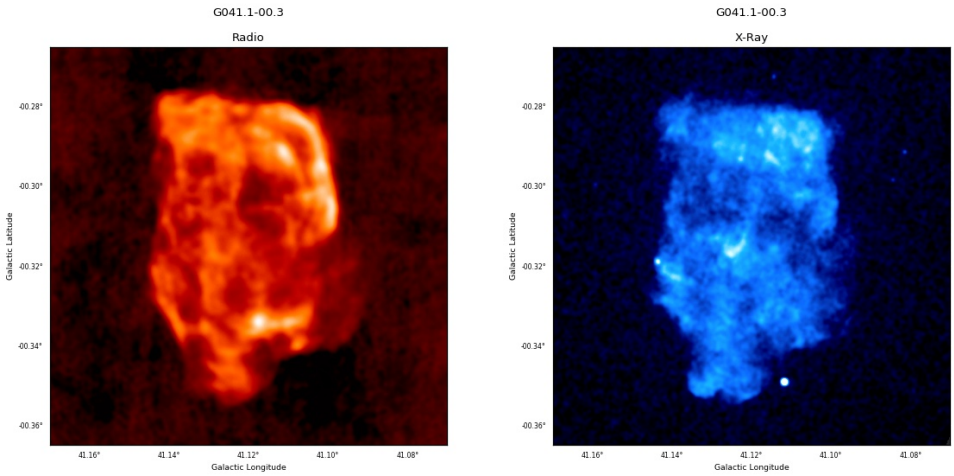

Figure 5.3: Radio and X-ray images of G41.1−0.3. Images from SNRcat[4].

5.1.3 G41.1−0.3

Referred to more frequently as "3C 397," G41.1−0.3 is a peculiar object. First discovered in 1959 as the 397th object of the third Cambridge catalogue (Edge et al. 1959), 3C 397 is one of the brightest Galactic SNRs in the radio regime, where it is classified as a shell-type SNR (Green 2025). In the X-ray regime, it has instead been classified as a composite SNR, owing to its centrally-bright nature, and it was one of the first remnants classified as a thermal composite due to this contrast between radio and X-ray morphologies (Rho & Petre 1998).

While 3C 397 is a peculiar object in many ways, none are more strikingly obvious than its appearance. To give it a single angular size would be difficult, as in both the radio and X-ray regimes, it appears to possess an angular, box-like shape. Its angular size, then, is best reported as 4.5×2.5 arcminutes. With an estimated distance of 8.5 kpc (Ranasinghe & Leahy 2018), this corresponds to physical dimensions of roughly 11×6 pc. This asymmetry

[4] http://snrcat.physics.umanitoba.ca/SNRrecord.php?id=G041.1m00.3

is likely due to interaction with a nearby molecular cloud, rather than due to any asymmetry in its progenitor explosion (Jiang et al. 2010; Lee et al. 2019). While it is well established that 3C 397 is a middle-aged remnant (Yamaguchi et al. 2014; Martínez-Rodríguez et al. 2020), age estimates vary, ranging from 1350 years (Leahy & Ranasinghe 2016) up to 5000 years (Safi-Harb et al. 2005).

The nature of 3C 397's supernova progenitor has long been the subject of some debate. Safi-Harb et al. (2000, 2005) suggested a CC origin, owing to its proximity to the Galactic plane, its proximity to molecular clouds, its highly-asymmetric morphology, and the abundances of some intermediate-mass elements. Conversely, Yamaguchi et al. (2014, 2015) has suggested a thermonuclear origin, owing mostly to its iron-group elements: the energy of its Fe K-shell centroid is slightly lower than the proposed divisor at $\sim$ 6.55 keV, and the abundances of the iron-group elements such as Mn, Cr, Fe, and Ni is notably high. Other recent attempts to study the remnant or determine the nature of its supernova progenitor have worked under the assumption of a thermonuclear origin (Dave et al. 2017; Martínez-Rodríguez et al. 2017, 2020).

5.1.4 G43.3−0.2

G43.3−0.2 is a region of the W49 complex first discovered by Westerhout (1958) through a 22 cm Galactic survey. Shortly thereafter, this complex was determined to be comprised of two distinct regions (Mezger et al. 1967): a thermal component known as W49A, thought to be a star-forming region; and a nonthermal component, known as W49B, which was proposed to be a supernova remnant. Further radio observations confirmed this suspicion (Downes & Wilson 1974), though it wasn't until 1984 that X-rays were detected (Pye et al. 1984). W49B

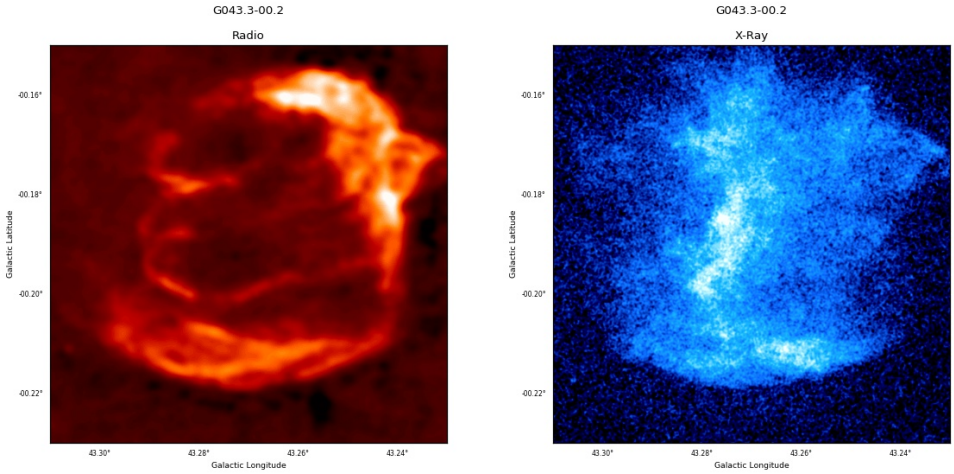

Figure 5.4: Radio and X-ray images of G43.3−0.2. Images from SNRcat[5].

is an interesting object for a number of reason, not the least of which are the titles it holds: it numbers amongst the galaxy's most X-ray luminous SNRs (Immler & Kuntz 2005); it is possessed of the galaxy's brightest Fe-Kα line in an SNR (Yamaguchi et al. 2014); and it was one of the first remnants found to be in an overionised state, suggestive of recombination (Ozawa et al. 2009).

W49B is a mixed-morphology remnant with a radio shell roughly 4 arcminutes in diameter, and an elongated, centrally-brightened X-ray morphology with a plume-like structure on either end of a central bar. Distance estimates place the remnant between $8 - 11.3$ kpc (Radhakrishnan et al. 1972; Moffett & Reynolds 1994; Zhu et al. 2014), while age estimates range from $1000 - 6000$ years (Pye et al. 1984; Hwang et al. 2000; Zhou & Vink 2018). Its spectrum shows clear evidence of enhanced Si, S, Ar, Ca, and Fe, and it is well-fit by a two-component thermal model with a high absorption, though the exact value varies somewhat by analysis: Miceli et al. (2006) determined absorptions between $4.22 - 4.8 \times 10^{22}$ cm^{-2},

[5] http://snrcat.physics.umanitoba.ca/SNRrecord.php?id=G043.3m00.2

while Zhou & Vink (2018) found a value of 8×10^{22} cm^{-2}. Temperatures for the two components range as well, with the colder component averaging 0.85 keV in Miceli et al. (2006), and 0.27 keV in Zhou & Vink (2018), whereas the hot component ranges from $1.77 - 3.0$ keV and $0.7 - 2.2$ keV, respectively.

Like 3C 397, the nature of W49B's supernova progenitor is a subject of much debate. Initially, a hypernova origin was put forward as a possible explanation for the remnant's peculiarity, but Miceli et al. (2006) showed that the explosion energy was likely in line with the canonical 10^{51} ergs of a supernova. Another proposal, put forward by Keohane et al. (2007), was that the remnant might have an origin related to a bipolar or jet-driven Type Ib/Ic explosion, owing to its elongated structure and the brightness of its Fe-Kα line; in line with this, Lopez et al. (2013) put forth evidence that the supernova event produced a black hole, rather than a neutron star, owing to lack of detection of any cooling neutron star. However, after examining the abundance ratios present in the remnant, Zhou & Vink (2018) determined that the remnant's abundance patterns cannot be adequately explained by any models of core collapse nucleosynthesis. Similarly, Sawada et al. (2025) note that the Fe-group ejecta in particular is in better agreement with models of thermonuclear nucleosynthesis.

5.1.5 G120.1+1.4

G120.1+1.4 is another historical SNR, associated with the supernova event of 1572 CE. It is often referred to as "Tycho's SNR," due to the work done by Danish astronomer Tycho Brahe in studying it, which was published in his work *De nova et nullius aevi memoria prius visa stella*. Brahe studied the event for more than a year, taking careful recordings that established a peak visual magnitude of -4.5. Brahe's recordings of the event's light curve and colours

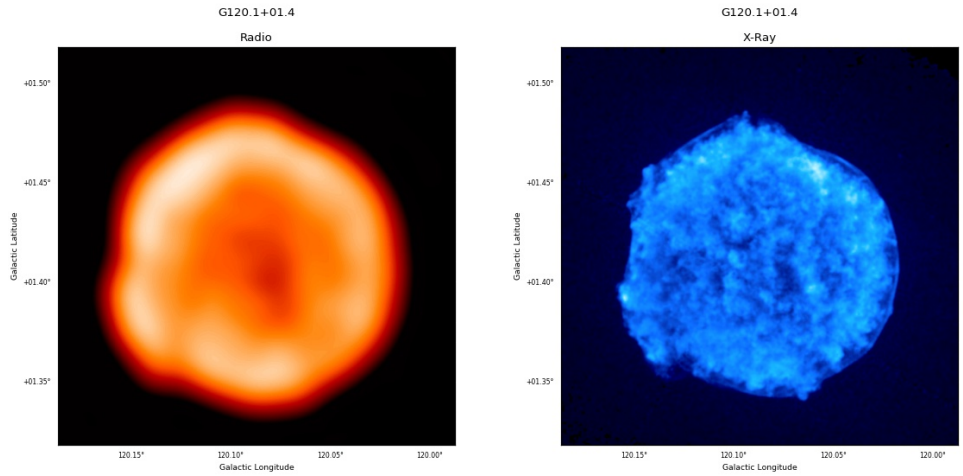

Figure 5.5: Radio and X-ray images of G120.1+1.4. Images from SNRcat[6].

were so thorough, in fact, that they could be used to infer the nature of the supernova even centuries later as a standard SN Ia (Ruiz-Lapuente 2004). This typing was later confirmed through the use of light echoes (Krause et al. 2008), making Tycho's SNR one of the few remnants for which we have a firm grasp on both their age and their supernova type.

Tycho's SNR exhibits a limb-brightened, almost circular shell with an angular diameter of roughly 8 arcminutes in both the X-ray and radio regime, and distance estimates of 3.6 kpc (Hayato et al. 2010) translate this into a linear diameter of about 9 pc. The sharp outer edges of its forward shock stand in stark contrast to the fluffy appearance of its interior, a phenomenon that likely arose due to Rayleigh-Taylor instabilities at the boundary between ejecta and ISM (Warren & Blondin 2013).

As a young, relatively bright SNR, G120.1+1.4 is one of the most well-observed and best-studied remnants in our galaxy. Its X-ray spectrum is dominated by emission from the intermediate mass elements of Mg, Si, S, Ar, and Ca, and features prominent emission from

[6] http://snrcat.physics.umanitoba.ca/SNRrecord.php?id=G120.1p01.4

both the Fe L and Fe K shells. Temperatures seem to average between $0.7 - 1.5$ keV, with ionisation timescales on the order of 10^{11} cm^{-3} s (Guo & Yang 2017). There appears to be a stratification of the elements within the remnant, with lighter elements appearing further out from the centre while Fe is primarily in the innermost regions (Hwang & Gotthelf 1997; Aschenbach 2002). The thermal emission from the ejecta has been fit with several NEI models, with super-solar abundances of Si, S, Ar, Ca, and Fe (Guo & Yang 2017). Emission from the forward shock, meanwhile, seems to be dominated by nonthermal synchrotron emission, which has been taken as evidence of cosmic ray acceleration (Warren et al. 2005; Cassam-Chenaï et al. 2007). Several bright knots of enhanced emission have been noted, particularly in the southeast, in which variations in the abundances of Si and Fe arise, pointing towards and incomplete mixing of the Si and Fe layers (Decourchelle et al. 2001). The most prominent of these knots was analysed by Miceli et al. (2015), who reported strong emission from Fe Kα, as well as the presence of Ti, Cr, and Mn. Yamaguchi et al. (2017), however, has disputed these claims, detecting no such emission in *Suzaku* data.

5.1.6 G272.2−3.2

Discovered in X-rays by the *ROSAT* All-Sky Survey (Greiner & Egger 1993) and later in radio using the Parkes, ATCA, and MOST radio telescopes (Duncan et al. 1997), G272.2−3.2 appears as a roughly circular object 15 arcminutes in diameter. Though its overall surface brightness is quite low, in X-rays it exhibits a centrally-brightened morphology, with its X-ray emission being predominantly thermal. In radio, it exhibits a fairly steep radio spectral index of -0.55 ± 0.15 ($S \propto \nu^{\alpha}$), typical of shell-type SNRs; it was this contrast that led Harrus et al. (2001) to classify it as a thermal composite SNR.

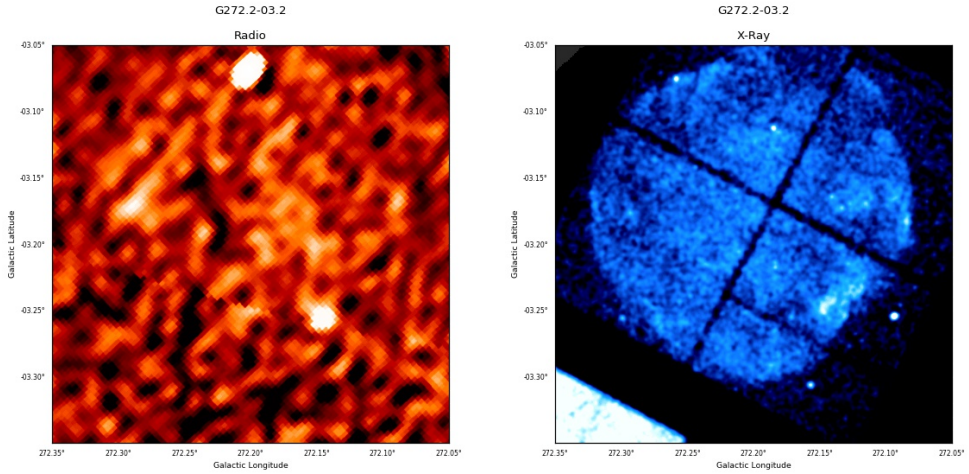

Figure 5.6: Radio and X-ray images of G272.2−3.2. Images from SNRcat[7].

The distance to G272.2−3.2 is not well constrained. Based on values of interstellar absorption, Greiner et al. (1994) initially estimated it to be $1.8^{+1.4}_{-0.8}$ kpc, while a statistical analysis performed by Harrus et al. (2001) estimated between $2 - 10$ kpc, adopting an intermediate value of 5 kpc. A more recent study by Kamitsukasa et al. (2016) suggests a distance of 2.5 kpc, using arguments of the interstellar absorption and the SNR's location with respect to the Galactic plane. Sezer & Gök (2012) calculated an upper limit to the remnant's age of 4300 years, while Sánchez-Ayaso et al. (2013) have estimated 3600 ± 1600 years, and Kamitsukasa et al. (2016) calculates a dynamical age of ~ 6000 years.

Initial studies reported that the remnant's X-ray spectrum could be described by a non-equilibrium ionisation model with an electron temperature of roughly 0.7 keV and an ionisation timescale on the order of 10^{10} cm^{-3} s. Using *Chandra* data, McEntaffer et al. (2013) confirmed the presence of an NEI plasma, and reported a temperature range of $0.7 - 1.5$ keV. Using *XMM-Newton* data, Sánchez-Ayaso et al. (2013) reported the presence of two NEI

[7] http://snrcat.physics.umanitoba.ca/SNRrecord.php?id=G272.2m03.2

plasmas with temperatures of 0.76 and 1.05 keV in the inner and outer plasmas, respectively. These studies have generally reported nonsolar values for the abundances of Ne, Mg, Si, S, and Fe, with Si, S, and Fe typically being super-solar while Ne and Mg are typically sub-solar, though these values vary across the remnant. Most studies of this SNR have been limited to below 3.0 keV, however, owing to very low emissions in that regime. Using approximately 150 ks of *Suzaku* observations, Kamitsukasa et al. (2016) were able to detect emission above this point, providing evidence for the existence of Ar and Ca. Both McEntaffer et al. (2013) and Kamitsukasa et al. (2016) have also reported the presence of a CIE plasma with a very low electron temperature of 0.2 keV with solar abundances, which is believed to be shock-heated ISM. Due to the abundance patterns (Sezer & Gök 2012; McEntaffer et al. 2013; Sánchez-Ayaso et al. 2013), lack of detection of any compact remnant (McEntaffer et al. 2013; Duncan et al. 1997), and energy of the Fe Kα line (Kamitsukasa et al. 2016), G272.2−3.2 is generally accepted as the remnant of a thermonuclear supernova.

5.1.7 G337.2−0.7

G337.2−0.7 was first identified as an SNR candidate based on its possible nonthermal radio emission by Green (1974), a suspicion which was confirmed through further radio observations by Whiteoak & Green (1996). It was discovered in X-rays by *ASCA*, which showed it to feature strong emission from heavy elements, and to be be dominated by metal-rich ejecta (Rakowski et al. 2001). In both regimes, it has an angular size of roughly 4.5×5.5 arcminutes. In radio, it exhibits a prominent (albeit incomplete and clumpy) elliptical ring of 2.0×3.2 arcminutes in the southern part of the SNR. While the X-ray regime also shows a brightening

[8] http://snrcat.physics.umanitoba.ca/SNRrecord.php?id=G337.2m00.7

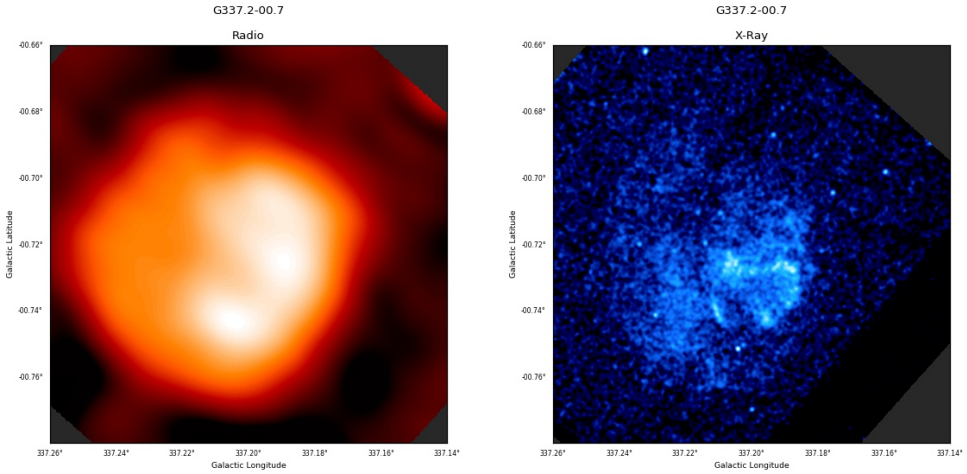

Figure 5.7: Radio and X-ray images of G337.2–0.7. Images from SNRcat[8].

in this region, the ring itself is not visible.

Radio HI absorption measurements by Rakowski et al. (2006) place the remnant between 2.0 ± 0.5 and 9.3 ± 0.3 kpc, and Takata et al. (2016) use arguments of X-ray absorption column density to place it at the further end of this range, i.e. at 9 kpc. Rakowski et al. (2006) also estimated the age of the remnant to lie between 750 and 3500 years, though with the caveat that the lower estimation of age would lead to an unreasonably low explosion energy of $E_0 = 10^{49}$ ergs, suggesting that the higher end of their estimates would prove more plausible. Takata et al. (2016), using an argument of plasma density acquired from their spectral fits, suggested an age of $\sim$ 5000 years, though that assumption was also predicated on the assumption of a distance of 9 kpc, as mentioned.

There have been three direct X-ray studies of G337.2–0.7. All three of these studies found that the global spectrum of the remnant was best fit by an NEI model, with a plasma temperature of 0.70 keV, an ionisation timescale on the order of 10^{11} cm^{-3} s, and a relatively high hydrogen column density of $N_{\mathrm{H}} \sim 3 \times 10^{22}$ cm^{-2}. Using *ASCA* data, Rakowski et al.

(2001) determined the presence of enhanced ejecta for Ne, Mg, Si, S, Ar, Ca, and Fe, though the abundances of Ne and Mg were determined to be negligible, and the other elements – while super-solar – were poorly constrained. Later, with *Chandra* and *XMM-Newton* data, Rakowski et al. (2006) found similar results from both global and spatially resolved studies, albeit with higher determined abundances of Ne, Mg, and Ca, and lower abundances of Fe. Takata et al. (2016) used *Suzaku* data, fitting the object's spectra with multiple NEI components and finding that three components of varying temperatures (0.70, 1.54, and 3.1 keV) producing the best results, with the highest-energy component being responsible for the Fe emission, the middle component being responsible for the Mg, Si, S, Ar, and Ca emission, and the lowest-energy component being tied to solar abundances. The general abundances found in this paper were typically higher than those found in the previous two, and it was the first to show evidence of Fe-K shell emission, likely owing to the significantly higher quality of data available for the *Suzaku* study (304 ks as opposed to 38 ks and 48 ks for *XMM-Newton* and *Chandra*, respectively). The SNR has been classified as a thermonuclear supernova remnant by Rakowski et al. (2006) and Takata et al. (2016), using arguments of abundance patterns and ejecta mass.

5.1.8 G344.7–0.1

G344.7–0.1 appears as an asymmetric and bright shell-like structure with a size of $8 - 10$ arcminutes in the radio regime where it was first detected by Clark et al. (1975), and later classified as a possible composite SNR by Dubner et al. (1993). In X-rays, it was first detected in an *ASCA* study by Sugizaki et al. (2001), where it appears as an extended source of thermal

[9] http://snrcat.physics.umanitoba.ca/SNRrecord.php?id=G344.7m00.1

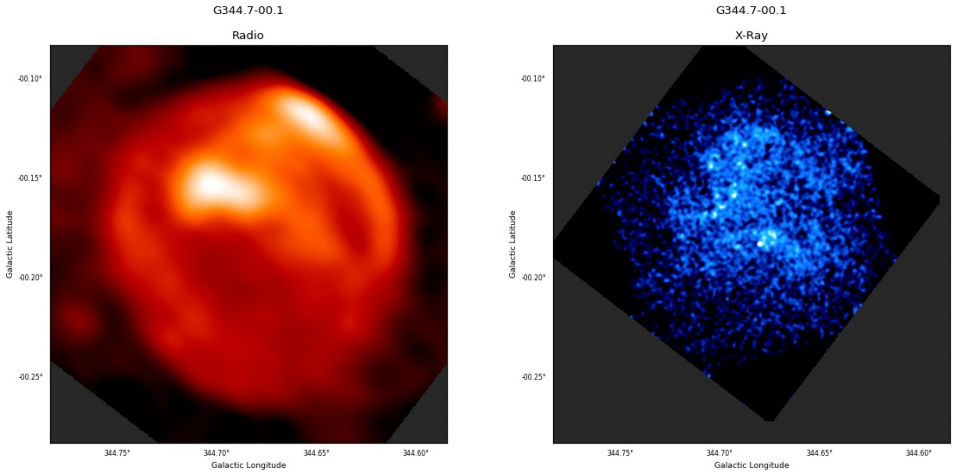

Figure 5.8: Radio and X-ray images of G344.7−0.1. Images from SNRcat[9].

emission roughly 6 arcminutes in diameter.

Though its age is uncertain, the remnant is believed to be somewhat older, with Combi et al. (2010) using the upper limit of its ionisation timescale to estimate an age of $\sim$ 6000 years, while Giacani et al. (2011) estimated an age of 3000 years using the same method. Initially, Dubner et al. (1993) determined a distance to the SNR of 14 kpc based on the Σ−D relation, and was redetermined to be 6.3 ± 0.1 kpc by Giacani et al. (2011). Yamaguchi et al. (2012) cautions against this distance calculation, however, and argues that Galactic HI column densities suggest a distance of at least 8.2 kpc (they adopt the previously-determined distance of 14 kpc). Fukushima et al. (2020), using the velocity ranges of the object's gas density map, also concludes a distance of $6.2 - 6.4$ kpc, in agreement with the value determined by Giacani et al. (2011).

In an *ASCA* study of G344.7−0.1, Yamauchi et al. (2005) determined that its X-ray spectrum featured emission lines from highly ionised Si, S, Ar, and Ca, as well as a strong Fe-Kα line. This was confirmed with the *XMM-Newton* and *Chandra* study of the object by Combi

et al. (2010), who fit the object with an absorbed PSHOCK model and found enhanced abundances, a hydrogen column density in excess of 5×10^{22} cm^{-2}, an ionisation timescale on the order of 10^{11} cm^{-3} s, and an average electron temperature of 1.17 keV. These results were refined by Giacani et al. (2011), who found a slightly higher electron temperature of 1.46 keV, super-solar abundances for Si, S, Ar, and Ca, and sub-solar abundances for Mg and Fe. They also found that a superior fit was determined through use of a VNEI model, as opposed to the PSHOCK model of Combi et al. (2010). Yamaguchi et al. (2012), using a VNEI model with *Suzaku* data, found similar results, albeit with a lower electron temperature of 0.97 keV, also noticing emission from Al, Cr, and Mn, which they accounted for by using Gaussians. Additionally, Fukushima et al. (2020) performed a study using deeper, more recent *Chandra* observations. These deeper observations again found that a VNEI model provided the best results, with values quite similar to those of Yamaguchi et al. (2012), as well as finding an apparent stratification of the heavy elements with the Fe ejecta concentrated in the remnant's centre, surrounded by the intermediate-mass elements of Si, S, Ar, and Ca. G344.7–0.1 was initially categorised as a core-collapse SNR by Lopez et al. (2011) and Giacani et al. (2011), using arguments of asymmetry and possible association with star-forming regions, respectively; however, the energy of the remnant's Fe Kα line, as well as the abundance patterns and distribution, have caused it to be reclassified as a thermonuclear SNR.

5.1.9 G352.7–0.1

G352.7–0.1 was first discovered in the radio regime by Clark et al. (1973), where it was classified as an SNR. Further radio studies by Caswell et al. (1983), Dubner et al. (1993), and

[10] http://snrcat.physics.umanitoba.ca/SNRrecord.php?id=G352.7m00.1

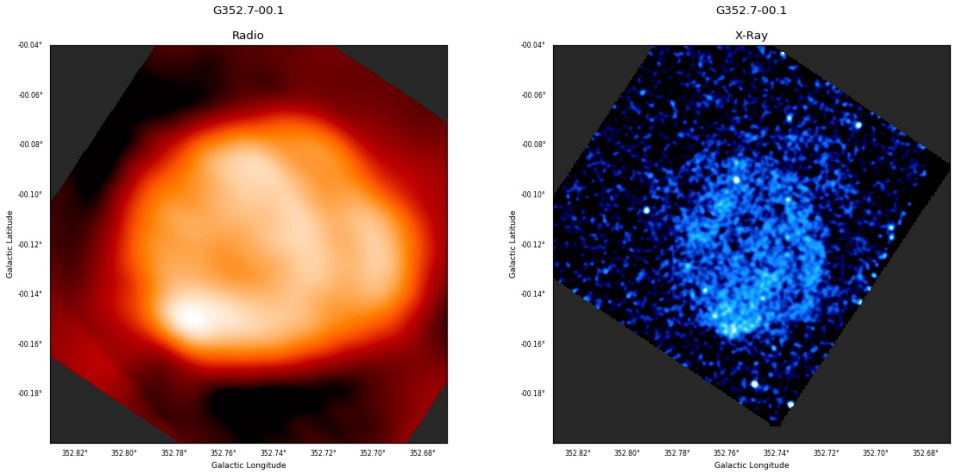

Figure 5.9: Radio and X-ray images of G352.7−0.1. Images from SNRcat[10].

Whiteoak & Green (1996) showed it to be a shell-like SNR (spectral index of -0.6) with two loop-like or lobe-like structures and an overall angular size of 8×6 arcminutes. X-ray emission from the remnant was first detected by Kinugasa et al. (1998), who described it as a shell-type SNR with a ring morphology similar to that seen in radio bands. Giacani et al. (2009), however, reclassified it as a mixed-morphology remnant due to the thermal nature of its X-ray emission.

The age of the SNR has been estimated to range from 2200 years (Kinugasa et al. 1998) to 7600 years (Leahy & Ranasinghe 2016), with the most recent estimate by Dang et al. (2024) suggesting a lower limit to the SNR's age of 4900 ± 1300 years. Distance estimates range from 7.5 ± 0.5 kpc, based on HI absorption profiles (Giacani et al. 2009), to 11 kpc (Dubner et al. 1993), based on the Σ–D relation. There remains little consensus on this value, with the most recent estimation by Zhang et al. (2023) being 10.5 kpc based on interactions between the SNR and a nearby molecular cloud.

The first X-ray studies of G352.7−0.1 by Kinugasa et al. (1998) showed that it featured

prominent emission from Si, S, and Ar, which was well-fit by an NEI model with enhanced abundances for Si and S, an electron temperature of 2.0 keV, an ionisation timescale on the order of 10^{11} $\mathrm{cm^{-3}\,s}$, and an absorption of 2.9×10^{22} $\mathrm{cm^{-2}}$. Giacani et al. (2009) found similar trends for the electron temperature, absorption, and abundances, but found a lower ionisation timescale of 4.5×10^{10} $\mathrm{cm^{-3}\,s}$ using *XMM-Newton* data, and noted emission from Fe Kα, which they compensated for by adding a Gaussian. Most of these results are supported by the *Chandra* and *XMM-Newton* data used in Pannuti et al. (2014), except they found a greater variation in the electron temperature, ranging from 0.68 to 2.03 keV, depending on where in the remnant the measurement was made. Sezer & Gök (2014), using *Suzaku* data, noted the detection of enhanced abundances for Ca and Fe, and fit the data with a two-component NEI model, rather than the one-component model used in previous fits; this resulted in electron temperatures of 0.6 and 4.3 keV and ionisation timescales of 3.4×10^{11} and 8.8×10^{9} $\mathrm{cm^{-3}\,s}$, respectively. More recently, Dang et al. (2024) detected emission from Mg, Si, S, Ar, Ca, and Fe in the *XMM-Newton* data, again fitting the remnant's spectra with single-component NEI models. This resulted in super-solar abundances for all reported elements, with other parameters being comparable to those found in previous studies.

The supernova classification for G352.7–0.1 is unclear. Given its barrel-shaped morphology, Giacani et al. (2009) suggested a possible CC origin from a massive star, and this was supported by Pannuti et al. (2014), who noted a large swept-up mass. On the other hand, Yamaguchi et al. (2014), Sezer & Gök (2014), and Fujishige et al. (2023) argue for a thermonuclear origin, primary along lines of the Fe Kα line energy and elemental abundances.

Table 5.2: Basic information for the six LMC SNRs

Equatorial Coordinates	Unique Name	Distance (kpc)	Size (arcmin.)	Age (yrs)
0505–67.9	DEM L71	50	1.4 x 1	4360 - 6600
0509–67.5		50	0.42	400
0509–68.7	N103B	50	0.50	860
0519–69.0		50	0.55	450
0534–69.9		50	2	10100
0548–70.4		50	1.8	7100

5.2 LMC SNRs

5.2.1 N0505–67.9

N0505–67.9 – also known as "DEM L71" for the catalogue of Davies, Elliot, & Meaburn – was first discovered in the optical band by Davies et al. (1976), and it was classified as a supernova remnant after it was first observed in the X-ray regime by the *Einstein* observatory (Long et al. 1981). Later observations with *Chandra* (Hughes et al. 2003; Rakowski et al. 2003) revealed a slightly elliptical outer rim roughly 1.4×1 arcminutes across that matches very closely the Hα emission in optical, something rather uncommon in SNRs. It also features a fainter, diffuse centre, suggesting a double-shock morphology of an outer blast wave shock surrounding a central region of reverse-shock heated ejecta.

As an LMC object, the distance to N0505–67.9 is approximately 50 kpc (Freedman et al. 2001), which corresponds to a physical size of approximately 20×14 pc for the remnant. Hughes et al. (1998), using *ASCA* data, estimated an age of 5000 years, while Ghavamian et al. (2003), using optical observations of the Balmer-dominated shock velocities, determined an age of 4360 ± 90 years, and Alan & Bilir (2022) estimated an upper limit to the remnant's age of 6600 ± 770 years.

ASCA observations by Hughes et al. (1998) indicated that the remnant was possessed of enhanced Fe emission, particularly from its centre. *Chandra* observations by Hughes et al. (2003) and Rakowski et al. (2003) confirmed this finding, also showing enhanced abundances of Mg, Si, and S, which they fit for using a single-component NEI model. van der Heyden et al. (2003), using *XMM-Newton* RGS data, found that the spectrum was best fit by two NEI components, with one at a temperature of 0.8 keV, and the other at a temperature of 0.2 keV. Using 103 ks of archival *Chandra* data, Alan & Bilir (2022) determined the presence of O, Ne, Mg, Si, and Fe, using a single-component NEI model and finding typically sub-solar abundances for all regions studied, with Fe being the main exception. Due to the generally enhanced abundances of Fe, and the estimated Fe ejecta mass of about $1.4\ M_\odot$ (Hughes et al. 2003; van der Heyden et al. 2003), N0505−67.9 is believed to be the remnant of a thermonuclear supernova.

5.2.2 N0509−67.5

The SNR N0509−67.5 was first discovered by the *Einstein* observatory by Long et al. (1981), during an X-ray survey of the LMC. In the optical regime, it appears largely circular (Tuohy et al. 1982). Its X-ray morphology is similar: a clearly circular shell of emission, with fairly faint emission in the centre. The southwestern half of the remnant shows brighter emission than the northeastern half, giving the remnant a distinct, two-halved appearance (Warren & Hughes 2004). Its angular size is roughly 0.42 arcminutes across.

At an LMC distance of 50 kpc, N0509−67.5's angular size corresponds to a physical size of roughly 6 pc (Warren & Hughes 2004). Its age was originally estimated to be quite young, with an age of less than 1000 years (Smith et al. 1991). The detection of light echoes from the

SNR's progenitor supernova by Rest et al. (2005) constrained this to 400 ± 120 years, and Badenes et al. (2008), using this information alongside historical records from the European exploration and colonisation of the Southern hemisphere to constrain this to within a few decades of 400 years.

An *Chandra* study of N0509–67.5 by Warren & Hughes (2004) revealed the presence of a strong emission line from Si Kα, alongside lines of S, Ar, Ca, and Fe. Using a PSHOCK model, they determined super-solar abundances of these elements save for Fe, alongside sub-solar abundances for O, and Mg. They also attempted to fit for Ne, but found that doing so did not improve the fit. Kosenko et al. (2008), using *XMM-Newton* data, found that the remnant's spectrum was best fit by a two-component NEI model, with one component providing the bulk of the emission and the other accounting for Fe K emission around 6.5 keV. N0509–67.5 has long been considered to be of a thermonuclear origin, due to X-ray observations of the elemental yields, and the detection of light echoes has helped enforce that claim.

5.2.3 N0509–68.7

The fourth brightest X-ray remnant in the LMC, N0509–68.7 was discovered by Long et al. (1981), and was identified as an SNR based on its non-thermal radio emission (Mathewson et al. 1983). Also known as N103B, it is a shell-type remnant with a radio spectral index of -0.53, and infrared measurements using the *Spitzer* Space Telescope have shown it to be interacting with a nearby molecular cloud (Williams et al. 2014), granting it a highly asymmetric morphology with the brightest enhancement towards the west.

With an angular size of 0.5 arcminutes, N0509–68.7 has an approximate physical size of

7.2 pc. Due to its small size, Hughes et al. (1995) estimated the age of the remnant to be 1500 years. Using a light echo from the supernova, Rest et al. (2005) determined a slightly younger age of 860 years, making it one of the younger remnants in the LMC, and this age estimate is supported by *Chandra* expansion measurements made by Williams et al. (2018), with overall average shock velocities being in excess of 4×10^3 km s^{-1}.

Hughes et al. (1995), while analysing *ASCA* data of the SNR, found strong emission lines from Si, S, Ar, Ca, and Fe, but little to no emission from O, Ne, or Mg. Similar results were found by van der Heyden et al. (2002), who used three components – one NEI, at roughly 3.5 keV; one CIE, at roughly 0.65 keV; and one between $0.2 - 0.55$ keV, for which the difference between CIE and NEI provided little difference to the overall fit – to produce a fit to the remnant, and who also noticed unambiguous emission from O, Ne, and Mg using *XMM-Newton*'s RGS spectrum. Someya et al. (2014) used four NEI components – three ISM components at 0.36, 0.56, and 0.92 keV, and one ejecta component at 3.96 keV – to reach the same conclusion, noting that there was a clear overabundance of Mg, Si, S, Ca, Fe, and Ni.

The supernova origin of N0509–68.7 is not well understood. Chu & Kennicutt (1988) reported the presence of an HII region nearby to the remnant, which is suggestive of a CC origin, and the O, Ne, and Mg abundances as determined by van der Heyden et al. (2002) support this, alongside the abundances of Mg, Fe, and Ni relative to Si, as determined by Someya et al. (2014). In contrast, Lewis et al. (2003) suggested the possibility of a thermonuclear origin, using the substantial Fe mass as evidence. Badenes et al. (2009) supported this argument, with a possible progenitor that underwent substantial mass loss before the explosion, and Lopez et al. (2011), using an argument of the remnant's morphology, argued for a

thermonuclear origin as well.

5.2.4 N0519–69.0

SNR N0519–69.0 is a somewhat irregular, patchy or clumpy SNR, showing a clear inner ejecta surrounded by a thin shell of swept-up ISM (Kosenko et al. 2010). It was first observed in the X-ray bands by Long et al. (1981), and follow-up observations by Tuohy et al. (1982) confirmed its nature as an SNR, and suggested a thermonuclear origin for the remnant. Further X-ray observations by Hughes et al. (1995) supported this, due to it being O-poor and Fe-rich.

The angular size of N0519–69.0 is approximately 0.55 arcminutes, which corresponds to a physical size of 8 pc. The age of the remnant was estimated to lie between $750 - 1500$ years by Smith et al. (1991) based on shock velocities determined from its optical spectrum. It is, however, one of several LMC SNRs for which light echoes were detected by Rest et al. (2005), from which an age of 600 ± 200 years was deduced. Kosenko et al. (2010), using measurements of circumstellar density and forward/reverse shock radii, determined an age of 450 ± 200 years, slightly lower than but largely consistent with the findings of Rest et al. (2005). Meanwhile, Guest et al. (2023) determined an upper limit to the age of 750 years, based on measurements of the SNR's expansion over the course of two decades.

Only a few studies of the X-ray emission from N0519–69.0 have been performed. As mentioned, Hughes et al. (1995) performed an analysis on the object, determining it to be O-poor and Fe-rich, and that it had a continuum temperature of 1.48 ± 0.13 keV. As well, Kosenko et al. (2010), using multi-component NEI models, noted the presence of Si, S, Ar, and Ca, in addition to the previously-detected Fe. It has been classified as a thermonuclear supernova

remnant, owing to the prominence of the emission lines from Si-Fe, which is inconsistent with non-Ia origins.

5.2.5 N0534–69.9

N0534–69.9 features a bright central region surrounded by a limb-brightened shell of swept-up ISM, and was first detected in the X-ray regime through the *Einstein* observatory survey by Long et al. (1981). Although it has a somewhat complicated morphology, it possesses an approximately circular shape with an angular size of nearly 2 arcminutes. This size – quite large for an LMC object – yields a physical size of approximately 13.7 pc, and corresponds to an estimated age of 10100 years, based on measurements of shock velocities by Hendrick et al. (2003).

Studies of N0534–69.9 are limited. Chu & Kennicutt (1988) made a detection of the object using *ROSAT*, but spectroscopic studies seem to have only begun with the *Chandra* observations by Hendrick et al. (2003), who detected strong emission from Fe, as well as K-shell emission from Mg, Si, and S. Using a PSHOCK model, they determined electron temperatures of 0.61 and 0.92 keV in the southern and northwestern parts of the remnant, and electron temperatures of 0.33 and 0.34 keV in the southern and northwestern limbs, respectively. Using *Suzaku* data, Takeuchi et al. (2016) obtained a two-component NEI model fit to the global spectrum of the remnant, detecting emission from O, Ne, Mg, Si, S, and Fe (detecting high abundances of O, and lower abundances of Ne, Mg, Si, and S with respect to Fe), and finding an overall electron temperature of 0.68 keV. The elemental abundances present within the remnant favour a thermonuclear origin.

5.2.6 N0548–70.4

Like most of the other LMC SNRs, N0548–70.4 was discovered in X-rays by Long et al. (1981). It is an approximately circular object with an angular radius of 1.8 arcminutes, corresponding to a physical size of approximately 12.1 pc. It possesses a bright central region alongside bright limbs which are most prominent on the eastern and western sides of the remnant. Like N0534–69.9, N0548–70.4 is a somewhat older remnant at 7100 years (Hendrick et al. 2003).

The X-ray emission of N0548–70.4 has not been extensively studied. Hendrick et al. (2003), using a one-component PSHOCK model, found that the X-ray spectrum of N0548–70.4 features strong emission from Fe, alongside low emission from the intermediate mass elements. Takeuchi et al. (2016), using a two-component NEI model, instead found higher emission from S as opposed to Fe. Both attempts found electron temperatures of approximately 0.60 keV. Like N0534–69.9, a thermonuclear origin is favoured owing to the elemental abundances detectable within the remnant.

6

Observations & Data Reduction

We detail now the observations used in this study, and the processes used in the reprocessing of such. The data used in this study was all archival data, captured by the *XMM-Newton* telescope and acquired from the *XMM-Newton* Science Archive.[1] The sole exception to this is the data for G1.9+0.3, for which no *XMM-Newton* observations exist; in this case, the data

[1] https://nxsa.esac.esa.int/nxsa-web

Table 6.1: Observational IDs and combined exposure times for each object studied in this work.

Object Name	Telescope	Observation ID(s)	Exposure Time (ks)
G1.9+0.3	*Chandra*	12689, 12690, 12691, 12692, 12693, 12694, 12695, 13407, 13509	980.5
G4.5+6.8	*XMM-Newton*	0842550101	140.5
G41.1−0.3	*XMM-Newton*	0085200301, 0085200401, 0085200501, 0830450101	200.5
G43.3−0.2	*XMM-Newton*	0084100401, 0084100501, 0724270101, 0724270201	227.6
G120.1+1.4	*XMM-Newton*	0412380101, 0412380201, 0412380301, 0412380401	149.6
G272.2−3.2	*XMM-Newton*	0112930101	38.4
G337.2−0.7	*XMM-Newton*	0087940101	40.2
G344.7−0.1	*XMM-Newton*	0111210101, 0111210401	22.2
G352.7−0.1	*XMM-Newton*	0150220101	30.7
N0505−67.9	*XMM-Newton*	0884620101	129.8
N0509−67.5	*XMM-Newton*	0111130201	44.3
N0509−68.7	*XMM-Newton*	0113000301	26.5
N0519−69.0	*XMM-Newton*	0113000501	48.4
N0534−69.9	*XMM-Newton*	0673780101	61.9
N0548−70.4	*XMM-Newton*	0883390101	59.9

used was archival data captured by the *Chandra* telescope, and acquired from the *Chandra* Data Archive.[2] Observations were chosen by selecting the proposal that resulted in the greatest combined exposure time. This was done in an attempt to limit the observations to a single epoch, so as to minimize the effect of expansion over time. The exceptions to this were the objects G41.1−0.3 and G43.3−0.2, for which two proposals were used in attempt to better constrain the uncertain natures of their progenitors. The observation IDs used, as well as their combined exposure times, can be found in Table 6.1.

[2] https://cda.harvard.edu/chaser/

Data processing for the *XMM-Newton* data made use of SAS version 21.0.0, and proceeded according to the guidelines laid out in the *XMM-Newton* User's Handbook.[3] Filtering was done by applying the recommended patterns for spectroscopy, with the filtering for good time intervals (GTI), bad pixels, and out of time events for the MOS and pn detectors done using the `emproc` and `epproc` commands, respectively. Observations were checked for any potential photon pile-up using the command `epatplot`, and the `evselect` command was used both to apply any filters, as well as to extract the data from relevant regions once region generation had been performed. Redistribution matrix files (RMF) and ancillary response files (ARF) were generated for each region using the `rmfgen` and `arfgen` commands, respectively, and backscaling was performed on both the regions and their backgrounds using the `backscale` command. Once extracted, spectra and response files were packaged together and grouped to a minimum of 20 counts per bin using the FTOOLS task GRPPHA.

Data processing for the *Chandra* data was done using CIAO version 4.16, and followed the standard procedure laid out in the CIAO Analysis Guides.[4] The `chandra_repro` command was used to reprocess the data before filtering was applied to limit the energies to the $0.3 - 10$ keV range, and periods of background flaring were removed through the use of GTI filters which were applied using the command `dmcopy`. Spectral extraction was performed using the `specextract` command, and once extracted, spectra were regrouped to a minimum of 20 counts per bin using the FTOOLS task GRPPHA.

For the majority of objects, region generation was performed by running the *contbin* algorithm on a combined MOS1 + MOS2 image, which itself was generated through use of the SAS command `merge`; this was done to increase the quality of the image, and to avoid

[3] https://xmm-tools.cosmos.esa.int/external/xmm_user_support/documentation/uhb
[4] https://cxc.harvard.edu/ciao/guides/index.html

potential detector bias. The pn image was excluded from this process as the pn CCDs are differently shaped compared to those of the MOS cameras, and these gaps would appear on the combined image as areas of lower surface brightness due to the relative simplicity of the `merge` command. Three exceptions were made, for G1.9+0.3, G272.2-3.2, and N0505-67.9.

For G1.9+0.3, as the data used was from *Chandra* rather than from *XMM-Newton*, we made use of the CIAO command `reproject_obs`, combining the data from all nine of our used observations to generate a combined image. While this image was initially used with the *contbin* algorithm as normal, as G1.9+0.3 is dominated by non-thermal emission (Reynolds et al. 2008, 2009), we found that the generated regions were similarly dominated, with no notable thermal emission to which we could fit our spectral models. However, the presence of thermal emission in the SNR was noted by Borkowski et al. (2010), largely concentrated in the SNR's northern rim. This emission was further isolated by Borkowski et al. (2013), who noted four distinct regions in which thermal emission was detected. For this object, we thus opted to reproduce these four regions for our study.

For G272.2-3.2, the object's size made use of the `merge` command insufficient: the angular size of G272.2-3.2 is greater than that of the central CCD of the MOS cameras, causing the gaps between CCDs to be a concern. To solve this issue, we instead made use of the Extended Source Analysis Software[5] (ESAS) pipeline, which allows for the combination of MOS1, MOS2, and pn camera data to generate exposure-corrected, background-subtracted images of a given object. This allowed us to create an image of the object which did not include any chip gaps, on which we were able to run the *contbin* algorithm as normal.

For N0505-67.9, we again made use of the ESAS pipeline, this time to correct for bands

[5] `https://heasarc.gsfc.nasa.gov/docs/xmm/xmmhp_xmmesas.html`

of dead pixels rather than chip gaps. While these are present in all *XMM-Newton* observations, the small angular size of N0505-67.9 combined with its location on the chip within the chosen observation made it so that the dead pixels took up a not-insignificant amount of the object's angular size, appearing as black bands when viewed in an image viewer. This resulted in the regions generated by the *contbin* algorithm being warped around these bands, as the algorithm interpreted these as areas with zero photon emission. As these dead pixels differ between the MOS1, MOS2, and pn cameras, the ESAS pipeline again allowed us to correct for them. The final selected regions for all objects can be seen in Figure 6.1.

When performing spectroscopy, it is necessary to provide a background, which will then be subtracted from the data of the selected region to ensure that the data of interest is free from any contamination that might result from background emission. To that end, the choice of background is a vital one. In this work, all backgrounds were manually chosen, but subject to the same criteria: the location of the background must be the same across all observations; the background must be chosen from the source-free region around the SNR; and the background should be located on the same CCD as the object, if possible. For the majority of objects, the background regions were chosen as an annulus extracted from the source-free region surrounding the SNR in question. For G1.9+0.3, a single region the same size and shape as the analysed region was chosen instead. For G41.1−0.3 and G43.3−0.2, circular source-free regions (three and four, respectively) were chosen roughly equidistantly placed around the object, and each region was assigned to the background region to which they were most closely located.

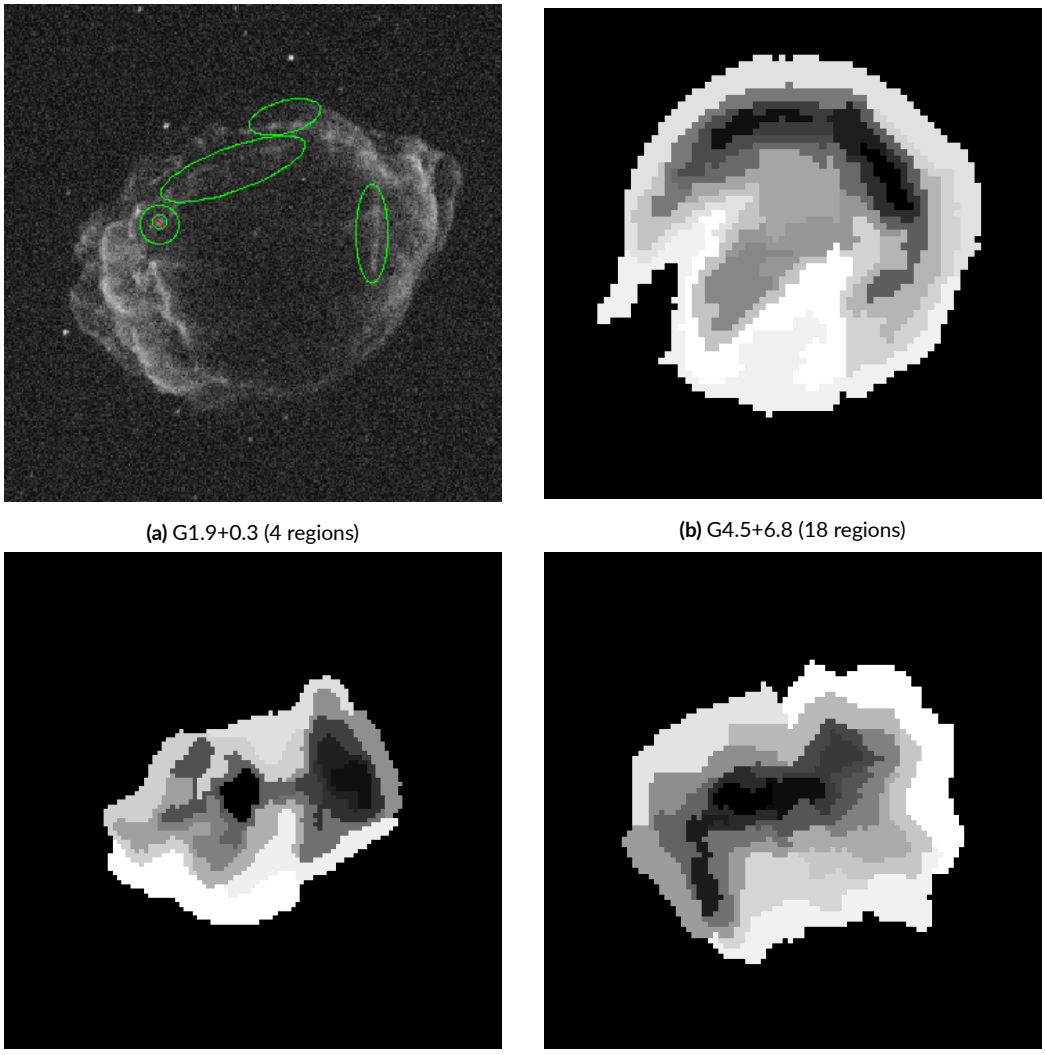

(a) G1.9+0.3 (4 regions)

(b) G4.5+6.8 (18 regions)

(c) G41.1−0.3 (17 regions)

(d) G43.3−0.2 (19 regions)

Figure 6.1: Final region maps for all objects involved in this study. For G1.9+0.3, the selected regions are indicated by green ellipses. For all other objects, the selected regions are indicated by varying shades on a white-black gradient.

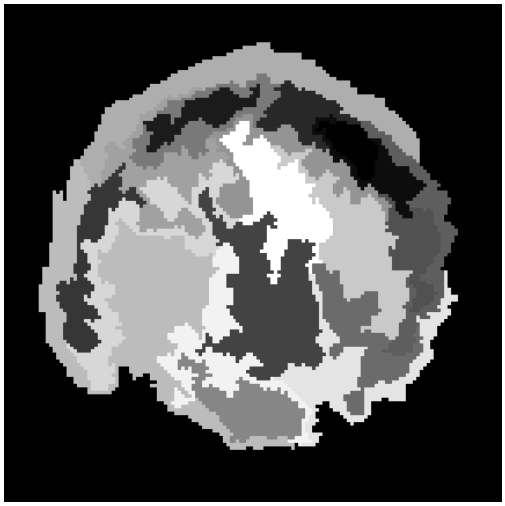

(e) G120.1+1.4 (20 regions)

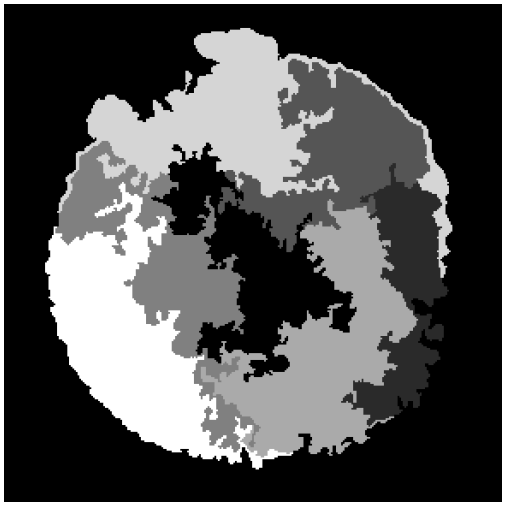

(f) G272.2−3.2 (7 regions)

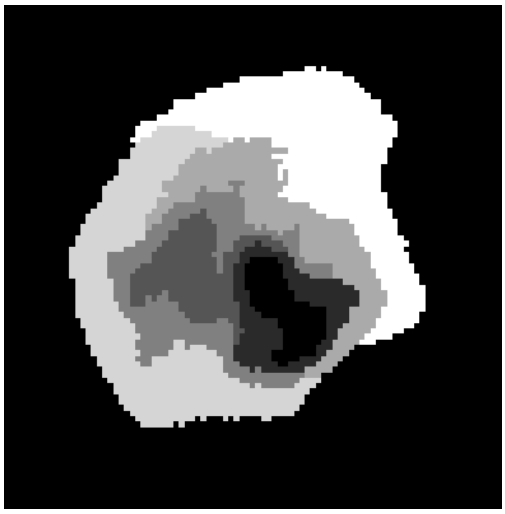

(g) G337.2−0.7 (7 regions)

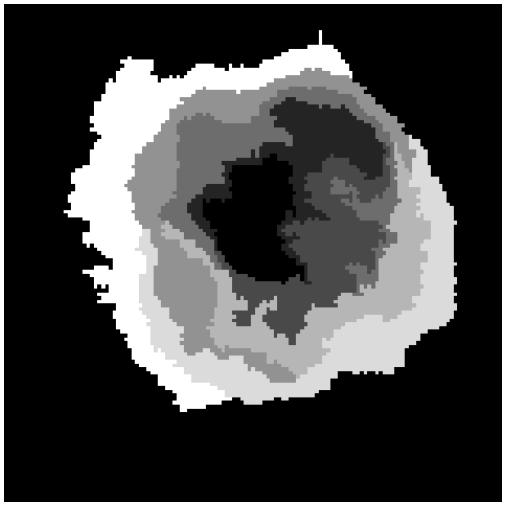

(h) G344.7−0.1 (8 regions)

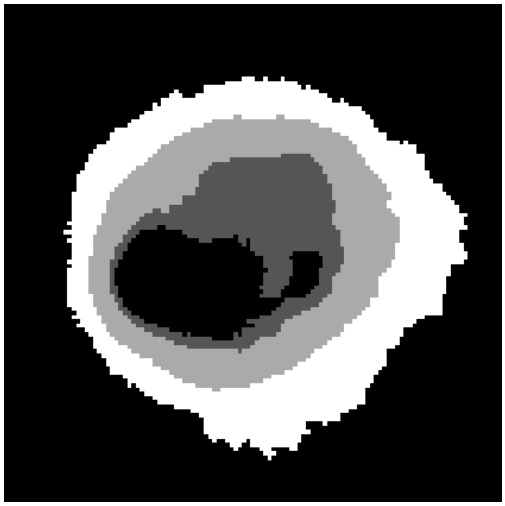

(i) G352.7−0.1 (4 regions)

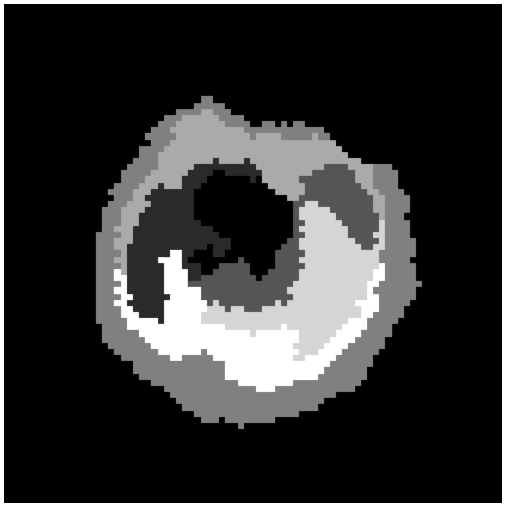

(j) N0505−67.9 (7 regions)

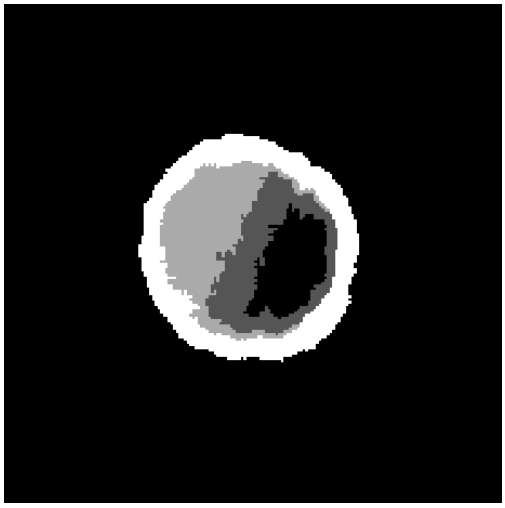

(k) N0509−67.5 (4 regions)

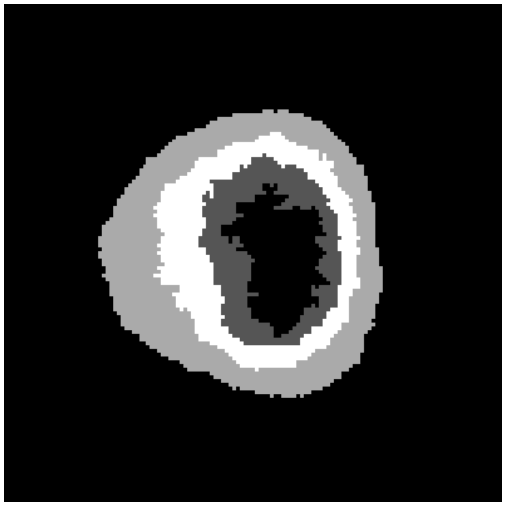

(l) N0509−68.7 (4 regions)

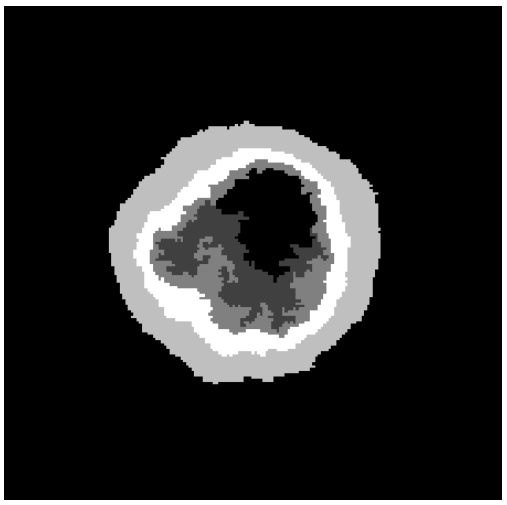

(m) N0519–69.0 (5 regions)

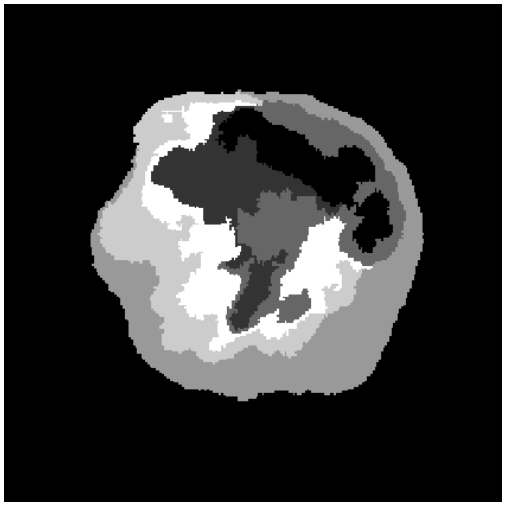

(n) N0534–69.9 (6 regions)

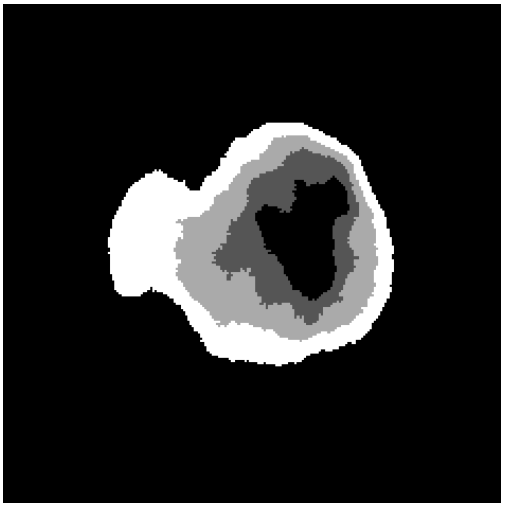

(o) N0548–70.4 (4 regions)

7

Spectroscopic Analysis

We move now to a description of our spatially resolved spectroscopy. This was performed on the regions generated via the *contbin* algorithm, as described in Chapter 6 and seen in Figure 6.1. For the spectral fitting, the datasets were fit using the XSPEC software version 12.14.1, using the solar abundance tables of Wilms et al. (2000). The models used in this study are listed and described in Subsection 4.6.3, and detailed lists of the parameters for each can be

found in Appendix A. Errors for individual parameters are reported to a significance of 90%, and were determined using the Markov Chain Monte Carlo method, using the Goodman-Weare algorithm as recommended by the XSPEC manual. The error analysis was performed with 16 walkers, a chain length of 200,000 steps, and a burn length of 100,000 steps.

For the LMC objects, a slightly different approach was needed to account for the differences in composition between the LMC and our own galaxy. To that end, two steps were taken: firstly, rather than use the TBABS model to account for interstellar absorption, we opted to use the TBVARABS model instead. In addition to accounting for hydrogen column density, the TBVARABS model allows one to vary the elemental abundances of the absorbing material. We chose to set these abundances to the average metal abundances of the LMC as determined by Dopita et al. (2019). As well, given that the LMC objects are located outside of our own galaxy, we also opted to use fixed values of N_H for each object. These absorption values were determined by using the HEASARC tool N_H,[1] using data provided by the HI4PI full-sky HI survey (HI4PI Collaboration et al. 2016). Secondly, whenever our fit seemed to require a second component, we opted to set the abundances in said component to the same average metal abundances of the LMC as were used for the absorption parameters.

When comparing our observations to models of supernova nucleosynthesis, we take the ratio of abundances with respect to that of Si. This is done to minimize systematic uncertainties in the absolute value of a given abundance, due to effects such as uncertainty in emission measures, instrumental calibrations, or possible degeneracies in the models. Si was chosen as it is typically a prominent line in supernova plasmas, and can thus be usually well constrained. These ratios are given in the form of $(X/Si)/(X/Si)_\odot$, where X is the abundance value of O,

[1] https://heasarc.gsfc.nasa.gov/cgi-bin/Tools/w3nh/w3nh.pl

Ne, Mg, S, Ar, Ca, or Fe with respect to the solar values of Wilms et al. (2000). To compare our results to the simulations of supernova nucleosynthesis, we performed a least squares analysis between these ratios and the same ratios for each model; the "best fit" models are those with the lowest fit parameter from this analysis. While the abundance ratios determined by these simulations are subject to uncertainties introduced by uncertainties in reaction rates, as well as due to simplifications made (e.g. dimensionality), or code-to-code differences, these uncertainties are unquantified in their respective sources, and as such, we instead treat said abundance ratios as exact, with zero theoretical uncertainty.

As this study includes objects for whom the nature of their progenitor is uncertain, we opted to include a comparison to models of core-collapse supernova nucleosynthesis in addition to the models of thermonuclear supernova nucleosynthesis detailed in Section 3.4.2. The core-collapse models included in this study are detailed in Appendix B.

7.1 G1.9+0.3

G1.9+0.3 was observed by *Chandra* nine times between the months of May and June, 2011, which combine for nearly one megasecond's worth of exposure time. Due to the fact that the emission from this remnant is dominated by non-thermal processes, the *contbin* algorithm proved unsuccessful at generating an appropriate region map for our purposes. Instead, we opted to manually reproduce the four regions used by Borkowski et al. (2013) in their study, as these regions were determined to be the primary locations of thermal emission within the SNR. Due to the poor photon statistics of the observations, these regions were grouped with a minimum of 10 counts per bin, rather than the standard 20 used in the rest of our study.

We fit each of these four regions with a single-component absorbed thermal model. Of the

Table 7.1: G1.9+0.3: Best fit parameters per region

Parameter	N	NE	NW	W
N_H (10^{22} cm^{-2})	$8.27^{+0.52}_{-0.32}$	$7.80^{+1.73}_{-0.82}$	$9.23^{+0.92}_{-0.45}$	$8.50^{+0.93}_{-0.35}$
kT (keV)	$3.54^{+0.00}_{-0.01}$	$5.36^{+0.43}_{-0.60}$	$3.61^{+0.10}_{-0.16}$	$4.43^{+0.10}_{-0.68}$
Si	$4.50^{+2.77}_{-1.54}$	$4.35^{+8.83}_{-3.64}$	$3.88^{+4.86}_{-3.38}$	$3.65^{+2.16}_{-2.92}$
S	$4.63^{+1.36}_{-1.40}$	$2.35^{+3.81}_{-2.15}$	-	$2.10^{+1.22}_{-1.24}$
Fe	$2.64^{+0.84}_{-0.76}$	$0.45^{+0.99}_{-0.39}$	$1.39^{+1.11}_{-1.02}$	-
τ (10^8 s cm^{-3})	$16.1^{+8.5}_{9.8}$	$8.99^{+28.6}_{-7.24}$	$4.46^{+40.4}_{-2.70}$	$9.69^{+69.1}_{-8.14}$
Redshift (10^{-3})	$-6.75^{+3.78}_{-6.15}$	6.91^{+57}_{-28}	$-5.57^{+12.9}_{-13.9}$	$3.69^{+14.4}_{-8.17}$
χ^2_ν (DoF)	0.93 (553)	0.92 (277)	0.92 (249)	0.91 (497)

four tested models (VPSHOCK, VNEI, VRNEI, and VAPEC), the VPSHOCK and VNEI models produced nearly identical results in terms of fit statistics. The VNEI model, however, was producing results with unreasonable values for the plasma temperature and ionisation timescale; as a result, we opted to use the VPSHOCK model to fit all four regions of this SNR. Additionally, we tested models with two thermal components. However, these additional components provided no notable improvements to the quality of the obtained fits, and as such were discarded in favour of the simpler one-component models.

Even with our specifically chosen regions, it is difficult to detect many of the common emission lines in the spectra of this SNR, owing mostly to poor photon statistics coupled with high interstellar absorption due to the SNR's proximity to the Galactic core. This resulted in only three elements being used for this study: Si, which featured a prominent emission line in all four of our regions; S, which was prominent in three (N, NE, W) of the four regions, but absent in the fourth (NW); and Fe, which was likewise present in three (N, NE, NW) of the regions, and absent in the fourth (W).

The results of our spectral fits can be seen in Table 7.1. The column density was consistently high, ranging from $7.80 - 9.23 \times 10^{22}\ \mathrm{cm}^{-2}$, which can be explained by the SNR's proximity to the Galactic centre. The plasma temperature was likewise high, between $3.54 - 5.36$ keV, while the ionisation timescale was quite low, ranging from $4.46 - 16.1 \times 10^{8}\ \mathrm{cm}^{-3}\ \mathrm{s}$, both of which are consistent with the extremely young age of the SNR. The abundances for Si were enhanced to super-solar values in all regions; S behaved similarly, save for the NW region, in which no S line was visible. Fe was enhanced in the N and NW; sub-solar in the NE; and was not visible in the W. These findings are largely consistent with the values reported by Borkowski et al. (2013), whose region map served as the basis for our own.

As we were only able to determine the abundances for three elements within the SNR, we are only able to produce two data points for use in our nucleosynthesis study, and as such, it is difficult to make any strong conclusions regarding the nature of G1.9+0.3's progenitor. However, some patterns do emerge: when looking at thermonuclear models, the best fits are obtained from those models which represent WDs with high mass, low DDT density, and high metallicity. When looking at the models of B19, those models using a CO reaction rate attenuated by 90% of the standard value produced more consistent fits than those using the standard reaction rate. From a statistical perspective using our goodness-of-fit parameter, the single best fit between all tested models was produced by the Ch-Mass, 1.20E+07 DDT Density model of B19 with a metallicity of $Z = 6.75 \times 10^{-2}$ and using the attenuated CO reaction rate.

A number of core-collapse models produced acceptable fits to the data, as well; however, there was a degree of inconsistency as to which progenitor masses worked well, with the best fits being largely arising from models with masses around $17.5\ \mathrm{M}_{\odot}$. The best fit from the

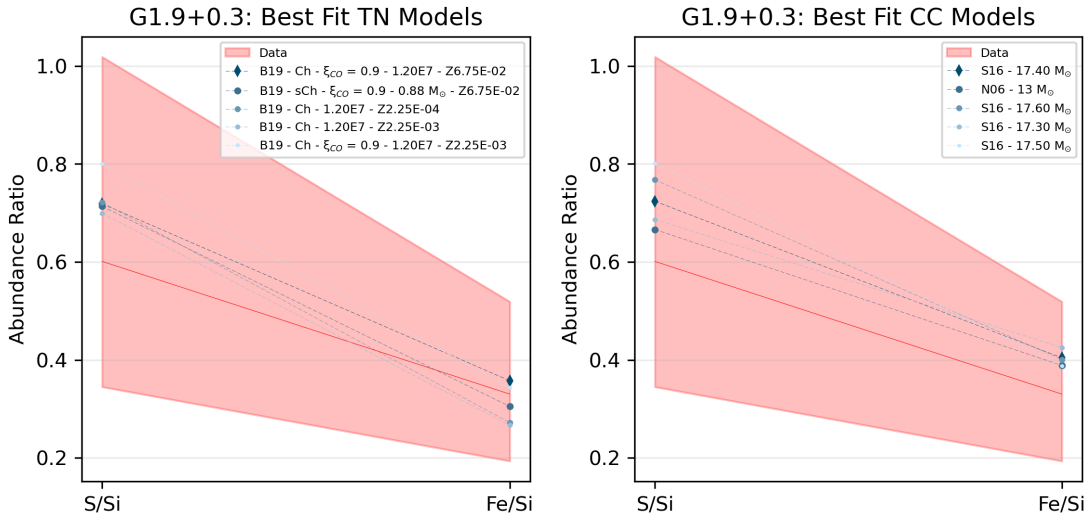

Figure 7.1: Best-fit nucleosynthesis models for G1.9+0.3, comparing to both thermonuclear (TN) and core-collapse (CC) supernova nucleosynthesis yields.

core-collapse models arose from the 17.4 $M_\odot$ model, with three more of the five best fits being similar: the 17.6 $M_\odot$, 17.3 $M_\odot$, and 17.5 $M_\odot$ models. The second best fit, however, arose from the 13.0 $M_\odot$ model of S16, and the 13.2 $M_\odot$, 13.5 $M_\odot$, and 13.3 $M_\odot$ models produced similar values. All of the best-fit core-collapse models mentioned come from S16.

7.2 G4.5+6.8

For G4.5+6.8 (Kepler's SNR), we made use of a single observation of roughly 140 ks, taken in 2020. The *contbin* algorithm was applied to a combined MOS1+MOS2 observation, resulting in the generation of an 18-region map from which spectra were extracted.

During the fitting process for G4.5+6.8, we noticed two things: firstly, the pn observation seemed slightly broadened with respect to the MOS observations. Secondly, there appeared to be a slight shift in the line centroids between our observations and the fitted models. For

the first of these issues, we were unable to find a spectral model capable of fitting simultaneously both the MOS and pn data while producing sensible results; as such, we opted to not make use of the pn observation for this object, instead only using the MOS1 and MOS2 observations. The second of these issues is likely caused by a bulk motion of the ejecta, and so we opted to allow the redshift parameters to vary, tying the redshift of the hotter component to that of the cooler component.

Our regions were initially tested with absorbed single-component models, but these proved unable to reproduce the observed spectra. We then fit each region with all two-component combinations of the VPSHOCK, VNEI, VRNEI, and VAPEC models, multiplied by the TBABS absorption model. We initially found that the VNEI+VNEI and VNEI+VAPEC model combinations were equally able to reproduce the given spectra; however, the age of G4.5+6.8 is low enough that it is unlikely for the remnant to be in CIE. As such, we re-fit the regions for which a VNEI+VAPEC fit had initially been found to be best with VNEI+VNEI models, paying close attention to the ionisation timescales. We found that our initial fits had been getting stuck in local minima; after compensating for this, our fits improved. We also noticed that there appeared to be an amount of excess emission around 1.2 keV that the models could not account for, likely arising from Fe L emission that is not incorporated into the presently-used atomic models (Yamaguchi et al. 2011). In compensation, we added a Gaussian at 1.2 keV for each region that exhibited the excess emission; the line energy of these Gaussians was allowed to vary during the fitting process. Ultimately, we were able to obtain acceptable fits ($\chi^2_\nu < 2.0$) for each region with an absorbed VNEI+VNEI model, with the exception of region R11. This region exhibited significant line-broadening, in particular around the Fe line, which our models could not fully account for. Although the abundances

within this region were in line with those of our other regions, we opted to exclude it from our nucleosynthesis calculations as a result.

The results of our spectral fits can be seen in Tables 7.2 and 7.3. We find relatively consistent values for the hydrogen column density, which ranges between $0.44-0.76\times10^{22}$ cm^{-2}. In the cold component, we find plasma temperatures that range between $0.41-0.72$ keV and ionisation timescales that range between $1.71-53.5\times10^{11}$ cm^{-3} s; however, if we exclude the two regions with the largest ionisation timescales, the upper limit on this range is reduced to 5.16×10^{11} cm^{-3} s, suggesting that the SNR largely remains in a state of NEI, with only a few small regions possibly approaching CIE. In the hot component, we note a larger range of variation in the plasma temperature, which ranges between $3.64-17.5$ keV, but a smaller range of variation in the ionisation timescale, which lies between $3.14-19.9\times10^{9}$ cm^{-3} s. Elemental abundances were fairly consistent across the remnant, with Ne and Mg being subsolar, while Si, S, Ar, Ca, and Fe were enhanced.

We can compare our findings to those of several previous studies. Sun & Chen (2019) used *Chandra* data to perform a spatially-resolved study of the SNR, using an adaptive binning method to subdivide the remnant into 4671 bins. Each bin was fit with an absorbed VNEI+srcut model, where the srcut model is a non-thermal model. While they understandably do not list the results for every region, they report an average plasma temperature of 0.52 keV, and an average ionisation timescale of 1.38×10^{11} cm^{-3} s, both of which agree with our findings in our lower-temperature component. While they examined the entire spectrum from $0.3-8.0$ keV, the emission above 2.0 keV was typically poorly constrained, owing to the small angular sizes of their regions. As a result, they only examined the elements of O, Mg, Si, S, and Fe. Their average abundances for O, Mg, and Si are quite similar to our own; however,

their average S abundance is somewhat higher than our findings, while their Fe abundances are notably lower. The difference in the Fe can be explained by the fact that they primarily looked at the Fe L shell, given the poorly-constrained data in the higher-energy regime. The difference in the abundance of S is more difficult to explain, though similar concerns of energy likely apply. Holland-Ashford et al. (2023), using *Suzaku* data, performed a global fit to the SNR using a model composed of four thermal components and one non-thermal component. They found a hydrogen column density of 0.763×10^{22} cm^{-2}, which lines up with the higher end of our observed range. Their thermal components showed plasma temperatures of 0.405, 0.606, 1.71, and 5.96 keV, with corresponding ionisation timescales of 4.36×10^{11}, 2.52×10^{11}, 5.86×10^{10}, and 3.7×10^{9} $\mathrm{cm}^{-3}\,\mathrm{s}$. The second and fourth of these components align very well with our own findings; as well, these two components are the ones in which they determined the bulk of the emission to be, with the latter being primarily emission from Fe-group elements. As they used a method in which the Si abundance is set to a fixed value, we cannot directly compare abundance values; however, we can make comparisons to abundance ratios. In doing so, we find comparable results for all of our examined elements.

In comparing to models of supernova nucleosynthesis, we find an interesting result: the best-fit model to our results is the D^6 model of T18. This is surprising in that, although the nature of G4.5+6.8's as a thermonuclear supernova is well-established, the formation channel – that is, whether it was the result of a single-degenerate or a double-degenerate explosion – is less well understood. The D^6 model, meanwhile, is notably a model of a double-degenerate scenario, and this finding could help further constrain the origin of an already fairly-well-understood object. However, it must be stressed that the D^6 model does not per-

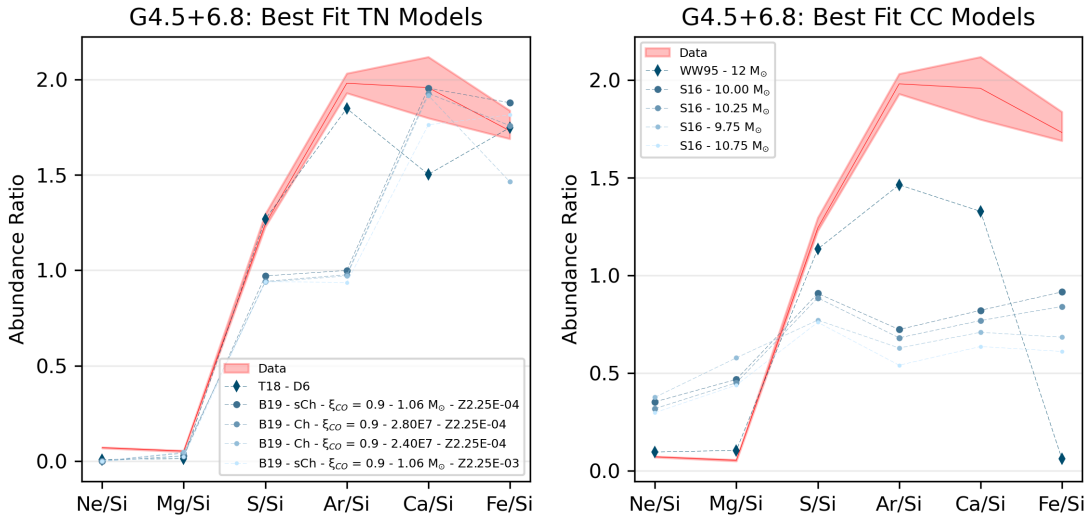

Figure 7.2: Best-fit nucleosynthesis models for G4.5+6.8, comparing to both thermonuclear (TN) and core-collapse (CC) supernova nucleosynthesis yields.

fectly reproduce our findings, as it slightly underproduces the Ar/Si and Ca/Si ratios. Some of the models found in B19 are able to come close to the D[6] model in reproducing our findings, with a higher-density Ch-mass progenitor even besting it in terms of reproducing the observed Ca/Si ratio. However, these models fall slightly short in reproducing the S/Si ratio, and significantly short in reproducing the Ar/Si ratio. For completion's sake, we also examined a core-collapse scenario, where we found the most successful of such models to be the 12 $M_\odot$ model of WW95, which was able to approximately reproduce the Ne/Si, Mg/Si, and S/Si ratios found in our results, with the agreement becoming increasingly poor as one examines the ratios for higher-mass elements. No other core-collapse model was able to reproduce our findings for any ratio, save that of Ne/Si.

Table 7.2: G4.5+6.8: Best fit parameters per region (R00 - R09)

Parameter	R00	R01	R02	R03	R04	R05	R06	R07	R08	R09
N_H ($\times 10^{22}$ cm^{-2})	$0.51^{+0.02}_{-0.02}$	$0.48^{+0.01}_{-0.01}$	$0.50^{+0.01}_{-0.01}$	$0.48^{+0.02}_{-0.01}$	$0.50^{+0.01}_{-0.01}$	$0.56^{+0.01}_{-0.01}$	$0.48^{+0.01}_{-0.01}$	$0.62^{+0.01}_{-0.02}$	$0.52^{+0.01}_{-0.01}$	$0.45^{+0.02}_{-0.01}$
kT_c (keV)	$0.72^{+0.01}_{-0.01}$	$0.71^{+0.01}_{-0.01}$	$0.71^{+0.01}_{-0.01}$	$0.71^{+0.01}_{-0.01}$	$0.71^{+0.01}_{-0.01}$	$0.64^{+0.01}_{-0.01}$	$0.66^{+0.01}_{-0.01}$	$0.56^{+0.01}_{-0.01}$	$0.70^{+0.01}_{-0.01}$	$0.66^{+0.01}_{-0.01}$
Ne	$0.74^{+0.05}_{-0.03}$	$0.37^{+0.05}_{-0.05}$	$0.37^{+0.03}_{-0.05}$	$0.55^{+0.03}_{-0.05}$	$0.28^{+0.01}_{-0.03}$	$0.29^{+0.05}_{-0.03}$	$0.60^{+0.04}_{-0.04}$	$0.22^{+0.03}_{-0.01}$	$0.27^{+0.01}_{-0.01}$	$0.49^{+0.05}_{-0.03}$
Mg	$0.66^{+0.08}_{-0.07}$	0	$0.12^{+0.06}_{-0.05}$	$0.46^{+0.05}_{-0.06}$	$0.04^{+0.02}_{-0.04}$	$0.01^{+0.07}_{-0.01}$	$0.32^{+0.05}_{-0.06}$	$0.01^{+0.02}_{-0.01}$	$0.09^{+0.06}_{-0.05}$	$0.51^{+0.02}_{-0.08}$
Si	$4.10^{+0.13}_{-0.15}$	$5.53^{+0.25}_{-0.17}$	$5.12^{+0.15}_{-0.21}$	$4.45^{+0.14}_{-0.16}$	$5.08^{+0.18}_{-0.18}$	$6.73^{+0.23}_{-0.13}$	$4.99^{+0.16}_{-0.16}$	$5.60^{+0.22}_{-0.19}$	$6.52^{+0.30}_{-0.13}$	$6.18^{+0.07}_{-0.26}$
S	$5.02^{+0.23}_{-0.20}$	$7.57^{+0.30}_{-0.30}$	$6.71^{+0.21}_{-0.28}$	$5.15^{+0.18}_{-0.24}$	$7.42^{+0.24}_{-0.35}$	$8.63^{+0.37}_{-0.24}$	$5.55^{+0.19}_{-0.24}$	$7.40^{+0.35}_{-0.21}$	$8.74^{+0.42}_{-0.18}$	$7.83^{+0.26}_{-0.33}$
Ar	$7.64^{+0.68}_{-0.81}$	$11.5^{+0.9}_{-1.0}$	$9.66^{+0.85}_{-0.85}$	$7.41^{+0.50}_{-0.69}$	$10.9^{+0.7}_{-0.9}$	$12.5^{+1.0}_{-1.0}$	$6.94^{+0.75}_{-0.98}$	$12.8^{+0.3}_{-1.8}$	$15.0^{+1.1}_{-1.0}$	$11.2^{+1.3}_{-1.4}$
τ_c ($\times 10^{11}$ s cm^{-3})	$2.08^{+0.16}_{-0.13}$	$2.69^{+0.12}_{-0.25}$	$2.39^{+0.23}_{-0.14}$	$1.96^{+0.10}_{-0.13}$	$3.09^{+0.15}_{-0.34}$	$2.93^{+0.24}_{-0.22}$	$2.45^{+0.19}_{-0.13}$	$2.83^{+0.93}_{-0.14}$	$2.30^{+0.24}_{-0.10}$	$2.02^{+0.13}_{-0.14}$
kT_h (keV)	$5.36^{+0.82}_{-0.54}$	$10.8^{+0.9}_{-1.0}$	$9.33^{+0.57}_{-0.54}$	$6.18^{+0.33}_{-0.78}$	$10.2^{+0.4}_{-1.}$	$5.34^{+0.26}_{-0.31}$	$6.70^{+0.75}_{-0.78}$	$4.46^{+0.30}_{-0.31}$	$10.9^{+2.4}_{-0.7}$	$4.88^{+0.17}_{-0.42}$
Ca	$9.05^{+1.55}_{-3.06}$	$17.4^{+3.2}_{-5.0}$	$17.3^{+3.2}_{-3.7}$	$12.3^{+3.6}_{-3.3}$	$21.8^{+4.1}_{-4.8}$	$10.8^{+4.4}_{-4.0}$	$8.51^{+4.26}_{-3.46}$	$9.51^{+3.62}_{-2.72}$	$15.5^{+2.4}_{-3.4}$	$10.6^{+5.3}_{-7.5}$
Fe	$7.35^{+0.85}_{-0.99}$	$8.71^{+0.74}_{-0.52}$	$7.05^{+0.58}_{-0.36}$	$10.2^{+1.9}_{-0.6}$	$9.61^{+0.69}_{-0.31}$	$13.2^{+1.2}_{-0.8}$	$7.22^{+1.02}_{-0.73}$	$15.9^{+1.6}_{-1.3}$	$4.45^{+0.22}_{-0.51}$	$25.1^{+2.1}_{-2.2}$
τ_h ($\times 10^{9}$ s cm^{-3})	$4.65^{+0.39}_{-0.32+08}$	$6.99^{+0.22}_{-0.29}$	$6.50^{+0.29}_{-0.31}$	$4.60^{+0.16}_{-0.34}$	$6.69^{+0.11}_{-0.33}$	$4.37^{+0.11}_{-0.15}$	$4.41^{+0.28}_{-0.27}$	$3.74^{+0.06}_{-0.22}$	$6.01^{+0.58}_{-0.19}$	$3.58^{+0.08}_{-0.18}$
Redshift (10^{-3})	$-3.96^{+0.03}_{-0.06}$	$-1.77^{+0.04}_{(-0.03}$	$-4.03^{+0.05}_{-0.01}$	$-2.98^{+0.01}_{-0.02}$	$-2.97^{+0.07}_{-0.02}$	$-1.77^{+0.04}_{-0.02}$	$-1.77^{+0.07}_{-0.02}$	$-2.97^{+0.06}_{-0.02}$	$-1.77^{+0.15}_{-0.01}$	$2.45^{+0.13}_{-0.01}$
Line Centroid (keV)	$1.21^{+0.01}_{-0.01}$	$1.21^{+0.01}_{-0.01}$	$1.22^{+0.01}_{-0.01}$	$1.20^{+0.01}_{-0.01}$	$1.21^{+0.01}_{-0.01}$	$1.18^{+0.00}_{-0.01}$	$1.20^{+0.01}_{-0.01}$	$1.20^{+0.01}_{-0.01}$	$1.20^{+0.01}_{-0.01}$	$1.14^{+0.01}_{0.00}$
χ^2_ν (DoF)	1.44 (1126)	1.89 (1172)	1.72 (1172)	1.46 (1113)	1.83 (1188)	1.89 (1181)	1.59 (1151)	1.88 (1196)	1.73 (1240)	1.71 (1102)

Table 7.3: G4.5+6.8: Best fit parameters per region (R10 - R17)

Parameter	R10	R11	R12	R13	R14	R15	R16	R17
N_H ($\times 10^{22}$ cm^{-2})	$0.44^{+0.03}_{-0.01}$	$0.55^{+0.02}_{-0.01}$	$0.53^{+0.01}_{-0.01}$	$0.56^{+0.01}_{-0.01}$	$0.44^{+0.01}_{-0.01}$	$0.64^{+0.02}_{-0.02}$	$0.76^{+0.01}_{-0.01}$	$0.59^{+0.01}_{-0.01}$
kT_c (keV)	$0.68^{+0.00}_{-0.01}$	$0.57^{+0.01}_{-0.01}$	$0.60^{+0.01}_{-0.01}$	$0.58^{+0.01}_{-0.01}$	$0.51^{+0.00}_{-0.01}$	$0.61^{+1.27}_{-0.01}$	$0.41^{+0.01}_{-0.01}$	$0.51^{+0.00}_{-0.01}$
Ne	$0.53^{+0.01}_{+0.01}$	$0.31^{+0.01}_{-0.06}$	$0.54^{+0.04}_{-0.04}$	$0.35^{+0.05}_{-0.04}$	$0.15^{+0.01}_{-0.01}$	$0.39^{+0.04}_{-0.19}$	$0.06^{+0.02}_{-0.03}$	$0.29^{+0.04}_{-0.07}$
Mg	$0.62^{+0.05}_{-0.05}$	$0.01^{+0.03}_{-0.01}$	$0.32^{+0.04}_{-0.06}$	$0.22^{+0.04}_{-0.11}$	$0.39^{+0.03}_{-0.03}$	$0.39^{+0.05}_{-0.36}$	$0.07^{+0.01}_{-0.04}$	$0.16^{+0.07}_{-0.04}$
Si	$4.46^{+0.14}_{-0.14}$	$6.18^{+0.04}_{-0.26}$	$6.13^{+0.15}_{-0.23}$	$6.90^{+0.21}_{-0.22}$	$8.05^{+0.33}_{-0.15}$	$5.53^{+1.15}_{-0.04}$	$8.19^{+0.22}_{-0.23}$	$7.93^{+0.36}_{-0.29}$
S	$5.14^{+0.24}_{-0.22}$	$7.12^{+0.09}_{-0.31}$	$5.87^{+0.27}_{-0.27}$	$8.92^{+0.39}_{-0.31}$	$9.82^{+0.69}_{-0.31}$	$7.16^{+4.76}_{-0.14}$	$11.2^{+0.6}_{-0.5}$	$9.07^{+0.62}_{-0.25}$
Ar	$7.24^{+1.03}_{-0.95}$	$8.78^{+0.77}_{-0.51}$	$6.40^{+0.75}_{-1.04}$	$14.2^{+1.6}_{-1.4}$	$20.0^{+1.7}_{-1.6}$	$12.1^{+1.2}_{-1.6}$	$32.8^{+2.2}_{-2.5}$	$13.1^{+1.7}_{-2.2}$
τ_c ($\times 10^{11}$ s cm^{-3})	$1.71^{+0.92}_{-0.91}$	$4.05^{+0.02}_{-0.91}$	$2.69^{+0.25}_{-0.12}$	$3.40^{+0.32}_{-0.33}$	$20.6^{+4.16}_{-4.65}$	$2.66^{+0.56}_{-2.49}$	$53.5^{+41.7}_{-29.3}$	$5.16^{+1.46}_{-0.64}$
kT_h (keV)	$5.26^{+0.20}_{-1.15}$	$5.57^{+0.05}_{-0.67}$	$4.61^{+0.28}_{-0.35}$	$4.32^{+0.50}_{-0.10}$	$17.5^{+1.2}_{-0.8}$	$5.00^{+0.50}_{-2.51}$	$4.40^{+0.06}_{-0.02}$	$3.64^{+0.17}_{-0.19}$
Ca	$12.4^{+7.0}_{-4.0}$	$7.29^{+2.28}_{-3.92}$	$9.00^{+4.60}_{-3.84}$	$8.99^{+4.14}_{-5.13}$	$6.59^{+0.33}_{-0.25}$	$11.03^{+2.63}_{-2.71}$	$10.8^{+1.1}_{-2.9}$	$6.00^{+2.61}_{-4.20}$
Fe	$12.4^{+5.3}_{-0.5}$	$9.90^{+1.03}_{-0.56}$	$12.5^{+1.8}_{-0.8}$	$12.6^{+0.9}_{-2.4}$	$2.65^{+0.18}_{-0.15}$	$4.52^{+6.66}_{-0.13}$	$5.28^{+0.21}_{-0.39}$	$13.2^{+1.0}_{-1.1}$
τ_h ($\times 10^{9}$ s cm^{-3})	$3.63^{+0.05}_{-0.49}$	$3.88^{+0.03}_{-0.25}$	$3.66^{+0.08}_{-0.20}$	$3.50^{+0.26}_{-0.08}$	$19.9^{+0.57}_{-0.62}$	$4.17E^{+0.19}_{-0.20}$	$3.16^{+0.10}_{-0.03}$	$3.14^{+0.09}_{-0.08}$
Redshift (10^{-3})	$1.06^{+0.01}_{-0.01}$	$-1.78^{+0.01}_{-0.03}$	$-1.76^{+0.05}_{-0.01}$	$1.15^{+0.03}_{-0.09}$	$1.16^{+0.23}_{-0.16}$	$-3.00^{+0.02}_{-0.01}$	$-2.34^{+0.01}_{-0.05}$	$-2.28^{+0.21}_{-0.01}$
Line Centroid (keV)	$1.14^{+0.01}_{-0.01}$	$1.18^{+0.01}_{0.01}$	$1.18^{+0.01}_{-0.01}$	$1.16^{+0.02}_{-0.01}$	$1.19^{+0.00}_{-0.01}$	$1.22^{+0.04}_{-0.01}$	$1.22^{+0.01}_{0.00}$	$1.15^{+0.01}_{-0.01}$
χ^2_ν (DoF)	1.69 (1101)	2.32 (1249)	1.87 (1166)	1.70 (1206)	1.88 (1205)	1.60 (1306)	1.84 (1426)	1.81 (1245)

7.3 G41.1−0.3

The analysis of G41.1−0.3 (3C 397) made use of four observations, taken from two separate epochs: observation IDs 0085200301, 0085200401, and 0085200501 were taken in 2004 for a total of roughly 60 ks, while the much longer observation ID 0830450101 was taken in 2018 for a total of 140 ks. The *contbin* algorithm was applied to the combined MOS1 and MOS2 observations, which resulting in the generation of 17 regions from which spectra were extracted. All regions were tested with all one- and two-component combinations of the VPSHOCK, VNEI, VRNEI, and VAPEC models, multiplied by a TBABS absorption component. We found that an absorbed two-component VNEI+VAPEC model most consistently produced the best fits across all regions. With this model chosen, we initially allowed the column density, plasma temperatures, normalisation constants, and ionisation timescales to vary freely, and were fit simultaneously. Then, we freed the elemental abundances for S, Fe (with Ni tied to Fe), Ar, and Ca in the hot component, followed by Si and Mg in the cold component, one at a time and fit. For some regions, the abundance of Ca became strikingly nonphysical when allowed to vary; for these regions, we instead froze this abundance to solar.

The results of our spectral fits for G41.1−0.3 can be seen in Tables 7.4 and 7.5. Each region was well fit (χ^2_ν<1.4) with the VNEI+VAPEC model described above. The column density ranged from $3.83 - 4.53 \times 10^{22}$ cm^{-2}, with the lowest column densities being associated with the north-eastern portions of the SNR and the highest column densities being associated with the interior regions in the SNR's western half. Temperatures for the hot component, associated with the VNEI model, range from $1.74 - 2.63$ keV, with a distribution somewhat opposite that of the column density, with the highest temperatures appearing in

the north-eastern portions of the SNR. The ionisation timescale in the hot component was fairly consistent, ranging between $3.81 - 15.5 \times 10^{10}$ cm^{-3} s, suggesting that the SNR is still in a state of NEI. The soft component, associated with the VAPEC model, displayed temperatures that range from $0.19 - 0.29$ keV, with the higher temperatures being associated with the northern portions of the SNR. The abundances of Mg, Si, S, Ar, Ca, and Fe within the SNR were enhanced above solar values except for Mg, which was subsolar in all cases. Most of these abundances appear to be highest in the eastern half of the SNR; Mg is an exception, in that it appears more concentrated in the western half of the SNR.

There are two previous studies to which we can compare our results. The first is a *Chandra* study by Safi-Harb et al. (2005). This was a spatially-resolved study in which an absorbed two-component VPSHOCK+VPSHOCK model was used. They found column densities between $2.27 - 4.10 \times 10^{22}$ cm^{-2}, hot component temperatures between $1.4 - 3.4$ keV, and cold component temperatures between $0.15 - 0.26$ keV, depending on which region, which are comparable to our results. They also found subsolar abundances for Mg, near-solar abundances for Si, enhanced abundances of S and Ca, and significantly enhanced abundances of Fe, all of which agree with our findings. The second study is from Martínez-Rodríguez et al. (2020), which looked at *Suzaku* data. They performed a global fit of the SNR using an absorbed three-component VVNEI+VNEI+NEI model, using the solar abundances from Wilms et al. (2000). They determined a column density of 3.49×10^{22} cm^{-2}, and a hottest component temperature of 1.89 keV, both slightly lower than our own. They did, however, find a cold component temperature of 0.22 keV, which matches our findings. Additionally, they found generally enhanced abundances for Si, S, Ar, and Ca, and significantly enhanced iron-group abundances, with the enhanced abundances being present in their higher-

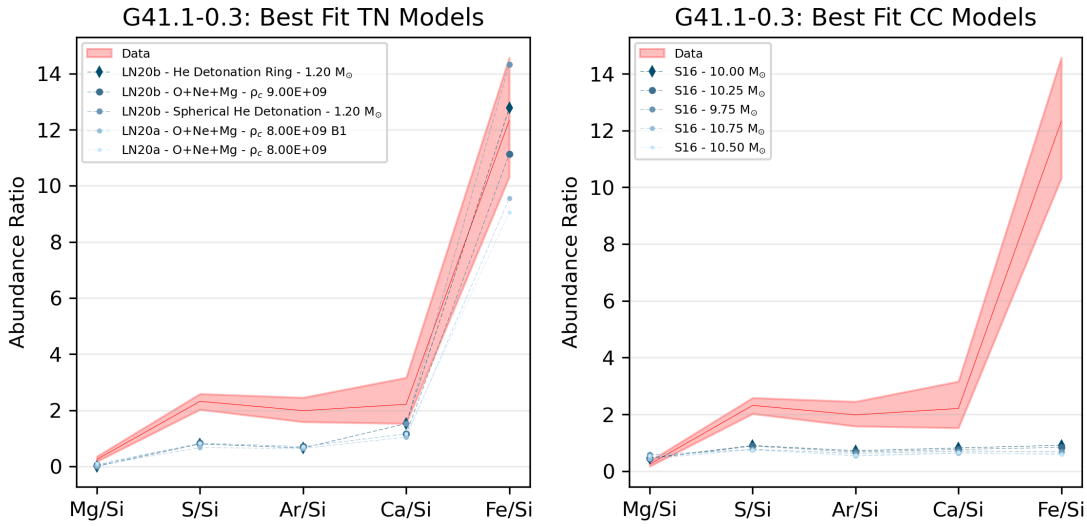

Figure 7.3: Best-fit nucleosynthesis models for G41.1−0.3, comparing to both thermonuclear (TN) and core-collapse (CC) supernova nucleosynthesis yields.

temperature components, all of which matches our results quite well.

In comparing to the nucleosynthesis models, we find that while no one model is capable of reproducing our results, the thermonuclear models fare significantly better at doing so than the core-collapse models. This is largely due to the particularly high Fe/Si ratio found in the SNR: only a few thermonuclear models are capable of reproducing this, with the best results coming from the He detonation and O+Ne+Mg WD models of LN20b. The Mg/Si ratio is reasonably well fit for most of the models tested, with the core-collapse models tending to produce slightly higher abundances than observed. The S/Si ratio is not well reproduced by any model, while the Ar/Si ratio only manages to be reproduced by the D^6 model of T18, although the 11 $M_\odot$ model of WW95 comes quite close. The Ca/Si ratio is well reproduced by a number of thermonuclear models: the models which can reproduce the Fe/Si ratio can also reproduce the Ca/Si ratio, and several of the models found in B19 can do so as well.

Table 7.4: G41.1−0.3: Best fit parameters per region (R00 - R09)

Parameter	R00	R01	R02	R03	R04	R05	R06	R07	R08	R09
N_H ($\times 10^{22}$ cm^{-2})	$4.18^{+0.06}_{-0.02}$	$4.32^{+0.03}_{-0.04}$	$4.33^{+0.04}_{-0.06}$	$4.39^{+0.02}_{-0.02}$	$4.53^{+0.04}_{-0.07}$	$3.99^{+0.03}_{-0.02}$	$3.96^{+0.07}_{-0.09}$	$4.45^{+0.04}_{-0.03}$	$4.26^{+0.04}_{-0.03}$	$4.22^{+0.27}_{-0.32}$
kT_c (keV)	$0.22^{+0.01}_{-0.01}$	$0.20^{+0.01}_{-0.01}$	$0.22^{+0.01}_{-0.01}$	$0.19^{+0.01}_{-0.001}$	$0.19^{+0.01}_{-0.01}$	$0.22^{+0.01}_{-0.01}$	$0.29^{+0.02}_{-0.01}$	$0.20^{+0.01}_{-0.01}$	$0.20^{+0.01}_{-0.01}$	$0.26^{+0.10}_{-0.09}$
Mg	$0.37^{+0.02}_{-0.06}$	$0.39^{+0.04}_{-0.08}$	$0.40^{+0.07}_{-0.03}$	$0.36^{+0.02}_{-0.05}$	$0.34^{+0.03}_{-0.06}$	$0.25^{+0.04}_{-0.06}$	$0.48^{+0.18}_{-0.08}$	$0.38^{+0.04}_{-0.03}$	$0.17^{+0.07}_{-0.04}$	$0.53^{+0.46}_{-0.32}$
Si	$1.24^{+0.07}_{-0.09}$	$1.53^{+0.08}_{-0.09}$	$1.35^{+0.06}_{-0.10}$	$1.42^{+0.07}_{-0.05}$	$1.32^{+0.10}_{-0.14}$	$1.07^{+0.14}_{-0.05}$	$0.99^{+0.10}_{-0.02}$	$1.28^{+0.08}_{-0.11}$	$1.44^{+0.10}_{-0.12}$	$1.29^{+0.02}_{-0.16}$
kT_h (keV)	$2.25^{+0.07}_{-0.14}$	$1.96^{+0.07}_{-0.06}$	$2.12^{+0.08}_{-0.04}$	$2.10^{+0.04}_{-0.06}$	$2.33^{+0.06}_{-0.12}$	$2.33^{+0.03}_{-0.11}$	$2.28^{+0.01}_{-0.08}$	$1.95^{+0.03}_{-0.05}$	$2.37^{+0.11}_{-0.03}$	$2.17^{+0.01}_{-0.13}$
S	$2.87^{+0.26}_{-0.22}$	$3.09^{+0.16}_{-0.21}$	$2.90^{+0.25}_{-0.14}$	$2.93^{+0.25}_{-0.19}$	$2.93^{+0.14}_{-0.08}$	$3.29^{+0.25}_{-0.29}$	$2.69^{+0.10}_{-0.48}$	$2.30^{+0.11}_{-0.17}$	$3.52^{+0.21}_{-0.23}$	$2.94^{+0.32}_{-0.67}$
Ar	$2.95^{+0.30}_{-0.70}$	$2.53^{+0.27}_{-0.34}$	$2.27^{+0.51}_{-0.54}$	$2.27^{+0.42}_{-0.33}$	$2.17^{+0.31}_{-0.30}$	$3.15^{+0.72}_{-0.60}$	$3.16^{+0.43}_{-0.50}$	$2.02^{+0.49}_{-0.36}$	$2.66^{+0.64}_{-0.51}$	$2.71^{+1.00}_{-0.09}$
Ca	-	$2.72^{+0.53}_{-1.32}$	$2.61^{+1.02}_{-0.57}$	$3.60^{+0.88}_{-0.82}$	$2.40^{+0.97}_{-0.67}$	$3.38^{+1.83}_{-1.98}$	$4.79^{+1.47}_{-0.91}$	$1.79^{+0.41}_{-0.31}$	$3.44^{+1.08}_{-0.54}$	$3.53^{+2.53}_{-0.48}$
Fe	$12.3^{+1.8}_{-1.0}$	$14.2^{+1.9}_{-1.7}$	$11.8^{+1.3}_{-1.6}$	$12.6^{+1.0}_{-0.5}$	$9.95^{+1.94}_{-0.85}$	$14.7^{+3.1}_{-1.7}$	$17.3^{+1.3}_{-1.7}$	$9.63^{+0.79}_{-0.55}$	$22.5^{+2.2}_{-3.7}$	$12.4^{+4.5}_{-2.3}$
τ_h ($\times 10^{10}$ s cm^{-3})	$5.80^{+0.01}_{-0.01}$	$6.18^{+0.01}_{-0.01}$	$6.70^{+0.01}_{-0.01}$	$7.54^{+0.01}_{-0.01}$	$7.53^{+0.01}_{-0.01}$	$6.87^{+0.01}_{-0.01}$	$6.23^{+0.60}_{-0.60}$	$11.2^{+0.01}_{-0.01}$	$4.48^{+0.01}_{-0.01}$	$6.83^{+2.18}_{-2.18}$
χ^2_ν (DoF)	1.17 (2199)	1.24 (1976)	1.15 (1974)	1.25 (2132)	1.18 (1822)	1.18 (1735)	1.28 (2087)	1.16 (2237)	1.14 (2156)	1.24 (2044)

Table 7.5: G41.1–0.3: Best fit parameters per region (R10 - R16)

Parameter	R10	R11	R12	R13	R14	R15	R16
N_H ($\times 10^{22}$ cm^{-2})	$3.94^{+0.02}_{-0.03}$	$4.31^{+0.03}_{-0.04}$	$3.83^{+0.03}_{-0.04}$	$3.84^{+0.05}_{-0.04}$	$4.26^{+0.04}_{-0.08}$	$4.36^{+0.03}_{-0.03}$	$4.03^{+0.02}_{-0.02}$
kT_c (keV)	$0.20^{+0.01}_{-0.01}$	$0.20^{+0.01}_{-0.01}$	$0.24^{+0.01}_{-0.01}$	$0.20^{+0.01}_{-0.01}$	$0.24^{+0.01}_{-0.01}$	$0.22^{+0.01}_{-0.01}$	$0.19^{+0.01}_{-0.01}$
Mg	$0.14^{+0.05}_{-0.05}$	$0.19^{+0.05}_{-0.02}$	$0.56^{+0.06}_{-0.01}$	$0.12^{+0.06}_{-0.06}$	$0.38^{+0.09}_{-0.08}$	$0.29^{+0.06}_{-0.04}$	$0.06^{+0.05}_{-0.05}$
Si	$1.34^{+0.13}_{-0.08}$	$1.19^{+0.08}_{-0.04}$	$1.37^{+0.16}_{-0.06}$	$1.60^{+0.14}_{-0.13}$	$1.43^{+0.07}_{-0.13}$	$1.24^{+0.07}_{-0.08}$	$1.32^{+0.11}_{-0.08}$
kT_h (keV)	$2.63^{+0.16}_{-0.12}$	$2.26^{+0.09}_{-0.04}$	$1.85^{+0.08}_{-0.06}$	$2.58^{+0.10}_{-0.11}$	$1.74^{+0.08}_{-0.02}$	$1.92^{+0.07}_{-0.06}$	$2.28^{+0.02}_{-0.08}$
S	$4.68^{+0.46}_{-0.33}$	$2.97^{+0.17}_{-0.21}$	$2.25^{+0.23}_{-0.14}$	$4.31^{+0.28}_{-0.65}$	$2.07^{+0.25}_{-0.24}$	$2.59^{+0.07}_{-0.09}$	$3.24^{+0.26}_{-0.18}$
Ar	$3.46^{+0.87}_{-0.81}$	$2.66^{+0.21}_{-0.46}$	$2.31^{+0.43}_{-0.27}$	$2.06^{+0.94}_{-0.85}$	$1.91^{+0.28}_{-0.37}$	$2.14^{+0.08}_{-0.30}$	$3.00^{+0.70}_{-0.28}$
Ca	$6.26^{+0.98}_{-0.88}$	$3.53^{+0.78}_{-0.76}$	$1.58^{+0.37}_{-0.58}$	-	$1.78^{+1.36}_{-0.84}$	$2.17^{+0.33}_{-0.40}$	$2.33^{+1.50}_{-0.29}$
Fe	$35.0^{+3.9}_{-3.5}$	$16.5^{+1.1}_{-1.6}$	$4.71^{+0.63}_{-0.69}$	$39.2^{+5.0}_{-7.9}$	$7.11^{+0.70}_{-0.94}$	$9.10^{+0.59}_{-0.80}$	$27.7^{+3.9}_{-1.0}$
τ_h ($\times 10^{10}$ s cm^{-3})	$4.21^{+0.01}_{-0.01}$	$5.34^{+0.01}_{-0.01}$	$15.5^{+0.01}_{-0.01}$	$3.81^{+0.01}_{-0.01}$	$8.03^{+0.01}_{-0.01}$	$8.82^{+0.01}_{-0.01}$	$4.49^{+0.01}_{-0.01}$
χ^2_ν (DoF)	1.14 (1943)	1.19 (2383)	1.31 (1938)	1.17 (1561)	1.21 (1697)	1.28 (2735)	1.19 (2340)

7.4 G43.3–0.2

For G43.3–0.2 (W49B), four observations across two epochs were used in our analysis: the observation IDs 0084100401 and 0084100501, from 2004; and the observation IDs 0724270101 and 0724270201, from 2014. All four observations combine to produce an exposure time of approximately 227 ks to which the *contbin* algorithm was applied, producing 19 regions. When fitting these regions, all one- and two-component combinations of the VPSHOCK, VNEI, VAPEC, and VRNEI models were tested, multiplied by a TBABS absorption component. It was determined that a two-component VAPEC+VRNEI model produced the best average fits across all regions. While fitting with this model, we initially allowed the column density, plasma temperatures, ionisation timescales, and normalisation constants were allowed to vary freely. After a preliminary fit to determine these parameters, the abundance values for the elements Si, S, Fe, Ar, Ca, Ni, and Mg were freed one at a time and allowed to vary. We initially attempted to tie the abundance of Ni to that of Fe; however, we found that the fits significantly improved when Ni was allowed to vary independently. In a few case, the abundance of some elements took on a nonphysical value following a fit; in such cases, the element in question was instead frozen to solar abundances.

The results of our spectral fits can be seen in Tables 7.6 and 7.7. Each region is well fit (χ^2_ν<1.25) with the VRNEI+VAPEC model described above. We find that the column density is quite high across the SNR, with values ranging from 4.88×10^{22} cm^{-2} to 10.33×10^{22} cm^{-2}, with the outer portions of the SNR displaying lower column densities on average. Temperatures for the hot component, associated with the VRNEI model, range from $0.64 - 1.65$ keV, with the north-eastern portions of the SNR displaying the highest values

thereof. Temperatures for the cold component, associated with the VAPEC model, showed a smaller range of variation, from $0.18 - 0.32$ keV. The lower temperatures emerge in the SNR's interior – particularly, in the western half of the SNR – while the higher temperatures appear in the outer portions of the SNR. The abundances within the SNR – those of Mg, Si, S, Ar, Ca, and Fe – were all consistently enhanced above solar values, with all of these abundances appearing highest in the north-eastern portion of the SNR.

We can compare our results to several previous studies. One such study is that of Keohane et al. (2007), in which *Chandra* data was used to perform a spatially resolved study of the SNR. An absorbed, single temperature VMEKAL model was used, yielding a global column density of 5.18×10^{22} cm^{-2} – slightly lower than our average value, but comparable to that found in some of our spectroscopic regions – and a plasma temperature of 1.58 keV. Enhanced abundances for Si, S, Ar, Ca, Fe, and Ni were found, in agreement with our findings. Lopez et al. (2013), using *Chandra* data, fit 136 small-scale regions using an absorbed single-component CIE model with the solar abundances of Asplund et al. (2009). They found values for N_H in the range of $4 - 12 \times 10^{22}$ cm^{-2} and kT from $0.7 - 2.5$ keV, both of which are wider ranges than our findings, but are not dissimilar. Though they did not report abundance values for each region of their analysis, they did report the average values, which we find to be notably lower than our findings, albeit with similar ratios between elements. Zhou & Vink (2018) similarly used *Chandra* data and the solar abundances of Asplund et al. (2009) to fit an absorbed VRNEI+VAPEC model to a selection of 177 arcsecond-scale regions. For this, they froze the value of N_H to 8×10^{22} cm^{-2}, which yielded values for kT_h between 0.7 and 2.2 keV, a mean value for kT_c of 0.27 keV, and ionization timescales ranging between $1 - 10 \times 10^{11}$ s cm^{-3}. They too found lower average abundances values for Si, S, Ar, Ca,

and Fe than our findings; the ratios between most of these elements were similar than ours, with the notable exception of Si, which appears lower relative to the other elements in their findings than in ours.

We can also compare our results to those of Holland-Ashford et al. (2020), who used *XMM-Newton* data, the solar abundances of Asplund et al. (2009), and a spatially-resolved binning method in which the SNR was divided into 46 regions of equal size. They fit these regions using an absorbed three-component model, resulting in either a VAPEC+VVRNEI+ VVRNEI or VAPEC+VVAPEC+VVRNEI model, dependent on the region in question. They found a range of column densities between $7.2 - 8.5 \times 10^{22}$ cm^{-2}, which is close to our findings. The plasma temperature for the APEC component averaged 0.18 keV, with little variation across the remnant, while the plasma temperatures for their hotter components ranged between $0.31 - 0.76$ keV and $0.87 - 1.62$ keV for the VVAPEC/VVRNEI and VVRNEI component, respectively. The abundances reported are quite similar to our own findings, with theirs being slightly higher on average. Finally, we can compare to Siegel et al. (2020), an *XMM-Newton* study using observation ID 0724270101. The authors used a smoothed particle inference (SPI) technique to study the entire SNR, using two models: an absorbed VMEKAL model with two temperatures components, as well as an absorbed VRNEI+APEC model. Both were reported in terms of the solar abundances reported in Anders & Grevesse (1989). The authors reported a column density and plasma temperature of 7.0×10^{22} cm^{-2} and 0.98 keV, respectively, both of which are notably lower than our findings. However, they also reported enhanced abundances of Si, S, Ar, Ca, Fe, and Ni, with Ni being poorly constrained, all of which were comparable to our results.

Comparing to the nucleosynthesis models, while we find that no tested models are able to

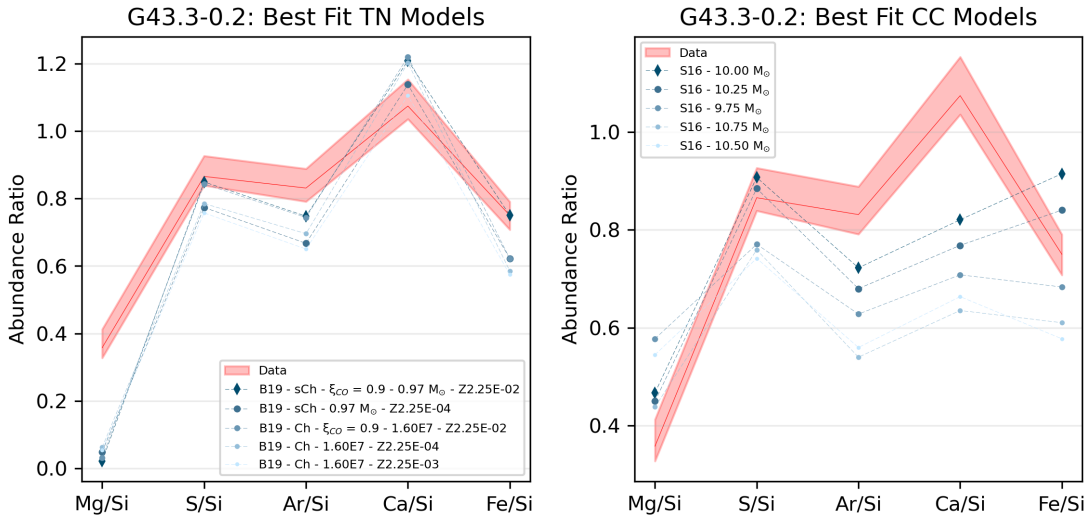

Figure 7.4: Best-fit nucleosynthesis models for G43.3−0.2, comparing to both thermonuclear (TN) and core-collapse (CC) supernova nucleosynthesis yields.

fully recreate the data, we do find close agreement between our data and several models. We find that the Mg/Si ratio cannot be reproduced by any of the tested thermonuclear models, all of which produce less Mg than found. Core-collapse models, comparatively, tend to produce larger amounts of Mg, resulting in a greater agreement with our results, with models such as the WW95 13 $M_\odot$ or 25 $M_\odot$, or the S16 20.5 $M_\odot$ or 26.0 $M_\odot$ being able to reproduce our findings. The S/Si and Ar/Si ratios can be accurately reproduced through a variety of both thermonuclear and core-collapse models, while the Ca/Si and Fe/Si ratios are generally only able to be reproduced by thermonuclear models, as the core-collapse models tend to produce too little of these elements. Overall, the best fit is achieved by the 10.0 $M_\odot$ model of S16; that being said, the abundance pattern much more closely resembles those observed in thermonuclear models, for which the best fit is achieved by a 0.97 $M_\odot$ progenitor of B19, with $\xi_{CO} = 0.9$. However, mass estimations place the total ejecta mass within the SNR

at at least $\sim 1.28\ M_\odot$, which is of course incompatible with a $0.97\ M_\odot$ progenitor. We thus suggest that the most likely progenitor for this SNR is a Ch-mass progenitor with a low DDT density and a moderate metallicity.

Table 7.6: G43.3−0.2: Best fit parameters per region (R00 - R09)

Parameter	R00	R01	R02	R03	R04	R05	R06	R07	R08	R09
N_H ($\times 10^{22}$ cm^{-2})	$6.95^{+0.05}_{-0.16}$	$9.68^{+0.30}_{-0.11}$	$9.33^{+0.01}_{-0.04}$	$10.15^{+0.06}_{-2.19}$	$10.33^{+0.01}_{-0.01}$	$9.48^{+0.17}_{-0.13}$	$10.14^{+0.07}_{-0.22}$	$9.81^{+0.15}_{-0.07}$	$9.44^{+0.13}_{-0.17}$	$9.68^{+0.01}_{-0.33}$
kT_c (keV)	$0.18^{+0.01}_{0.01}$	$0.18^{+0.01}_{-0.01}$	$0.20^{+0.01}_{-0.01}$	$0.18^{+0.01}_{-0.01}$	$0.16^{+0.01}_{-0.01}$	$0.17^{+0.01}_{-0.01}$	$0.17^{+0.01}_{-0.01}$	$0.18^{+0.01}_{-0.01}$	$0.19^{+0.01}_{-0.01}$	$0.17^{+23.99}_{-0.01}$
kT_h (keV)	$1.63^{+0.06}_{-0.01}$	$1.48^{+0.01}_{-0.08}$	$1.56^{+0.40}_{-0.01}$	$1.65^{+0.51}_{-0.01}$	$1.07^{+0.01}_{-0.01}$	$0.90^{+0.04}_{-0.03}$	$0.94^{+0.02}_{-0.04}$	$1.58^{+0.01}_{-0.04}$	$1.15^{+0.04}_{-0.04}$	$0.81^{+0.06}_{-0.04}$
Mg	$7.66^{+4.22}_{-2.00}$	-	-	$9.12^{+5.93}_{-0.03}$	$7.10^{+0.01}_{-0.01}$	$4.56^{+3.05}_{-1.39}$	-	$4.22^{+2.74}_{-1.50}$	-	$2.96^{+7.19}_{-2.90}$
Si	$9.23^{+1.27}_{-0.60}$	$9.06^{+1.74}_{-0.26}$	$12.9^{+3.0}_{-0.1}$	$12.7^{+0.1}_{-5.4}$	$9.87^{+0.01}_{-0.01}$	$14.1^{+2.0}_{-0.3}$	$10.7^{+1.1}_{-0.5}$	$11.0^{+1.4}_{-0.2}$	$10.6^{+1.3}_{-0.9}$	$12.6^{+7.1}_{-2.9}$
S	$9.03^{+1.08}_{-0.58}$	$6.61^{+1.18}_{-0.10}$	$10.3^{+0.6}_{-0.1}$	$8.90^{+3.84}_{-0.01}$	$6.83^{+0.01}_{-0.02}$	$11.8^{+1.3}_{-0.5}$	$8.69^{+0.82}_{-0.30}$	$7.59^{+0.81}_{-0.11}$	$8.54^{+0.91}_{-0.54}$	$10.2^{+7.4}_{-0.4}$
Ar	$6.74^{+0.58}_{-0.57}$	$5.58^{+0.95}_{-0.21}$	$8.78^{+0.01}_{-0.36}$	$7.62^{+0.01}_{-6.30}$	$6.63^{+0.02}_{-0.02}$	$13.2^{+1.4}_{-1.0}$	$8.18^{+1.47}_{-0.07}$	$5.59^{+1.09}_{-0.16}$	$8.31^{+0.96}_{-0.84}$	$10.4^{+6.5}_{-3.4}$
Ca	$9.74^{+1.09}_{-0.66}$	$9.11^{+1.79}_{-0.32}$	$12.0^{+0.1}_{-0.3}$	$11.1^{+9.1}_{-0.1}$	$9.71^{+0.01}_{-0.01}$	$15.9^{+2.0}_{-0.6}$	$11.0^{+1.9}_{-0.1}$	$9.30^{+1.00}_{-0.20}$	$12.0^{+1.3}_{-1.1}$	$13.4^{+8.3}_{-3.9}$
Fe	$10.4^{+1.1}_{-0.8}$	$12.6^{+1.8}_{-0.4}$	$16.1^{+0.1}_{-4.3}$	$12.9^{+0.1}_{-6.9}$	$4.55^{+0.01}_{-0.01}$	$8.69^{+1.38}_{-0.76}$	$7.22^{+1.13}_{-0.61}$	$10.3^{+0.9}_{-0.2}$	$9.40^{+1.81}_{-0.91}$	$6.09^{+3.82}_{-2.93}$
Ni	$32.5^{+9.32}_{-4.8}$	$40.9^{+17.0}_{-5.2}$	$66.5^{+0.4}_{-64.4}$	$31.4^{+10.3}_{-0.2}$	$11.4^{+0.1}_{-0.1}$	$25.8^{+9.1}_{-5.1}$	$23.1^{+6.8}_{-6.9}$	$26.4^{+6.9}_{-2.1}$	$39.4^{+10.7}_{-11.1}$	$17.7^{+19.6}_{-0.2}$
τ_h ($\times 10^{11}$ s cm^{-3})	$9.67^{+1.89}_{-0.60}$	$7.46^{+0.25}_{-1.19}$	$9.75^{+9.33}_{-0.01}$	$9.85^{+0.18}_{-1.42}$	$5.79^{+0.01}_{-0.01}$	$4.37^{+0.21}_{-0.11}$	$4.75^{+0.14}_{-0.25}$	$11.2^{+0.1}_{-0.5}$	$5.99^{+0.35}_{-0.31}$	$4.56^{+0.01}_{-0.58}$
Redshift (10^{-3})	$-2.72^{+0.29}_{-0.04}$	$-2.81^{+0.03}_{-0.01}$	$-2.78^{+0.20}_{-0.01}$	$-2.92^{+0.08}_{-0.05}$	$-2.47^{+0.02}_{-0.01}$	$-2.13^{+0.08}_{-0.15}$	$-1.25^{+0.32}_{-0.19}$	$-1.93^{+0.24}_{-0.25}$	$-1.10^{+0.07}_{-0.82}$	$-1.06^{+0.07}_{-0.09}$
χ^2_ν (DoF)	1.17 (4277)	1.25 (4001)	1.24 (3856)	1.16 (4243)	1.19 (4260)	1.11 (4500)	1.15 (4034)	1.21 (4303)	1.25 (3629)	1.14 (4018)

Table 7.7: G43.3−0.2: Best fit parameters per region (R10 - R18)

Parameter	R10	R11	R12	R13	R14	R15	R16	R17	R18
N_H ($\times 10^{22}$ cm^{-2})	$10.33^{+0.08}_{-0.26}$	$9.21^{+0.14}_{-0.14}$	$9.24^{+0.27}_{-0.11}$	$8.94^{+0.10}_{-0.10}$	$8.64^{+0.48}_{-0.13}$	$9.13^{+0.18}_{-0.17}$	$9.14^{+0.24}_{-0.05}$	$7.68^{+0.10}_{-0.14}$	$4.88^{+0.06}_{-0.08}$
kT_c (keV)	$0.17^{+0.01}_{-0.01}$	$0.19^{+0.01}_{-0.01}$	$0.17^{+0.01}_{-0.01}$	$0.19^{+0.01}_{-0.01}$	$0.18^{+0.01}_{-0.01}$	$0.19^{+0.01}_{-0.01}$	$0.21^{+0.01}_{-0.01}$	$0.32^{+0.03}_{-0.02}$	$0.21^{+0.01}_{-0.01}$
kT_h (keV)	$1.59^{+0.06}_{-0.02}$	$1.16^{+0.03}_{-0.04}$	$0.76^{+0.02}_{-0.02}$	$0.85^{+0.04}_{-0.02}$	$0.67^{+0.01}_{-0.01}$	$0.78^{+0.02}_{-0.03}$	$1.62^{+0.05}_{-0.05}$	$0.64^{+0.01}_{-0.03}$	$0.63^{+0.02}_{-0.02}$
Mg	-	-	$5.70^{+1.84}_{-1.34}$	$7.34^{+1.87}_{-1.56}$	$2.47^{+0.58}_{-0.01}$	-	-	$8.06^{+2.26}_{-2.47}$	-
Si	$10.2^{+1.3}_{-0.6}$	$12.2^{+1.3}_{-1.1}$	$10.9^{+1.3}_{-0.9}$	$9.76^{+1.17}_{-0.77}$	$5.68^{+2.64}_{-0.05}$	$5.77^{+0.45}_{-0.63}$	$9.48^{+1.36}_{-0.49}$	$12.3^{+2.3}_{-1.1}$	$2.60^{+0.17}_{-0.30}$
S	$7.59^{+0.73}_{-0.39}$	$9.66^{+1.30}_{-0.92}$	$9.70^{+1.07}_{-0.61}$	$8.72^{+1.08}_{-0.73}$	$5.24^{+2.34}_{-0.01}$	$5.39^{+0.30}_{-0.49}$	$8.06^{+0.94}_{-0.59}$	$14.0^{+2.3}_{-1.1}$	$3.70^{+0.19}_{-0.26}$
Ar	$5.60^{+0.86}_{-0.39}$	$9.58^{+1.38}_{-1.01}$	$9.79^{+0.81}_{-0.81}$	$9.11^{+1.53}_{-0.76}$	$5.61^{+1.71}_{-0.03}$	$5.53^{+0.34}_{-0.58}$	$7.43^{+1.14}_{-0.89}$	$18.2^{+3.2}_{-1.2}$	$3.35^{+0.26}_{-0.33}$
Ca	$8.38^{+1.09}_{-0.67}$	$12.9^{+1.5}_{-1.3}$	$11.2^{+1.4}_{-0.8}$	$11.2^{+1.1}_{-1.2}$	$5.92^{+1.51}_{-0.01}$	$6.95^{+0.49}_{-0.72}$	$10.4^{+1.55}_{-1.45}$	$20.6^{+3.5}_{-1.4}$	$3.43^{+0.33}_{-0.41}$
Fe	$10.2^{+0.9}_{-0.6}$	$10.5^{+1.5}_{-0.8}$	$2.91^{+0.41}_{-0.33}$	$5.05^{+0.95}_{-0.45}$	$0.87^{+0.35}_{-0.01}$	$1.81^{+0.26}_{-0.29}$	$14.0^{+1.6}_{-1.2}$	$6.92^{+1.38}_{-0.99}$	$0.63^{+0.09}_{-0.06}$
Ni	$17.2^{+5.3}_{-3.3}$	$37.3^{+12.7}_{-8.1}$	$8.43^{+1.28}_{-1.94}$	$11.0^{+5.5}_{-2.9}$	$2.08^{+4.90}_{-0.02}$	$9.79^{+2.32}_{-2.89}$	$36.0^{+10.2}_{-7.5}$	$34.5^{+14.5}_{-9.9}$	$0.46^{+0.74}_{-0.29}$
τ_h ($\times 10^{11}$ s cm^{-3})	$10.4^{+1.0}_{-0.1}$	$6.34^{+0.30}_{-0.48}$	$4.60^{+0.18}_{-0.10}$	$4.88^{+0.13}_{-0.18}$	$4.88^{+0.08}_{-0.03}$	$5.14^{+0.14}_{-0.12}$	$9.02^{+1.49}_{-0.82}$	$4.39^{+0.27}_{-0.14}$	$4.91^{+0.12}_{-0.16}$
Redshift (10^{-3})	$-2.78^{+0.03}_{-0.03}$	$-2.72^{+0.32}_{-0.08}$	$-1.00^{+0.11}_{-0.08}$	$-1.95^{+0.02}_{-0.02}$	$-1.93^{+0.04}_{-0.01}$	$-2.13^{+0.21}_{-0.44}$	$-2.79^{+0.05}_{-0.03}$	$-0.58^{+0.06}_{-0.11}$	$-1.67^{+0.31}_{-0.73}$
χ^2_ν (DoF)	1.16 (4542)	1.20 (4105)	1.08 (3851)	1.15 (4351)	1.11 (3599)	1.12 (3437)	1.19 (4619)	1.17 (3358)	1.11 (3781)

7.5 G120.1+1.4

Four observations were fit simultaneously for our analysis of G120.1+1.4 (Tycho's SNR): observations IDs 0412380101, 0412380201, 0412380301, 0412380401, which combine for just under 150 ks of total exposure time. From these, a combined MOS1+MOS2 image was created, and the *contbin* algorithm was subsequently used to generate a region map comprised of 20 regions.

While fitting the spectra of G120.1+1.4, we noticed a discrepancy in the spectra between the pn and MOS observations. Specifically, between approximately $1.5 - 1.8$ keV, the pn spectra exhibited a noticeably higher count rate than the MOS spectra. This resulted in the overall quality of the fit being reduced, as the fit statistic for the pn data would be higher than that of the MOS data. While we attempted to correct for this discrepancy through our models, our attempts were unsuccessful; as a result, we opted to not make use of the pn observations for this object, using instead the MOS1 and MOS2 observations.

For our spectral fitting, we attempted multiple different combinations of models to fit the regional spectra of G120.1+1.4. We initially attempted to fit the regional spectra with absorbed one-component models: while we found that these one-component models were incapable of reproducing the complexity of the observed spectra, we found that VPSHOCK and VNEI models produced notably better fits than VRNEI or VAPEC models. We then proceeded to attempt to fit using both two- and three-component models. While both proved capable of producing acceptable fits, the three-component models proved unwieldy, with the spectral fitting process more frequently becoming stuck in local minima producing unrealistic results for one or more of the involved components, and providing only a small increase in

fit quality for a significant increase in computation time. As such, we opted to continue with a two-component model, ultimately settling upon an absorbed VPSHOCK+VPSHOCK model. O, Mg, Si, S, Ar, Ca, and Fe were freed and allowed to fit. We attempted to fit for the Ne abundance; while freeing this abundance did improve the quality of the fit, the Ne abundance would invariably collapse to a near-zero value. As a result, we froze the Ne abundance at zero for all regions. Further, we noticed excess emission at several points in the spectrum that our models were unable to account for. Both of these likely represent lines in the Fe L complex that the atomic models used do not presently incorporate (Yamaguchi et al. 2011). In response, we opted to add two Gaussians to our models – one at 0.72 keV, and the other at 1.2 keV – to account for this emission. As a result, we were able to obtain acceptable fits ($\chi^2_\nu < 2$) for all regions with the exceptions of R05 and R19, both of which exhibited notable line broadening that we were unable to account for with our models. While the values and abundances within these regions were comparable to those of our other regions, we opted to exclude them from our nucleosynthesis calculations as a result.

Our spectral fits to G120.1+1.4 can be seen in Tables 7.8 and 7.9. Our hydrogen column densities range from $0.98 - 1.28 \times 10^{22}$ cm^{-2}, with the lower values found primarily in the northern portion of the SNR. In the cold component, our plasma temperatures range between $0.40 - 0.95$ keV, while the ionisation timescales lie between $0.45 - 3.82 \times 10^{11}$ $\mathrm{cm}^{-3}\,\mathrm{s}$. The abundance for O is enhanced to slightly over solar values, while Mg is consistently sub-solar. Si, S, and Ar are all significantly enhanced. In the hot component, the plasma temperatures range between $2.14 - 10.3$ keV, while the ionisation timescales lie between $0.10 - 7.53 \times 10^{9}$ $\mathrm{cm}^{-3}\,\mathrm{s}$, signifying that the hot component primarily represents recently-shocked ejecta. The Fe abundance is enhanced to above solar abundances, though

not to as significant a degree as that of Si, S, or Ar. The Ca abundance in G120.1+1.4 proved unique in our study. While it is clear that the Ca abundance is enhanced to super-solar values, it was also present at two distinct temperatures, and as such, we found that it was necessary to allow the Ca abundance to vary in both the hot and the cold components. While this resulted in a notable improvement in the quality of the fit over simply allowing the Ca to be present in one of the two components, it also resulted in the Ca – particularly, the abundance determined by the cold component – to become poorly constrained, and enhanced to values well above what would normally be expected.

As G120.1+1.4 is a well-studied object, there are many studies to which we can compare our results. However, two of the most recent studies are also the most relevant, as they both performed a thorough spectroscopic study of the entire SNR: those of Godinaud et al. (2025) and Holland-Ashford et al. (2025). Godinaud et al. (2025) used *Chandra* data to perform a detailed mapping of ejecta properties, using an adaptive binning method to divide the SNR into 211 regions, based upon maps of the integrated line-of-sight velocity of the remnant. To each of these regions, an absorbed VNEI+VNEI model was fit, alongside a non-thermal component and several Gaussians to account for low-energy emission that the atomic models do not include. They found a median hydrogen column density of 0.70×10^{22} cm^{-2}, which is below our own findings. For plasma temperatures, their two thermal components yielded median values of 1.3 and 9.0 keV, both of which are notably higher than our own. The ionisation timescales of 4.7×10^{10} cm^{-3} s for their cold component and 9.0×10^{9} cm^{-3} s for their hot component also differ somewhat from our own, but given the differences in plasma temperatures, this was to be expected. In terms of abundances, they found comparable Mg/Si, S/Si, and Fe/Si ratios to our own findings; their Ar/Si and Ca/Si ratios,

however, are generally lower than our own. Holland-Ashford et al. (2025) used *Suzaku* data to fit the global spectrum of the SNR. Their final model was quite complex: an absorbed, five-component model comprised of three VPSHOCK components, a VVNEI component, and a non-thermal component, in addition to multiple Gaussians. They found a hydrogen column density of 1.351×10^{22} cm^{-2}, which is slightly higher than our findings. For plasma temperatures, their four components yielded values of 0.225, 0.827, 1.65, and 4.73 keV; as was the case in their study of G4.5+6.8, the second and fourth components are most comparable to our findings, and likely represent the same emission. These two components showed ionisation timescales of 1.22×10^{11} and 2.88×10^{9} cm^{-3} s, which are both comparable to our ionisation timescales in the respective components. The abundance ratios determined in their fits are also similar to our own, though we find a larger abundance of Ar relative to Si than do their results. They also found that Ca had to be accounted for in multiple components in order to acquire a good fit; however, their Ca abundance was more constrained than our findings, and the Ca/Si ratio was notably lower.

When comparing our results to models of supernova nucleosynthesis, we find good agreement between our observations and the models for the O/Si, Mg/Si, and S/Si ratios. Both thermonuclear and core-collapse models are able to reproduce these ratios, though the thermonuclear models fare better, as the core-collapse models tend to overproduce O and Mg relative to Si. The observed Fe/Si ratio aligns closer to models of core-collapse nucleosynthesis; however, thermonuclear models featuring low-mass (for the subCh-mass case) or low DDT-density (for the Ch-mass case) WDs are also able to reproduce our findings, as these explosions tend towards producing smaller amounts of Fe. The Ar/Si ratio is high, and is only reproduced by two models: the D^6 model of T18, and the 12 M$_\odot$ model of WW95.

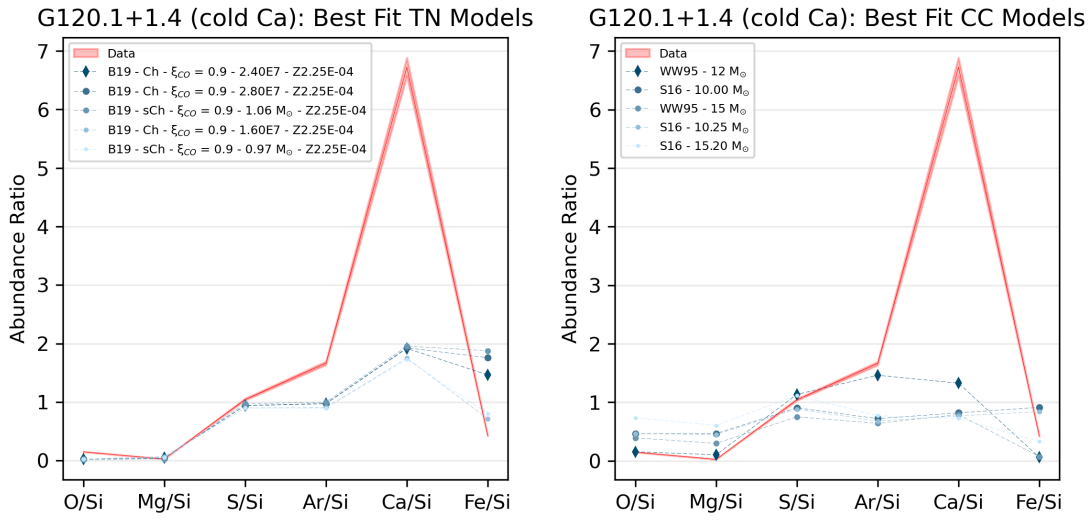

Figure 7.5: Best-fit nucleosynthesis models for G272.2−3.2, comparing to both thermonuclear (TN) and core-collapse (CC) supernova nucleosynthesis yields. Ca/Si ratio uses the Ca abundance from the cold component.

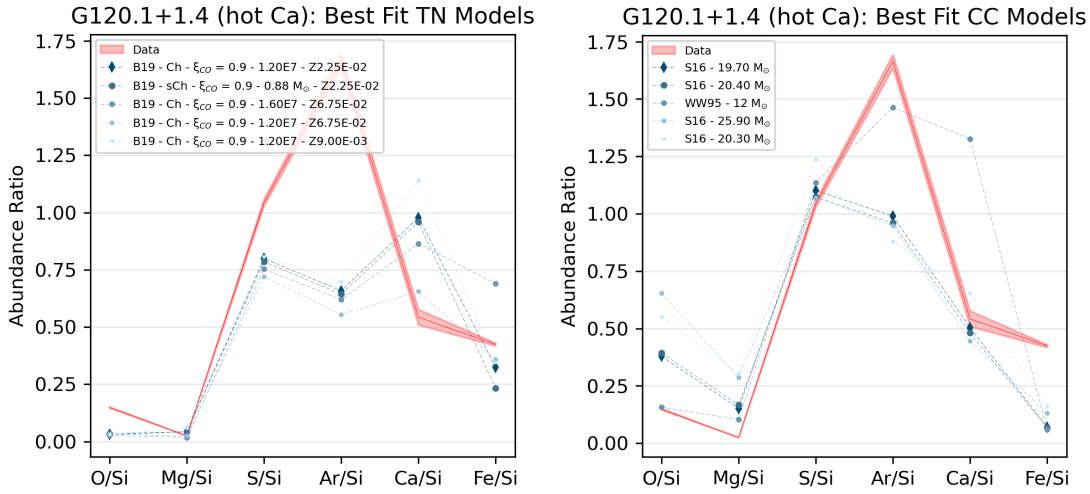

Figure 7.6: Best-fit nucleosynthesis models for G272.2−3.2, comparing to both thermonuclear (TN) and core-collapse (CC) supernova nucleosynthesis yields. Ca/Si ratio uses the Ca abundance from the hot component.

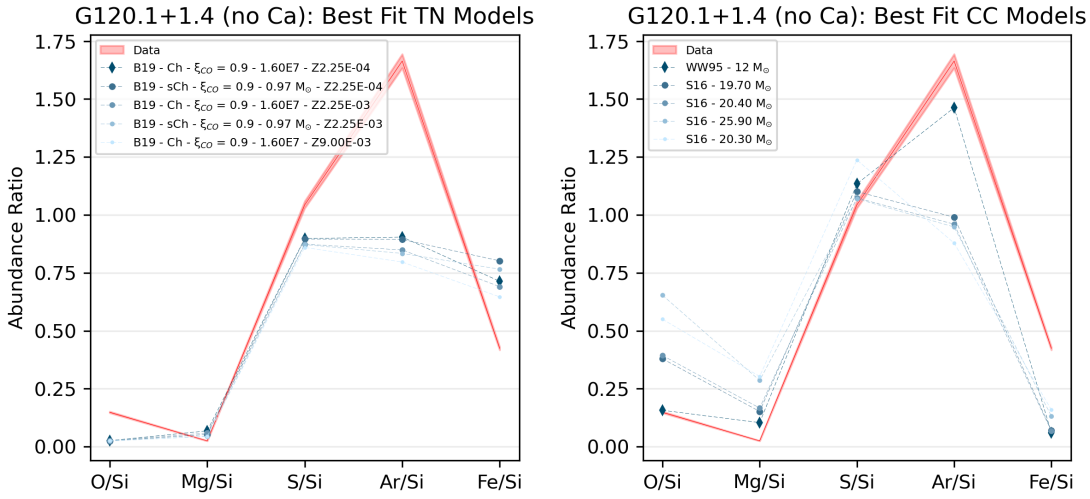

Figure 7.7: Best-fit nucleosynthesis models for G272.2–3.2, comparing to both thermonuclear (TN) and core-collapse (CC) supernova nucleosynthesis yields. The Ca/Si ratio is omitted.

The large abundance of Ca makes it difficult to come to a conclusion, as no tested model is able to reproduce such a high ratio of Ca/Si. As a result, we opt to perform this analysis in three parts: once utilising the Ca abundance from the cold component, once using the Ca abundance from the hot component, and once omitting the Ca abundance altogether. We find a general agreement between the comparisons using the cold Ca, and those omitting Ca altogether, with a medium-DDT density Ch-mass WD producing the best results for both models. The comparison to the hot Ca, however, is suggestive instead of a slightly lower DDT density. Further, the comparisons differ in that the hot Ca more strongly aligns with a high-metallicity progenitor, while the cold Ca and no Ca comparisons suggest a low-metallicity progenitor instead. The core-collapse models, for their part, are somewhat inconsistent: estimates for progenitor mass among the best fits ranges from approximately 10 $M_\odot$ to 26 $M_\odot$. The 12 $M_\odot$ model of WW95 fares particularly well, largely due to its ability to reproduce the

Ar/Si ratio. Given the uncertainty that arises from our Ca abundance, we cannot determine with certainty a progenitor for this SNR. However, as it has been previously established that G120.1+1.4 arose as a result of a thermonuclear supernova, we suggest a Ch-mass progenitor with a low-to-medium DDT density as a possible source.

Table 7.8: G120.1+1.4: Best fit parameters per region (R00 - R09)

Parameter	R00	R01	R02	R03	R04	R05	R06	R07	R08	R09
N_H ($\times 10^{22}$ cm^{-2})	$0.98^{+0.01}_{-0.01}$	$0.98^{+0.01}_{-0.02}$	$1.09^{+0.01}_{-0.01}$	$1.01^{+0.01}_{-0.01}$	$1.10^{+0.01}_{-0.01}$	$1.21^{+0.01}_{-0.01}$	$1.17^{+0.01}_{-0.02}$	$1.08^{+0.01}_{-0.01}$	$1.28^{+0.01}_{-0.01}$	$1.05^{+0.01}_{-0.01}$
kT_c (keV)	$0.56^{+0.06}_{-0.02}$	$0.68^{+0.01}_{-0.01}$	$0.52^{+0.04}_{-0.01}$	$0.55^{+0.02}_{-0.06}$	$0.44^{+0.02}_{-0.01}$	$0.48^{+0.01}_{-0.04}$	$0.46^{+0.01}_{-0.06}$	$0.61^{+0.01}_{-0.02}$	$0.47^{+0.01}_{-0.05}$	$0.83^{+0.03}_{-0.03}$
O	$1.78^{+0.20}_{-0.07}$	$1.96^{+0.09}_{-0.09}$	$2.31^{+0.34}_{-0.01}$	$2.53^{+0.16}_{-0.12}$	$1.13^{+0.08}_{-0.09}$	$2.13^{+0.03}_{-0.13}$	$3.75^{+0.28}_{-0.27}$	$2.90^{+0.06}_{-0.09}$	$7.32^{+0.49}_{-0.24}$	$3.78^{+0.11}_{-0.21}$
Mg	$0.56^{+0.06}_{-0.02}$	$0.68^{+0.01}_{-0.01}$	$0.52^{+0.04}_{-0.01}$	$0.55^{+0.02}_{-0.06}$	$0.44^{+0.02}_{-0.01}$	$0.48^{+0.01}_{-0.04}$	$0.46^{+0.01}_{-0.06}$	$0.61^{+0.01}_{-0.02}$	$0.47^{+0.01}_{-0.05}$	$0.83^{+0.03}_{-0.03}$
Si	$27.2^{+1.3}_{-0.6}$	$28.9^{+1.0}_{-0.1}$	$31.6^{+1.5}_{-0.3}$	$23.8^{+0.6}_{-1.2}$	$11.6^{+0.5}_{-0.2}$	$24.8^{+0.1}_{-1.5}$	$30.0^{+1.9}_{-0.9}$	$15.4^{+0.2}_{-0.4}$	$36.0^{+1.9}_{-0.6}$	$25.7^{+0.6}_{-0.7}$
S	$29.0^{+1.6}_{-0.6}$	$29.7^{+1.0}_{-0.1}$	$33.7^{+1.8}_{-0.3}$	$25.3^{+0.6}_{-1.4}$	$12.3^{+0.6}_{-0.2}$	$30.6^{+0.6}_{-1.7}$	$31.7^{+1.7}_{-1.2}$	$16.1^{+0.3}_{-0.6}$	$36.7^{+2.0}_{-0.9}$	$26.1^{+1.0}_{-0.6}$
Ar	$42.9^{+2.3}_{-1.2}$	$42.9^{+2.4}_{-0.5}$	$55.0^{+3.0}_{-1.3}$	$38.4^{+2.2}_{-0.9}$	$18.5^{+0.7}_{-0.9}$	$65.3^{+4.9}_{-2.2}$	$53.3^{+1.3}_{-2.7}$	$24.7^{+0.7}_{-0.5}$	$63.9^{+3.9}_{-1.7}$	$32.3^{+2.8}_{-1.1}$
Ca	112^{+7}_{-5}	117^{+5}_{-9}	162^{+14}_{-14}	113^{+7}_{-4}	$79.6^{+6.6}_{-4.1}$	254^{+16}_{-12}	256^{+9}_{-30}	$68.9^{+1.9}_{-2.1}$	326^{+33}_{-17}	102^{+10}_{-5}
τ_c ($\times 10^{11}$ s cm^{-3})	$2.22^{+0.22}_{-0.11}$	$2.47^{+0.05}_{-0.13}$	$2.18^{+0.12}_{-0.15}$	$2.09^{+0.12}_{-0.24}$	$1.41^{+0.14}_{-0.10}$	$0.53^{+0.03}_{-0.02}$	$2.27^{+0.36}_{-0.12}$	$3.82^{+0.83}_{-0.29}$	$2.84^{+0.05}_{-0.12}$	$1.89^{+0.07}_{-0.16}$
kT_h (keV)	$3.19^{+0.09}_{-0.07}$	$3.25^{+0.15}_{-0.01}$	$3.60^{+0.01}_{-0.01}$	$3.13^{+0.10}_{-0.13}$	$4.11^{+0.24}_{-0.30}$	$2.14^{+0.02}_{-0.08}$	$2.99^{+0.17}_{-0.06}$	$6.21^{+0.60}_{-0.39}$	$3.01^{+0.09}_{-0.07}$	$3.54^{+0.14}_{-0.09}$
Ca	$25.2^{+4.0}_{-4.1}$	$26.3^{+2.4}_{-4.8}$	$39.4^{+7.5}_{-5.7}$	$7.46^{+2.89}_{-4.95}$	$7.46^{+1.79}_{-2.24}$	-	$12.0^{+1.9}_{-2.6}$	$4.25^{+0.73}_{-1.39}$	$9.28^{+1.87}_{-1.92}$	$26.0^{+4.2}_{-5.5}$
Fe	$14.1^{+0.3}_{-0.7}$	$15.4^{+0.1}_{-1.5}$	$13.1^{+0.2}_{-0.4}$	$11.2^{+0.5}_{-0.2}$	$4.48^{+0.32}_{-0.40}$	$21.3^{+3.2}_{0.9}$	$10.5^{+0.2}_{-1.0}$	$1.20^{+0.12}_{-0.30}$	$8.09^{+0.28}_{-0.42}$	$14.5^{+0.5}_{-0.6}$
τ_h ($\times 10^{9}$ s cm^{-3})	$7.36^{+0.29}_{-0.06}$	$7.14^{+0.20}_{-0.04}$	$7.09^{+0.27}_{-0.02}$	$6.68^{+0.11}_{-0.15}$	$6.11^{+0.35}_{-0.25}$	$4.05^{+0.10}_{-0.22}$	$6.54^{+0.15}_{-0.03}$	$0.10^{+0.20}_{-0.02}$	$6.05^{+0.18}_{-0.09}$	$6.75^{+0.26}_{-0.13}$
Redshift (10^{-3})	$-0.58^{+0.03}_{-0.09}$	$-2.38^{+0.01}_{-0.06}$	$-0.55^{+0.16}_{-0.06}$	$-0.51^{+0.01}_{-0.05}$	$-2.96^{+0.10}_{-0.03}$	$-0.64^{+0.09}_{-0.01}$	$-1.58^{+0.01}_{-0.20}$	$-2.10^{+0.01}_{-0.01}$	$-1.78^{+0.01}_{-0.01}$	$-0.30^{+0.01}_{-0.01}$
Line Centroid (keV)	$0.74^{+0.01}_{-0.01}$	$0.74^{+0.01}_{-0.01}$	$0.73^{+0.01}_{-0.01}$	$0.73^{+0.01}_{-0.01}$	$0.73^{+0.01}_{-0.01}$	$0.73^{+0.01}_{-0.01}$	$0.73^{+0.01}_{-0.01}$	$0.72^{+0.01}_{-0.01}$	$0.73^{+0.01}_{-0.01}$	$0.73^{+0.01}_{-0.01}$
Line Centroid (keV)	$1.23^{+0.01}_{-0.01}$	$1.23^{+0.01}_{-0.01}$	$1.23^{+0.01}_{-0.01}$	$1.23^{+0.01}_{-0.01}$	$1.24^{+0.01}_{-0.01}$	$1.23^{+0.01}_{-0.01}$	$1.23^{+0.01}_{-0.01}$	$1.23^{+0.01}_{-0.01}$	$1.23^{+0.01}_{-0.01}$	$1.23^{+0.01}_{-0.01}$
χ^2_ν (DoF)	1.79 (4824)	1.93 (4844)	1.74 (4811)	1.72 (4961)	1.51 (5404)	2.31 (5426)	1.90 (5169)	1.69 (5645)	1.72 (5610)	1.79 (4948)

Table 7.9: G120.1+1.4: Best fit parameters per region (R10 - R19)

Parameter	R10	R11	R12	R13	R14	R15	R16	R17	R18	R19
N_H ($\times 10^{22}$ cm^{-2})	$1.26^{+0.01}_{-0.01}$	$0.99^{+0.01}_{-0.01}$	$1.14^{+0.01}_{-0.01}$	$1.19^{+0.01}_{-0.01}$	$1.13^{+0.01}_{-0.01}$	$1.14^{+0.02}_{-0.01}$	$1.14^{+0.01}_{-0.01}$	$1.28^{+0.01}_{-0.01}$	$1.28^{+0.01}_{-0.01}$	$1.20^{+0.02}_{-0.01}$
kT_c (keV)	$0.51^{+0.02}_{-0.02}$	$0.60^{+0.03}_{-0.03}$	$0.95^{+0.09}_{-0.06}$	$0.40^{+0.02}_{-0.01}$	$0.63^{+0.02}_{-0.01}$	$0.47^{+0.03}_{-0.02}$	$0.81^{+0.04}_{-0.04}$	$0.44^{+0.01}_{-0.04}$	$0.76^{+0.04}_{-0.05}$	$0.42^{+0.02}_{-0.03}$
O	$2.42^{+0.06}_{-0.35}$	$2.22^{+0.08}_{-0.08}$	$4.12^{+0.43}_{-0.18}$	$5.12^{+0.13}_{-0.18}$	$1.41^{+0.11}_{-0.01}$	$4.19^{+0.35}_{-0.62}$	$2.94^{+0.16}_{-0.23}$	$7.86^{+0.65}_{-0.32}$	$4.40^{+0.36}_{-0.48}$	$2.91^{+0.31}_{-0.34}$
Mg	$0.51^{+0.02}_{-0.02}$	$0.60^{+0.03}_{-0.03}$	$0.95^{+0.09}_{-0.06}$	$0.40^{+0.02}_{-0.01}$	$0.63^{+0.02}_{-0.01}$	$0.47^{+0.03}_{-0.02}$	$0.81^{+0.04}_{-0.04}$	$0.44^{+0.01}_{-0.04}$	$0.76^{+0.04}_{-0.05}$	$0.42^{+0.02}_{-0.03}$
Si	$27.0^{+0.6}_{-1.8}$	$27.2^{+0.3}_{-0.4}$	$35.7^{+3.1}_{-1.7}$	$8.79^{+0.17}_{-0.11}$	$17.8^{+0.8}_{-0.1}$	$31.3^{+1.9}_{-2.6}$	$28.8^{+1.1}_{-1.1}$	$26.5^{+2.0}_{-0.7}$	$37.1^{+1.7}_{-2.7}$	$26.3^{+1.5}_{-2.5}$
S	$33.9^{+0.5}_{-2.6}$	$26.5^{+0.3}_{-0.5}$	$34.8^{+3.3}_{-1.6}$	$8.55^{+0.16}_{-0.10}$	$20.0^{+0.85}_{-0.3}$	$32.5^{+1.7}_{-2.1}$	$27.7^{+1.2}_{-1.2}$	$26.5^{+2.1}_{-0.6}$	$39.0^{+1.4}_{-3.3}$	$26.6^{+0.8}_{-1.6}$
Ar	$75.6^{+1.1}_{-9.4}$	$35.9^{+1.5}_{-0.5}$	$51.3^{+5.6}_{-2.5}$	$9.93^{+0.25}_{-0.20}$	$35.6^{+1.2}_{-1.0}$	$50.7^{+5.3}_{-0.3}$	$43.9^{+1.0}_{-2.4}$	$42.0^{+3.0}_{-1.4}$	$78.6^{+7.3}_{-6.5}$	$47.0^{+3.7}_{-3.0}$
Ca	296^{+17}_{-23}	104^{+7}_{-7}	233^{+32}_{-16}	$25.5^{+1.6}_{-1.9}$	132^{+8}_{-6}	237^{+23}_{-4}	222^{+20}_{-15}	193^{+20}_{-5}	588^{+48}_{-527}	258^{+18}_{-11}
τ_c ($\times 10^{11}$ s cm^{-3})	$0.69^{+0.01}_{-0.05}$	$1.95^{+0.06}_{-0.08}$	$3.24^{+0.44}_{-0.06}$	$1.69^{+0.09}_{-0.05}$	$0.45^{+0.01}_{-0.01}$	$3.70^{+0.27}_{-0.62}$	$2.59^{+0.11}_{-0.18}$	$2.74^{+0.27}_{-0.03}$	$1.71^{+0.10}_{-0.09}$	$1.43^{+0.16}_{-0.31}$
kT_h (keV)	$2.57^{+0.13}_{0.04}$	$3.53^{+0.01}_{-0.01}$	$3.03^{+0.09}_{-0.07}$	$10.3^{+0.7}_{-2.1}$	$2.62^{+0.02}_{-0.11}$	$3.00^{+0.07}_{-0.05}$	$2.90^{+0.09}_{-0.05}$	$3.47^{+0.04}_{-0.13}$	$2.74^{+0.04}_{-0.07}$	$2.53^{+0.05}_{-0.05}$
Ca	$11.6^{+1.2}_{-7.2}$	$29.5^{+11.4}_{-3.3}$	$17.9^{+3.6}_{-0.4}$	$2.76^{+0.87}_{-0.61}$	-	$12.5^{+2.1}_{-3.9}$	$15.8^{+2.5}_{-3.5}$	$5.98^{+2.93}_{-0.63}$	$7.65^{+1.99}_{-1.81}$	$7.70^{+3.65}_{-3.49}$
Fe	$11.5^{+0.3}_{-0.9}$	$15.9^{+0.7}_{-0.5}$	$10.6^{+0.3}_{-0.2}$	$0.50^{+0.14}_{-0.06}$	$8.62^{+0.47}_{-0.13}$	$13.5^{+0.4}_{-1.2}$	$11.0^{+0.5}_{-0.9}$	$6.11^{+0.30}_{-0.12}$	$9.62^{+0.79}_{-0.36}$	$17.1^{+1.5}_{-0.9}$
τ_h ($\times 10^{9}$ s cm^{-3})	$4.96^{+0.25}_{-0.08}$	$6.72^{+0.09}_{-0.08}$	$5.23^{+0.10}_{-0.09}$	$7.53^{+0.52}_{-1.37}$	$3.87^{+0.13}_{-0.03}$	$5.84^{+0.29}_{-0.07}$	$4.93^{+0.08}_{-0.08}$	$6.37^{+0.01}_{-0.19}$	$5.01^{+0.12}_{-0.21}$	$5.17^{+0.13}_{-0.10}$
Redshift (10^{-3})	$-1.76^{+0.03}_{-0.01}$	$-2.67^{+0.01}_{-0.01}$	$-2.54^{+0.05}_{-0.07}$	$-0.26^{+0.05}_{-0.02}$	$-2.26^{+0.05}_{-0.09}$	$-2.97^{+0.38}_{-0.02}$	$-2.50^{+0.02}_{-0.11}$	$-0.59^{+0.04}_{-0.19}$	$-1.83^{+0.06}_{-0.27}$	$-2.67^{+0.01}_{-0.02}$
Line Centroid (keV)	$0.73^{+0.01}_{-0.01}$	$0.74^{+0.01}_{-0.01}$	$0.73^{+0.01}_{-0.01}$	$0.72^{+0.01}_{-0.01}$	$0.73^{+0.01}_{-0.01}$	$0.73^{+0.01}_{-0.01}$	$0.73^{+0.01}_{-0.01}$	$0.73^{+0.01}_{-0.01}$	$0.72^{+0.01}_{-0.01}$	$0.73^{+0.01}_{-0.01}$
Line Centroid (keV)	$1.23^{+0.01}_{-0.01}$	$1.23^{+0.01}_{-0.01}$	$1.23^{+0.01}_{-0.01}$	$1.22^{+0.01}_{-0.01}$	$1.23^{+0.01}_{-0.01}$	$1.23^{+0.01}_{-0.01}$	$1.23^{+0.01}_{-0.01}$	$1.23^{+0.01}_{-0.01}$	$1.23^{+0.01}_{-0.01}$	$1.23^{+0.01}_{-0.01}$
χ^2_ν (DoF)	1.76 (5121)	1.83 (4894)	1.55 (5071)	1.76 (5757)	1.95 (6426)	1.97 (5657)	1.50 (5257)	1.64 (5659)	1.71 (5167)	2.23 (5106)

7.6 G272.2−3.2

There is only a single *XMM-Newton* observation of G272.2−3.2: a 38 ks observation taken in 2001. Due to the size of this object relative to the field of view of *XMM-Newton* EPIC, we used the ESAS pipeline to create a merged, background-subtracted, vignetting-corrected image of G272.2−3.2. The *contbin* algorithm was applied on this combined image, generating seven regions from which we extracted spectra. In the *XMM-Newton* observation used for this study, G272.2−3.2 has the peculiar property of being largely undetected above 3.0 keV: when viewed in such a regime, it is indistinguishable from the background. While we first thought that this may have been due to improper processing, this issue was also reported by Sánchez-Ayaso et al. (2013), and as such we were unable to correct for it. This lack of detection extends to its spectrum, as well, for which any data points above 3.0 keV appear largely as noise. To this end, during our analysis of G272.2−3.2, we opted to examine the $0.5 - 3.0$ keV range, rather than the $0.5 - 8.0$ keV range used for other remnants.

When fitting the spectra for G272.2−3.2, we initially fit each spectra with an absorbed single-component thermal model. Out of the four models used in this study – VPSHOCK, VNEI, VRNEI, and VAPEC – we found that the VNEI model was best able to reproduce the observations. Attempts to add a second thermal component yielded little improvement, and so we proceeded with a single absorbed VNEI component. Our fitting process proceeded as follows: first, the column density, temperature, ionisation timescale, and normalisation constant were freed and allowed to fit. Then, we freed and fit the abundances in the order of Si, S, Fe, Mg, Ne one at a time. Attempts to free and fit Ar or Ca proved unfruitful, owing to the limited energy range in which we performed our analysis. Ne and Mg tended to hover

Table 7.10: G272.2−3.2: Best fit parameters per region

Parameter	R00	R01	R02	R03	R04	R05	R06
N_H (10^{22} cm^{-2})	$1.37^{+0.19}_{-0.04}$	$1.09^{+0.10}_{-0.09}$	$1.28^{+0.05}_{-0.04}$	$1.26^{+0.04}_{-0.19}$	$1.17^{+0.05}_{-0.03}$	$1.32^{+0.12}_{-0.04}$	$1.21^{+0.04}_{-0.05}$
kT (keV)	$0.73^{+0.05}_{-0.03}$	$0.70^{+1.08}_{-0.12}$	$0.74^{+0.07}_{-0.05}$	$0.79^{+1.91}_{-0.06}$	$0.85^{+0.10}_{-0.07}$	$0.77^{+0.09}_{-0.14}$	$0.98^{+0.14}_{-0.10}$
Ne	$1.08^{+0.71}_{-0.21}$	$1.05^{+0.13}_{-0.10}$	$1.11^{+0.15}_{-0.12}$	$0.99^{+0.17}_{-0.41}$	$1.05^{+0.59}_{-0.12}$	$1.03^{+0.20}_{-0.18}$	$0.95^{+0.17}_{-0.15}$
Mg	$1.23^{+1.46}_{-0.13}$	$1.08^{+0.37}_{-0.16}$	$1.05^{+0.18}_{-0.12}$	$1.12^{+0.21}_{-0.12}$	$1.19^{+0.17}_{-0.26}$	$1.03^{+0.19}_{-0.22}$	$1.14^{+0.19}_{-0.13}$
Si	$5.12^{+0.61}_{-1.41}$	$1.06^{+0.29}_{-0.13}$	$1.82^{+0.27}_{-0.17}$	$2.79^{+0.32}_{-0.25}$	$2.27^{+0.30}_{-1.04}$	$2.28^{+0.38}_{-0.26}$	$1.29^{+0.22}_{-0.15}$
S	$5.58^{+0.64}_{-2.28}$	$0.72^{+0.74}_{-0.25}$	$2.24^{+0.47}_{-0.32}$	$3.21^{+0.53}_{-0.59}$	$2.73^{+0.59}_{-2.73}$	$3.05^{+1.52}_{-0.59}$	$1.31^{+0.38}_{-0.29}$
Fe	$2.89^{+5.06}_{-0.34}$	$0.87^{+0.21}_{-0.19}$	$1.17^{+0.27}_{-0.18}$	$1.60^{+0.30}_{-0.23}$	$1.06^{+0.14}_{-0.84}$	$1.16^{+0.35}_{-0.32}$	$1.23^{+0.26}_{-0.18}$
τ (10^{10} s cm^{-3})	$6.78^{+27.3}_{-1.18}$	$6.51^{+1.63}_{-5.16}$	$6.57^{+1.23}_{-1.12}$	$5.00^{+1.35}_{-3.88}$	$4.65^{+1.04}_{-3.61}$	$4.84^{+1.64}_{-1.38}$	$3.85^{+0.94}_{-0.75}$
Line Centroid (keV)	$1.24^{+0.01}_{-0.11}$	-	-	$1.24^{+0.01}_{-0.01}$	$1.22^{+0.01}_{-0.09}$	$1.24^{+0.01}_{-0.01}$	-
χ^2_ν (DoF)	1.24 (855)	1.09 (640)	1.19 (792)	1.09 (814)	0.99 (899)	1.03 (799)	1.06 (825)

near to solar abundances, while Si, S, and Fe were typically super-solar. In four of our seven regions, we noted an underfitting of the spectrum at approximately 1.2 keV; this likely corresponds to the Fe L shell, for which there is an uncertainty in the VNEI code used in XSPEC. For the regions in which we encountered this excess, we added a Gaussian at 1.2 keV. All other parameters were frozen while initially adding this Gaussian; afterwards, the Gaussian was frozen while all other parameters were allowed to vary, until finally, both the parameters from the thermal model as well as the parameters from the Gaussian were allowed to vary simultaneously. All of our regions were well fit ($\chi^2_\nu < 1.25$).

The results of our spectral fitting for G272.2−3.2 can be seen in Table 7.10. The column density, plasma temperature, and ionisation timescale showed little variation across the remnant, ranging between $1.09 - 1.37 \times 10^{22}$ cm^{-2}, $0.70 - 0.98$ keV, and $3.85 - 6.78 \times 10^{10}$ cm^{-3} s, respectively. These low ionisation timescales suggest that the remnant is still in NEI,

and are somewhat surprising given its proposed age. The abundances were largely consistent and enhanced to supersolar values across the remnant, except for those in the brightest region, Roo, which exhibited notably higher abundances for all elements than any other region, and especially so for Si, S, and Fe.

We can compare our results to those of several previous studies. Sezer & Gök (2012), using data taken by *Suzaku*, found that the spectrum for the entire SNR could be reproduced using a single absorbed VNEI model, with a hydrogen column density of $1.1 \times 10^{22}\ \mathrm{cm}^{-2}$, plasma temperature $\mathrm{kT_e} \sim 0.77$ keV, an ionisation timescale $\tau \sim 6.5 \times 10^{10}\ \mathrm{cm}^{-3}\,\mathrm{s}$, all of which are in agreement with our own findings. Their elemental abundances are similar to ours, though there is a slight disagreement in the Ne abundance, for which they determined slightly lower values than what we determined. Sánchez-Ayaso et al. (2013) performed a similar study, using combined *XMM-Newton* and *Chandra* data to fit the spectrum of the entire SNR, the central region, and the outer region with an absorbed VNEI model. Their spectral parameters ($\mathrm{N_H}$, kT, τ) were in agreement with our own; however, the metal abundances determined in their fit to the whole SNR and the outer region appeared notably lower than our own. Their fit to the central region produced values that were more comparable to ours, excepting the abundances of Ne and Mg, which were also lower than our own. Finally, Kamitsukasa et al. (2016) used *Suzaku* data to fit the whole SNR, as well as five concentric rings and a "hot-spot," though rather than using a single absorbed VNEI model, they used four VNEI models and an APEC model, all multiplied by an absorption parameter. Their determined hydrogen column density of $0.99 \times 10^{22}\ \mathrm{cm}^{-2}$ was comparable to – though slightly lower than – that of previous studies, and our own. Their plasma temperatures varied greatly, due to the use of a model with several plasma components, ranging between $0.172 - 2.76$ keV.

For their first two VNEI components – the ones which appear to correlate most closely to the emission observed by *XMM-Newton*, and thus the ones most comparable to our results – they found plasma temperatures of 0.62 and 0.80 keV, which largely agrees with our findings. However, their ionisation timescales were notably different from our own: for the majority of the emission, they found a value of $12.3 \times 10^{10}\ \mathrm{cm^{-3}\ s}$ (the value for VNEI components 2 and 3 were tied to that of component 1), while their highest-temperature component used a value frozen at $1 \times 10^{10}\ \mathrm{cm^{-3}\ s}$. The abundances determined by their study differed slightly from our results: their study to the whole SNR determined abundances notably lower than what we found in any given region, while their concentric rings instead found values more comparable to our own, save for Ne and Fe, which were considerably lower.

When we compare to the supernova nucleosynthesis models, we find an amount of disagreement between our findings and the models of thermonuclear supernovae. This disagreement arises primarily due to the Ne/Si and Mg/Si ratios, which appear much higher in this SNR than those found in the models. The S/Si and Fe/Si ratios are more consistent, with multiple models able to replicate our findings. The S/Si ratio is, in general, only reproducible via models with the reduced CO reaction rate found in B19, or a few of the low metallicity models of LN18, while the Fe/Si ratio is more generally reproducible. All of the best-fit thermonuclear models share a low metallicity, but the mass is uncertain, as both Ch-mass and subCh-mass models provide good results. A low-density WD seems likely, however, as low DDT-density explosions provide the best fits among Ch-mass models, while low overall WD-mass models provide the best fits among those with subCh-masses.

Slightly better agreement is found with the core-collapse models, but only amongst the models with lower progenitor masses, as higher masses tend to overproduce the Ne/Si and

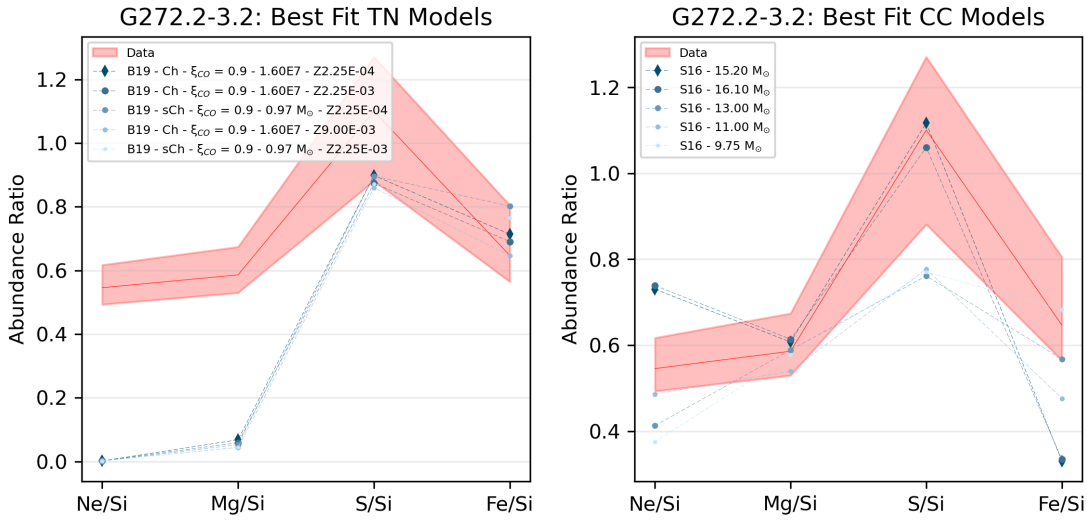

Figure 7.8: Best-fit nucleosynthesis models for G272.2−3.2, comparing to both thermonuclear (TN) and core-collapse (CC) supernova nucleosynthesis yields.

Mg/Si ratios. The S/Si ratio can be reproduced by a variety of models and mass ranges, but the Fe/Si ratio is only reproduced by a narrow range of masses between $9 - 13$ $M_\odot$, and only those around 10 $M_\odot$ are able to come close to reproducing both. The overall best fit between both thermonuclear and core-collapse models is found in the 15.2 $M_\odot$ model of S16, owing to the close agreement between this model and the Mg/Si and S/Si ratios found in the SNR. However, the inconsistency in the masses of the best-fit core collapse models, compared to the relative consistency in the properties of the best-fit thermonuclear models, suggests a thermonuclear origin, with a possible Ch-mass progenitor.

7.7 G337.2−0.7

For G337.2−0.7, we made use of a single 40 ks observation taken in 2001, from which a *contbin* region map of seven regions was generated. We fit these regions using a single, absorbed

Table 7.11: G337.2–0.7: Best fit parameters per region

Parameter	R00	R01	R02	R03	R04	R05	R06
N_H (10^{22} cm^{-2})	$3.44^{+0.20}_{-0.17}$	$3.68^{+0.12}_{-0.13}$	$4.06^{+0.29}_{-0.22}$	$4.15^{+0.37}_{-0.23}$	$4.35^{+0.46}_{-0.31}$	$3.95^{+0.36}_{-0.26}$	$4.83^{+0.87}_{-0.36}$
kT (keV)	$1.38^{+0.15}_{-0.20}$	$1.28^{+0.12}_{-0.10}$	$0.93^{+0.14}_{-0.14}$	$1.16^{+0.19}_{-0.22}$	$1.56^{+0.34}_{-0.30}$	$0.91^{+0.15}_{-0.15}$	$0.99^{+0.22}_{-0.27}$
Mg	$0.67^{+0.31}_{-0.26}$	$0.76^{+0.24}_{-0.18}$	$1.28^{+0.38}_{-0.29}$	$1.29^{+2.64}_{-0.33}$	$1.47^{+0.98}_{-0.42}$	$0.96^{+0.34}_{-0.22}$	$1.34^{+1.35}_{-0.40}$
Si	$4.48^{+0.80}_{-0.62}$	$3.97^{+0.50}_{-0.35}$	$3.77^{+0.72}_{-0.61}$	$3.93^{+6.20}_{-0.82}$	$5.41^{+1.53}_{-0.90}$	$3.03^{+0.71}_{-0.47}$	$4.36^{+1.66}_{-0.71}$
S	$4.36^{+0.78}_{-0.55}$	$3.74^{+0.46}_{-0.32}$	$3.61^{+0.64}_{-0.46}$	$3.86^{+5.75}_{-0.56}$	$4.38^{+1.09}_{-0.63}$	$3.32^{+0.69}_{-0.42}$	$4.69^{+1.25}_{-0.69}$
Ar	$4.60^{+1.34}_{-1.03}$	$4.34^{+0.80}_{-0.67}$	$4.48^{+1.69}_{-1.12}$	$5.48^{+7.08}_{-1.48}$	$5.37^{+2.16}_{-1.26}$	$3.01^{+2.34}_{-1.44}$	$5.88^{+5.99}_{-2.36}$
Ca	$9.45^{+2.86}_{-2.08}$	$7.36^{+1.65}_{-1.33}$	$5.55^{+6.57}_{-4.07}$	$6.64^{+10.4}_{-4.33}$	$12.4^{+5.7}_{-4.0}$	$13.2^{+17.4}_{-7.6}$	$17.9^{+42.4}_{-9.6}$
τ (10^{10} s cm^{-3})	$12.7^{+6.1}_{-2.4}$	$14.7^{+3.5}_{-2.6}$	$8.56^{+4.19}_{-2.39}$	$4.42^{+2.28}_{-2.26}$	$4.23^{+1.54}_{-1.01}$	$6.49^{+3.62}_{-1.86}$	$3.89^{+3.23}_{-0.94}$
χ^2_ν (DoF)	1.17 (302)	1.13 (558)	1.01 (318)	1.12 (305)	1.21 (324)	1.03 (309)	1.05 (307)

VNEI model across an energy range of $0.5 - 8.0$ keV. The column density, plasma temperature, ionisation timescale, and normalisation constant were first freed and allowed to vary together, while the abundances of Si, S, Ar, Ca, and Mg were freed and fit one at a time. Fe was tested, but the fits proved insensitive to the parameter, and so it was frozen at solar values. All seven regions were well-fit ($\chi^2_\nu < 1.25$) with this model.

Spectral fits for G337.2–0.7 can be seen in Table 7.11. The hydrogen column density ranges from $3.44 - 4.83 \times 10^{22}$ cm^{-2}, tending to increase the further away one gets from R00. The plasma temperature exists between $0.91 - 1.56$ keV and generally follows a similar trend to the hydrogen column density, though it experiences a spike in R04, which lies between the SNR's bright core and the faint northern plume. The ionisation timescale behaves in much the opposite way: though it ranges from $3.89 - 14.7 \times 10^{10}$ cm^{-3} s, these values appear highest in the central regions and decrease as one approaches the outer regions of the SNR. This also suggests an age on the lower side of the rather wide range currently associ-

ated with the SNR, as it rather clearly is still in a state of NEI. The elemental abundances are largely consistent for all examined elements, though Ca does show a notable increase in the outermost regions as opposed to the innermost ones.

There are three previous studies to which we can compare our results. The first of these – Rakowski et al. (2001) – was an *ASCA* study of G337.2–0.7 and a second SNR, G309.2-0.6. They fit the spectrum of the whole SNR with a single absorbed VNEI model, finding a hydrogen column density of 3.5×10^{22} cm^{-2}, a plasma temperature of 0.85 keV, and an ionisation timescale of of 1.8×10^{12} cm^{-3} s. We find that their column density is comparable to our own, though the plasma temperature and ionisation timescale differ notably: the plasma temperature is lower than our own, excepting for the outer regions of the SNR, in which it is comparable; and the ionisation timescale is significantly higher than any of our own results. Their abundance values were comparable to our own for Mg, Si, and S, while we find higher values of Ar and Ca, likely owing to the increased sensitivity of *XMM-Newton* at high energies in comparison to *ASCA*. The authors repeated their study in Rakowski et al. (2006), this time using data from *XMM-Newton* and *Chandra*. Their global VNEI fit this time found similar results for the column density, plasma temperature, and ionisation timescale, but notably higher Mg and Ca, both of which were then comparable to our own. Their spatially-resolved study noted similar variations in abundances as is seen in our results, with Ca notably being more prominent in the outer portions of the SNR. Finally, Takata et al. (2016) fit the *Suzaku* spectrum of the SNR with a three-component NEI model. They report plasma temperatures of 0.70, 1.54, and 3.1 keV, alongside ionisation timescales of 5.7×10^{11}, 3.6×10^{11}, and 2.1×10^{10} cm^{-3} s. We find greater agreement with their findings than with those of Rakowski et al. (2001, 2006) in terms of plasma temperature and ionisation timescale, sug-

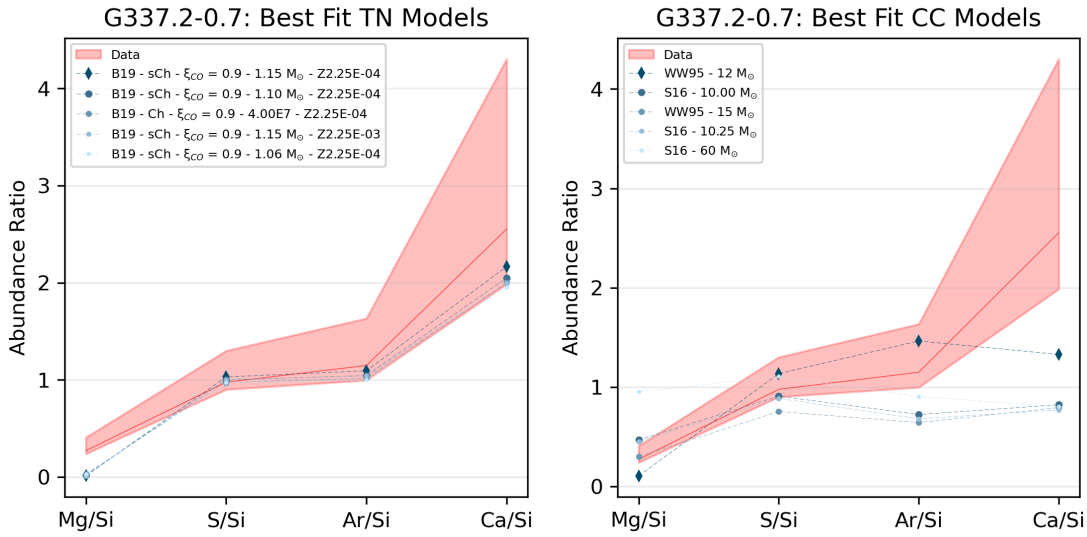

Figure 7.9: Best-fit nucleosynthesis models for G337.2−0.7, comparing to both thermonuclear (TN) and core-collapse (CC) supernova nucleosynthesis yields.

gesting that the spectrum of this SNR is more complex than is revealed by the relatively short *XMM-Newton* observation.

We find a strong agreement between our results and several models of supernova nucleosynthesis. In particular, the models for subCh-mass progenitors with a reduced CO reaction rate and low density from B19 produce a result that is very closely comparable to our findings for all tested abundance ratios save for that of Mg/Si, which these models underproduce. Four out of our five best fitted models were from subCh-mass WDs, with the one remaining best fit being the result of a Ch-mass WD. However, the subCh-mass WDs in question were all above 1 $M_\odot$, and the Ch-mass model was that of a high DDT density. In contrast, the core-collapse models are incapable of reproducing our results for any element heavier than S. As such, we agree with the conclusions of previous studies in suggesting a thermonuclear origin for this SNR. We further suggest a WD with a mass between $1.00 - 1.20\ M_\odot$ and low

metallicity as the most likely progenitor.

7.8 G344.7–0.1

Our analysis of G344.7–0.1 made use of two observations for a total of 22.2 ks of observation time. While Obs. Id. 0111210401 was made using the EPIC MOS cameras in Full Frame mode and EPIC pn in Extended Full Frame mode, Obs. Id. 0111210101 only made use of EPIC pn in Extended Full Frame mode; this observation did not contain data from the EPIC MOS cameras. The *contbin* algorithm was applied on a combined MOS image from Obs. Id. 0111210401, and resulted in the generation of a map containing eight regions. After extracting and processing data from these regions, they were individually fit with an absorbed single-component VNEI model. The column density, plasma temperature, ionisation timescale, and normalisation constant were allowed to vary for the initial fit, while the abundances for the elements of Si, S, Ar, Ca, and Mg were freed and allowed to fit one at a time for subsequent fits. All regions were well fit, with values of $\chi^2_\nu < 1.35$ for all regions.

Our results can be seen in Table 7.12. We find consistent values across the remnant for the absorption coefficient across the remnant, which lies between $4.84 - 5.97 \times 10^{22}\ \mathrm{cm}^{-2}$. The plasma temperature and ionisation timescale show similar amounts of consistency, ranging between $1.16 - 2.18$ keV and $2.99 - 8.61 \times 10^{10}\ \mathrm{cm}^{-3}\ \mathrm{s}$, respectively. The largest exception to this is R04, which simultaneously exhibits the highest value of kT and the lowest values for N_H and τ. This is likely due to the region's location along the north-eastern edge of the remnant, suggesting that this region is composed of material that has been more recently shock-heated than the other tested regions. The abundances of Si, S, Ar, and Ca are enhanced throughout the remnant, although the fit was insensitive to Ca in R04 and R05, where it was

Table 7.12: G344.7–0.1: Best fit parameters per region

Parameter	R00	R01	R02	R03	R04	R05	R06	R07
N_H (10^{22} cm^{-2})	$5.70^{+1.00}_{-0.38}$	$5.49^{+0.63}_{-0.39}$	$5.41^{+0.48}_{-0.41}$	$5.97^{+0.46}_{-0.32}$	$4.84^{+0.59}_{-0.71}$	$5.72^{+0.68}_{-0.55}$	$4.90^{+0.67}_{-0.43}$	$5.53^{+0.51}_{-1.65}$
kT (keV)	$1.23^{+0.15}_{-0.18}$	$1.41^{+0.27}_{-0.33}$	$1.85^{+0.43}_{-0.36}$	$1.16^{+0.15}_{-0.17}$	$2.18^{+2.38}_{-0.58}$	$1.48^{+0.46}_{-0.33}$	$1.53^{+0.34}_{-0.40}$	$1.55^{+0.25}_{-0.18}$
Mg	$0.64^{+1.44}_{-0.39}$	-	-	-	-	-	-	-
Si	$1.87^{+0.61}_{-0.30}$	$2.38^{+0.69}_{-0.63}$	$3.01^{+0.78}_{-0.63}$	$1.96^{+0.43}_{-0.35}$	$3.03^{+1.25}_{-0.61}$	$2.50^{+0.92}_{-0.64}$	$2.53^{+0.68}_{-0.69}$	$3.09^{+0.95}_{-0.67}$
S	$1.93^{+0.44}_{-0.29}$	$2.36^{+0.67}_{-0.56}$	$3.67^{+0.91}_{-0.62}$	$2.20^{+0.44}_{-0.34}$	$3.25^{+1.25}_{-0.64}$	$3.15^{+1.06}_{-0.69}$	$2.78^{+0.76}_{-0.68}$	$3.57^{+2.87}_{-0.62}$
Ar	$2.25^{+1.01}_{-0.78}$	$1.97^{+1.15}_{-0.89}$	$2.78^{+1.24}_{-0.98}$	$3.32^{+1.68}_{-1.09}$	$2.02^{+2.00}_{-1.39}$	$4.74^{+2.21}_{-1.47}$	$2.81^{+1.49}_{-1.11}$	$3.36^{+2.27}_{-1.20}$
Ca	$2.86^{+2.71}_{-1.82}$	$4.60^{+4.41}_{-2.46}$	$5.91^{+3.28}_{-2.31}$	$4.27^{+6.02}_{-3.18}$	-	-	$2.51^{+4.28}_{-1.87}$	$5.13^{+3.81}_{-2.56}$
τ (10^{10} s cm^{-3})	$8.61^{+3.25}_{-2.55}$	$6.35^{+3.57}_{-1.67}$	$5.50^{+1.85}_{-1.19}$	$5.26^{+2.21}_{-1.36}$	$2.99^{+1.20}_{-0.77}$	$6.02^{+3.47}_{-2.00}$	$6.35^{+3.77}_{-1.84}$	$6.64^{+3.36}_{-4.02}$
χ^2_ν (DoF)	1.13 (219)	1.35 (213)	1.14 (243)	0.91 (227)	0.95 (205)	0.97 (200)	1.29 (221)	1.27 (211)

instead frozen to solar values.

We can compare our results to those of several previous studies. Combi et al. (2010), using *XMM-Newton* and *Chandra* data and an absorbed PSHOCK model, found comparable results for the column density, slightly lower average plasma temperatures, and slightly higher ionisation timescales. They found generally higher average abundances, but the use of a PSHOCK model meant that they could not discern which abundances were being probed. Giacani et al. (2011), using data from *XMM-Newton*, found a slightly lower column density of 4.5×10^{22} cm^{-2}, but highly comparable plasma temperature, ionisation timescale, and abundances with their global VNEI fit. Yamaguchi et al. (2012) fit the SNR's global *Suzaku* spectrum with a two-component VNEI model. They found slightly lower column density, but that can be expected given that they made use of the absorption model of Anders & Grevesse (1989), rather than Wilms et al. (2000) as in our study. With their two-component model, they found plasma temperatures of $0.92 - 0.96$ keV and $2.8 - 3.6$ keV, with the

higher temperature component being primarily for emission from the Fe K-shell, which was not well resolved in our data. Their ionisation timescale for the bulk emission was broadly higher than our own, but the Fe K-shell emission was lower than our findings, suggesting a more recently-shocked componen, while their abundances were comparable to our own.

Our findings compare relatively well to models of thermonuclear supernova nucleosynthesis. The models of B19 most closely reproduce our findings in that regard, with models of Ch-mass WDs producing better results than those of subCh-mass WDs. However, the Mg/Si, S/Si, and Ar/Si ratios are underproduced by almost all thermonuclear models, with the lighter elements exhibiting a larger discrepancy. The Ca/Si ratio is adequately explained by the majority of models from B19, with some models of LN18 – namely, those with low-metallicity – also producing comparable results. The Fe/Si ratio exhibits a somewhat opposite effect, with most models producing a larger ratio than what we observe. The B19 models again provide the best results, with models from low DDT density explosions (for Ch-mass WDs) and low-mass (for subCh-mass WDs) yielding the closest matches. The Ar/Si and Ca/Si ratios suggest an attenuated CO reaction rate, as the standard CO reaction rate is less capable of producing such results.

The vast majority of core-collapse models are incapable of reproducing our findings: while the Mg/Si ratio, S/Si ratio, and Fe/Si ratio are more commonly reproduced by core-collapse models, the Ar/Si and Ca/Si are not so. The Ca/Si ratio in particular is only reproduced by a single core-collapse model: the 12 $M_\odot$ model of WW95. Perhaps surprisingly, this model actually produces the best single fit between both core-collapse and thermonuclear models, though it underproduces the Mg/Si and Fe/Si ratios. However, due to the overall pattern of abundances found in the SNR, as well as the more broad agreement found with thermonu-

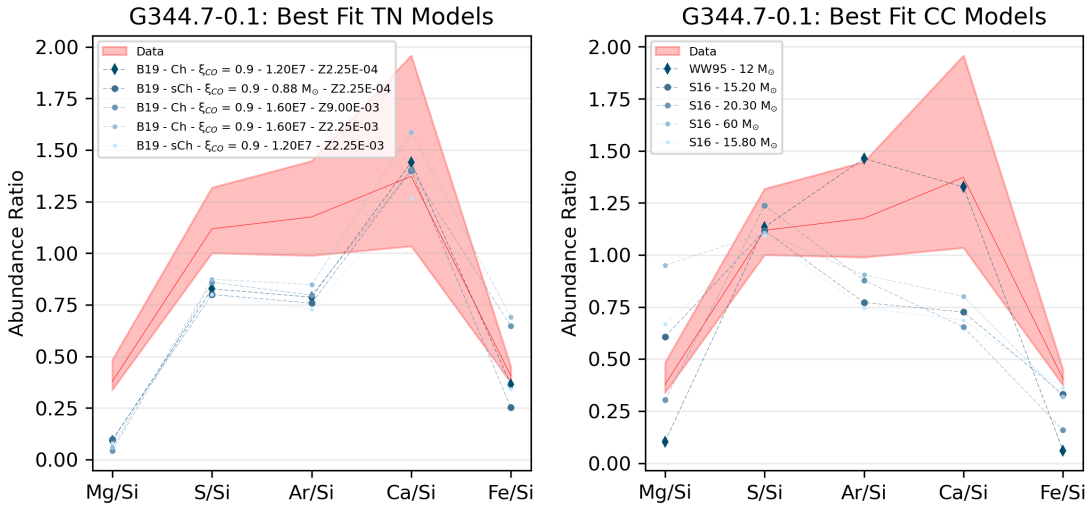

Figure 7.10: Best-fit nucleosynthesis models for G344.7–0.1, comparing to both thermonuclear (TN) and core-collapse (CC) supernova nucleosynthesis yields.

clear models, we suggest a thermonuclear progenitor for this object. In particular, a Ch-mass WD with low metallicity and a low DDT density seems the most likely source.

7.9 G352.7–0.1

G352.7–0.1 was observed in 2002 for 30 ks by *XMM-Newton*. Using this observation, we generated a four-region map through the use of *contbin*. After preliminary testing using the VPSHOCK, VNEI, VRNEI, and VAPEC models, we fit all four of these regions using an absorbed, single-component VNEI model across the $0.5-8.0$ keV energy range. Attempts to fit these regions using a two-component model produced no noticeable improvement. The fitting process began by allowing the column density, plasma temperature, ionisation timescale, and normalisation constant to freely vary. The abundances for Si, S, Fe, Ar, Ca, and Mg were then freed individually and allowed to fit. All regions were well fit, with a $\chi^2_\nu < 1.5$.

Table 7.13: G352.7–0.1: Best fit parameters per region

Parameter	R00	R01	R02	R03
N_H (10^{22} cm^{-2})	$4.75^{+0.77}_{-0.07}$	$3.36^{+0.70}_{-0.31}$	$5.08^{+1.65}_{0.61}$	$4.50^{+2.42}_{-0.09}$
kT (keV)	$1.76^{+0.08}_{-0.36}$	$2.34^{+0.54}_{-0.55}$	$1.98^{+0.15}_{-0.86}$	$3.89^{+0.93}_{-2.24}$
Mg	$3.00^{+1.18}_{-1.18}$	$0.99^{+0.60}_{-0.29}$	$4.55^{+1.53}_{-1.36}$	$1.93^{+2.59}_{-1.91}$
Si	$8.68^{+0.89}_{-0.88}$	$3.60^{+1.08}_{-0.56}$	$8.67^{+1.36}_{-1.15}$	$8.80^{+1.93}_{-1.68}$
S	$7.68^{+0.80}_{-0.76}$	$2.76^{+0.56}_{-0.45}$	$6.18^{+0.94}_{-0.85}$	$7.58^{+1.65}_{-1.38}$
Ar	$6.87^{+2.52}_{-2.40}$	$2.82^{+1.75}_{-1.50}$	$6.31^{+3.58}_{-3.25}$	$3.76^{+4.45}_{-3.76}$
Ca	$13.2^{+7.4}_{-6.6}$	$6.02^{+5.90}_{-4.20}$	-	$12.1^{+11.8}_{-10.5}$
Fe	$15.5^{+5.8}_{-4.4}$	$1.40^{+2.27}_{-0.75}$	$11.2^{+6.2}_{-5.4}$	$8.08^{+11.9}_{-5.28}$
τ (10^{10} s cm^{-3})	$3.92^{+1.68}_{-3.77}$	$2.62^{+0.66}_{-0.33}$	$2.59^{+0.86}_{-0.55}$	$2.52^{+3.08}_{-0.21}$
χ^2_ν (DoF)	1.10 (251)	1.43 (242)	1.05 (246)	0.98 (221)

The spectral fits for G352.7–0.1 can be found in Table 7.13. Column densities show minor variation across the remnant, ranging between $3.36 - 5.08 \times 10^{22}$ cm^{-2}. Plasma temperatures are high across the remnant, ranging from $1.79 - 3.89$ keV, and ionisation timescales are consistently low, ranging from $2.52 - 3.92 \times 10^{10}$ cm^{-3} s, indicative that the remnant is still in a state of NEI. The elemental abundances are consistently enhanced to super-solar values, though R01 does exhibit notably lower abundances than the three other regions. Zhang et al. (2023) notes interaction with a nearby molecular cloud in the general vicinity of this region, which could explain the discrepancy in abundances.

We can compare our results to those of previous studies. Kinugasa et al. (1998) studied the SNR using *ASCA*, fitting the global spectrum with an absorbed NEI model, finding a lower column density (2.9×10^{22} cm^{-2}) and higher ionisation timescale ($\sim 10^{11}$ cm^{-3} s), but comparable plasma temperature (2.0 keV) and abundances for Si and S; they were unable to

determine the abundances for any other elements, owing to the limitations of *ASCA*. Giacani et al. (2009), using *XMM-Newton* data, performed a similar study and found results that were quite close to those of Kinugasa et al. (1998), save for finding a lower ionisation timescale (4.5×10^{10} cm^{-3} s) which more closely agrees with our own findings, alongside being able to probe the Ar abundance and finding it enhanced. Pannuti et al. (2014) performed a spatially-resolved study using *Chandra* data, using both an absorbed single-component VNEI model, as well as an absorbed two-component VNEI model. In both cases, they found ionisation timescales that were similar to our own; however, their single-component study found plasma temperatures and column densities that were notably lower than our findings. Their two-component study, however, produced results much more closely aligned with our own. Both studies only probed the abundances of Si and S, and found comparable results. Perhaps the most relevant study is that of Dang et al. (2024), as it is both the most recent result, and made use of the same *XMM-Newton* data as us. We find that their values for the column density ($3.85 - 4.66 \times 10^{22}$ cm^{-2}), plasma temperature ($0.99 - 3.77$ keV), and ionisation timescale ($2.14 - 6.11 \times 10^{10}$ cm^{-3} s) are all comparable to our findings, and the general abundance pattern of enhanced ejecta is largely identical.

In comparing to models of supernova nucleosynthesis, we find a rather consistent result of a Ch-mass progenitor from B19. Namely, all five our of best fits emerge from a Ch-mass WD with a medium-high DDT density, low metallicity, and the standard CO reaction rate. These models produce ratios for S/Si, Ar/Si, Ca/Si, and Fe/Si that agree well with our findings; only the Mg/Si ratio is not adequately explained by these models, which produce less then the observed ratio. Core-collapse models – particularly those of a $\sim$ 10 M$_\odot$ progenitor – are also able to reproduce our results, but the majority of core-collapse models are incapable

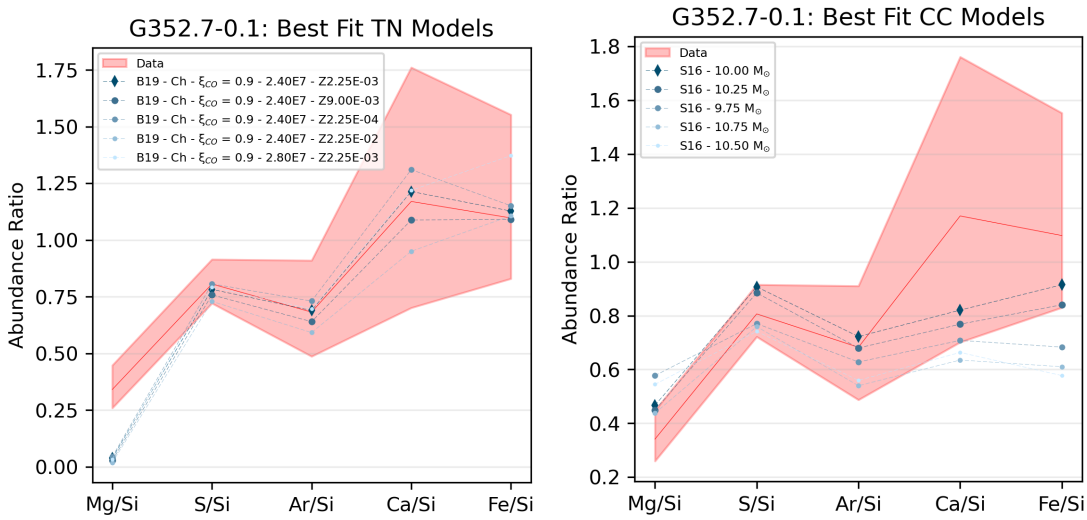

Figure 7.11: Best-fit nucleosynthesis models for G352.7−0.1, comparing to both thermonuclear (TN) and core-collapse (CC) supernova nucleosynthesis yields.

of reproducing the observed Fe/Si ratio, and the overall abundance pattern is notably more favourable towards thermonuclear models. As such, we suggest a low-metallicity, medium DDT-density, Ch-mass WD progenitor for this SNR.

7.10 N0505−67.9

The LMC SNR N0505−67.9 was observed by *XMM-Newton* for just under 130 ks. From this, seven regions were generated through the use of the *contbin* algorithm. We initially fit these regions with a absorbed, single-component thermal models (using the TBVARABS absorption model, with abundances set to the average LMC abundances), testing the VPSHOCK, VNEI, VRNEI, and VAPEC models. While we found that a VPSHOCK model produced the most acceptable fit, we also found that that a single-component model was insufficient to obtain good fits to our regions. We thus added a second VPSHOCK compo-

Table 7.14: N0505–67.9: Best fit parameters per region

Parameter	R00	R01	R02	R03	R04	R05	R06
kT_c (keV)	$0.21^{+0.01}_{-0.01}$	$0.22^{+0.01}_{-0.01}$	$0.21^{+0.01}_{-0.01}$	$0.20^{+0.01}_{-0.01}$	$0.20^{+0.01}_{-0.01}$	$0.20^{+0.01}_{-0.01}$	$0.21^{+0.01}_{-0.01}$
τ_c (10^{13} s cm^{-3})	$0.62^{+1.17}_{-0.18}$	$0.26^{+0.51}_{-0.02}$	$4.79^{+0.19}_{-0.62}$	$4.91^{+0.08}_{-1.32}$	$4.95^{+0.04}_{-0.63}$	$4.91^{+0.07}_{-1.72}$	$4.62^{+0.36}_{-0.89}$
kT_h (keV)	$0.81^{+0.02}_{-0.02}$	$0.80^{+0.01}_{-0.02}$	$0.79^{+0.03}_{-0.01}$	$0.78^{+0.05}_{-0.01}$	$0.80^{+0.01}_{-0.02}$	$0.82^{+0.01}_{-0.01}$	$0.84^{+0.02}_{-0.02}$
O	$0.50^{+0.29}_{-0.13}$	-	$0.31^{+0.09}_{-0.08}$	$0.61^{+0.06}_{-0.04}$	$0.20^{+0.14}_{-0.11}$	$0.56^{+0.16}_{-0.03}$	$0.39^{+0.18}_{-0.04}$
Ne	$0.84^{+0.38}_{-0.07}$	$1.27^{+0.43}_{-0.14}$	$0.95^{+0.10}_{-0.19}$	$0.99^{+0.02}_{-0.05}$	$0.92^{+0.11}_{-0.07}$	$1.18^{+0.18}_{-0.04}$	$1.01^{+0.28}_{-0.06}$
Mg	$1.08^{+0.33}_{-0.04}$	$1.42^{+0.32}_{-0.09}$	$0.91^{+0.13}_{-0.10}$	$0.96^{+0.11}_{-0.06}$	$0.97^{+0.13}_{-0.02}$	$1.26^{+0.22}_{-0.07}$	$1.12^{+0.13}_{-0.09}$
Si	$1.30^{+0.37}_{-0.03}$	$1.45^{+0.29}_{-0.12}$	$1.10^{+0.05}_{-0.07}$	$1.01^{+0.10}_{-0.06}$	$1.27^{+0.09}_{-0.06}$	$1.35^{+0.28}_{-0.06}$	$1.18^{+0.13}_{-0.05}$
S	$1.53^{+0.59}_{-0.08}$	$1.31^{+0.34}_{-0.16}$	$1.34^{+0.24}_{-0.12}$	$1.12^{+0.19}_{-0.21}$	$1.21^{+0.12}_{-0.10}$	$1.23^{+0.19}_{-0.09}$	$0.96^{+0.12}_{-0.16}$
Fe	$2.26^{+0.46}_{-0.03}$	$1.77^{+0.22}_{-0.08}$	$1.37^{+0.14}_{-0.05}$	$0.91^{+0.16}_{-0.04}$	$1.29^{+0.13}_{-0.04}$	$1.48^{+0.22}_{-0.06}$	$1.30^{+0.12}_{-0.08}$
τ_h (10^{11} s cm^{-3})	$3.70^{+1.58}_{-0.42}$	$6.17^{+2.18}_{-0.60}$	$4.28^{+1.11}_{-1.05}$	$2.61^{+0.10}_{-0.32}$	$3.12^{+1.02}_{-0.36}$	$3.98^{+0.62}_{-0.50}$	$4.11^{+1.59}_{-0.44}$
Line Centroid (keV)	$1.24^{+0.01}_{-0.01}$	$1.25^{+0.01}_{-0.01}$	$1.24^{+0.1}_{-0.01}$	$1.24^{+0.01}_{-0.01}$	$1.25^{+0.01}_{-0.01}$	$1.23^{+0.01}_{-0.01}$	$1.25^{+0.02}_{-0.01}$
χ^2_ν (DoF)	1.34 (782)	1.52 (813)	1.22 (801)	1.41 (803)	1.42 (776)	1.33 (839)	1.39 (827)

nent, with the abundances set to average LMC abundances. The column density was fixed to a value of $N_H = 0.170 \times 10^{22}$ cm^{-2}, and we allowed the plasma temperatures, ionisation timescales, and normalisation constants to vary independently before freeing the abundances of Si, S, Fe, Mg, Ne, and O one at a time to freely fit. Six of the seven regions were well fit with $\chi^2_\nu < 1.5$, while one was only slightly worse at $\chi^2_\nu = 1.52$.

The results of this spectral fitting can be seen in Table 7.14. The cold component features temperatures that are consistent across the remnant at $0.20 - 0.22$ keV, while the ionisation timescale shows some variation, with the two innermost regions R00 and R01 exhibiting a timescale an order of magnitude lower than the rest of the regions. These high ionisation timescales are such that the cold component is likely to be in a state of CIE; however, as these parameters of our fit were relatively consistent and well constrained, we opted to maintain the

use of a VNEI model to represent this component. The hot component shows similarly consistent plasma temperatures, ranging from $0.78 - 0.84$ keV., while the ionisation timescale exhibits a range between $2.61 - 6.17 \times 10^{11}$ cm^{-3} s. The abundances are largely consistent across the SNR. O shows sub-solar abundances in all regions, while Ne and Mg are slightly enhanced in some regions, while being slightly sub-solar in others. All other abundances are consistently enhanced above solar, though not significantly, with the Fe in R00 being the only abundance that is enhanced to more than twice that of solar abundances. R03 – the outermost region just outside of the bright outer rim – exhibits the lowest average abundances, alongside the lowest ionisation timescale in the hot component, suggesting that may have only recently been shock-heated.

We can compare our results to those of previous studies. Hughes et al. (2003), using *Chandra* data, studied four small regions within the SNR: two in the object's core, and two along its outer rim. Each region was fit with an absorbed NEI thermal model. They found plasma temperatures of $0.41 - 0.67$ keV, and ionisation timescales of 6.3×10^{10} to 4.6×10^{11} cm^{-3} s. While these are somewhat lower than our own findings, the value we used for our hydrogen column density is greater than the values that they found, which could explain the discrepancy. For abundance values, they studied the same elements as did our work, and found similar values: namely, that the abundances in the SNR are not significantly enhanced, and tend to remain close to solar values. They also found notably lower abundances in their "rim" regions than in their "core" regions, and we find a similar reduction in abundances in the outer regions as opposed to inner regions. Another study to which we can compare is van der Heyden et al. (2003), who used *XMM-Newton* data to fit the shell and central regions with NEI plasma models. The shell – which they fit with two NEI components – exhibited plasma

temperature of 0.36 and 0.79 keV and ionisation timescales of 4.7×10^{10} and 1.11×10^{11}, $\mathrm{cm}^{-3}\,\mathrm{s}$ both of which are quite close to our findings. Lastly, we can compare to Alan & Bilir (2022), who used *Chandra* data to perform a spatially-resolved study of the SNR. They fit the spectra of the interior regions with two-component VPSHOCK models, and found a wide range of values for the plasma temperature ($0.30 - 1.08$ keV) and ionisation timescale that range between $\sim 10^{10}$ and $\sim 10^{12}\ \mathrm{cm}^{-3}\,\mathrm{s}$. While our findings do not exhibit quite so large a range, they do fall within the same range. The abundance values they found are typically lower than our own: most notably, our determined abundance of Si is typically three to four times greater than their reported values, while O and Fe are comparable in some circumstances. This can in part be explained by their use of the solar abundances of Anders & Grevesse (1989), but it is more likely owed to the fact that our regions are notably larger, and thus more likely to be affected by some degree of inter-region contamination.

Agreement with any model of supernova nucleosynthesis for N0505–67.9 is poor. For thermonuclear models, this disagreement largely arises due to the ratios of lower-mass elements O/Si, Ne/Si, and Mg/Si, as these ratios are significantly higher in our observations that those found in any thermonuclear model. The S/Si ratio fares better, with multiple models of high DDT-density Ch-mass progenitors or high-mass subCh-mass progenitors from B19 being able to reproduce the S/Si ratio. The Fe/Si ratio fares better still, as a wide variety of models are able to reproduce it, with the models of LN18 proving most successful while also being able to reproduce the S/Si ratio in some cases. Core-collapse models fare better, in that the O/Si, Ne/Si, and Mg/Si ratios are all reproducible within the existing models. However, no model proves capable of reproducing these ratios simultaneously, and very few are able to reproduce any two. The S/Si ratio shows more general agreement, with a large number

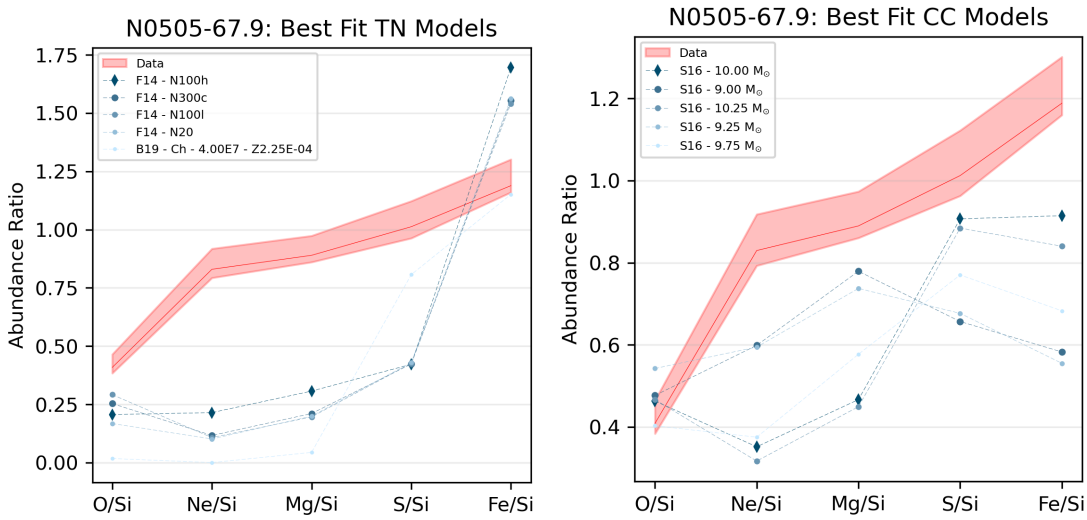

Figure 7.12: Best-fit nucleosynthesis models for N0505–67.9, comparing to both thermonuclear (TN) and core-collapse (CC) supernova nucleosynthesis yields.

of models – most notably, those from S16 above 15.0 $M_\odot$ – producing similar yields. The Fe/Si ratio, meanwhile, cannot be matched by any core-collapse model, all of which produce less than the observed abundance. While the overall abundance pattern more closely matches those of core-collapse supernovae, we are unable to draw any firm conclusions from our results.

7.11 N0509–67.5

A 44.3 ks observation of N0509–67.5, taken by *XMM-Newton* in 2000, was used for our study, which resulted in a region map comprised of four regions. We found that an absorbed two-component VPSHOCK+VAPEC model produced the best fits across these four regions, with the abundances of the VAPEC component set to the average abundance of the LMC. The column density was fixed to a value of $N_H = 0.166 \times 10^{22}$ cm^{-2}, while the plasma

Table 7.15: N0509–67.5: Best fit parameters per region

Parameter	R00	R01	R02	R03
kT_c (keV)	$0.41^{+0.02}_{-0.02}$	$0.38^{+0.02}_{-0.02}$	$0.37^{+0.02}_{-0.02}$	$0.40^{+0.02}_{-0.02}$
Ne	$1.72^{+0.18}_{-0.13}$	$1.64^{+0.17}_{-0.20}$	$1.38^{+0.14}_{-0.13}$	$1.33^{+0.15}_{-0.10}$
Mg	$0.82^{+0.39}_{-0.49}$	$1.05^{+0.38}_{-0.40}$	$0.76^{+0.36}_{-0.37}$	$0.92^{+0.32}_{-0.43}$
Si	$44.0^{+7.7}_{-5.3}$	$52.4^{+9.2}_{-7.0}$	$52.2^{+9.3}_{-6.7}$	$51.0^{+9.3}_{-6.1}$
S	$66.4^{+10.4}_{-8.1}$	$74.9^{+10.4}_{-8.7}$	$77.9^{+10.7}_{-9.2}$	$70.5^{+11.1}_{-8.9}$
Fe	$2.94^{+0.42}_{-0.39}$	$2.67^{+0.45}_{-0.43}$	$2.69^{+0.45}_{-0.38}$	$2.58^{+0.39}_{-0.37}$
τ_c (10^{11} s cm^{-3})	$3.81^{+0.15}_{-0.91}$	$5.31^{+2.75}_{-1.42}$	$4.91^{+2.06}_{-1.44}$	$3.86^{+1.94}_{-0.99}$
kT_h (keV)	$3.41^{+2.01}_{-0.68}$	$4.24^{+4.63}_{-1.26}$	$4.86^{+4.53}_{-1.47}$	$3.63^{+1.76}_{-0.65}$
Line Centroid (keV)	$1.21^{+0.02}_{-0.02}$	$1.19^{+0.03}_{-0.04}$	$1.16^{+0.04}_{-0.06}$	$1.21^{+0.02}_{-0.02}$
χ^2_ν (DoF)	1.10 (496)	1.27 (498)	1.42 (501)	1.27 (513)

temperatures, ionisation timescales, and normalisation constants of both components were freed initially and allowed to vary independently, before the Si, S, Fe, Mg, and Ne of the VPSHOCK component were freed one at a time and allowed to vary. Excess emission was noted around 1.2 keV, and a Gaussian was added to compensate. As a result, all four regions were well-fit, with $\chi^2_\nu < 1.5$.

The final results of our spectral fits for N0509–67.5 can be found in Table 7.15. The plasma temperatures for the cold component is consistent, with a range between $0.37 - 0.41$ keV across the four regions, while the plasma temperature in the hot component shows slightly more variation, ranging between $3.41 - 4.86$ keV. The ionisation timescales are also quite similar, between $3.81 - 5.31 \times 10^{11}$ cm^{-3} s. Elemental abundances are consistent across the remnant, but vary greatly from element to element: Ne and Fe are slightly enhanced, Mg is slightly below solar abundances, and both S and Si are significantly enhanced

to abundances around $50\times$ those of solar.

We can compare these results to those of previous studies, such as that of Warren & Hughes (2004), who performed a global fit using *Chandra* data. With an NEI model, they found a notably higher plasma temperature and lower ionisation timescale than we did; however, they also opted to fit for the hydrogen column density, which resulted in a value lower than our own. Their abundances are similarly enhanced in comparison to our own, resulting in similar ratios. However, the absolute abundances are lower, which could be explained by their using the solar abundances of Anders & Grevesse (1989). Kosenko et al. (2008) performed a similar global fit, using the data from *XMM-Newton* EPIC and RGS to fit an NEI model to the SNR's global spectrum. They find similar values for the plasma temperature and ionisation timescale as Warren & Hughes (2004); however, it is unclear what value they used for the hydrogen column density. Their abundance values are reported in terms of ratios, and appear largely consistent with our own findings.

In comparing our results to models of supernova nucleosynthesis, we find a moderate amount of agreement with both thermonuclear and core-collapse models, though for different reasons. For the thermonuclear models, there is good agreement with the Ne/Si and Mg/Si ratios across the vast majority of models. Issues arise when comparing to the S/Si and Fe/Si ratios: the S/Si ratio is quite high, and can only be matched by a select few models. The Fe/Si ratio, on the other hand, is quite low, and only the very low mass explosions of LN20b are able to replicate it. However, it is worth noting that the higher-energy regime in which the most prominent Fe K emission is found was notably absent in our study, likely owing to the lower duration of the observation. It is possible, then, that the Fe present in the SNR is higher than observed, and that our findings may be more akin to a lower limit on the Fe/Si

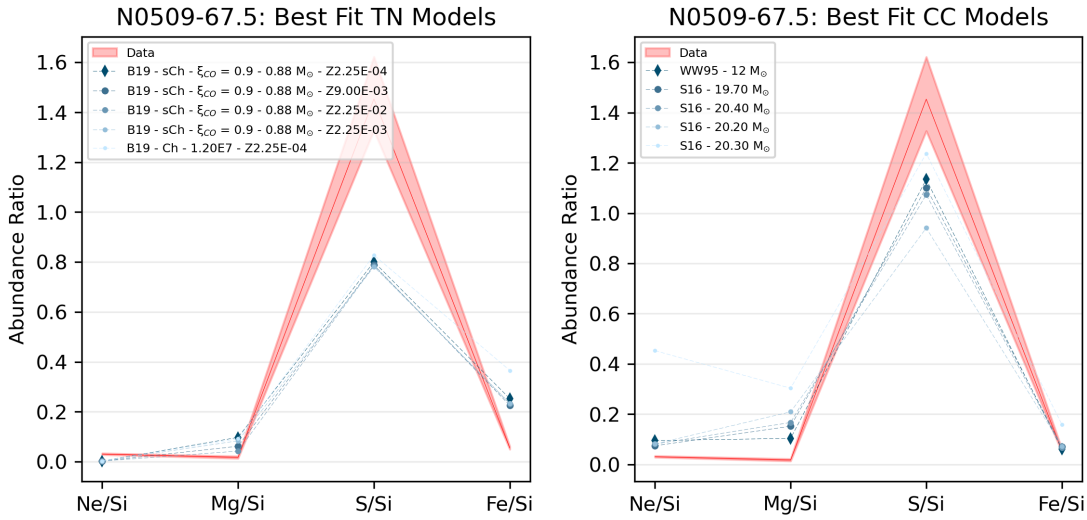

Figure 7.13: Best-fit nucleosynthesis models for N0509−67.5, comparing to both thermonuclear (TN) and core-collapse (CC) supernova nucleosynthesis yields.

ratio. Should this be the case, then we would find a much stronger agreement with the thermonuclear models: namely, the low-density, low-metallicity progenitors of LN18, and the D^6 model of T18 are all capable of producing abundance ratios that very nearly match our own for Ne/Si, Mg/Si, and S/Si, but produce a larger Fe/Si ratio than is observed at present.

Core-collapse models fare better on average when comparing to the S/Si and Fe/Si ratios, but tend to produce more Ne and Mg than we find in the SNR, and thus the Ne/Si and Mg/Si ratios fare worse. Models with progenitors between $19 - 21\ M_\odot$ from S16, alongside the $12\ M_\odot$ model of WW95, produce the closest fits among core-collapse models. However, due to the closer matching of the Ne/Si and Mg/Si ratios, alongside the possibility of missing emission from the Fe K-shell, we suggest a low-mass, low-metallicity, subCh-mass WD progenitor for this SNR.

7.12 N0509–68.7

N0509–68.7 was observed by *XMM-Newton* for 26.5 ks in 2000. A variety of filters were used for this observation: the MOS1 observations were taken in both Large Window, Medium Filter mode, as well as Large Window, Thin Filter mode; the MOS2 observation was taken in Full Window, Medium Filter mode; and the pn observation was taken in both Full Window, Medium Filter mode, as well as Small Window, Medium Filter mode. Each of these different modes were processed and filtered individually, and after initial filtering, applying the *contbin* algorithm to this observation resulted in the generation of four regions. One-component models proved insufficient to reproduce the spectra for these regions; after testing, we found that an absorbed, two-component VAPEC+VPSHOCK model most accurately fit the data. The abundances of the VAPEC component were set to the average LMC abundances, the column density was set to a value of $\mathrm{N_H} = 0.255 \times 10^{22}\ \mathrm{cm}^{-2}$, and the electron temperatures, ionisation timescales, and normalisation constants were freed and allow to vary independently. Following that, the abundances in the VPSHOCK component were freed one at a time and allowed to fit, in the order of Si, S, Fe, Ar, Ca, Mg, Ne, O. In each region, we found an underfitting of the spectrum around 1.2 keV, likely representing emission from the Fe L-shell complex that is not accounted for in the NEI code present in XSPEC. To compensate, we added a Gaussian at 1.2 keV; all other parameters were frozen to their best-fit values while the Gaussian was allowed to fit, after which this was reversed, freezing the Gaussian to its newest fit results while allowing the other parameters to vary once more. Finally, both the thermal models and the Gaussian were freed and allowed to fit, which produced our final results, with each region being very well fit ($\chi^2_\nu < 1.25$).

Table 7.16: N0509–68.7: Best fit parameters per region

Parameter	R00	R01	R02	R03
kT_c (keV)	$0.74^{+0.01}_{-0.02}$	$0.74^{+0.02}_{-0.01}$	$0.75^{+0.02}_{-0.02}$	$0.76^{+0.02}_{-0.01}$
kT_h (keV)	$3.03^{+0.68}_{-0.42}$	$3.08^{+0.97}_{-0.50}$	$3.44^{+0.47}_{-0.60}$	$2.89^{+0.32}_{-0.47}$
O	$1.34^{+0.52}_{-0.21}$	$1.39^{+0.63}_{-0.19}$	$1.27^{+0.56}_{-0.23}$	-
Ne	$3.11^{+1.85}_{-0.88}$	$2.76^{+2.42}_{-0.72}$	$1.84^{+1.97}_{-0.96}$	$2.05^{+1.09}_{-0.92}$
Mg	$0.93^{+0.86}_{-0.63}$	$1.70^{+1.05}_{-0.42}$	$2.31^{+1.04}_{-0.40}$	$0.85^{+0.72}_{-0.65}$
Si	$7.79^{+2.90}_{-1.20}$	$8.34^{+3.96}_{-1.41}$	$11.3^{+3.3}_{-1.7}$	$8.06^{+1.38}_{-0.91}$
S	$8.20^{+2.47}_{-1.38}$	$9.33^{+3.98}_{-1.62}$	$11.5^{+3.7}_{-1.6}$	$8.63^{+1.53}_{-1.15}$
Ar	$10.5^{+4.8}_{-2.8}$	$12.1^{+5.4}_{-2.9}$	$12.7^{+7.2}_{-1.4}$	$8.75^{+4.39}_{-2.67}$
Ca	$7.32^{+6.24}_{-4.35}$	$10.8^{+14.1}_{-4.0}$	$18.9^{+9.0}_{-5.3}$	$7.28^{+7.80}_{-4.80}$
Fe	$2.42^{+1.15}_{-0.58}$	$3.23^{+1.67}_{-0.83}$	$5.12^{+1.61}_{-0.91}$	$3.24^{+0.66}_{-0.58}$
τ_h ($\times 10^{11}$ s cm^{-3})	$1.20^{+0.30}_{-0.19}$	$1.09^{+0.29}_{-0.17}$	$1.10^{+0.26}_{-0.15}$	$1.34^{+0.31}_{-0.21}$
Line Centroid (keV)	$1.29^{+0.03}_{-0.03}$	$1.25^{+0.01}_{-0.01}$	$1.24^{+0.01}_{-0.01}$	$1.27^{+0.02}_{-0.03}$
χ^2_ν (DoF)	1.20 (1080)	1.07 (1060)	1.11 (1071)	1.09 (1070)

Our final results for N0509–68.7 can be seen in Table 7.16. The plasma temperatures for the cold component are consistent across the remnant, ranging between $0.74 - 0.76$ keV, while those of the hot component exhibit slightly more variation, going from 2.89 keV up to 3.44 keV. The elemental abundances in the hot component are notably enhanced above solar abundances for all elements, and tend to increase in regions further from the centre of the SNR. R03 – the outermost region of the SNR – is an exception to this, as it exhibits abundances similar to that of the innermost region, R00. The ionisation timescales are quite consistent across the SNR, ranging between $1.09 - 1.34 \times 10^{11}$ cm^{-3} s.

We are able to compare our results to those of van der Heyden et al. (2002), who used data from both *Chandra* and *XMM-Newton*. They fit an absorbed three-component NEI model

to the global spectrum, finding plasma temperatures of 0.55, 0.65, and 3.5 keV, alongside ionisation timescales of 2.3×10^{10}, $> 250 \times 10^{10}$, and 5.3×10^{10} $\mathrm{cm}^{-3}\,\mathrm{s}$. Their second component aligns rather well with our VAPEC component, as the high ionisation timescale suggests a component that is in or near-to CIE. Their third component, similarly, aligns well with our VPSHOCK component. In terms of abundances, we find slightly more uniform abundance ratios than their study, particularly amongst the Ar/Si and Ca/Si ratios. This is likely due to the global nature of their study, as the global spectrum may be more strongly influenced by the regions with higher abundance values.

The nucleosynthesis models for N0509–68.7 tend to favour Ch-mass WDs with a low DDT-density and low metallicity, and the models with a reduced CO reaction rate from B19 tend to fare better than those with the standard CO reaction rate. The general abundance pattern tends to closely follow these models, though only the Ca/Si ratio can be reliably reproduced within error. The Mg/Si and S/Si ratios found in the models tend to be slightly lower than our observations, while the O/Si, Ne/Si, and Ar/Si ratios are underproduced in almost all cases. The Fe/Si ratio can be met by the aforementioned low DDT-density Ch-mass models, but most models produce Fe in greater amounts than is observed in this SNR. Further, the models which are capable of reproducing the Fe/Si ratio do so at the expense of the Ar/Si ratio, which is notably underproduced when the Fe/Si ratio is met.

The single best nucleosynthesis model in terms of fit is the 12 $\mathrm{M}_\odot$ model of WW95, which very accurately reproduces the O/Si, Mg/Si, S/Si, Ar/Si, and Ca/Si ratios. However, this model is an outlier amongst the larger bulk of core-collapse models: while these models are often capable of reproducing the abundance ratios for O, Ne, Mg, S, or Fe, most models cannot do so for more than two such elements. The S16 models between $15 - 18$ $\mathrm{M}_\odot$ are

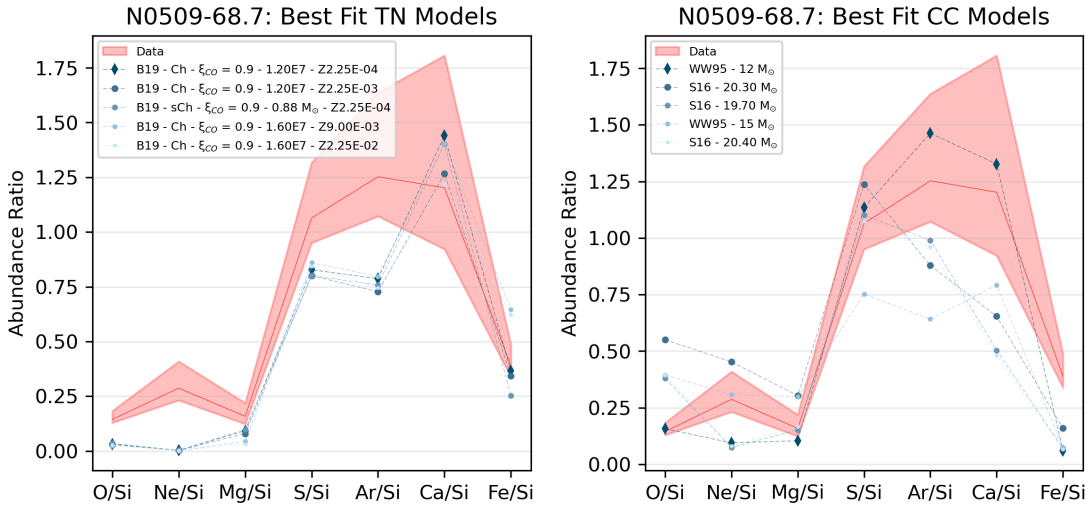

Figure 7.14: Best-fit nucleosynthesis models for N0509−68.7, comparing to both thermonuclear (TN) and core-collapse (CC) supernova nucleosynthesis yields.

generally able to reproduce the S/Si and Fe/Si ratios, while the $19 - 21\ M_\odot$ and $25 - 27\ M_\odot$ models from the same source generally match the Mg/Si and S/Si ratios. As such, and owing to the general pattern of abundances, we consider the low DDT-density, low metallicity Ch-mass models to be the most appropriate models for this SNR.

7.13 N0519−69.0

For N0519−69.0, we made use of a 48.4 ks *XMM-Newton* observation taken in 2001. For this observation, MOS1 made use of both the Full Frame, Medium Filter mode as well as the Full Frame, Thin Filter mode. For both the MOS2 and pn observations, only the Full Frame, Medium Filter mode was used. Each of these different observation modes was processed individually, and after doing so, a map of five regions was generated through the use of *contbin*. We initially tested fitting each region with an absorbed, one-component thermal

Table 7.17: N0519–69.0: Best fit parameters per region

Parameter	R00	R01	R02	R03	R04
kT_c (keV)	$0.40^{+0.03}_{-0.05}$	$0.41^{+0.05}_{-0.04}$	$0.38^{+0.02}_{-0.03}$	$0.36^{+0.01}_{-0.10}$	$0.66^{+0.04}_{-0.03}$
kT_h (keV)	$0.84^{+0.01}_{-0.01}$	$0.83^{+0.02}_{-0.01}$	$0.83^{+0.01}_{-0.01}$	$0.88^{+0.01}_{-0.07}$	$2.19^{+0.37}_{-0.31}$
Ne	-	$1.07^{+0.60}_{-0.74}$	-	$0.61^{+4.23}_{0.01}$	$0.70^{+0.39}_{-0.31}$
Mg	$0.46^{+0.27}_{-0.13}$	$0.29^{+0.19}_{-0.20}$	$0.71^{+0.26}_{-0.18}$	$0.59^{+0.71}_{-0.46}$	$0.77^{+0.18}_{-0.76}$
Si	$2.64^{+0.56}_{-0.26}$	$2.56^{+0.37}_{-0.32}$	$3.40^{+0.52}_{-0.28}$	$3.52^{+2.88}_{-0.02}$	$5.65^{+0.66}_{-0.60}$
S	$4.24^{+0.78}_{-0.51}$	$3.81^{+0.65}_{-0.57}$	$4.72^{+0.76}_{-0.78}$	$5.33^{+4.15}_{-0.15}$	$9.16^{+1.64}_{-1.07}$
Fe	$1.64^{+0.24}_{-0.14}$	$1.47^{+0.22}_{-0.14}$	$1.80^{+0.19}_{-0.14}$	$1.92^{+0.86}_{-0.18}$	$5.85^{+0.53}_{-0.82}$
τ_h (10^{12} s cm^{-3})	$3.77^{+7.47}_{-1.07}$	$3.84^{+4.10}_{-1.64}$	$4.80^{+11.3}_{-1.51}$	$1.66^{+1.79}_{-0.37}$	$0.06^{+0.01}_{-0.01}$
Line Centroid (keV)	$1.25^{+0.01}_{-0.01}$	$1.23^{+0.01}_{-0.01}$	$1.24^{+0.01}_{-0.01}$	$1.22^{+0.02}_{-0.17}$	$1.24^{+0.06}_{-0.01}$
χ^2_ν (DoF)	1.40 (775)	1.26 (766)	1.25 (762)	1.21 (769)	1.28 (769)

model, but this was unable to reproduce our spectra. After adding a second thermal component, we found that best-fits were produced by a VPSHOCK+VAPEC model, where the abundances in the VAPEC component were set to the average abundances of the LMC. We initially proceeded by fixing the column density to $N_H = 0.217 \times 10^{22}$ cm^{-2}, and allowing the plasma temperatures, ionisation timescale, and normalisation constants to fit freely and independently of each other. We then freed and fit the abundances one at a time, in the order of Si, S, Fe, Mg, and Ne. In each of our five regions, we noted excess emission around the 1.2 keV mark, and we again added a Gaussian at this energy in order to compensate. As such, this resulted in each of our regions being well-fit, with a $\chi^2_\nu < 1.5$.

The results of our spectral fits for N0519–69.0 can be found in Table 7.17. Plasma temperatures and ionisation timescales are largely consistent across the remnant, at $0.36 - 0.41$ keV, $1.66 - 4.80 \times 10^{12}$ cm^{-3} s, respectively, and elemental abundances show similar consistency,

with Mg being subsolar, Ne being subsolar or near to solar, and Si, S, and Fe being notably enhanced. The exception to all of this is the outermost region of our study, R04, which shows notably higher values for plasma temperatures and abundances, with a significantly lower ionisation timescale. The high ionisation timescales in the interior regions suggest that the majority of the remnant may be in or near to a state of CIE, while the much lower value in R04 suggests a state of NEI. This, combined with the much higher plasma temperature in this region, could be indicative of a blast wave origin; however, the enhanced metal abundances – both in general, and with respect to the rest of the SNR – make this an unlikely scenario.

The only previous study to which we can compare our spectroscopic results is that of Kosenko et al. (2010), who used data from both *XMM-Newton* and *Chandra* to analyse the SNR. One of the methods that they used to do so was a one-component NEI model. From their one-component model, they determined plasma temperatures between $1.73 - 2.88$ keV and ionisation timescales between $2.22 - 3.9 \times 10^{10}$, dependant upon which instruments were being used. They did not directly report the abundances determined from this fit, but did provide a figure showing the ratios with respect to Si, which reflect fairly well our own findings. Curiously, their plasma temperature and ionisation timescales are notably higher than what we found in the majority of our regions – the exception to this being R04, in which our results agree quite well with theirs. It is possible, then, that their analysis was biased towards emission from the outer regions of the SNR, which could explain the discrepancy between their results and ours for the remaining regions.

From a nucleosynthesis perspective, the abundances within N0519–69.0 are well reproduced by models of both thermonuclear and core-collapse supernovae. The Ne/Si and Mg/Si

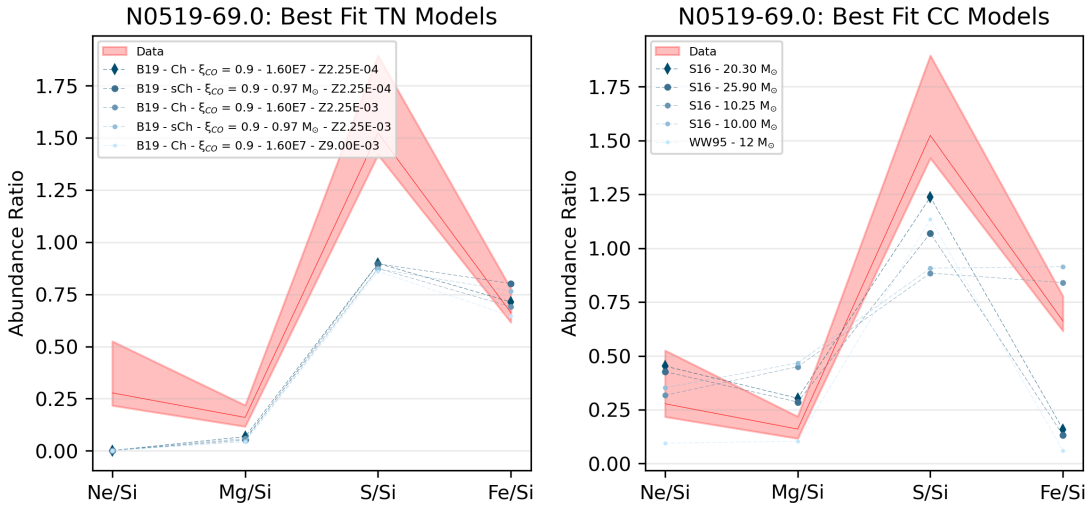

Figure 7.15: Best-fit nucleosynthesis models for N0519−69.0, comparing to both thermonuclear (TN) and core-collapse (CC) supernova nucleosynthesis yields.

ratios are more frequently reproduced by core-collapse models, though the majority of such models produce greater amounts of these elements than observed, whereas thermonuclear models tend to produce less. The S/Si and Fe/Si ratios, meanwhile, are more closely reproduced by thermonuclear models. The S/Si ratio in particular, however, is only able to be matched by two models: the C-DEF model of M10, and the low-density $Z = 0.1$ model of LN18, both of which are thermonuclear models. For the Fe/Si ratio, the thermonuclear models generally produce higher amounts than are observed, but models with low-density explosions tend to come closer. Given the overall pattern of abundances, a thermonuclear origin is more likely, and under that assumption, a low-energy explosion stemming from a lower mass / lower density WD with low metallicity seems the most probably scenario.

Table 7.18: N0534–69.9: Best fit parameters per region

Parameter	R00	R01	R02	R03	R04	R05
kT (keV)	$0.54^{+0.12}_{-0.08}$	$0.69^{+0.11}_{-0.03}$	$0.68^{+0.05}_{-0.10}$	$0.72^{+0.13}_{-0.06}$	$0.88^{+0.18}_{-0.15}$	$0.66^{+0.09}_{-0.07}$
O	$0.38^{+0.02}_{-0.06}$	$0.47^{+0.15}_{-0.05}$	$0.56^{+0.11}_{-0.12}$	$0.62^{+0.29}_{-0.08}$	$0.66^{+0.24}_{-0.15}$	$0.90^{+0.31}_{-0.17}$
Ne	$0.58^{+0.82}_{-0.08}$	$1.08^{+0.27}_{-0.15}$	$1.03^{+0.21}_{-0.19}$	$1.21^{+0.53}_{-0.13}$	$1.03^{+0.30}_{-0.21}$	$1.30^{+0.43}_{-0.23}$
Mg	$0.54^{+0.61}_{-0.12}$	$0.66^{+0.09}_{-0.09}$	$0.66^{+0.10}_{-0.63}$	$0.83^{+0.44}_{-0.17}$	$0.64^{+0.35}_{-0.24}$	$0.83^{+0.46}_{-0.30}$
Si	$0.32^{+0.29}_{-0.19}$	$0.90^{+0.55}_{-0.27}$	$0.78^{+0.45}_{-0.30}$	$1.27^{+0.79}_{-0.28}$	$0.98^{+0.57}_{-0.37}$	$1.54^{+0.89}_{-0.58}$
Fe	$0.54^{+0.40}_{-0.13}$	$1.42^{+0.57}_{-0.17}$	$1.30^{+0.31}_{-0.36}$	$1.77^{+0.96}_{-0.24}$	$1.73^{+0.69}_{-0.45}$	$1.54^{+0.63}_{-0.32}$
τ (10^{10} s cm^{-3})	$10.9^{+9.4}_{-10.9}$	$6.95^{+1.29}_{-2.25}$	$4.20^{+2.50}_{-7.64}$	$4.05^{+0.88}_{-1.23}$	$2.90^{+1.26}_{-0.76}$	$3.56^{+1.03}_{-0.81}$
Line Centroid (keV)	-	$1.25^{+0.01}_{-0.01}$	$1.25^{+0.08}_{-0.01}$	$1.26^{+0.02}_{-0.02}$	$1.26^{+0.02}_{-0.02}$	$1.27^{+0.03}_{-0.02}$
χ^2_ν (DoF)	1.15 (349)	1.19 (429)	1.05 (408)	1.40 (415)	1.31 (404)	1.25 (395)

7.14 N0534–69.9

N0534–69.9 has one *XMM-Newton* observation with a length of 61.9 ks. After standard processing and filtering, the *contbin* algorithm produced a map consisting of six regions from which spectra were extracted. Each region was tested with a VPSHOCK, VNEI, VRNEI, and VAPEC model, all multiplied by a TBVARABS absorption model, and we found that the absorbed VPSHOCK model produced the best fits across remnant. To produce our fits, we first set the column density to a value of $N_H = 0.255 \times 10^{22}$ cm^{-2} before the plasma temperature, ionisation timescale, and normalisation constant were allowed to vary. We then freed the abundances for Si, Fe, Mg, Ne, and O one at a time, fitting each individually. For the regions R01 through R05, there was notable excess emission around 1.2 keV; this was fit by adding a Gaussian to our fits after the rest of the spectra had been fit by the thermal model. The result of this was each region being well-fit ($\chi^2_\nu < 1.5$) by the absorbed VPSHOCK model.

Our spectral fits for N0534–69.9 can be seen in Table 7.18. The plasma temperatures range from $0.54 - 0.88$ keV, with a general trend to increase the closer to the edges of the remnant one gets. O, Ne, Mg, Si, and Fe all followed similar patterns, with O and Mg being subsolar, while Ne and Fe were typically supersolar. The ionisation timescale behaved counter to this, tending to decrease the closer to the edge the region in question was; this parameter ranged from $2.90 - 6.95 \times 10^{10}\ \mathrm{cm}^{-3}\ \mathrm{s}$, except for the brightest region R00, where it was notably higher at $10.9 \times 10^{11} \mathrm{cm}^{-3}\ \mathrm{s}$; however, this value was poorly constrained in comparison to the other regions. Given that the largest ionisation timescale is on the order of $10^{11}\ \mathrm{cm}^{-3}\ \mathrm{s}$, the remnant appears to still be in NEI.

We only have one previous study of N0534–69.9 to which we can compare our results: that of Hendrick et al. (2003). They performed a spatially-resolved spectroscopic study of the object using *Chandra* data, but opted not to cover the entire remnant with their region selection, choosing instead four distinct regions: two smaller regions in the centre, which can be approximately correlated with our R00 and R01; one smaller region along the north-western edge, which has overlap with our R02; and one larger region covering the southern edge, which largely matches our R03. They found plasma temperatures for the edges of 0.33 and 0.34 keV, which is lower than our findings. They also found ionisation timescales of 2.43×10^{11} and $2.63 \times 10^{11}\ \mathrm{cm}^{-3}\ \mathrm{s}$ for these regions, which are higher than ours. However, their abundances in these regions (save for that of Ne, which ranged between $0.59 - 0.68$) were not allowed to vary, and instead were frozen to a value of 0.4 times solar to account for LMC abundances. Our abundances were allowed to freely vary, and as a result were broadly higher, which could explain these discrepancies. Their fits to the central regions produced plasma temperatures of $0.61 - 0.92$ keV, comparable to our findings. Their ionisation

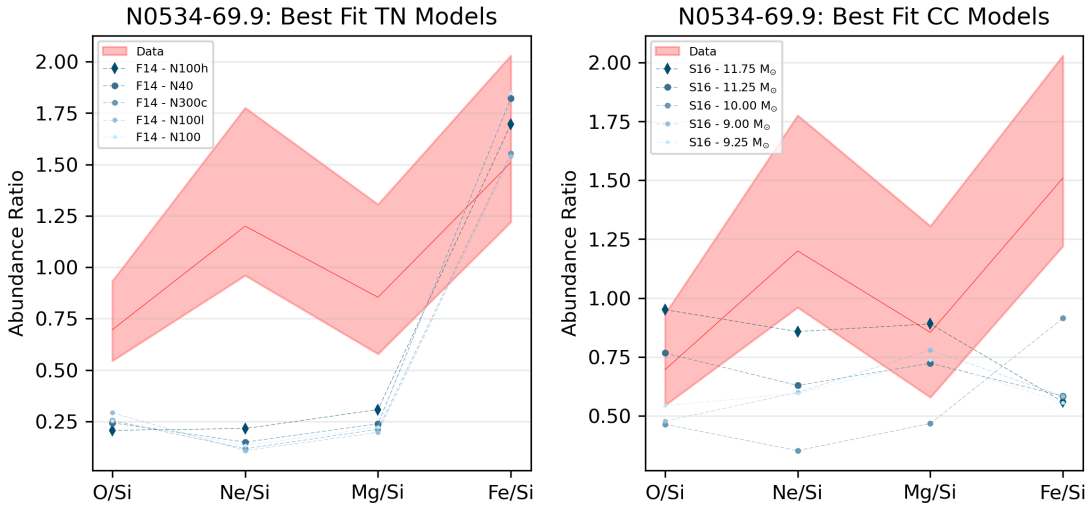

Figure 7.16: Best-fit nucleosynthesis models for N0534−69.9 comparing to both thermonuclear (TN) and core-collapse (CC) supernova nucleosynthesis yields.

timescales were 0.97×10^{11} and 1.46×10^{11} cm^{-3} s, which are quite close to our findings in these regions.

As the supernova origin of N0534−69.9 has not been thoroughly studied, we compared the results of our spectroscopic study to models of both thermonuclear and core-collapse supernova nucleosynthesis. In general, the Fe/Si ratio is highly favourable to a thermonuclear origin, while the O/Si, Ne/Si, and Mg/Si ratios are suggestive of a core-collapse source. Of the thermonuclear models, the models of F14 – specifically, the N100H model – yielded the closest agreement to the observations, reproducing the Fe abundance very well but underproducing the abundances for O, Ne, and Mg. Core-collapse models fared slightly better, with the models of S16 for a star whose mass is in the range of $9 - 12$ $\mathrm{M}_\odot$ producing the best results. The best fit overall came from the 11.75 $\mathrm{M}_\odot$ model of S16, which was able to very closely reproduce the abundance ratios of O and Mg, but underproduced Fe. The 30

$M_\odot$ model of N06 was also able to reproduce values for the O/Si, Ne/Si, and Mg/Si ratios, but produced a notably lower Fe/Si ratio than was observed. However, given the overall low abundances of O across the remnant – especially in comparison to the abundances of Fe – we find a core-collapse origin less plausible than a thermonuclear one.

7.15 N0548–70.4

A roughly 60 ks *XMM-Newton* observation was used for our analysis of N0548–70.4. Following standard processing and filtering, spectra were extracted from four regions generated by *contbin*. After testing each region with an absorbed single-component thermal model, we found we were unable to reproduce the observed spectrum. We thus added a second thermal component, testing each combination of VPSHOCK, VNEI, VRNEI, and VAPEC models, until settling upon an absorbed VPSHOCK+VPSHOCK model as the one that produced the best results. The abundances of the second VPSHOCK component were set to the average abundances of the LMC, the column density was set to $N_H = 0.377 \times 10^{22}$ cm^{-2}, and the plasma temperatures, ionisation timescales, and normalisation constants were initially allowed to vary independently. We found that allowing the ionisation timescales to be independent produced worse results than otherwise; we thus tied the ionisation timescale of the cold component to that of the hot component. We then freed the abundances in the hot component one at a time, in order of Si, S, Fe, Mg, and Ne. We freed the abundance of O as well, but doing so only produced a notable improvement to the fit in R03. As in other objects, there was excess emission around the 1.2 keV mark that the models used could not account for; to compensate, we added a Gaussian at this energy. All regions were very well fit ($\chi^2_\nu < 1.25$) as a result.

Table 7.19: N0548–70.4: Best fit parameters per region

Parameter	R00	R01	R02	R03
kT_c (keV)	$0.29^{+0.13}_{-0.03}$	$0.25^{+0.01}_{-0.04}$	$0.26^{+0.04}_{-0.04}$	$0.31^{+0.11}_{-0.22}$
kT_h (keV)	$0.69^{+0.09}_{-0.02}$	$0.69^{+0.01}_{-0.04}$	$0.68^{+0.03}_{-0.05}$	$0.68^{+0.13}_{-0.29}$
O	-	-	-	$0.61^{+0.17}_{-0.07}$
Ne	$1.16^{+0.84}_{-0.24}$	$1.01^{+2.54}_{-0.26}$	$1.05^{+0.55}_{-0.21}$	$0.86^{+0.08}_{-0.12}$
Mg	$1.13^{+0.58}_{-0.56}$	$0.87^{+1.37}_{-0.40}$	$0.43^{+0.31}_{-0.36}$	$0.66^{+0.05}_{-0.09}$
Si	$1.94^{+2.89}_{-0.02}$	$2.41^{+2.53}_{-0.20}$	$2.76^{+1.04}_{-0.55}$	$2.41^{+0.29}_{-0.55}$
S	$1.22^{+2.93}_{-0.59}$	$2.49^{+3.13}_{-1.05}$	$2.87^{+2.12}_{-1.09}$	$2.17^{+0.88}_{-1.43}$
Fe	$1.40^{+1.36}_{-0.02}$	$1.44^{+1.29}_{-0.09}$	$1.35^{+0.30}_{-0.18}$	$0.88^{+0.17}_{-0.30}$
τ_h (10^{11} s cm^{-3})	$3.54^{+3.09}_{-1.58}$	$6.18^{+40.3}_{-2.48}$	$5.08^{+3.15}_{-2.08}$	$1.38^{+1.72}_{-0.37}$
Line Centroid (keV)	$1.21^{+0.07}_{-0.07}$	$1.25^{+0.03}_{-0.05}$	$1.26^{+0.03}_{-0.03}$	$1.24^{+0.28}_{-0.01}$
χ^2_ν (DoF)	1.06 (363)	0.90 (368)	1.02 (373)	1.01 (350)

The final results of our fit to N0548–70.4 can be seen in Table 7.19. We find that the plasma temperatures are very consistent across the remnant, with the cold component ranging from $0.29 - 0.31$ keV, while the hot component exhibits nearly no fluctuation at $0.68 - 0.69$ keV. We find near-solar abundances of Ne, Mg, and Fe throughout the remnant, with the highest values nearby to the bright central region, which gradually fall off the further one goes from the core. Si and S exhibit a behaviour that is largely the opposite of this, with their lowest abundances being present in the central region, gradually increasing with increasing radius. The outermost region – R03 – exhibits the lowest average abundances of all regions, with subsolar abundances for O, Ne, Mg, and Fe. The ionisation timescale is relatively consistent across the remnant, ranging from $1.24 - 6.18 \times 10^{11}$ cm^{-3} s, with the lowest value being found in the outermost region of R03.

There is only one previous study to which we can compare our results: Hendrick et al.

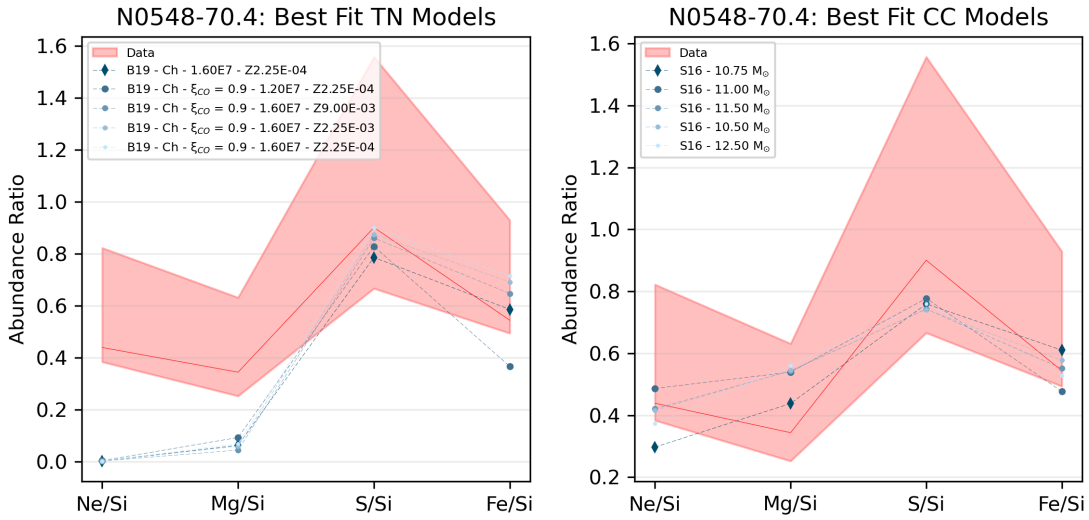

Figure 7.17: Best-fit nucleosynthesis models for N0548–70.4, comparing to both thermonuclear (TN) and core-collapse (CC) supernova nucleosynthesis yields.

(2003). Hendrick et al. (2003) performed a spatially-resolved study of N0548–70.4 using *Chandra* data; however, they only analysed three regions covering the bright centre and the limbs on the east and west of the remnant, the sum total of which did not cover the entire SNR. Their east and west limbs are comparable in spatial area to our R03, and our results are quite similar: they found a kT of 0.54 and $0.79^{+0.96}_{-0.54}$ keV, which are both quite close to our R03 value of $0.68^{+0.13}_{-0.29}$ keV. Similarly, their ionisation timescales of $1.89^{+0.95}_{-0.71} \times 10^{11}$ and $1.89^{+2.41}_{-1.15} \times 10^{11}$ cm^{-3} s agree well with our value of $1.38^{+1.72}_{-0.37} \times 10^{11}$ cm^{-3} s. They found Ne abundances of $0.55^{+0.15}_{-0.11}$ and $0.52^{+0.17}_{-0.15}$, which are somewhat lower than our abundance of $0.86^{+0.08}_{-0.12}$; however, they set the rest of the abundances in these regions to 0.4, which likely resulted in an overall reduction in abundances vis-a-vis what we found. For their central region, which corresponds to our R00-R02, they found a plasma temperature of $0.62^{+0.04}_{-0.03}$, which is in agreement with our values. Their ionisation timescale of $4.15^{+1.99}_{-1.40} \times 10^{11}$ cm^{-3} s agrees

with our values, as well. They found Fe abundances of approximately 1.2 times solar values, which largely agree with our findings; however, the abundances for the other elements (Ne, Mg, Si, S) were found to be lower than this, which is not the case for our results.

In terms of nucleosynthesis, as N0548–70.4 is a poorly-studied object, we compared our spectroscopic results to models of both thermonuclear and core-collapse supernova nucleosynthesis. Should the remnant be the result of a thermonuclear supernova, we found that a Chandrasekhar-mass WD with low metallicity would be the most likely origin, as the S/Si and Fe/Si ratios most closely match those of B19. However, the Mg/Si and Ne/Si ratios in the object were higher than the majority of thermonuclear models were able to reproduce. As a result, we found that the closest agreement came not from thermonuclear models, but from core-collapse models: specifically, the models of S16 for a star with a mass between $10 - 12\ M_\odot$, with the best individual fit being the $10.75\ M_\odot$ model of S16.

8

Discussion

We have performed a spectroscopic study for the 15 objects laid out in Chapter 5, and compared those results to the leading models of supernova nucleosynthesis yields for both thermonuclear and core-collapse supernovae; a summary of our findings can be seen in Table 8.1. For some of these objects, these results were able to be well reproduced by the existing nucleosynthesis models, while for others there exists a notable discrepancy between observations

Table 8.1: Summary of nucleosynthesis results. Details on the conclusions can be found in the relevant sections of Chapter 7. Conclusions indicated with a "?" were those for which there was no clear result. For details on the models mentioned, please refer to Section 3.4.2 for TN models and Appendix B for CC models.

SNR	Uncertain Nature?	Best TN Model	Best CC Model	Best Model Type (TN/CC)	Type Conclusion	Subtype Conclusion
G1.9+0.3	N	B19 Ch-Mass, $\xi_{CO} = 0.9$ $\rho_{DDT} = 1.20E{+}07$, $Z = 6.75E{-}02$	S16 17.4 $M_\odot$	TN	TN	Ch-mass WD, low DDT density, high metallicity
G4.5+6.8	N	T18 D[6]	WW95 12 $M_\odot$	TN	TN	D[6]
G41.1−0.3	Y	LN20b Mass-Based He Detonation Ring - 1.20 $M_\odot$	S16 10.0 $M_\odot$	TN	TN	High-mass WD, possible ONeMg
G43.3−0.2	Y	B19 subCh-Mass, $\xi_{CO} = 0.9$ M_{WD} = 0.97 $M_\odot$, $Z = 2.25E{-}02$	S16 10.0 $M_\odot$	CC	TN	Ch-mass WD, low DDT density, med-high metallicity
G120.1+1.4	N	B19 Ch-Mass, $\xi_{CO} = 0.9$ $\rho_{DDT} = 2.40E{+}07$, $Z = 2.25E{-}04$	WW95 12$M_\odot$	TN	TN	?
G272.2−3.2	N	B19 Ch-Mass, $\xi_{CO} = 0.9$ $\rho_{DDT} = 1.60E{+}07$, $Z = 2.25E{-}04$	S16 15.2$M_\odot$	CC	TN	Ch-mass WD, low DDT density, low metallicity
G337.2−0.7	N	B19 subCh-Mass, $\xi_{CO} = 0.9$ M_{WD} = 1.15 $M_\odot$, $Z = 2.25E{-}04$	WW95 12$M_\odot$	TN	TN	subCh-mass WD ($1.1 - 1.2$ $M_\odot$), low metallicity
G344.7−0.1	Y	B19 Ch-Mass, $\xi_{CO} = 0.9$ $\rho_{DDT} = 1.20E{+}07$, $Z = 2.25E{-}04$	WW95 12$M_\odot$	TN	TN	Ch-mass WD, low DDT density, low metallicity
G352.7−0.1	Y	B19 Ch-Mass $\rho_{DDT} = 2.40E{+}07$, $Z = 2.25E{-}03$	S16 10.0 $M_\odot$	TN	TN	Ch-mass WD, med DDT density, low-med metallicity
0505−67.9	N	F14 N100Hdef	S16 10.0 $M_\odot$	CC	?	?
0509−67.5	N	B19 subCh-Mass, $\xi_{CO} = 0.9$ M_{WD} = 0.88 $M_\odot$, $Z = 2.25E{-}04$	WW95 12$M_\odot$	CC	TN	subCh-mass WD (< 1.0 $M_\odot$), low metallicity
0509−68.7	Y	B19 Ch-Mass, $\xi_{CO} = 0.9$ $\rho_{DDT} = 1.20E{+}07$, $Z = 2.25E{-}04$	WW95 12 $M_\odot$	CC	TN	Ch-mass WD, low DDT density, low metallicity
0519−69.0	N	B19 Ch-Mass, $\xi_{CO} = 0.9$ $\rho_{DDT} = 1.60E{+}07$, $Z = 2.25E{-}04$	S16 20.3 $M_\odot$	TN	TN	Low-mass sCh WD / low DDT density Ch-mass WD
0534−69.9	Y	F14 N100Hdef	S16 11.75 $M_\odot$	CC	TN	?
0548−70.4	Y	B19 Ch-Mass $\rho_{DDT} = 1.60E{+}07$, $Z = 2.25E{-}04$	S16 10.75 $M_\odot$	CC	CC	$10 - 12$ $M_\odot$ CC

and simulations. In general, the models that exist are not able to fully recreate the entirety of the observed abundance ratios present in these objects, with certain elements faring better than others in the reliability with which they are reproduced. Here, we will discuss some of the broader findings of our study: in Section 8.2, we address the question of progenitor classification for SNRs whose origins have not been firmly established; in Section 8.3, we examine the possibility of a D^6 origin for one of the remnants; in Section 8.4, we investigate whether or not a reduced $^{12}C + ^{16}O$ reaction rate more accurately reproduces observational values; and in Section 8.5, we explore the discrepancies that exist between observations and simulations, while providing some possible methods for future simulations to address them. However, we first highlight some of the caveats that exist in our methodology.

8.1 Caveats

As a technique for the study of supernova remnants, X-ray spectroscopy offers us a broad range of powerful tools that can provide us with valuable insights into the nature of these objects. However, it is not without its faults, and there exist limitations that may be detrimental to the reliability and interpretation of results gathered through such a process. In this study, we have shown that, while the determined abundances in some supernova remnants can be matched well to models of supernova nucleosynthesis, the same can not be said for all such objects. Here, we list some caveats in the observations or analysis that may account for these discrepancies between simulation and observation, both those unique to our study and those of more general application. There exist as well limitations in the models and simulations; these will be discussed in Section 8.5.

First, the ejecta components of supernova remnants from which we have inferred our

metal abundances are quite complex, and the degree of this complexity likely displays some degree of spatial variation – that is to say, it varies from region to region. We attempt to account for this variation through two methods: our use of spatially-resolved spectroscopy, and our use of thermal models. For the second of these methods, however, it is very possible that the one- and two-component models used for our spectral fits are still too simplistic in their assumptions, and that more components could be required to accurately represent the data.

Second, while our analysis has been performed on the shock-heated ejecta present within these SNRs, it is possible that not all of the ejecta has been shock-heated. This is particularly true for the younger SNRs in our study, in which elements such as Fe may not be fully shocked. As well, it is possible that some of the ejecta is otherwise not visible in the X-ray band, such as for those SNRs which are more heavily absorbed, as high extinction can impair the detection of lighter elements such as O and Ne.

Third, while this study was spatially-resolved in nature, our comparisons were produced by the averaging out of ejecta yields across the SNRs. It is possible that some regions within these objects would be a better representation of the expected nucleosynthetic yields, given the likelihood of asymmetry in the explosions. It is also possible that external influences – such as environmental factors – could have some impact on select regions, causing their observed compositions to differ from what can be predicted through supernova properties alone.

Fourth, the spectral resolutions of the *XMM-Newton* and *Chandra* CCDs are not so fine as to be able to resolve every possible emission line in the observed energy range. This may introduce some degree of degeneracy in the parameters, leading to a less accurate measurement of the plasma properties.

Finally, there exist systematic errors in the telescope calibration and plasma models (in this

case, ATOMDB) used in this study. For the telescope calibrations, possible residual calibration uncertainties unaccounted for in the calibration files could potentially bias abundance ratios, particularly for lighter elements and those found in a lower energy range. For the plasma models, missing transitions – such as those possibly found in the Fe L-shell around 1.2 keV – could lead to an underestimation of certain spectral properties. For the latter of these subjects, the recent launch of the *XRISM* space telescope has spurred an increase in research – see, e.g. Plucinsky et al. (2025) – with the aim of updating current plasma models to account for the increased spectral resolution afforded by the Resolve calorimeter.

8.2 SNRs with Uncertain Classifications

When we embarked upon this journey, we opted to limit ourselves to studying supernova remnants that were typically considered of a thermonuclear origin. However, it can be at times difficult to definitively classify such objects, and so when determining our targets, we instead limited ourselves to supernova remnants that were "known to be, believed to be, or which have been accused of being" of such a type. As such, several of our targets were thus objects whose classification remains uncertain, either due to conflicting data, different interpretations of results, or simply to a lack of study. Herein, we will discuss the objects whose natures were previously considered uncertain, as well as those for which our results may be contrary to those currently accepted.

The first object to be discussed is G41.1–0.3 (3C 397), whose progenitor nature has historically been the subject of some debate. Initial studies by Safi-Harb et al. (2000, 2005) suggested a core-collapse origin, owing to several factors: its location nearby to the Galactic plane, its proximity to a molecular cloud, its highly-asymmetric morphology, and the abundances

of several IMEs. More recently, Yamaguchi et al. (2014, 2015) used the energy of its Fe Kα line centroid alongside the abundances of the iron-group elements of Mn, Cr, Fe, and Ni to propose a thermonuclear progenitor, and several studies since then have operated under the assumption of such an origin. Our results much more strongly favour a thermonuclear origin, as well, owing primarily to the particularly large Fe/Si ratio found in this SNR. While thermonuclear models are also capable of reproducing the Ca/Si and – in a few cases – the Mg/Si ratio, they struggle to reproduce the S/Si and Ar/Si ratios, which are much higher than predicted by any model. Core-collapse models fare worse, however: while the Mg/Si ratio can be met, not a single one of the core-collapse models tested in our study is capable of reproducing any of the remaining four abundance ratios observed in this SNR. Interestingly, the thermonuclear models that prove capable of reproducing the Fe/Si ratio (and thus which fare the best in reproducing our findings overall) uniformly tend towards being models of high-mass progenitors, with several of the best fits arising from model predictions for ONeMg white dwarfs rather than the traditional CO white dwarfs that are preferred by most other models. For that reason, we propose a thermonuclear origin for this SNR, with a high-mass, high-density WD – possibly of an ONeMg nature – as the progenitor.

Next – and perhaps the most appropriate object on this list – is G43.3–0.2 (W49B). The nature of this remnant's progenitor is a subject of great debate: original assumptions leant themselves towards a core-collapse origin, based on studies by Miceli et al. (2006), Keohane et al. (2007), and Lopez et al. (2013). More recent studies by Zhou & Vink (2018) and Sawada et al. (2025) have questioned this assumption, proposing a thermonuclear origin based on abundance patterns in general, and the Fe-group elements in particular. While both core-collapse and thermonuclear models were able to reproduce several of the determined abun-

dance ratios, we find that our results are more suggestive of a thermonuclear origin, primarily due to the general pattern of abundances. For the core-collapse scenario, the Mg/Si and S/Si are generally reproducible by a large number of models. The Ar/Si and Fe/Si are only reproducible by a small number of models, however, and none are capable of reproducing the observed Ca/Si ratio. There is, however, a decent amount of consistency in the best fits, which tend to arise from models nearby to 10 $M_\odot$. For the thermonuclear models, we find strong agreement for all elements save for Mg/Si across a fairly wide variety of models. The best fits tend to arise from models with low densities and low metallicities, with both subCh-mass and Ch-mass producing strong fits. While the best fit arises from a subCh-mass model, previous measurements of the ejecta mass in the SNR have placed it at above 1.20 $M_\odot$, making the possibility of a subCh-mass progenitor less likely. As a result of this, and owing to the strong agreement between the determined abundances and the abundance patterns present in the thermonuclear models, we propose a Ch-mass progenitor for this SNR, with a low DDT density and low metallicity.

Next, we consider G344.7–0.1. While it was originally considered a core-collapse remnant owing to its morphology (Lopez et al. 2011) and its proximity to a star-forming region (Giacani et al. 2011), measurements of the elemental abundances by Yamaguchi et al. (2012) and Fukushima et al. (2020), alongside measurements of the Fe Kα line centroid by Yamaguchi et al. (2014) have shifted the argument over to a thermonuclear origin. Our findings largely support this: the Ca/Si and Fe/Si ratios present within the SNR match up well with predictions from several thermonuclear models. Similarly, the S/Si and Ar/Si ratios can be reproduced by a select number of subCh-mass models; while some of these models are also capable of reproducing the Ca/Si ratio, no model is able to reproduce all four simultaneously. For

core-collapse models, we find that the Mg/Si and S/Si ratios are reproducible by a number of models; however, these models are generally unable to match our findings for any heavier element. The sole exception to this is the 12 $M_\odot$ model of WW95, which successfully reproduces the S/Si, Ar/Si, and Ca/Si ratios within error. Outside of this one model, the core-collapse models tend to fare notably worse than the thermonuclear models. Additionally, the core-collapse models show a large degree of inconsistency in terms of the progenitor mass for the best fit models, which range from $12 - 60$ $M_\odot$. The thermonuclear models, meanwhile, show a much larger degree of consistency: the best fit models tend towards Ch-mass progenitors with low metallicity. We thus propose that this SNR was the result of a Ch-mass progenitor with low metallicity and a low DDT density.

Fourth on our list is G352.7–0.1. Arguments of morphology (Giacani et al. 2009) and location (Pannuti et al. 2014) have been made to support a core-collapse origin, while arguments of elemental abundances (Sezer & Gök 2014; Fujishige et al. 2023) and the Fe Kα line centroid (Yamaguchi et al. 2014) have been made to support a thermonuclear origin. From our results, both origins are possible, as there is good agreement between the observations and the models of both thermonuclear and core-collapse supernova nucleosynthesis. For the core-collapse scenario, models of low-mass ($9-11$ $M_\odot$) progenitors tend to work best, with a select few models nearby to 10 $M_\odot$ being able to reproduce the determined abundance ratios for all elements within error. Despite this, we find both a better agreement and a greater degree of consistency in progenitor information with thermonuclear models. In particular, several of the Ch-mass progenitors of B19 provide a strong reproduction of the determined abundance ratios for all elements save for the Mg/Si ratio, for which none of our thermonuclear models are able to reproduce our findings. Owing to this, and the fact that the determined

abundance ratios very closely follow the abundance patterns found in many thermonuclear models, we propose a Ch-mass progenitor with a low-to-moderate metallicity and a moderate DDT density.

We now turn to the LMC objects, starting with N0509–68.7. Though fairly well-studied, the supernova origin of N0509–68.7 is not well understood. A core-collapse origin has been proposed by Chu & Kennicutt (1988), based on the SNR's proximity to an HII region, as well as by van der Heyden et al. (2002) and Someya et al. (2014), based on the remnant's elemental abundances. In contrast, a thermonuclear origin has been proposed by Lewis et al. (2003), owing to the Fe mass, and by Lopez et al. (2011), owing to the remnant's morphology. For our findings, in terms of which types of models are able to reproduce our observed abundances, we find moderate agreement between both thermonuclear and core-collapse models. Among the core-collapse models, the agreement largely arises from the ability of the models to reproduce the abundance ratios of the lower-mass elements involved in the study: the O/Si, Ne/Si, Mg/Si, and S/Si ratios. Curiously, the best-fit arises as a result of the 12 $M_\odot$ model of WW95 – a core-collapse model. However, this model is alone amongst the core-collapse models in its ability to reproduce the Ar/Si and Ca/Si ratios. Further, the core-collapse models that can be considered best-fits vary widely in terms of expected progenitor mass, ranging between $12 - 20.4$ $M_\odot$. In contrast, the thermonuclear models are largely consistent in their prediction of a Ch-mass progenitor with a low density for the DDT transition during the supernova event. The thermonuclear models are moderately successful at reproducing the Mg/Si and S/Si ratios, and succeed in reproducing the Ca/Si and Fe/Si ratios present within the remnant, as well. In particular, the low Fe/Si ratio is strongly suggestive of a low-metallicity progenitor. As a result, we propose that N0509–68.7 is the result of a thermonu-

clear supernova that arose from a low-metallicity Ch-mass progenitor that underwent DDT at a low density.

Next, we have N0534–69.9. A poorly-studied object, N0534–69.9 has only received two studies of note. The first of these is the *Chandra* study of Hendrick et al. (2003), who determined a thermonuclear origin using the low O/Fe ratio detected in the SNR's central regions and strong emission from the Fe L shell. A *Suzaku* study by Takeuchi et al. (2016) confirmed these findings, and – based on the elemental abundances detected within the SNR – supported a thermonuclear origin. Our findings for this SNR are unclear: while the relatively high Fe/Si ratio is indicative of a thermonuclear origin, the comparatively high O/Si, Ne/Si, and Mg/Si ratios are suggestive instead of a core-collapse origin. Further, due to the limited duration of the *XMM-Newton* observation used in this study, we were unable to determine the abundances of any other IMEs, making it difficult to make any strong judgment. However, given that the detected Fe/Si ratio is above that found in any core-collapse model, as well as the fact that the O/Si and Ne/Si ratios are reproducible by a handful of thermonuclear models (namely, some of the models of LN20a), we concur with the previous determination of a thermonuclear origin.

Finally, we consider N0548–70.4 Like N0534–69.9, N0548–70.4 is an object that has not received much attention, and as such, is poorly understood. Hendrick et al. (2003), using *Chandra* data, determined a thermonuclear origin for the SNR, primarily based on the observed O/Fe ratio in its core, alongside its location in the LMC and its lack of proximity to any known OB association. While their main argument – that of the O/Fe ratio – was based on the O/Fe being lower than expected for a core-collapse remnant, they also note that it appears higher than would be expected for the remnant of a thermonuclear supernova. A later

Suzaku study by Takeuchi et al. (2016) determined an O/Fe ratio significantly lower than the previous measurement, and using an argument of the Fe/Ne ratio being greater than the mean LMC value, once again suggested a thermonuclear origin. Our results, however, are somewhat at odds with this: while there is a degree of agreement between our spectroscopic results and the models of thermonuclear supernova nucleosynthesis, we find much stronger agreement with the models of core-collapse supernovae, instead. In particular, while the S/Si and Fe/Si ratios find strong agreement in both regimes, the ratios of Ne/Si and Mg/Si are greater in this SNR than can be explained by the majority of thermonuclear models, while simultaneously being aligned quite well with predictions for core-collapse nucleosynthesis of a $10 - 12\,M_{\odot}$ progenitor.

We thus have determined that of the seven objects in this study for which a progenitor class has not been firmly established or for which the progenitor class is still a matter of debate, six possess spectroscopic features that more closely align with the predicted features of thermonuclear supernovae than they do core-collapse supernovae, lending support to the most common interpretation of their origins. These six objects are G41.1–0.3, G43.3–0.2, G344.7–0.1, G352.7–0.1, N0509–68.7, and N0534–69.9. The remaining object – N0548–70.4 – possesses features that are more suggestive of a core-collapse origin, which is contrary to the previously proposed origin for the object.

8.3 Possible Evidence of a D^6 Supernova

The dynamically driven double-degenerate double-detonation model – also known as the "D^6" model – presents an interesting scenario. The most defining characteristic of this model is the possibility that the companion WD can survive the thermonuclear explosion of the pri-

mary WD, rather than being destroyed in the process. Additionally, due to the proximity of the companion to the primary, it instead becomes accelerated to a velocity potentially exceeding $10^3\,\mathrm{km\,s^{-1}}$ following the explosion. Further, the survival of the companion WD can lead to the creation of a so-called "ejecta shadow" that is fainter than the surrounding ejecta, and which can remain visible in the resulting supernova remnant for several hundred years (Ferrand et al. 2022). The detection of either of these two features thus leads to two potentially unique methods for determining a D^6 origin.

As a supernova model, the D^6 model also has its own unique nucleosynthesis signatures that can be used to classify a supernova remnant, which have been determined by Tanikawa et al. (2018), which is primarily categorized by notably higher ratios of S/Si, Ar/Si, and Ca/Si than most other models of thermonuclear supernova nucleosynthesis. Our study has revealed only one possible SNR for which this model uniquely produces the best fit: that of G4.5+6.8. We now turn our discussion to this object.

More often referred to as Kepler's SNR, G4.5+6.8 is the remnant of a historical SNR, and as such, is well-studied. When the remnant of SN 1604 was discovered by Baade (1943), its status as the remnant of a core-collapse supernova or a thermonuclear supernova was poorly understood. Evidence of emission from high-density material with enhanced N abundances were used to support a core-collapse origin, while arguments of its position high above the Galactic plane were used to support a thermonuclear origin instead (Minkowski 1943; Dennefeld 1982; Leibowitz & Danziger 1983; Blair et al. 1991). With the advancement of detector technology, the subsequent discovery of a large amount of Fe emission by Kinugasa et al. (1998) led to an increase in support for the thermonuclear scenario, and subsequent findings have been sufficient to decidedly declare it the remnant of a thermonuclear supernova

(Reynolds et al. 2007; Patnaude et al. 2012; Kerzendorf et al. 2014).

Despite this conclusion, the exact nature of Kepler's progenitor has yet to be determined. Several attempts have been made to locate a companion star, though none have yet succeeded. However, only the inner portions of the SNR have been examined: Kerzendorf et al. (2014) searched through a region of $38'' \times 38''$ at the center of the SNR – corresponding to a maximum companion velocity of approximately $1420\,\mathrm{km\,s^{-1}}$ at an assumed distance of 6.4 kpc – examining the 24 brightest stars found within this region, and found no stars whose properties would be consistent with those expected of a donor star. Similarly, Ruiz-Lapuente et al. (2018) examined the innermost $24''$ of the SNR with similar results. Both of these studies suggest that the SD scenario is less likely, with Ruiz-Lapuente et al. (2018) suggesting a possible core-degenerate or DD scenario. Given that our spectroscopic study of this object was displayed strong agreement with the D[6] model, a deeper examination of this SNR to search specifically for a hypervelocity WD companion may be appropriate.

8.4 The Effect of the $^{12}C + ^{16}O$ Reaction Rate on Nucleosynthesis

The sensitivity of the yields of intermediate mass elements from a thermonuclear supernova to the level of neutronisation in said supernova's ejecta – in particular, the yields of Ca and S – presents an interesting opportunity for measuring the neutronisation level of a supernova (De et al. 2014). While using this method, Martínez-Rodríguez et al. (2017) noticed that the Ca/S mass ratio predicted by several models of supernova nucleosynthesis was considerably lower ($\sim 50\%$) than their own observations. They determined that a significant source of this deviation was due to the reaction rate of $^{12}C + ^{16}O$. Specifically, they determined that the Ca/S mass ratio is very sensitive to this reaction rate: as shown by De et al. (2014) and

Miles et al. (2016), the mass ratio of Ca/S in a thermonuclear supernova remnant scales as the square of the abundance of α-particles present in the explosion. The $^{12}C + ^{16}O$ reaction, in turn, acts to reduce the abundance of α-particles, leading to a reduction in the resultant Ca/S mass ratio, with a higher reaction rate resulting in a greater reduction. Given the Ca/S mass ratios observed in several SNRs, they determined that the $^{12}C + ^{16}O$ reaction rate must be attenuated in nature compared to the commonly used value, with an upwards of 90% attenuation required to reproduce their observations.

From a theoretical perspective, an attenuation of the reaction rate to this degree is hard to explain. While there is a degree of uncertainty in the understood reaction rate, only an uncertainty of $\sim$ 50% can be accounted for based on the currently measured experimental values for the reaction, which falls short of the $\sim$ 90% needed to explain the findings of Martínez-Rodríguez et al. (2017). Despite this, Shen et al. (2018) chose to investigate these results, and found that an attenuation of 90% did produce a notable improvement over conventional values. Bravo et al. (2019) chose to investigate these findings further, computing the nucleosynthesis and hydrodynamics for a series of spherically symmetric thermonuclear supernovae. In addition to addressing both the Ch-mass and subCh-mass scenarios, they also repeated each simulation for the case in which the $^{12}C + ^{16}O$ reaction rate has been attenuated by 90%. They found that these simulations – which they labelled as "SNR-calibrated SN Ia models" – produced significantly higher Ca/S and Ar/S mass ratios than the simulations with the standard $^{12}C + ^{16}O$ reaction rate, and that the changes were needed in order to reconcile the models with the measured abundances.

As a part of our analysis, we compared our results to these SNR-calibrated SN Ia models, and we report here our findings on their ability to reproduce the observations. In general,

we find that the models of Bravo et al. (2019) produced notably better-than-average fits to our data, yielding good fits to a majority of our objects. While this may in part be due to the amount of models that comprise this set – of the 213 thermonuclear models considered in this study, 100 of these belong to the set of B19 – the effect is disproportionately in favour of the models of B19, which produced the best-fit for 11 of our 15 objects when considering only thermonuclear models.

Further, of the 11 objects for which the models of B19 produce the best fits, 9 of these 11 were produced by models utilising the reduced $^{12}C + ^{16}O$ reaction rate. The main advantage that these models have over those with the standard $^{12}C + ^{16}O$ reaction rate is that the reduced-rate models produce significant increases in the Ar/Si and Ca/Si ratios, and notable increase in the S/Si and Fe/Si ratios. While lower-mass elements – such as O, Ne, and Mg – are impacted by the change in the reaction rate, they are also not typically created in great quantities in thermonuclear supernovae, and as such, do not have as strong an impact on the quality of a fit.

One might be tempted to assume that the existence of such an uncertainty might presuppose that other reaction rates may be similarly poorly constrained. However, studies on the sensitivity of explosive nucleosynthesis to individual reaction rates (e.g. Bravo & Martínez-Pinedo (2012), Rauscher et al. (2016)) have found that, outside of specific reactions (such as those involving ^{12}C and/or ^{16}O), most yields are largely insensitive to changes in these reaction rates, with even a tenfold change in reaction rate yielding only a modest change in resultant yields. As such, the sensitivity of yields to uncertainties in the reaction rates tend to be small in comparison to uncertainties that arise from details surrounding the explosion itself. That being said, uncertainties in these other reaction rates do exist, and it may be pru-

dent to consider them in future studies and simulations.

8.5 The Discrepancy Between Observations and Simulations

As we have shown, the majority of our results are only partially reproducible by existing models of supernova nucleosynthesis, with the abundance ratios for nearly all of our objects being at best only partial matches for any of the broad range of nucleosynthesis models used in this study. Due to limitations in available computational power, all of the models used in this study made use of assumptions and simplifications that limit their ability to fully reproduce the physical processes present in a supernova. As an example, the models of B19 were able to explore a large parameter space, allowing for the varying of properties such as progenitor metallicity and $^{12}C + ^{16}O$ reaction rate that other models were unable to explore. However, this came as a result of the model's one-dimensional nature, which severely limits the effects that turbulence, convection, and possible asymmetries could have on the progenitor's evolution during the supernova process. Herein, we discuss how well each abundance ratio tended to work when performing these comparisons, and offer some explanations for each scenario as to why this might be the case. We also provide some possible avenues of consideration for future simulations, both those that might lead to an improvement for particular abundance ratios, as well as more general observations that might improve upon these results.

We begin by considering what did not work. Of note, the abundance ratios for the lightest considered elements – namely, the O/Si, Ne/Si, and Mg/Si ratios – tended to be notably underproduced by the thermonuclear models when compared to our observations. This is particularly true for the models of B19, which otherwise produced the best fits to our results. This is likely the result of the 1D-nature of these simulations, as opposed to the 2D- and

3D-natures of the other sets of simulations. These elements are primarily found in the outer layers of a progenitor, where temperatures and pressures are less likely to reach the required values for explosive burning. As a result, these elements are more likely to be unburned or only partially burned during the supernova. The amount of this burning, however, can be adjusted through the turbulent mixing of these outer layers with the inner layers – a process that 1D simulations are notably less capable of capturing and reproducing. Indeed, we find that the models that made use of higher-dimensional simulations – such as the 3D-simulations of F14 – showed a significantly larger variation in the O/Si, Ne/Si, and Mg/Si ratios. In order to better reproduce the observed abundances of these elements, it is thus vital that future simulations make use of higher dimensionality to more accurately recreate the complex mixing that occurs between the different layers of a WD.

The intermediate mass elements fared better than the light elements in our study, but were not consistently reproducible by the used models. While the S/Si, Ar/Si, and Ca/Si ratios proved less potent as probes of supernova classification when trying to determine between a core-collapse or a thermonuclear origin, they oftentimes proved strong determinants of subclassification, as they often varied strongly between different models. As mentioned in Section 8.4, the $^{12}C + ^{16}O$ reaction rate has a strong impact on the relative abundances of these elements, and any future studies should take into account the possibility of an attenuated reaction rate. Further, the production of these elements is strongly influenced by progenitor metallicity and neutronisation, as a lower electron fraction Y_e alters which isotopes are favoured during nuclear burning. During the burning phase, variations in Y_e can significantly alter the yields of these intermediate-mass elements, with more neutron-rich isotopes becoming more prevalent at lower Y_e. Precise modelling of the neutronisation rate and the

effects of metallicity are thus essential for being able to accurately reproduce the observed abundance yields for these elements.

Next, let us consider what did work. The Fe/Si ratio, in particular, proved a strong differentiator of supernova type, particularly when attempting to discriminate between a thermonuclear and a core-collapse origin. This is largely expected: the most prominent isotope produced by a thermonuclear supernova is ^{56}Ni, which decays via ^{56}Co into ^{56}Fe. Through the resulting emission of γ-rays and positrons, this radioactive decay heats the ejecta, and is one of the main sources of power behind the optical light curve of a Type Ia supernova. Given this, there exists a relation between the peak luminosity of a Type Ia event and the amount of ^{56}Ni produced in the associated thermonuclear supernova, and as a result, ^{56}Ni production is oftentimes used as a calibration marker for simulations of thermonuclear supernova nucleosynthesis. One would then expect that the ^{56}Fe – as a decay product of ^{56}Ni – would be a fairly reliable marker to which to compare results, which matches our findings.

One aspect of progenitor properties that has not been fully explored is the effect of metallicity. Of the models tested, only two sets – those of LN18 and B19 – included the progenitor metallicity as a variable in their parameter space. Almost uniformly, the models with lower metallicities exhibited higher abundance ratios than those with higher metallicities, which generally resulted in an improved agreement between these models and our observations. An obvious reason for this low progenitor metallicity would be the delay time: thermonuclear supernovae arise from white dwarf stars, which themselves form at the end of the life of lower-mass stars. As a star's lifetime is inversely related to its mass, these lower-mass progenitors live longer, and thus presumably be of an older stellar population which exhibits a lower average metallicity. Our results appear to support the idea of lower metallicity progenitors for these

events. While older studies have tended towards an assumption of solar metallicity, there has been a recent increase in models including metallicity in their parameter spaces, and our results support this as an important feature for future simulations.

Finally, we come to the matter of explosion energy. The canonical explosion energy for a supernova is 10^{51} erg, and many models tend to use a single explosion energy for their calculations, assuming an energy very close to the canonical value. However, several studies (e.g. Foley et al. (2009); Lovegrove & Woosley (2013); Stritzinger et al. (2014)) have determined explosion energies for supernovae that vary significantly from this canonical value, sometimes by several orders of magnitude. While certain studies have examined explosion processes that are nominally lower energy (e.g. deflagration models vis-a-vis detonation models), we are only aware of one such study that has considered the parametrisation of the energy, that being Fryer et al. (2018), which explored core-collapse supernovae broadly parametrised based on the injection energy. To our knowledge, no such study exploring the explosion energy for thermonuclear supernovae exists, despite evidence suggesting variations from the canonical explosion energy. Given this, it is clear that a single explosion energy cannot accurately reflect the reality for every supernova event, and that such a parameter must be examined in future simulations.

9

Conclusions and Future Work

9.1 Conclusions

The work that we have now presented is a systematic study of supernova remnants against a selection of the most commonly-used models of supernova nucleosynthesis available in the literature, comprising 335 individual models across 11 sets of simulations. The targets selected for this study consist of SNRs that are believed to be of a thermonuclear origin; however, due

to the difficulty associated with determining such a property, several objects whose natures have not been firmly established have been included in our study, as well. As an X-ray study, a secondary criterion of evidence of enhanced ejecta was also required. To that end, fifteen targets were selected: G1.9+0.3, G4.5+6.8, G41.1−0.3, G43.3−0.2, G120.1+1.4, G272.2−3.2, G337.2−0.7, G344.7−0.1, G352.7−0.1, N0505−67.9, N0509−67.5, N0509−68.7, N0519−69.0, N0534−69.9, and N0548−70.4. Owing to its powerful combination of angular resolution, spectral resolution, and field-of-view, all objects made use of archival *XMM-Newton* data with the single of exception of G1.9+0.3, which made use of archival *Chandra* data instead due to a lack of available data for *XMM-Newton*.

As a spatially-resolved study, the regions chosen for spectroscopic analysis were generated by an algorithm based on a nearest neighbour analysis of pixels. This analysis follows the object's surface brightness, as evidence suggests that there exists a correlation between surface brightness and physical properties such as density, temperature, and elemental abundances (Sanders 2006). The sole exception to this was the SNR G1.9+0.3, for which regions were selected based upon a previous study on account of the predominance of non-thermal emission in the SNR. From each region, X-ray spectra were extracted and fit using plasma models appropriate for modelling such objects. The results were then compared to a selection of the most prominent models of supernova nucleosynthesis yields in an attempt to determine specific details about the progenitor. These models included seven sets pertaining to nucleosynthesis in thermonuclear supernovae (Maeda et al. (2010); Seitenzahl et al. (2013); Fink et al. (2014); Leung & Nomoto (2018); Tanikawa et al. (2018); Bravo et al. (2019); Leung & Nomoto (2020a,b)), alongside four sets pertaining to nucleosynthesis in core-collapse supernovae (Woosley & Weaver (1995); Maeda & Nomoto (2003); Nomoto et al. (2006); Sukhbold

et al. (2016)). We have also explored the effect of different explosion energies within the core-collapse explosion models of Fryer et al. (2018).

From an observational standpoint, we acquired spectroscopic information for each region of every involved SNR, determining both elemental abundances for the applicable elements from O, Ne, Mg, Si, S, Ar, Ca, and Fe, as well as parameters such as plasma temperatures and ionisation timescales. By comparing the elemental abundances to the yields predicted by the previously mentioned models of supernova nucleosynthesis, we identified the models that best reproduce the observed abundances for each object and used these comparisons to determine the classifications and sub-classifications of their progenitors. We find that, while for some objects there is strong agreement between the models and observations, in general, the observed abundances do not match the entirety of the predicted yields for any of the models. As a result, while we present conclusions for the classification of each involved object, these conclusions are largely based upon the ratios of only a select few elements, rather than all of those which were examined for a given object.

From a theoretical perspective, we identify some limitations in the current nucleosynthesis models that might lead to these disagreements, and explore them further. We examine what aspects of the models tend to work well, as well as those that fare more poorly, identifying some possible physical considerations that might result in the various levels of agreement. Finally, we provide feedback for the modelling community to help inform future simulations by identifying some parameters that would lend themselves well to further exploration. Specifically, we identify four areas that future simulations should focus on that might help account for our findings: a refinement of the reaction rates for certain nuclear reactions, such as that of $^{12}C+^{16}O$; an increase in dimensionality to ensure simulations can accurately capture

the effects of turbulence, mixing, and convection; exploring the parameter space of progenitor metallicity due to its effects on certain reaction rates; and investigating further the possibility of explosion energies that vary from the canonical value of 10^{51} erg due to observations and studies that suggest that such a value may not always be the case.

9.2 Future Work

There are many avenues available for future work on this subject. While we aimed to study a broad range of SNRs that met our target criteria, the objects chosen were by no means the only ones available for such a study. A future study incorporating more of these objects and modifying some of our criteria – such as opting to include SNRs that are synchrotron-dominated (e.g. SN 1006 or RCW 86), or those with a non-thermonuclear origin – is a possibility. Conversely, rather than expanding the study to include more targets, performing an enhanced study on the targets already selected could be a viable option: while our spectroscopic study was spatially resolved in nature, we opted to make use of regions that were generally larger in scale, owing largely to computational constraints. More powerful devices could conceivably be used to perform a similar analysis with a much finer, more granular scale, allowing for a more accurate determination of the remnant's elemental abundances, and for the spatial distribution of the examined elements to be determined with much higher precision.

There are other aspects of supernova remnants that may be worth exploring in a similar manner. For example, by performing an imaging or morphological analysis one could choose to explore the asymmetries present within these objects to explore various aspects of the progenitors and their supernova explosions such as explosion asymmetries, progenitor rotation,

and instabilities. Numerical simulations are capable of tracking the amount and location of shocked ejecta as a function of time, so by comparing the observed distributions of certain ejecta components such as ^{56}Fe to the results of forward-propagated simulations, one would have an additional tool by which to determine progenitor properties. This would be particularly useful for the younger SNRs in which much of the ejecta has not yet been shocked, as such simulations may help constrain the location of ejecta that would otherwise be difficult to isolate. Incorporating such morphological studies alongside our spectroscopic analysis would help provide a more complete picture of these remnants and their evolution, and help further constrain the details of their progenitors.

The most obvious method of expanding this study, however, is the incorporation of new data, both through the acquisition of new, deeper observations to enable the study of faint emission and better observe the spatial distribution of the ejecta, as well as through the use of different telescopes. In addition to exploring other energy regimes – such as by utilising the *James Webb Space Telescope* (JWST) to explore unshocked ejecta in the infrared regime – there are a number of other X-ray telescopes that could be utilised. The bulk of this work was performed using data obtained by *XMM-Newton*, as it provided a strong combination of good angular resolution and spectral resolution, high-throughput, and a large field-of-view that made it ideal for our purposes. The *Chandra* (which was briefly utilised in this study) and *Suzaku* telescopes are two similar options to *XMM-Newton*, and incorporating their data could enhance the study, whether by removing potential sources of instrumental bias that may have gone unnoticed, or by simply increasing the observation time for a given object.

Of course, the future of X-ray astronomy lies not with the aforementioned telescopes, but with newer, more powerful devices that have launched in recent years, or which will launch in

the coming ones. The most recently launched X-ray spectroscopy mission is *XRISM* – the X-ray Imaging and Spectroscopy Mission. *XRISM* is a joint NASA / JAXA mission launched in late 2023, and is equipped with a microcalorimeter that affords it an unparalleled energy resolution, capable of resolving emission lines significantly more fine than anything previously available. This would allow us to better constrain abundance measurements and detect an even broader range of elements, which could significantly improve our fits to models of supernova nucleosynthesis. Future missions include *AXIS* – the Advanced X-ray Imaging Satellite – which is a NASA probe mission currently competing for launch in 2032, and which would boast a spatial resolution better than that of *Chandra* alongside a higher count-rate and lower detector background (Reynolds et al. 2023). Finally, there is ESA's *NewATHENA* – the New Advanced Telescope for High-Energy Astrophysics. *NewATHENA* is a retooled version of the previously-proposed *ATHENA* telescope, and is presently set to launch in 2037. The capabilities of *NewATHENA* are expected to exceed those of *XMM-Newton* and *Chandra* across several of its main operating parameters by over an order of magnitude, simultaneously (Cruise et al. 2025). While the path forward is not without its challenges and uncertainties, the next generation of telescopes that these three comprise offers tremendous potential should we be bold enough to grasp it. With them lighting the way, the future of X-ray astronomy shines with the promise of possibility, inviting us to explore and understand the high-energy universe more deeply than ever before.

A

XSPEC Models

Brief descriptions of the models described herein in terms of their meaning and applications can be found in Subsection 4.6.3.

Table A.1: TBABS Model Parameters

Parameter	Units	Description
N_H	$x10^{22}$ atoms cm^{-2}	Equivalent hydrogen column density

Table A.2: TBVARABS Model Parameters

Parameter	Units	Description
N_H	x10^{22} atoms cm^{-2}	Equivalent hydrogen column density
He	-	Helium abundance ratio $^{(a)}$
C	-	Carbon abundance ratio $^{(a)}$
N	-	Nitrogen abundance ratio $^{(a)}$
O	-	Oxygen abundance ratio $^{(a)}$
Ne	-	Neon abundance ratio $^{(a)}$
Na	-	Sodium abundance ratio $^{(a)}$
Mg	-	Magnesium abundance ratio $^{(a)}$
Al	-	Aluminum abundance ratio $^{(a)}$
Si	-	Silicon abundance ratio $^{(a)}$
S	-	Sulfur abundance ratio $^{(a)}$
Cl	-	Chlorine abundance ratio $^{(a)}$
Ar	-	Argon abundance ratio $^{(a)}$
Ca	-	Calcium abundance ratio $^{(a)}$
Cr	-	Chromium abundance ratio $^{(a)}$
Fe	-	Iron abundance ratio $^{(a)}$
Co	-	Cobalt abundance ratio $^{(a)}$
Ni	-	Nickel abundance ratio $^{(a)}$
H_2	x10^{22} atoms cm^{-2}	Molecular hydrogen column density
ρ	g cm^{-3}	Grain density
a_{min}	μm	Grain minimum size
a_{max}	μm	Grain maximum size
PL	-	Power-law index of grain sizes
He_{dep}	-	Helium grain depletion fraction
C_{dep}	-	Carbon grain depletion fraction
N_{dep}	-	Nitrogen grain depletion fraction
O_{dep}	-	Oxygen grain depletion fraction
Ne_{dep}	-	Neon grain depletion fraction
Na_{dep}	-	Sodium grain depletion fraction
Mg_{dep}	-	Magnesium grain depletion fraction
Al_{dep}	-	Aluminum grain depletion fraction
Si_{dep}	-	Silicon grain depletion fraction
S_{dep}	-	Sulfur grain depletion fraction

Continued on next page

Parameter	Units	Description
Cl_{dep}	-	Chlorine grain depletion fraction
Ar_{dep}	-	Argon grain depletion fraction
Ca_{dep}	-	Calcium grain depletion fraction
Cr_{dep}	-	Chromium grain depletion fraction
Fe_{dep}	-	Iron grain depletion fraction
Co_{dep}	-	Cobalt grain depletion fraction
Ni_{dep}	-	Nickel grain depletion fraction
z	-	Redshift

$^{(a)}$ Abundance ratios are relative to solar values, where solar is 1

Table A.3: VNEI Model Parameters

Parameter	Units	Description
kT	keV	Plasma temperature
H	-	Hydrogen abundance [a]
He	-	Helium abundance ratio [b]
C	-	Carbon abundance ratio [b]
N	-	Nitrogen abundance ratio [b]
O	-	Oxygen abundance ratio [b]
Ne	-	Neon abundance ratio [b]
Mg	-	Magnesium abundance ratio [b]
Si	-	Silicon abundance ratio [b]
S	-	Sulfur abundance ratio [b]
Ar	-	Argon abundance ratio [b]
Ca	-	Calcium abundance ratio [b]
Fe	-	Iron abundance ratio [b]
Ni	-	Nickel abundance ratio [b]
τ	s cm^{-3}	Ionization timescale
z	-	Redshift
norm	-	$\frac{10^{-14}}{4\pi[D_A(1+z)]^2}\int n_e n_H \mathrm{dV}$ [c]

[a] Set to 0 for no free-free continuum, otherwise 1

[b] Abundance ratios are relative to solar values, where solar is 1

[c] Where D_A is the angular diameter distance to the source in cm; dV is the volume element in cm^3; and n_e and n_H are the electron and hydrogen densities in atoms per cm^3, respectively

Table A.4: VPSHOCK Model Parameters

Parameter	Units	Description
kT	keV	Plasma temperature
H	-	Hydrogen abundance [a]
He	-	Helium abundance ratio[b]
C	-	Carbon abundance ratio[b]
N	-	Nitrogen abundance ratio[b]
O	-	Oxygen abundance ratio[b]
Ne	-	Neon abundance ratio[b]
Mg	-	Magnesium abundance ratio[b]
Si	-	Silicon abundance ratio[b]
S	-	Sulfur abundance ratio[b]
Ar	-	Argon abundance ratio[b]
Ca	-	Calcium abundance ratio[b]
Fe	-	Iron abundance ratio[b]
Ni	-	Nickel abundance ratio[b]
τ_l	s cm^{-3}	Lower limit on ionization timescale
$\tau_{\rm u}$	s cm^{-3}	Upper limit on ionization timescale
z	-	Redshift
norm	-	$\frac{10^{-14}}{4\pi[D_A(1+z)]^2}\int n_e n_H {\rm dV}$ [c]

[a] Set to 0 for no free-free continuum, otherwise 1

[b] Abundance ratios are relative to solar values, where solar is 1

[c] Where D_A is the angular diameter distance to the source in cm; dV is the volume element in cm^3; and n_e and n_H are the electron and hydrogen densities in atoms per cm^3, respectively

Table A.5: VRNEI Model Parameters

Parameter	Units	Description
kT	keV	Plasma temperature
kT_{init}	keV	Initial plasma temperature
H	-	Hydrogen abundance [a]
He	-	Helium abundance ratio [b]
C	-	Carbon abundance ratio [b]
N	-	Nitrogen abundance ratio [b]
O	-	Oxygen abundance ratio [b]
Ne	-	Neon abundance ratio [b]
Mg	-	Magnesium abundance ratio [b]
Si	-	Silicon abundance ratio [b]
S	-	Sulfur abundance ratio [b]
Ar	-	Argon abundance ratio [b]
Ca	-	Calcium abundance ratio [b]
Fe	-	Iron abundance ratio [b]
Ni	-	Nickel abundance ratio [b]
τ	s cm^{-3}	Ionization timescale
z	-	Redshift
norm	-	$\frac{10^{-14}}{4\pi[D_A(1+z)]^2} \int n_e n_H \mathrm{dV}$ [c]

[a] Set to 0 for no free-free continuum, otherwise 1

[b] Abundance ratios are relative to solar values, where solar is 1

[c] Where D_A is the angular diameter distance to the source in cm; dV is the volume element in cm^3; and n_e and n_H are the electron and hydrogen densities in atoms per cm^3, respectively

Table A.6: VAPEC Model Parameters

Parameter	Units	Description
kT	keV	Plasma temperature
He	-	Helium abundance ratio [a]
C	-	Carbon abundance ratio [a]
N	-	Nitrogen abundance ratio [a]
O	-	Oxygen abundance ratio [a]
Ne	-	Neon abundance ratio [a]
Mg	-	Magnesium abundance ratio [a]
Al	-	Aluminum abundance ratio [a]
Si	-	Silicon abundance ratio [a]
S	-	Sulfur abundance ratio [a]
Ar	-	Argon abundance ratio [a]
Ca	-	Calcium abundance ratio [a]
Fe	-	Iron abundance ratio [a]
Ni	-	Nickel abundance ratio [a]
z	-	Redshift
norm	-	$\frac{10^{-14}}{4\pi[D_A(1+z)]^2}\int n_e n_H \mathrm{dV}$ [b]

[a] Abundance ratios are relative to solar values, where solar is 1

[b] Where D_A is the angular diameter distance to the source in cm; dV is the volume element in cm^3; and n_e and n_H are the electron and hydrogen densities in atoms per cm^3, respectively

B

Models of Core Collapse Supernova Nucleosynthesis

This work was focused on the study of supernova remnants whose presumed origins are thermonuclear in nature. However, several of the objects studied have origins that are uncertain or inconclusive; for these objects, the consideration only of models of thermonuclear super-

nova nucleosynthesis would be insufficient: we must consider models of core collapse supernovae, as well. Herein, we give brief descriptions of some of the most prominent models of nucleosynthesis in core collapse supernovae, discussing the basic modelling methods and assumptions used by each.

B.1 Woosley & Weaver 1995 (WW95)

One of the first models for which the products of explosive nucleosynthesis were published, Woosley & Weaver (1995) considered several stars of varying masses and metallicities. A nuclear reaction network of 200 isotopes was used to evolve stars of masses 11, 12, 13, 15, 18, 19, 20, 22, 25, 30, 35, and 40 $M_\odot$ from a pre-supernova phase of hydrogen up until silicon core burning, with some amount of convection present in some of the shells. Following this evolution, an artificial shock wave was induced to simulate the supernova explosion, although convective mixing was not enabled for the explosion itself. The shock was allowed to propagate through the star until temperatures fell to a point where nuclear reactions ceased. For each explosion, a light curve was generated, and the explosion energies were calibrated such that each produced a light curve appropriate for a typical Type II-P supernova. r-, p-, and γ-processes were not accounted for in the reaction network, but s-process reactions were considered for isotopes below A=66.

B.2 Maeda & Nomoto 2003 (MN03)

Maeda & Nomoto (2003) explores bipolar supernova explosions that are driven by accretion onto a central object due to a jet. This allows for higher explosion energies and different emergent ejecta patterns than one would expect to see in a typical spherical explosion model,

and is able to explain some of the features found in the lightcurves of hypernovae (supernova explosions with energies 10 or more times larger than the canonical value). They explored a variety of model parameters for the jets over two masses – 25 and 40 $M_\odot$ – and used a reaction network of 222 isotopes to determine the final nucleosynthetic products.

B.3 Nomoto et al. 2006 (N06)

The models of Nomoto et al. (2006) examines stellar mass (using stars of 13, 15, 18, 20, 25, 30, and 40 $M_\odot$), metallicity (using values for Z of 0, 0.001, 0.02, and 0.004), and energies (using the canonical value of 10^{51} ergs, as well as values of$1 - 4 \times 10^{52}$ ergs) to explore nucleosynthesis yields for supernova and hypernovae. The model uses the same code as Woosley & Weaver (1995), but adds mixing and fallback into the model through the inclusion of Rayleigh-Taylor instabilities during the shock propagation. This results in asymmetrical, high-energy explosions, not unlike those caused by the jets of Maeda & Nomoto (2003). The authors do not note what form of reaction network is used in their simulations.

B.4 Sukhbold et al. 2016 (S16)

One of the few sets of core collapse models that considers masses below 15 $M_\odot$, Sukhbold et al. (2016) presents a large set of 200 models with masses ranging from 9.0 $M_\odot$ up to 120 $M_\odot$, though whose metallicities are all presumed to be solar. These simulations made use of a novel neutrino transport model for the explosion. One-dimensional code was initially used to generated six different "central engines": five corresponding to SN1987A (the well-studied SN event in the LMC), and one corresponding to SN1054 (the SN event responsible for the creation of the Crab Nebula). The parameters for these central engines were adjusted so as to

yield appropriate kinetic energies, neutrino-burst timescales, and ^{56}Ni mass based on which SN event they corresponded to, and were placed in the 200 pre-SN stars to explore the outcomes. An adaptive nuclear reaction network of up to 2000 nuclei – including nucleosyntheis from the r-, s-, and γ-processes – was used, and the electron abundance was updated at each step unlike the constant value used in other models.

C

Supplementary Data

In the interest of space, we have elected to not include the entirety of our resultant data in the body of this work. Instead, we have elected to include them electronically, via the Center for Open Science's Open Science Framework (OSF). Below, one will find links to the full tables used to determine the goodness of fit, as well as the complete collection of nucleosynthesis plots for each object. To view the data in question, please follow the relevant link, then select

the "Project → Project Details → Files" tab on the left of the screen.

C.1 Goodness of Fit Tables

The full tables used in our determination of the quality of a fit when comparing models of supernova nucleosynthesis yields to our observations of supernova remnants can be found at the following link:

https://osf.io/9dkfs/?view_only=fddc33c85319450eb626890598722676

C.2 Nucleosynthesis Plots

The complete collection of nucleosynthesis plots for each object involved in this study, in which each object is compared to every tested model of supernova nucleosynthesis, can be found at the following link:

https://osf.io/3t2w7/?view_only=bad66f66f3654a7b84060c207f140b93

References

Aharonian, F., Akhperjanian, A. G., Barres de Almeida, U., et al. 2008, A&A, 488, 219

Alan, N. & Bilir, S. 2022, MNRAS, 511, 5018

Anders, E. & Grevesse, N. 1989, Geochimica et Cosmochimica Acta, 53, 197

Arnaud, K. A. 1996, in Astronomical Society of the Pacific Conference Series, Vol. 101, Astronomical Data Analysis Software and Systems V, ed. G. H. Jacoby & J. Barnes, 17

Arnett, D. 1996, Supernovae and Nucleosynthesis: An Investigation of the History of Matter from the Big Bang to the Present (Princeton University Press)

Aschenbach, B. 2002, in Neutron Stars, Pulsars, and Supernova Remnants, ed. W. Becker, H. Lesch, & J. Trümper, 13

Asplund, M., Grevesse, N., Sauval, A. J., & Scott, P. 2009, Annual Review of Astronomy and Astrophysics, 47, 481

Baade, W. 1943, ApJ, 97, 119

Badenes, C., Harris, J., Zaritsky, D., & Prieto, J. L. 2009, ApJ, 700, 727

Badenes, C., Hughes, J. P., Cassam-Chenaï, G., & Bravo, E. 2008, ApJ, 680, 1149

Blair, W. P., Long, K. S., & Vancura, O. 1991, ApJ, 366, 484

Borkowski, K. J., Lyerly, W. J., & Reynolds, S. P. 2001, ApJ, 548, 820

Borkowski, K. J., Reynolds, S. P., Green, D. A., et al. 2010, ApJ, 724, L161

Borkowski, K. J., Reynolds, S. P., Hwang, U., et al. 2013, ApJ, 771, L9

Boyle, W. & Smith, G. 1970, Bell System Technical Journal, 49, 587

Branch, D. & Wheeler, J. C. 2017, Supernova Explosions (Springer Berlin, Heidelberg)

Bravo, E., Badenes, C., & Martínez-Rodríguez, H. 2019, MNRAS, 482, 4346

Bravo, E. & Martínez-Pinedo, G. 2012, Phys. Rev. C, 85, 055805

Burbidge, E. M., Burbidge, G. R., Fowler, W. A., & Hoyle, F. 1957, Reviews of Modern Physics, 29, 547

Cassam-Chenaï, G., Decourchelle, A., Ballet, J., et al. 2004, A&A, 414, 545

Cassam-Chenaï, G., Hughes, J. P., Ballet, J., & Decourchelle, A. 2007, ApJ, 665, 315

Caswell, J. L., Haynes, R. F., Milne, D. K., & Wellington, K. J. 1983, MNRAS, 203, 595

Chiotellis, A., Schure, K. M., & Vink, J. 2012, A&A, 537, A139

Chu, Y.-H. & Kennicutt, Jr., R. C. 1988, AJ, 96, 1874

Clark, D. H., Caswell, J. L., & Green, A. J. 1973, Nature, 246, 28

Clark, D. H., Caswell, J. L., & Green, A. J. 1975, Australian Journal of Physics Astrophysical Supplement, 37, 1

Combi, J. A., Albacete Colombo, J. F., López-Santiago, J., et al. 2010, A&A, 522, A50

Cruise, M., Guainazzi, M., Aird, J., et al. 2025, Nature Astronomy, 9, 36

Dang, L.-X., Zhou, P., Sun, L., et al. 2024, MNRAS, 529, 4117

Danziger, I. J. & Goss, W. M. 1980, Monthly Notices of the Royal Astronomical Society, 190, 47P

Dave, P., Kashyap, R., Fisher, R., et al. 2017, ApJ, 841, 58

Davies, R. D., Elliott, K. H., & Meaburn, J. 1976, MmRAS, 81, 89

De, S., Timmes, F. X., Brown, E. F., et al. 2014, ApJ, 787, 149

Decourchelle, A., Sauvageot, J. L., Audard, M., et al. 2001, A&A, 365, L218

Dennefeld, M. 1982, A&A, 112, 215

Dopita, M. A., Seitenzahl, I. R., Sutherland, R. S., et al. 2019, AJ, 157, 50

Downes, D. & Wilson, T. L. 1974, A&A, 34, 133

Dubner, G. M., Moffett, D. A., Goss, W. M., & Winkler, P. F. 1993, AJ, 105, 2251

Duncan, A. R., Stewart, R. T., Haynes, R. F., & Jones, K. L. 1997, MNRAS, 287, 722

Dyson, J. E. & Williams, D. A. 1997, The physics of the interstellar medium (CRC Press)

Edge, D. O., Shakeshaft, J. R., McAdam, W. B., Baldwin, J. E., & Archer, S. 1959, MmRAS, 68, 37

Ferrand, G. & Safi-Harb, S. 2012, Advances in Space Research, 49, 1313

Ferrand, G., Tanikawa, A., Warren, D. C., et al. 2022, ApJ, 930, 92

Fink, M., Kromer, M., Seitenzahl, I. R., et al. 2014, MNRAS, 438, 1762

Foley, R. J., Chornock, R., Filippenko, A. V., et al. 2009, AJ, 138, 376

Foster, A., Chakraborty, P., Okon, H., et al. 2023, in American Astronomical Society Meeting Abstracts, Vol. 242, American Astronomical Society Meeting Abstracts, 318.02

Freedman, W. L., Madore, B. F., Gibson, B. K., et al. 2001, ApJ, 553, 47

Fruscione, A., McDowell, J. C., Allen, G. E., et al. 2006, in Society of Photo-Optical Instrumentation Engineers (SPIE) Conference Series, Vol. 6270, Observatory Operations: Strategies, Processes, and Systems, ed. D. R. Silva & R. E. Doxsey, 62701V

Fryer, C. L., Andrews, S., Even, W., Heger, A., & Safi-Harb, S. 2018, ApJ, 856, 63

Fujishige, A., Yamauchi, S., Nobukawa, K. K., & Nobukawa, M. 2023, PASJ, 75, 907

Fukushima, K., Yamaguchi, H., Slane, P. O., et al. 2020, ApJ, 897, 62

Gamezo, V. N., Khokhlov, A. M., Oran, E. S., Chtchelkanova, A. Y., & Rosenberg, R. O. 2003, Science, 299, 77

García-Berro, E. & Lorén-Aguilar, P. 2016, Dynamical Mergers (Cham: Springer International Publishing), 1–19

Ghavamian, P., Rakowski, C. E., Hughes, J. P., & Williams, T. B. 2003, The Astrophysical Journal, 590, 833

Giacani, E., Smith, M. J. S., Dubner, G., & Loiseau, N. 2011, A&A, 531, A138

Giacani, E., Smith, M. J. S., Dubner, G., et al. 2009, A&A, 507, 841

Godinaud, L., Acero, F., Decourchelle, A., & Ballet, J. 2025, A&A, 693, A234

Green, A. J. 1974, A&AS, 18, 267

Green, D. A. 2025, Journal of Astrophysics and Astronomy, 46, 14

Green, D. A. & Gull, S. F. 1984, Nature, 312, 527

Greiner, J. & Egger, R. 1993, IAU Circ., 5709, 2

Greiner, J., Egger, R., & Aschenbach, B. 1994, A&A, 286, L35

Guest, B. T., Borkowski, K. J., Ghavamian, P., et al. 2023, ApJ, 946, 44

Guo, Y.-D. & Yang, X.-J. 2017, Research in Astronomy and Astrophysics, 17, 16

Harrus, I. M., Slane, P. O., Smith, R. K., & Hughes, J. P. 2001, ApJ, 552, 614

Hayato, A., Yamaguchi, H., Tamagawa, T., et al. 2010, ApJ, 725, 894

HEASARC XSPEC Development Team. 2014, RNEI non-equilibrium recombining collisional plasma model in XSPEC, NASA / HEASARC, model introduced in XSPEC v12.8.2 release; see XSPEC manual Appendix I.

Hendrick, S. P., Borkowski, K. J., & Reynolds, S. P. 2003, ApJ, 593, 370

Herwig, F. 2013, Evolution of Solar and Intermediate-Mass Stars (Dordrecht: Springer Netherlands), 397–445

HI4PI Collaboration, Ben Bekhti, N., Flöer, L., et al. 2016, A&A, 594, A116

Hillebrandt, W., Kromer, M., Röpke, F. K., & Ruiter, A. J. 2013, Frontiers of Physics, 8, 116

Hoeflich, P. 2017, Explosion Physics of Thermonuclear Supernovae and Their Signatures (Cham: Springer International Publishing), 1–34

Holland-Ashford, T., Lopez, L. A., & Auchettl, K. 2020, ApJ, 903, 108

Holland-Ashford, T., Slane, P., Lopez, L. A., Auchettl, K., & Kashyap, V. 2023, ApJ, 955, 77

Holland-Ashford, T., Slane, P., & Williams, B. 2025, ApJ, 986, 216

Hughes, J. P., Ghavamian, P., Rakowski, C. E., & Slane, P. O. 2003, ApJ, 582, L95

Hughes, J. P., Hayashi, I., Helfand, D., et al. 1995, ApJ, 444, L81

Hughes, J. P., Hayashi, I., & Koyama, K. 1998, ApJ, 505, 732

Hwang, U. & Gotthelf, E. V. 1997, ApJ, 475, 665

Hwang, U., Petre, R., & Hughes, J. P. 2000, ApJ, 532, 970

Immler, S. & Kuntz, K. D. 2005, ApJ, 632, L99

Isern, J. 2023, White Dwarf (Berlin, Heidelberg: Springer Berlin Heidelberg), 3243–3249

Jiang, B., Chen, Y., Wang, J., et al. 2010, ApJ, 712, 1147

Kamitsukasa, F., Koyama, K., Nakajima, H., et al. 2016, PASJ, 68, S7

Kasuga, T., Vink, J., Katsuda, S., et al. 2021, ApJ, 915, 42

Katsuda, S., Mori, K., Maeda, K., et al. 2015, ApJ, 808, 49

Keohane, J. W., Reach, W. T., Rho, J., & Jarrett, T. H. 2007, ApJ, 654, 938

Kerzendorf, W. E., Childress, M., Scharwächter, J., Do, T., & Schmidt, B. P. 2014, ApJ, 782, 27

Kinugasa, K., Torii, K., Tsunemi, H., et al. 1998, PASJ, 50, 249

Kinugasa, K. & Tsunemi, H. 1999, PASJ, 51, 239

Koester, D. 2013, White Dwarf Stars (Dordrecht: Springer Netherlands), 559–612

Kosenko, D., Helder, E. A., & Vink, J. 2010, A&A, 519, A11

Kosenko, D., Vink, J., Blinnikov, S., & Rasmussen, A. 2008, A&A, 490, 223

Krause, O., Tanaka, M., Usuda, T., et al. 2008, Nature, 456, 617

Landau, L. D. & Lifshitz, E. M. 1959, Course of Theoretical Physics (Pergamon Press)

Leahy, D. A. & Ranasinghe, S. 2016, ApJ, 817, 74

Lee, Y.-H., Koo, B.-C., Lee, J.-J., Burton, M. G., & Ryder, S. 2019, AJ, 157, 123

Leibowitz, E. M. & Danziger, I. J. 1983, MNRAS, 204, 273

Leung, S.-C. & Nomoto, K. 2018, ApJ, 861, 143

Leung, S.-C. & Nomoto, K. 2020a, ApJ, 900, 54

Leung, S.-C. & Nomoto, K. 2020b, ApJ, 888, 80

Lewis, K. T., Burrows, D. N., Hughes, J. P., et al. 2003, ApJ, 582, 770

Liu, Z.-W., Röpke, F. K., & Han, Z. 2023, Research in Astronomy and Astrophysics, 23, 082001

Livio, M. & Mazzali, P. 2018, Phys. Rep., 736, 1

Long, K. S., Helfand, D. J., & Grabelsky, D. A. 1981, ApJ, 248, 925

Longair, M. S. 2011, High Energy Astrophysics (Cambridge University Press)

Lopez, L. A., Ramirez-Ruiz, E., Castro, D., & Pearson, S. 2013, ApJ, 764, 50

Lopez, L. A., Ramirez-Ruiz, E., Huppenkothen, D., Badenes, C., & Pooley, D. A. 2011, ApJ, 732, 114

Lovegrove, E. & Woosley, S. E. 2013, ApJ, 769, 109

Maeda, K. & Nomoto, K. 2003, ApJ, 598, 1163

Maeda, K., Röpke, F. K., Fink, M., et al. 2010, ApJ, 712, 624

Maguire, K. 2016, Type Ia Supernovae (Cham: Springer International Publishing), 1–24

Martínez-Rodríguez, H., Badenes, C., Yamaguchi, H., et al. 2017, ApJ, 843, 35

Martínez-Rodríguez, H., Lopez, L. A., Auchettl, K., et al. 2020, arXiv e-prints, arXiv:2006.08681

Mathewson, D. S., Ford, V. L., Dopita, M. A., et al. 1983, ApJS, 51, 345

McEntaffer, R. L., Grieves, N., DeRoo, C., & Brantseg, T. 2013, ApJ, 774, 120

Mezger, P. G., Schraml, J., & Terzian, Y. 1967, ApJ, 150, 807

Miceli, M., Decourchelle, A., Ballet, J., et al. 2006, A&A, 453, 567

Miceli, M., Sciortino, S., Troja, E., & Orlando, S. 2015, ApJ, 805, 120

Miles, B. J., van Rossum, D. R., Townsley, D. M., et al. 2016, ApJ, 824, 59

Minkowski, R. 1943, ApJ, 97, 128

Moffett, D. A. & Reynolds, S. P. 1994, ApJ, 437, 705

NASA/CXC/SAO. 2005, G21.5-0.9: Cosmic Shell-Seekers Find a Beauty, [Online; accessed January 24, 2025]

NASA/CXC/SAO. 2015, X-ray & Infrared Images of W44, [Online; accessed September 14, 2025]

NASA/CXC/SAO. 2017a, Chandra Reveals the Elementary Nature of Cassiopeia A, [Online; accessed January 24, 2025]

NASA/CXC/SAO. 2017b, Crab Nebula: Observatories Combine to Crack Open the Crab Nebula, [Online; accessed January 24, 2025]

Nomoto, K. & Leung, S.-C. 2017, Thermonuclear Explosions of Chandrasekhar Mass White Dwarfs (Cham: Springer International Publishing), 1–39

Nomoto, K., Thielemann, F. K., & Yokoi, K. 1984, ApJ, 286, 644

Nomoto, K., Tominaga, N., Umeda, H., Kobayashi, C., & Maeda, K. 2006, Nucl. Phys. A, 777, 424

Ozawa, M., Koyama, K., Yamaguchi, H., Masai, K., & Tamagawa, T. 2009, ApJ, 706, L71

Pakmor, R. 2016, Violent Mergers (Cham: Springer International Publishing), 1–17

Pannuti, T. G., Kargaltsev, O., Napier, J. P., & Brehm, D. 2014, ApJ, 782, 102

Patnaude, D. J., Badenes, C., Park, S., & Laming, J. M. 2012, ApJ, 756, 6

Plucinsky, P., Agarwal, M., Gu, L., et al. 2025, arXiv e-prints, arXiv:2508.01089

Pye, J. P., Becker, R. H., Seward, F. D., & Thomas, N. 1984, MNRAS, 207, 649

Radhakrishnan, V., Goss, W. M., Murray, J. D., & Brooks, J. W. 1972, ApJS, 24, 49

Rakowski, C. E., Badenes, C., Gaensler, B. M., et al. 2006, ApJ, 646, 982

Rakowski, C. E., Ghavamian, P., & Hughes, J. P. 2003, ApJ, 590, 846

Rakowski, C. E., Hughes, J. P., & Slane, P. 2001, ApJ, 548, 258

Ranasinghe, S. & Leahy, D. A. 2018, AJ, 155, 204

Rauscher, T. 2020, Essentials of Nucleosynthesis and Theoretical Nuclear Astrophysics, 2514-3433 (IOP Publishing)

Rauscher, T., Nishimura, N., Hirschi, R., et al. 2016, MNRAS, 463, 4153

Reinecke, M., Hillebrandt, W., Niemeyer, J. C., Klein, R., & Gröbl, A. 1999, A&A, 347, 724

Rest, A., Suntzeff, N. B., Olsen, K., et al. 2005, Nature, 438, 1132

Reynolds, C. S., Kara, E. A., Mushotzky, R. F., et al. 2023, in Society of Photo-Optical Instrumentation Engineers (SPIE) Conference Series, Vol. 12678, UV, X-Ray, and Gamma-Ray Space Instrumentation for Astronomy XXIII, ed. O. H. Siegmund & K. Hoadley, 126781E

Reynolds, S. P. 2016, Dynamical Evolution and Radiative Processes of Supernova Remnants (Cham: Springer International Publishing), 1–24

Reynolds, S. P., Borkowski, K. J., Green, D. A., et al. 2008, ApJ, 680, L41

Reynolds, S. P., Borkowski, K. J., Green, D. A., et al. 2009, ApJ, 695, L149

Reynolds, S. P., Borkowski, K. J., Hwang, U., et al. 2007, ApJ, 668, L135

Reynoso, E. M. & Goss, W. M. 1999, AJ, 118, 926

Rho, J. & Petre, R. 1998, ApJ, 503, L167

Röpke, F. K. & Sim, S. A. 2018, Space Science Reviews, 214, 72

Ruiz-Lapuente, P. 2004, ApJ, 612, 357

Ruiz-Lapuente, P., Damiani, F., Bedin, L., et al. 2018, ApJ, 862, 124

Rybicki, G. B. & Lightman, A. P. 1979, Radiative processes in astrophysics (John Wiley & Sons, Ltd)

Safi-Harb, S., Burdge, K. B., Bodaghee, A., et al. 2023, arXiv e-prints, arXiv:2311.07673

Safi-Harb, S., Dubner, G., Petre, R., Holt, S. S., & Durouchoux, P. 2005, ApJ, 618, 321

Safi-Harb, S., Petre, R., Arnaud, K. A., et al. 2000, ApJ, 545, 922

Sánchez-Ayaso, E., Combi, J. A., Bocchino, F., et al. 2013, A&A, 552, A52

Sanders, J. S. 2006, MNRAS, 371, 829

Sankrit, R., Blair, W. P., Delaney, T., et al. 2005, Advances in Space Research, 35, 1027

Sato, T. & Hughes, J. P. 2017, ApJ, 845, 167

Sawada, M., Sato, T., Maeda, K., & Itonaga, K. 2025, PASJ

Sedov, L. I. 1959, Similarity and Dimensional Methods in Mechanics (Academic Press)

Seitenzahl, I. R., Ciaraldi-Schoolmann, F., Röpke, F. K., et al. 2013, MNRAS, 429, 1156

Seitenzahl, I. R. & Pakmor, R. 2023, Nucleosynthesis and Tracer Methods in Type Ia Supernovae (Singapore: Springer Nature Singapore), 3809–3842

Seitenzahl, I. R., Timmes, F. X., Marin-Laflèche, A., et al. 2008, ApJ, 685, L129

Seitenzahl, I. R. & Townsley, D. M. 2017, Nucleosynthesis in Thermonuclear Supernovae (Cham: Springer International Publishing), 1–24

Seward, F. D. & Charles, P. A. 2010, Exploring the X-ray Universe (Cambridge University Press)

Sezer, A. & Gök, F. 2012, MNRAS, 421, 3538

Sezer, A. & Gök, F. 2014, ApJ, 790, 81

Shen, K. J., Boubert, D., Gänsicke, B. T., et al. 2018, ApJ, 865, 15

Siegel, J., Dwarkadas, V. V., Frank, K. A., & Burrows, D. N. 2020, ApJ, 904, 175

Smith, R. C., Kirshner, R. P., Blair, W. P., & Winkler, P. F. 1991, ApJ, 375, 652

Smith, R. K., Brickhouse, N. S., Liedahl, D. A., & Raymond, J. C. 2001, ApJ, 556, L91

Someya, K., Bamba, A., & Ishida, M. 2014, PASJ, 66, 26

Stritzinger, M. D., Hsiao, E., Valenti, S., et al. 2014, A&A, 561, A146

Sugizaki, M., Mitsuda, K., Kaneda, H., et al. 2001, ApJS, 134, 77

Sukhbold, T., Ertl, T., Woosley, S. E., Brown, J. M., & Janka, H. T. 2016, ApJ, 821, 38

Sun, L. & Chen, Y. 2019, ApJ, 872, 45

Takata, A., Nobukawa, M., Uchida, H., et al. 2016, PASJ, 68, S3

Takeuchi, Y., Yamaguchi, H., & Tamagawa, T. 2016, PASJ, 68, S9

Tanikawa, A., Nomoto, K., & Nakasato, N. 2018, ApJ, 868, 90

Taubenberger, S. 2016, The Extremes of Thermonuclear Supernovae (Cham: Springer International Publishing), 1–57

Taylor, G. 1950, Proceedings of the Royal Society of London Series A, 201, 159

The AXIS Collaboration, Koss, M., Aftab, N., Allen, S. W., et al. 2025, arXiv e-prints, arXiv:2511.00253

Thielemann, F. K., Nomoto, K., & Yokoi, K. 1986, A&A, 158, 17

Travaglio, C., Hillebrandt, W., Reinecke, M., & Thielemann, F. K. 2004, A&A, 425, 1029

Treyturik, C., Braun, C., Safi-Harb, S., Fryer, C., & Ferrand, G. in press

Treyturik, C., Safi-Harb, S., & Ferrand, G. 2024, in Supernova Remnants III: An Odyssey in Space after Stellar Death, 8

Tsuji, N., Uchiyama, Y., Khangulyan, D., & Aharonian, F. 2021, ApJ, 907, 117

Tuohy, I. R., Dopita, M. A., Mathewson, D. S., Long, K. S., & Helfand, D. J. 1982, ApJ, 261, 473

van den Bergh, S., Marscher, A. P., & Terzian, Y. 1973, ApJS, 26, 19

van der Heyden, K. J., Behar, E., Vink, J., et al. 2002, A&A, 392, 955

van der Heyden, K. J., Bleeker, J. A. M., Kaastra, J. S., & Vink, J. 2003, A&A, 406, 141

Vink, J. 2016, X-Ray Emission Properties of Supernova Remnants (Cham: Springer International Publishing), 1–24

Vink, J. 2020, Physics and Evolution of Supernova Remnants (Springer Cham)

Warren, D. C. & Blondin, J. M. 2013, MNRAS, 429, 3099

Warren, J. S. & Hughes, J. P. 2004, ApJ, 608, 261

Warren, J. S., Hughes, J. P., Badenes, C., et al. 2005, ApJ, 634, 376

Westerhout, G. 1958, Bull. Astron. Inst. Netherlands, 14, 215

Whiteoak, J. B. Z. & Green, A. J. 1996, A&AS, 118, 329

Williams, B. J., Blair, W. P., Borkowski, K. J., et al. 2018, ApJ, 865, L13

Williams, B. J., Borkowski, K. J., Reynolds, S. P., et al. 2014, ApJ, 790, 139

Willingale, R. 2000, in Encyclopedia of Astronomy and Astrophysics, ed. P. Murdin, 4387

Wilms, J., Allen, A., & McCray, R. 2000, ApJ, 542, 914

Wolter, H. 1952a, Annalen der Physik, 445, 94

Wolter, H. 1952b, Annalen der Physik, 445, 286

Woosley, S. E. & Weaver, T. A. 1995, ApJS, 101, 181

Yamaguchi, H., Badenes, C., Foster, A. R., et al. 2015, ApJ, 801, L31

Yamaguchi, H., Badenes, C., Petre, R., et al. 2014, ApJ, 785, L27

Yamaguchi, H., Hughes, J. P., Badenes, C., et al. 2017, ApJ, 834, 124

Yamaguchi, H., Koyama, K., & Uchida, H. 2011, PASJ, 63, S837

Yamaguchi, H., Tanaka, M., Maeda, K., et al. 2012, ApJ, 749, 137

Yamauchi, S., Ueno, M., Koyama, K., & Bamba, A. 2005, PASJ, 57, 459

Zhang, Q.-Q., Zhou, P., Chen, Y., et al. 2023, ApJ, 952, 107

Zhou, P. & Vink, J. 2018, A&A, 615, A150

Zhu, H., Tian, W. W., & Zuo, P. 2014, ApJ, 793, 95

University of Manitoba

This thesis was typeset using LaTeX, originally developed by Leslie Lamport and based on Donald Knuth's TeX. The body text is set in 12 point Egenolff-Berner Garamond, a revival of Claude Garamont's humanist typeface. A template that can be used to format a PhD thesis with this look and feel has been released under the permissive MIT (X11) license, and can be found online at github.com/suchow/Dissertate or from its author, Jordan Suchow, at suchow@post.harvard.edu.